



HAL
open science

Analyse, caractérisation et modélisation des matériaux viscoélastiques et poro-viscoélastiques

Isadora Ruas Henriques

► **To cite this version:**

Isadora Ruas Henriques. Analyse, caractérisation et modélisation des matériaux viscoélastiques et poro-viscoélastiques. Mécanique [physics]. HESAM Université; Universidade federal do Rio de Janeiro, 2020. Français. NNT : 2020HESAC044 . tel-04018898

HAL Id: tel-04018898

<https://theses.hal.science/tel-04018898v1>

Submitted on 8 Mar 2023

HAL is a multi-disciplinary open access archive for the deposit and dissemination of scientific research documents, whether they are published or not. The documents may come from teaching and research institutions in France or abroad, or from public or private research centers.

L'archive ouverte pluridisciplinaire **HAL**, est destinée au dépôt et à la diffusion de documents scientifiques de niveau recherche, publiés ou non, émanant des établissements d'enseignement et de recherche français ou étrangers, des laboratoires publics ou privés.

ÉCOLE DOCTORALE SCIENCES DES MÉTIERS DE L'INGÉNIEUR
Laboratoire de Mécanique des Structures et des Systèmes Couplés
Laboratório de Acústica e Vibrações

THÈSE

présentée par : **Isadora RUAS HENRIQUES**
soutenue le : **18 décembre 2020**

pour obtenir le grade de : **Docteur d'HESAM Université**

préparée au : **Conservatoire national des arts et métiers et de
l'Universidade Federal do Rio de Janeiro**

Discipline : **Mécanique, génie mécanique, génie civil**

Spécialité : **Mécanique**

Analysis, characterization and modeling of viscoelastic and poro-viscoelastic materials

THÈSE dirigée par :

M. Jean-François DEÛ Professeur des Universités, Cnam Paris

M. Daniel CASTELLO Associate Professor, UFRJ

et co-encadrée par :

Mme Lucie ROULEAU Maître de Conférences, Cnam Paris

Jury

M. Domingos RADE

Professor, ITA

Président

M. Gaël CHEVALLIER

Professeur des Universités, UFC

Rapporteur

M. Marcelo TRINDADE

Professor, USP

Rapporteur

M. Thiago RITTO

Associate Professor, UFRJ

Examineur

M. Jean-François DEÛ

Professeur des Universités, Cnam Paris

Examineur

M. Daniel CASTELLO

Associate Professor, UFRJ

Examineur

Mme Lucie ROULEAU

Maître de Conférences, Cnam Paris

Examineur

T
H
È
S
E

“Learn from yesterday, live for today, hope for tomorrow. The important thing is not to stop questioning.”- Albert Einstein

Acknowledgements

Foremost, I would like to thank God who always is at my side, guiding me in the moments of doubt and uncertainty, giving me strength in difficult times. I am grateful for the victories accomplished, for the prevailed challenges, the knowledge acquired and all support during this journey.

I would like to express my sincere gratitude to my advisors Professors Daniel Castello, Jean-François Deü and Lucie Rouleau for the motivation and support along this journey. I am very grateful to you for organizing this collaboration, which gave me the opportunity to witness and experience two different approaches of the academic world. Also, I would like to acknowledge the guidance and teaching of Professor Lavinia Borges who also contributed to this work.

I gratefully acknowledge the members of my thesis committee for their availability, attention and professionalism: Professors Gaël Chevallier and Marcelo Trindade for their role as reviewers of the manuscript for this thesis, and Professors Domingos Rade and Thiago Ritto for accepting to be president of the jury and examiner, respectively.

I would also like to thank Professors Bluma Soares, Marysilvia Costa and Marcelo Savi for allowing me to use testing equipment at their laboratories.

To all the people I met at UFRJ and Cnam, who have contributed to create a really nice work environment on a daily basis. Special thanks goes to Aline Rigueti, Chaïma Soussi, Henrique Costa, Naim Ayoub, Pedro Ponte and Reniene Barbosa.

I must mention my parents, my sister and my partner Dimitri Costa who provided me with unfailing support and encouragement throughout my years of study. I also thank the rest of my family and my dear friends, both near and far. I know I have not been very available in the past few years for you and it's up to me to make that change.

To CAPES for the financial support.

ACKNOWLEDGEMENTS

ACKNOWLEDGEMENTS

ACKNOWLEDGEMENTS

Résumé

Cette thèse porte sur la modélisation et la caractérisation du comportement thermomécanique des matériaux viscoélastiques et poro-viscoélastiques. Le travail est divisé en deux parties principales : une concerne la technique expérimentale d'analyse mécanique dynamique (Dynamic Mechanical Analysis DMA) et l'autre s'intéresse aux performances d'amortissement des matériaux poro-viscoélastiques. Dans la première partie, les propriétés viscoélastiques décrites à partir du module complexe et mesurées par DMA en flexion, sont analysées en profondeur à la fois d'un point de vue théorique et expérimental. Une attention particulière est accordée aux effets des modes opératoires et des machines d'essais utilisées sur les propriétés mesurées. Afin d'obtenir une meilleure analyse de l'influence des écarts constatés, des modèles à dérivées fractionnaires (FDM) sont calibrés dans le cadre bayésien. Les résultats montrent qu'il existe une grande variabilité en fonction des modes de fonctionnement ou des fabricants de machines et que les modèles statistiques peuvent expliquer ces différences. Dans la deuxième partie, la dissipation de l'énergie mécanique due à la viscoélasticité de trois matériaux poreux différents est explorée dans la gamme des basses fréquences. Dans un premier temps, une approche numérique est proposée pour générer des prédictions dans le domaine temporel du comportement hystérique des matériaux sous différentes conditions de chargement. Ensuite, un modèle éléments finis utilisant un FDM est proposé pour décrire le comportement de panneaux simplement appuyés et recouverts d'une couche libre de matériau poreux. Des expériences sont réalisées pour valider le modèle proposé. Enfin, une méthode inverse basée sur l'inférence bayésienne est présentée pour identifier les propriétés viscoélastiques de ces matériaux à partir d'essais de vibration. Les résultats de ces analyses montrent le grand potentiel des matériaux poro-viscoélastiques pour l'amortissement des vibrations mécaniques.

Mots-clés : Matériaux viscoélastiques, Matériaux poreux, DMA, Essais mécaniques, Modélisation thermomécanique, Inférence bayésienne.

RESUME

Abstract

This thesis deals with the modeling and characterization of the thermomechanical behavior of viscoelastic and poro-viscoelastic materials. The work is divided into two main parts: one concerning the experimental technique Dynamic Mechanical Analysis (DMA) and the other related to the damping performance of poro-viscoelastic materials. In the first part, the viscoelastic property known as complex modulus measured by the flexural modes of DMA is deeply examined theoretically and experimentally. Special attention is paid to the effects of operational modes and machines on various properties. Aiming to obtain a better analysis of the impacts of the discrepancies found, fractional derivative models (FDM) are calibrated within the Bayesian framework. Results show that DMAs have a great variability between modes or manufacturers and statistical models may mitigate these issues. In the second part, the dissipation of mechanical energy inherent to the viscoelasticity of three different porous materials is explored in the low-frequency range. Initially, a numerical approach is proposed to generate predictions in the time domain of the hysteretic behavior of the analyzed materials under different loading conditions. Then, a finite element model that considers a FDM is proposed to describe the behavior of simply supported panels covered with a free-layer of porous material. Experiments are carried out to validate the proposed model. Finally, an inverse method based on Bayesian inference was presented to identify the viscoelastic properties of these materials from vibration tests. The results of these analyses showed the great potential of poro-viscoelastic materials to be applied to damp mechanical vibrations.

Keywords : Viscoelastic materials, Porous materials, DMA, Mechanical testing, Thermomechanical modeling, Bayesian inference.

ABSTRACT

Résumé étendu

1. Introduction

Au cours des dernières années, différentes industries ont développé de nouveaux matériaux visant à améliorer les performances de leurs produits. Dans ce contexte, il est possible de mettre en évidence les progrès liés à l'utilisation de matériaux dit viscoélastiques, notamment à des fins de contrôle du bruit et des vibrations.

Ces matériaux ont des caractéristiques à la fois élastiques et visqueuses, ce qui les rend capables de dissiper une partie de l'énergie vibratoire. Néanmoins, leur réponse peut varier considérablement en fonction des conditions auxquelles ils sont soumis. Une caractérisation appropriée et une modélisation soignée de ces matériaux deviennent donc de la plus haute importance pour la conception et l'analyse des structures [7, 14].

Dans cette thèse, on se concentre initialement sur le module complexe mesuré par la technique expérimentale appelée Analyse Mécanique Dynamique. L'idée centrale est évaluer les formulations mathématiques, la répétabilité et la reproductibilité des essais expérimentaux et la manière dont ces incertitudes affectent les prédictions des modèles viscoélastiques.

En outre, on vise aussi à explorer la viscoélasticité de certains matériaux poreux dont la matrice est en polymère. D'abord, on propose des modèles simplifiés pour décrire leur comportement d'amortissement dans les domaines temporel et fréquentiel. Cela permet d'avoir un bon compromis entre précision et temps de calcul. Ensuite, on présente une approche inverse pour l'identification des propriétés viscoélastiques par l'inférence bayésienne.

Ce travail a été réalisé dans le cadre d'une cotutelle de thèse entre l'Universidade Federal do Rio de Janeiro (UFRJ) à Rio de Janeiro et le Conservatoire National des Arts et Métiers (Cnam) à Paris, co-encadré par Professeurs Daniel Castello, Jean-François Deü et Lucie Rouleau.

Partie I. Aspects Théoriques

La première grande partie de cette thèse présente les principaux aspects théoriques qui ont permis le développement de ce manuscrit. Elle se compose de deux chapitres décrits ci-dessous.

2. Viscoélasticité linéaire

Ce chapitre aborde les concepts fondamentaux liés à la théorie de la viscoélasticité linéaire afin de faciliter la compréhension du lecteur sur la suite du manuscrit. Tout d'abord, la définition des matériaux viscoélastiques est présentée, ainsi que les trois phénomènes qui leur sont couramment associés : la relaxation, la fluage et les phénomènes d'hystérésis. Ensuite, la loi de comportement sous la forme d'une intégrale héréditaire est établie par le principe de superposition de Boltzmann, ce qui met en évidence la dépendance temporelle. Le comportement de ces matériaux est alors analysé lorsqu'ils sont soumis à un chargement dynamique, permettant de faire apparaître la notion de module complexe. Différents modèles mathématiques basés sur des analogues mécaniques (ressort-amortisseur) et des dérivés fractionnaires sont également abordés. Enfin, les effets du temps/de la fréquence et de la température sur leurs propriétés mécaniques sont abordés. On se concentre principalement sur les matériaux thermo-rhéologiques et le principe de superposition temps-température. Les équations et les concepts de chaque sujet sont détaillés dans la thèse.

3. Problèmes inverses dans le cadre bayésien

Le troisième chapitre de la thèse aborde les principales idées de calibration et de validation des modèles mathématiques, en plus de la quantification des incertitudes. Dans un premier temps, l'estimation des paramètres par une approche bayésienne est contextualisée. Ensuite, la méthode numérique de Monte Carlo par chaîne de Markov (en anglais, *Markov Chain Monte Carlo*, MCMC), notamment utilisée pour résoudre ce type de problème, est présentée. Les principaux algorithmes de Metropolis-Hastings (MH), Adaptive Metropolis (AM), Delayed Rejection (DR) et Delayed Rejection Adaptive metropolis (DRAM) sont discutés. Après, les concepts et méthodes de validation et de vérification (V&V) sont définis. Enfin, la quantification des incertitudes par la méthode de Monte Carlo est abordée. Les détails de chaque sujet sont présentés dans la thèse.

Partie II. Analyse Mécanique Dynamique

L'analyse mécanique dynamique (en anglais, *dynamic mechanical analysis*, DMA) est une méthode couramment utilisée pour caractériser le comportement des matériaux. Elle permet d'étudier plusieurs aspects des matériaux tels que la composition, le comportement physique et les propriétés viscoélastiques.

D'une manière générale, cette technique est polyvalente. Différents types d'essais et différentes conditions de test peuvent être utilisés, selon le modèle d'équipement et ses accessoires. Néanmoins, une analyse de la littérature montre que les valeurs absolues du module complexe et des températures liées aux transitions de phase peuvent diverger entre les échantillons, les porte-échantillons et les paramètres de test.

Cette seconde partie de la thèse est dédiée à l'étude du module complexe, qui est la principale propriété viscoélastique identifiée par DMA, mesuré par les modes de flexion. Elle est divisée en deux chapitres comme décrits ci-dessous.

4. Module complexe mesuré par un analyseur mécanique dynamique

L'objectif de ce chapitre est d'évaluer les impacts de différents modes de flexion et équipements sur les mesures du module complexe. Tout d'abord, on détaille la formulation mathématique utilisée par chaque machine testée dans ce travail. Ensuite, on effectue un premier cas d'étude concernant ces effets sur le module complexe dépendant de la température et sur la température de transition vitreuse. Enfin, un deuxième cas d'étude est analysé pour étudier l'influence de la fréquence et de la température sur le module complexe et sur le comportement à long terme du matériau. Une attention particulière est portée à la répétabilité et à la reproductibilité des essais.

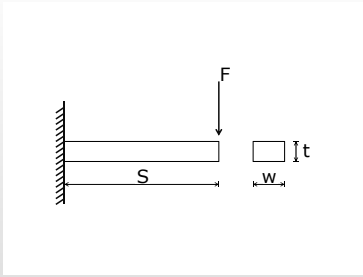
4.1. Formulation mathématique

Les trois modes de flexion existant dans les équipements DMA sont un simple encastrement (en anglais, *single cantilever*, SC), un double encastrement (en anglais, *dual cantilever*, DC) et une flexion 3 points (en anglais, *three-point bending*, 3PT). Chacun correspond à un modèle mathématique spécifique pour le calcul du module complexe. De façon plus générale, ces formulations sont basées sur les conditions aux limites (figures 1-3), les théories d'élasticité et de viscoélasticité, en plus des hypothèses

retenues par le fabricant de la machine.

Dans cette thèse, on utilise trois équipements de différents fabricants : PerkinElmer 8000 (PE), TA Q800 (TA) et Netzsch 242 E Artemis (NET). Les équations pour chaque mode de flexion sont présentées ci-dessous, où K_s est la rigidité mesurée définie comme le rapport entre la force appliquée à l'échantillon F et l'amplitude du déplacement a , S est la distance entre les appuis fixes, $l = S/2$, I est le moment d'inertie, t est l'épaisseur de l'échantillon et ν est le coefficient de Poisson.

Simple encastrement (SC)



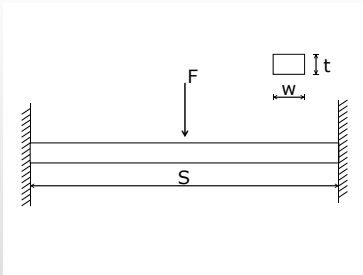
$$|E_{SC}^*(\omega)|_{PE} = K_s \frac{S^3}{12I} \left[1 + 2.9 \left(\frac{t}{S} \right)^2 \right], \quad (1a)$$

$$|E_{SC}^*(\omega)|_{TA} = \frac{1}{F_c} K_s \frac{S^3}{12I} \left[1 + 2.4(1 + \nu) \left(\frac{t}{S} \right)^2 \right], \quad (1b)$$

$$|E_{SC}^*(\omega)|_{NET} = K_s \frac{S^3}{12I}. \quad (1c)$$

Figure 1: Modèle SC

Double encastrement (DC)



$$|E_{DC}^*(\omega)|_{PE} = K_s \frac{l^3}{24I} \left[1 + 2.9 \left(\frac{t}{l} \right)^2 \right], \quad (2a)$$

$$|E_{DC}^*(\omega)|_{TA} = \frac{1}{F_c} K_s \frac{S^3}{24I} \left[1 + 2.4(1 + \nu) \left(\frac{2t}{S} \right)^2 \right], \quad (2b)$$

$$|E_{3PT}^*(\omega)|_{NET} = K_s \frac{S^3}{192I}. \quad (2c)$$

Figure 2: Modèle DC

Flexion 3 points (3PT)

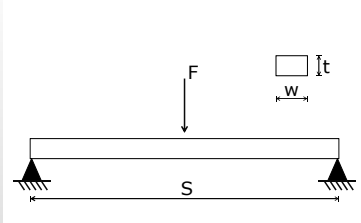


Figure 3: Modèle 3PT

$$|E_{3PT}^*(\omega)|_{PE} = K_s \frac{S^3}{48I} \left[1 + 2.9 \left(\frac{t}{S} \right)^2 \right], \quad (3a)$$

$$|E_{3PT}^*(\omega)|_{TA} = K_s \frac{S^3}{6I} \left[1 + 0.6(1 + \nu) \left(\frac{2t}{S} \right)^2 \right], \quad (3b)$$

$$|E_{3PT}^*(\omega)|_{NET} = K_s \frac{S^3}{48I}. \quad (3c)$$

4.2. Dispositif expérimental et matériau testé

Comme indiqué précédemment, les trois machines utilisées sont PerkinElmer 8000 (PE), TA Q800 (TA) et Netzsch 242 E Artemis (NET). Leurs limites opérationnelles sont résumées dans le tableau 1.

Quant au matériau testé, on choisit la résine époxy car sa procédure de fabrication des échantillons est bien maîtrisée. Deux lots d'échantillons (un pour chaque étude) ont été produits et conditionnés de la même manière, ce qui réduit encore les incertitudes quant à la variabilité du matériau.

Table 1: Caractéristiques techniques de chaque machine DMA.

| Caractéristiques | NET | PE 8000 | TA Q800 |
|---|-------------|-------------|--------------------|
| Plage de temperature [°C] | -170 to 600 | -190 to 400 | -150 to 600 |
| Vitesse de chauffage [°C/min] | 0.01 to 20 | 0 to 20 | 0.1 to 20 |
| Bande de fréquence [Hz] | 0.01 to 100 | 0 to 600 | 0.01 to 200 |
| Résolution de fréquence [Hz] | | 0.001 | |
| Plage de déplacement [μm] | ± 240 | ± 1000 | ± 0.5 to 10000 |
| Résolution de déplacement [μm] | 0.0005 | 0.001 | 0.001 |
| Force [N] | 24 | ± 10 | ± 18 |
| Résolution de la force [N] | 0.0005 | 0.002 | 0.00001 |

4.3. Cas d'étude I: influence de la température

Dans cette étude, on évalue la répétabilité et la reproductibilité des valeurs estimées pour le module complexe lorsqu'il est mesuré en fonction de la température par les essais de flexion (SC, DC et 3PT) sur trois machines DMA (PE, TA et NET). De plus, on vise également à observer expérimentalement les effets de la géométrie d'échantillon.

Pour atteindre ces objectifs, on a appliqué des conditions de test (plage de température, vitesse de chauffage, amplitude de déplacement, tailles des échantillons) assez similaires, respectant les limites opérationnelles de chaque équipement. Aussi, on a testé des échantillons de tailles très différentes sur l'équipement PE grâce à la flexibilité de ses porte-échantillons. Les conditions et paramètres de chaque test sont détaillés dans la thèse.

La figure 4 montre les valeurs moyennes et les écarts types du module de stockage mesurés expérimentalement. On vérifie qu'on obtient une bonne répétabilité des tests. Cependant, les valeurs estimées pour le module sont nettement altérées par le mode de fonctionnement, l'équipement et même les dimensions des échantillons. On observe que les valeurs les plus élevées sont obtenues pour le mode 3PT.

Le tableau 2 montre les valeurs moyennes et les écarts types de la température de transition vitreuse identifiée. Comme le plus grand écart type est égal à 1.42 °C, on peut donc considérer une bonne répétabilité. Les différences entre les modes peuvent être attribuées à la position du capteur de température par rapport à l'échantillon et aussi, à la taille de la chambre thermique.

Table 2: Température de transition vitreuse.

| DMA Machine | PE - Set 1 | PE - Set 2 | TA | NET |
|-------------|--------------|--------------|--------------|--------------|
| SC | 61.21 ± 0.34 | 61.80 ± 0.60 | 63.99 ± 1.42 | - |
| DC | 56.44 ± 1.03 | 59.30 ± 0.39 | 61.59 ± 0.99 | - |
| 3PT | 51.57 ± 0.52 | 56.86 ± 0.50 | 58.63 ± 0.11 | 56.95 ± 0.56 |

Enfin, on réalise une étude paramétrique sur les effets des dimensions et des propriétés mécaniques (S, w, t, K_s, ν) qui interviennent dans les formulations mathématiques. Il est évident que les différentes équations estiment différentes valeurs. De plus, le mode DC est le plus sensible aux changements.

4.4. Cas d'étude II: influence de la température et de la fréquence

Cette étude a deux objectifs principaux. Le premier est lié à l'analyse de la répétabilité et la reproductibilité des valeurs estimées pour le module lorsqu'il est mesuré en fonction de la température et de la fréquence par les modes de flexion. Le second consiste à de déterminer le comportement à long terme du matériau par le principe de superposition et à évaluer sa variabilité selon le type de test.

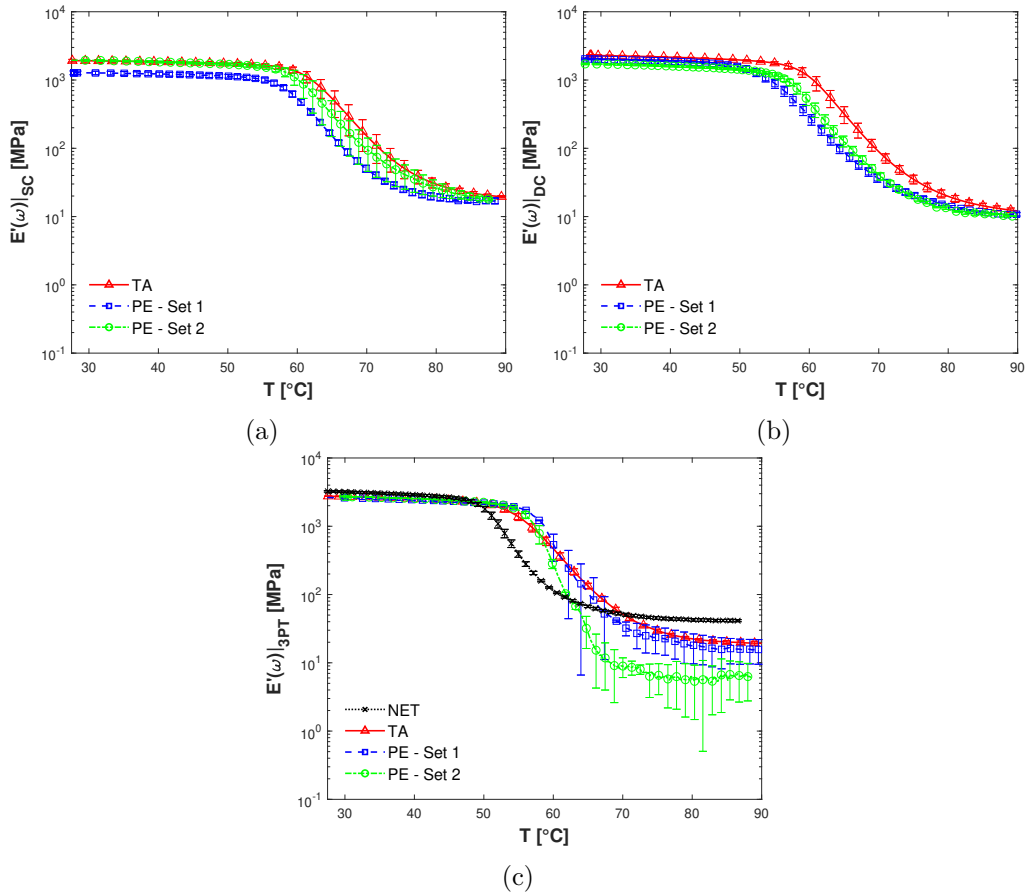


Figure 4: Comparaison entre les modules de stockage mesurés par différentes machines. (a) $E'(\omega)|_{SC}$, (b) $E'(\omega)|_{DC}$ et (c) $E'(\omega)|_{3PT}$.

Pour cela, on effectue des essais avec les modes SC, DC et 3PT sur les équipements TA et PE. On choisit des conditions de test similaires, respectant les limites opérationnelles de chaque équipement. Les détails sont présentés dans la thèse.

Comme pour le premier cas d'étude, on obtient une répétabilité des tests satisfaisante. On peut aussi vérifier que les effets de la température et de la fréquence sont compatibles avec la théorie de la viscoélasticité. En revanche, des différences entre les modes et machines peuvent être observées. Quelques résultats obtenus pour le module de stockage sur la machine TA et tracés sur la figure 5 en témoignent.

Une fois le module complexe mesuré, on procède à la validation du comportement thermorhéologique simple. A cet effet, on trace les diagrammes de Cole-Cole et Black. On peut visualiser que cette hypothèse est vérifiée pour tous les résultats malgré les différences entre les valeurs estimées du module.

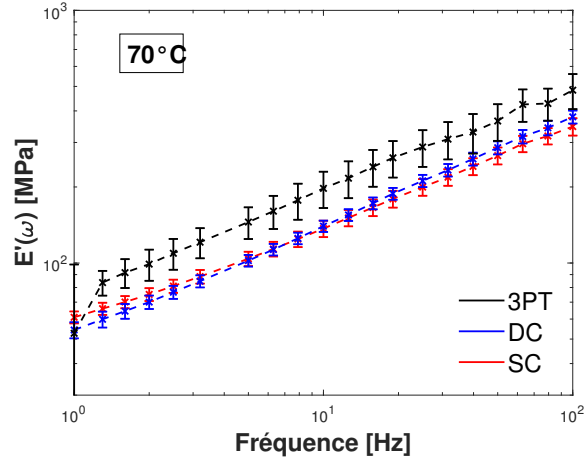


Figure 5: Module de stockage $E'(\omega, T_0)|_{TA}$ mesuré par la machine TA.

Enfin, on applique le principe de superposition temps-température pour générer des courbes maîtresses et par conséquent, identifier le comportement à long terme. Les facteurs de translation horizontale nécessaires à cette procédure sont déterminés par la méthode proposée par Rouleau et al. [2] puis validés par la calibration du modèle de l'équation Williams–Landel–Ferry (WLF). Les figures 6 et 7 montrent les courbes maîtresses générées pour les modules de stockage et de perte dans tous les tests effectués.

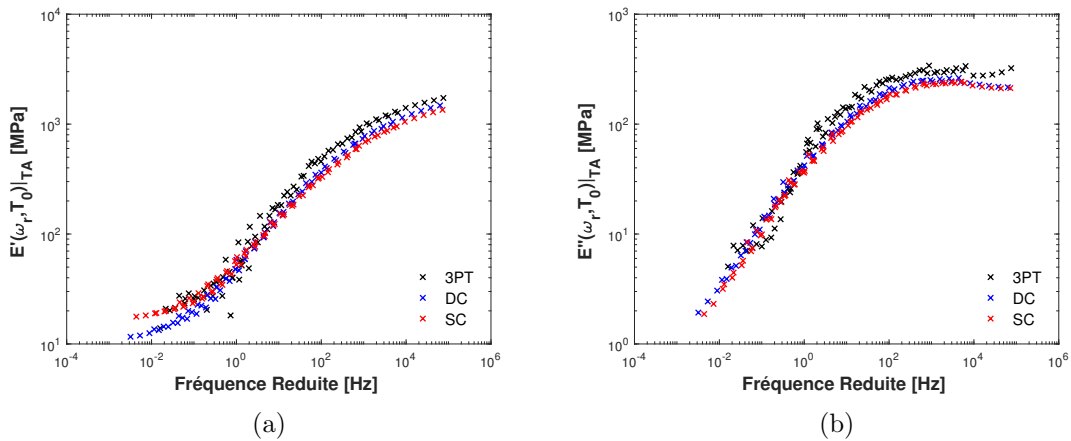


Figure 6: Comparaison entre les courbes maîtresses générées à partir des mesures obtenues par la machine TA. (a) Module de stockage $E'(\omega, T_0)|_{TA}$ et (b) module de perte $E''(\omega, T_0)|_{TA}$.

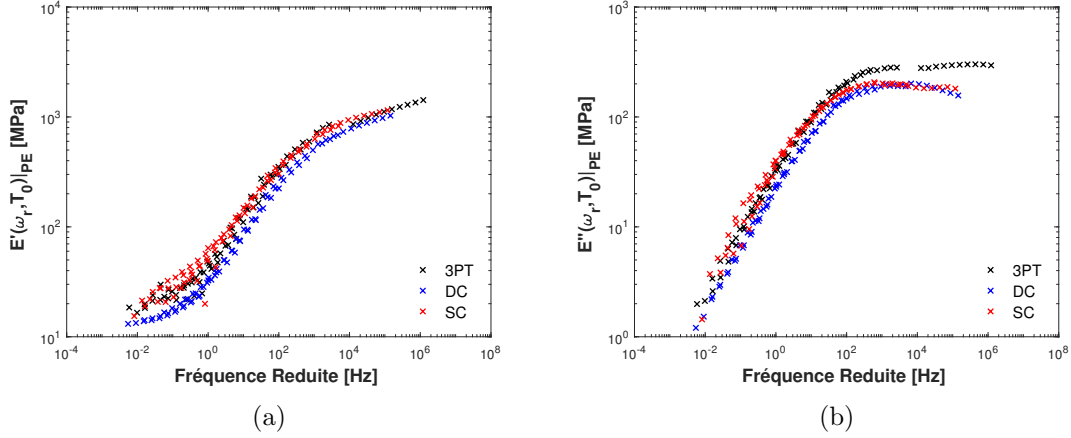


Figure 7: Comparaison entre les courbes maîtresses générées à partir des mesures obtenues par la machine PE. (a) Module de stockage $E'(\omega, T_0)|_{PE}$ et (b) module de perte $E''(\omega, T_0)|_{PE}$.

5. Modélisation du module complexe par approche bayésienne

Ce chapitre traite de la calibration de modèles viscoélastiques par approche bayésienne pour le module complexe. L'objectif principal est d'analyser les effets des incertitudes inhérentes aux mesures des trois modes de flexion par DMA dans les prédictions de modèles calibrés. Pour cela, on considère les courbes maîtresses expérimentales obtenues au chapitre précédent.

5.1. Modèle viscoélastique

Pour décrire le comportement du module complexe, on choisit le modèle à dérivée fractionnaire à cinq paramètres. En effet, il permet de prédire l'asymétrie observée dans les courbes expérimentales du module de perte, et le comportement du module de stockage aux hautes fréquences. Ainsi, le module complexe est exprimé par

$$E^*(\omega) = E_0 + \frac{(E_\infty - E_0)(j\omega\tau)^\alpha}{1 + (j\omega\tau)^\beta}, \quad (4)$$

où E_0 est le module relaxé, E_∞ est le module non-relaxé, τ est le temps de relaxation, α et β sont les ordres fractionnaires. Ces cinq paramètres doivent respecter les conditions thermodynamiques suivantes: $E_\infty > E_0 > 0$, $\tau > 0$, $0 < \alpha < 1$, $0 < \beta < 1$ et $\alpha > \beta$. De plus, ils doivent être estimés à partir d'une méthode inverse.

5.2. Description du processus de calibration

Dans ce travail, on utilise l'approche bayésienne pour estimer les cinq paramètres du modèle choisi, $\theta = \{E_0, E_\infty, \tau, \alpha, \beta\}$. Pour cela, on considère une loi a priori non informative: chaque paramètre est décrit par une loi a priori uniforme. L'hypothèse d'une indépendance mutuelle a été adoptée. Par ailleurs, on considère que le bruit est additif ce qui conduit à une fonction de vraisemblance décrite par une loi Gaussienne.

Le processus de calibration comprend deux étapes. La première réalise une analyse déterministe utilisant l'estimateur du maximum a posteriori (MAP). La seconde étape consiste à appliquer la méthode de Monte Carlo par chaîne de Markov (MCMC) en utilisant l'algorithme DRAM. Les détails théoriques et pratiques d'implémentation sont donnés dans la thèse.

5.3. Résultats

Le tableau 3 montre la valeur attendue ainsi que l'intervalle de confiance à 95 % de chaque paramètre estimé en considérant les résultats expérimentaux de la machine TA. On note que les valeurs varient selon le mode de fonctionnement et que les plus élevées sont estimées en général pour le mode 3PT. Cependant, on obtient une bonne concordance entre les intervalles de confiance. Sur la figure 8, on compare les modèles stochastiques obtenus dans cette analyse, ce qui met en évidence l'importance de considérer les incertitudes dans les prédictions du modèle.

Par ailleurs, on peut parvenir à des conclusions similaires si l'on analyse les résultats obtenus pour le module complexe mesuré par la machine PE. Ils sont présentés dans la thèse.

Table 3: Valeur attendue et intervalle de confiance (CI) à 95 % de chaque paramètre inconnu θ obtenus à partir de données provenant de la machine TA.

| Mode | $\mathbb{E}[E_0]$ [$\times 10^7$ Pa] | $\mathbb{E}[E_\infty]$ [$\times 10^9$ Pa] | $\mathbb{E}[\tau]$ [$\times 10^{-3}$ s] | $\mathbb{E}[\alpha]$ | $\mathbb{E}[\beta]$ |
|------|---------------------------------------|--|--|----------------------|---------------------|
| | 95 % CI | 95 % CI | 95 % CI | 95 % CI | 95 % CI |
| SC | 2.19 | 0.80 | 1.68 | 0.55 | 0.46 |
| | [0.11, 5.26] | [0.48, 1.24] | [0.21, 5.24] | [0.44, 0.72] | [0.36, 0.59] |
| DC | 2.54 | 0.75 | 3.43 | 0.63 | 0.51 |
| | [0.13, 6.74] | [0.40, 1.30] | [0.27, 13.26] | [0.44, 0.89] | [0.36, 0.74] |
| 3PT | 3.43 | 0.71 | 8.64 | 0.70 | 0.57 |
| | [0.14, 8.57] | [0.39, 1.26] | [0.64, 35.56] | [0.49, 0.96] | [0.38, 0.80] |

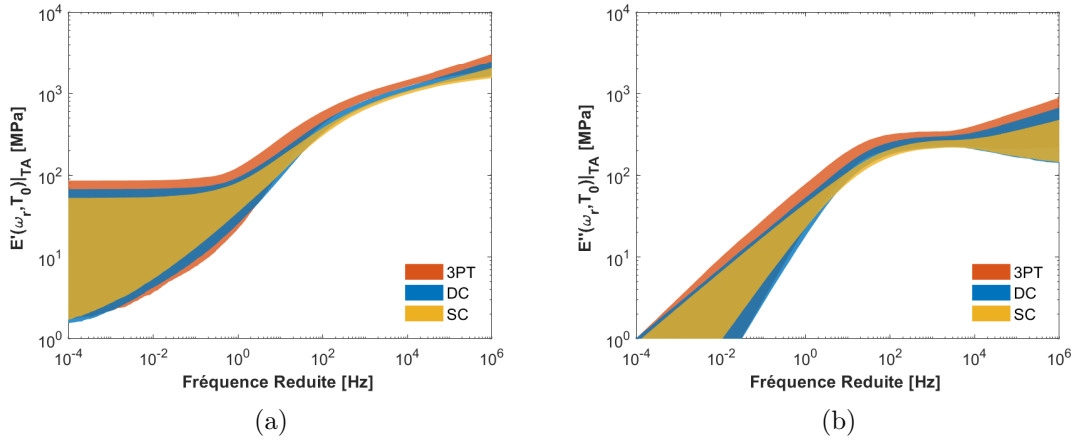


Figure 8: Comparaison entre les modèles calibrés des modes SC, DC et 3PT. (a) $E'(\omega_r, T_0)|_{TA}$ et (b) $E''(\omega_r, T_0)|_{TA}$.

Partie III. Matériaux Poro-viscoélastiques

La troisième grande partie est consacrée à l'étude du comportement dissipatif de différents matériaux poreux dans la gamme des basses fréquences. Elle est également composée de deux chapitres décrits ci-dessous.

6. Performances d'amortissement des mousses polymères dans la gamme des basses fréquences

Dans ce chapitre, on modélise la dissipation de l'énergie mécanique de deux mousses polymères lorsque ces matériaux sont soumis à des charges cycliques (domaine temporel) et à des vibrations structurelles (domaine fréquentiel). L'objectif est de relier les propriétés viscoélastiques mesurées par des tests DMA à leurs performances d'amortissement dans les applications dynamiques à basse fréquence. Pour cela, on considère uniquement la phase viscoélastique solide puisque les interactions fluide-structure peuvent être négligées dans la région des basses fréquences.

6.1. Description des matériaux testés

Afin d'explorer les différents comportements viscoélastiques, on étudie une mousse de mélamine à cellules ouvertes (mousse A) et une mousse de polyurethane à cellules fermées (mousse B). Ces deux matériaux ont été caractérisés précédemment par Bonfiglio et al. [98] et Henriques et al. [1].

Le tableau 4 ci-dessous présente les paramètres du modèle fractionnaire de Zener identifiés à 20 °C par Henriques et al. [1]. Ils seront utilisés dans ce chapitre pour décrire le module de cisaillement complexe.

Table 4: Paramètres du modèle fractionnaire de Zener, où G_0 est le module de cisaillement relaxé, G_∞ est le module de cisaillement non-relaxé, τ est le temps de relaxation et α est l'ordre fractionnaire.

| Mousse | G_0 [Pa] | G_∞ [Pa] | τ [s] | α |
|--------|--------------------|--------------------|-----------------------|----------|
| A | 4.79×10^4 | 8.63×10^4 | 1.32×10^{-1} | 0.43 |
| B | 1.31×10^4 | 2.11×10^6 | 4.70×10^{-8} | 0.30 |

6.2. Cas d'étude I: chargement cyclique

La première étude propose une approche numérique pour estimer la dissipation de l'énergie mécanique lorsque des mousses polymères sont soumises à des chargements cycliques unidimensionnels dans le domaine temporel. Pour ce faire, on considère ici que le comportement de ces matériaux est décrit par le modèle de Zener dont la relation constitutive est présentée dans l'équation 5 et dont les paramètres sont indiqués dans le tableau 4.

$$\sigma(t) + \tau^\alpha \frac{d^\alpha \sigma(t)}{dt^\alpha} = G_0 \varepsilon(t) + G_\infty \tau^\alpha \frac{d^\alpha \varepsilon(t)}{dt^\alpha}. \quad (5)$$

L'approche consiste à appliquer un chargement cyclique unidimensionnel sur le matériau puis à estimer sa réponse à partir de son équation constitutive en utilisant la méthode d'intégration numérique basée sur des matrices bandes triangulaires [133]. Enfin, on trace le graphique des contraintes et déformations pour analyser les cycles d'hystérésis et, par conséquent, la performance d'amortissement de ces matériaux.

Deux cas numériques sont étudiés dans ce manuscrit. Le premier évalue l'influence du chargement cyclique. Ce cas met en évidence que plus la vitesse et l'amplitude du chargement sont élevées, plus la dissipation est importante, comme le montre la figure 9. Le second cas analyse l'influence de la température puisque les matériaux possèdent un comportement thermorhéologique simple. Pour cela, on a pris en compte les facteurs de translation horizontale déterminés par Henriques et al. [1]. Les effets de la température sont présentés sur la figure 10. Par ailleurs, ces exemples permettent notamment d'observer que la mousse B a une bonne capacité à dissiper de l'énergie mécanique.

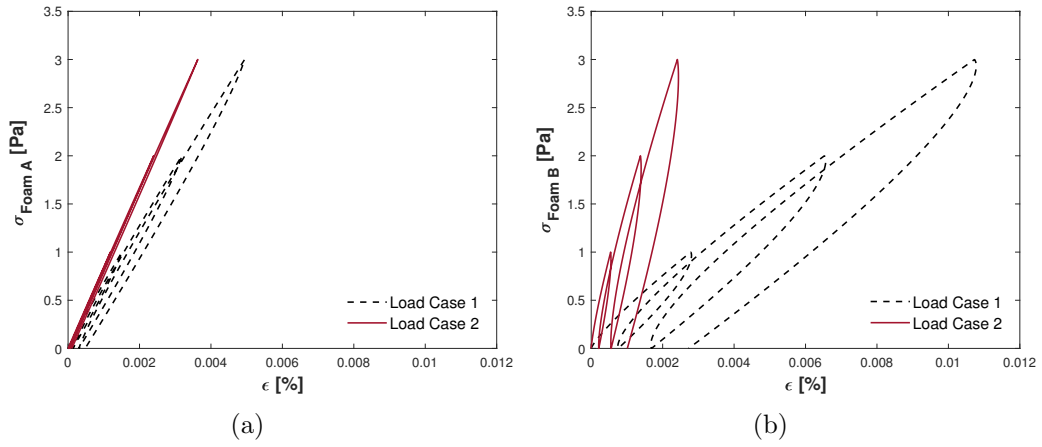


Figure 9: Comparaison entre les boucles d’hystérésis de l’étude des effets de fréquence d’excitation. Mousses (a) A et (b) B.

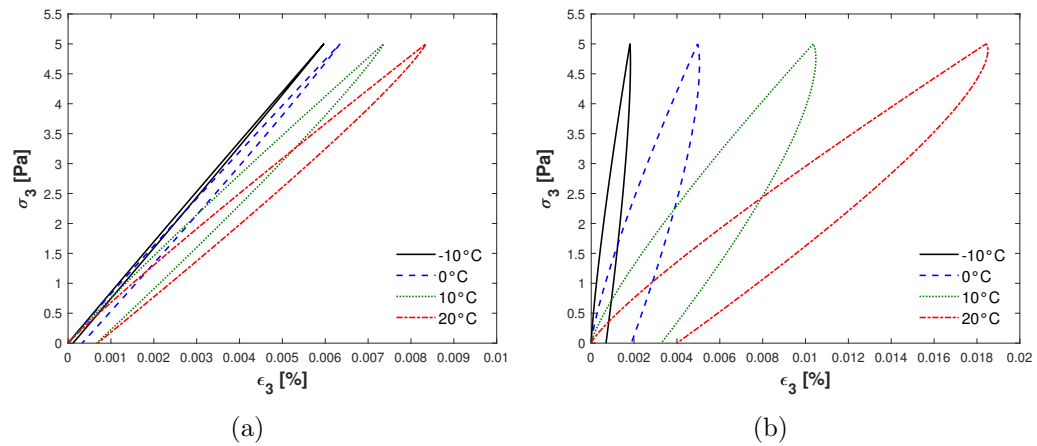


Figure 10: Comparaison entre les boucles d’hystérésis de l’étude des effets de température. Mousse (a) A et (b) B.

6.3. Cas d’étude II: panneaux simplement appuyés

La deuxième étude développe et valide expérimentalement un modèle éléments finis 3D pour prédire le comportement des mousses polymères dans le domaine fréquentiel lorsqu’elles sont appliquées à des structures vibrantes. On analyse également la performance d’amortissement de chaque mousse.

D’abord, on effectue des essais de vibrations mécaniques sur des panneaux simplement appuyés assemblés en deux configurations (sans et avec mousse de polymère), comme le montre la figure 11. Un effort ponctuel est appliqué par un marteau d’impact sur la face nue de la plaque. On mesure

l'accélération aux quatre points sur la même surface, comme indiqué sur la figure 12, sur la bande de fréquence [0-800] Hz à la température ambiante. La comparaison en figure 13 entre résultats des configurations montre que la structure composée de la mousse B a une bonne capacité d'amortissement.

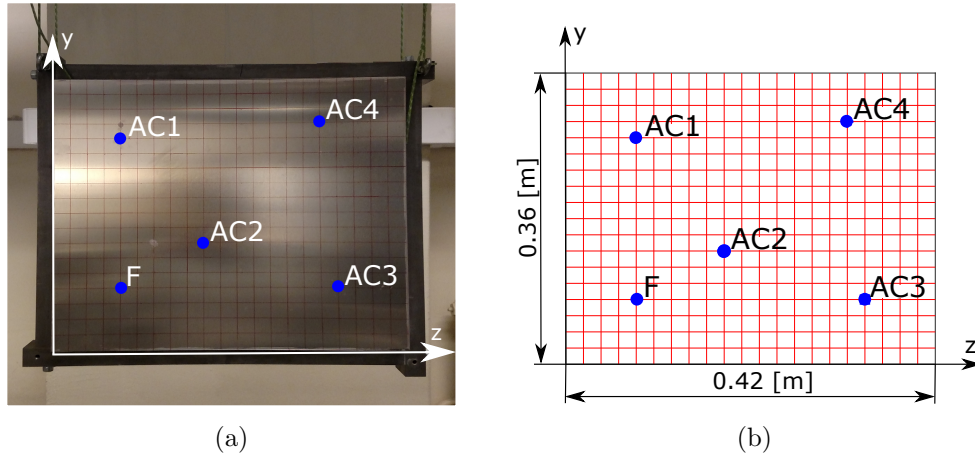
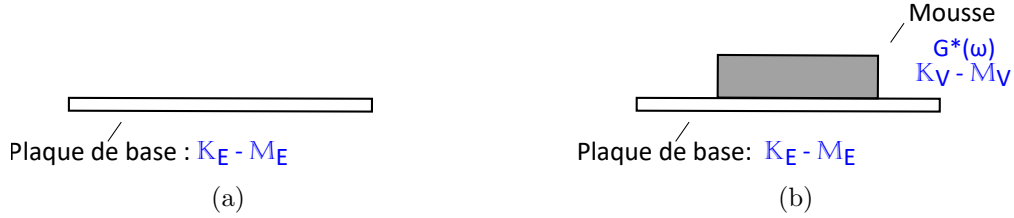


Figure 12: L'emplacement des mesures d'excitation et d'accélération. (a) Photographie de la configuration expérimentale et (b) diagramme schématique.

Ensuite, on procède à la modélisation du comportement des structures testées. Pour ce faire, on fait les hypothèses suivantes. La plaque de base est modélisée comme un milieu élastique linéaire homogène isotrope, avec amortissement structural. La mousse de polymère est quant à elle modélisée comme un milieu viscoélastique linéaire homogène isotrope dont les propriétés sont dépendantes de la fréquence. Son coefficient de Poisson, cependant, est considéré comme constant, ce qui fait que toutes ses propriétés mécaniques ont la même dépendance à la fréquence.

Les formulations éléments finis pour les configurations 1 et 2 sont, respectivement,

$$[(1 + j\eta)\mathbb{K}_E - \omega^2\mathbb{M}_E]\mathbf{U}^S(\omega) = \mathbf{F}^S(\omega) \quad (6)$$

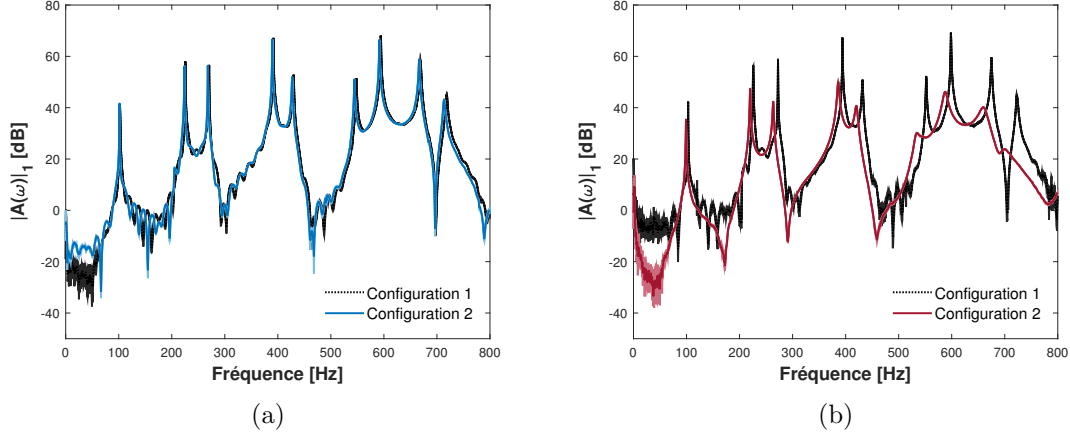


Figure 13: Comparaisons entre les FRF mesurés des configurations 1 et 2. Mousse (a) A et (b) B.

et

$$[\mathbb{K}_E + G^*(\omega)\mathbb{K}_V^0 - \omega^2(\mathbb{M}_E + \mathbb{M}_V)]\mathbf{U}^S(\omega) = \mathbf{F}^S(\omega), \quad (7)$$

où $j^2 = -1$, η est le facteur d'amortissement structural, \mathbb{K}_E et \mathbb{M}_E sont les matrices respectivement de raideur et de masse liées à la partie élastique de la structure, \mathbb{K}_V et \mathbb{M}_V sont les matrices respectivement de raideur et de masse liées à la partie viscoélastique de la structure, $\mathbf{F}^S(\omega)$ le vecteur des sollicitations et $\mathbf{U}^S(\omega)$ le vecteur de degrés de liberté. Le module de cisaillement $G^*(\omega)$ de la mousse est décrit par le modèle fractionnaire de Zener qui est défini par

$$G^*(\omega) = \frac{G_0 + G_\infty(j\omega\tau)^\alpha}{1 + (j\omega\tau)^\alpha}, \quad (8)$$

où les coefficients $\{G_0, G_\infty, \tau, \alpha\}$ sont donnés dans le tableau 4.

En figures 14 et 15, on présente chaque configuration expérimentale avec le modèle éléments finis implémenté pour les simulations. Les comparaisons entre les résultats expérimentaux et numériques sont représentées sur les figures 16 et 17. On prouve que le modèle développé est capable de prédire le comportement de la structure dans la bande fréquentielle choisie.

7. Caractérisation inverse des propriétés viscoélastiques des matériaux poreux

Ce chapitre propose une méthodologie expérimentale-numérique pour la caractérisation inverse des propriétés viscoélastiques des matériaux poreux. L'objectif est de calibrer des modèles fractionnaires

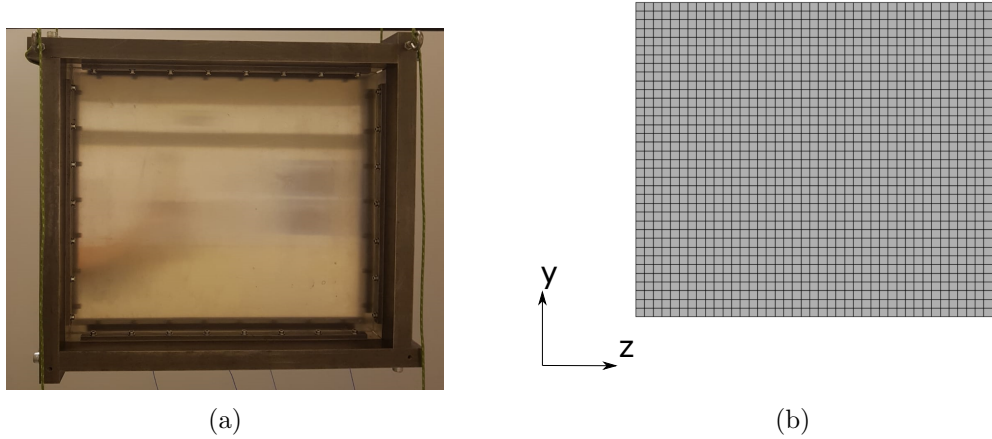


Figure 14: Configuration 1. (a) Plaque d'aluminium en appuis simples sur un cadre en acier et (b) maillage de la structure correspondant.

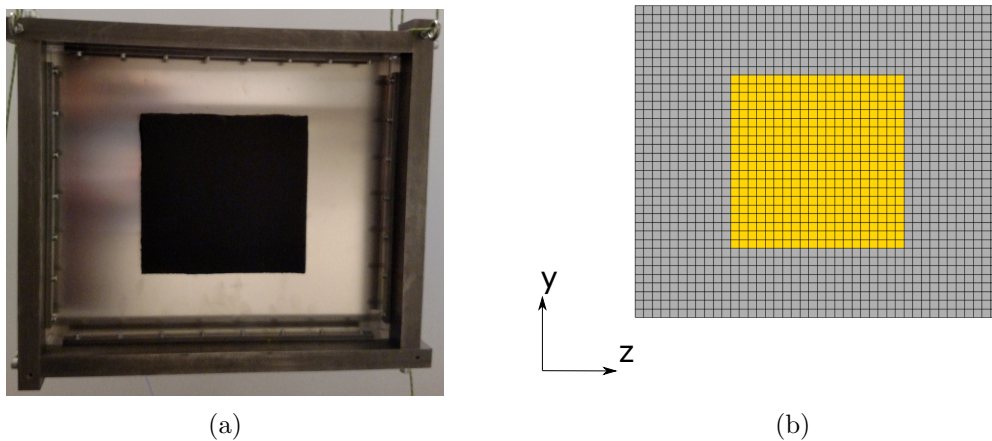


Figure 15: Configuration 1. (a) Plaque d'aluminium en appuis simples sur un cadre en acier avec la mousse B et (b) maillage de la structure correspondant.

par une approche bayésienne, lors de la modélisation de matériaux poreux en tant que solides viscoélastiques monophasés avec des propriétés dépendant de la fréquence. Pour ce faire, on considère le modèle éléments finis 3D développé et validé au Chapitre 6.

7.1. Méthodologie

La méthodologie de caractérisation inverse proposée comprend quatre étapes. Dans un premier temps, on effectue des essais vibratoires sur des panneaux simplement appuyés pour obtenir leurs

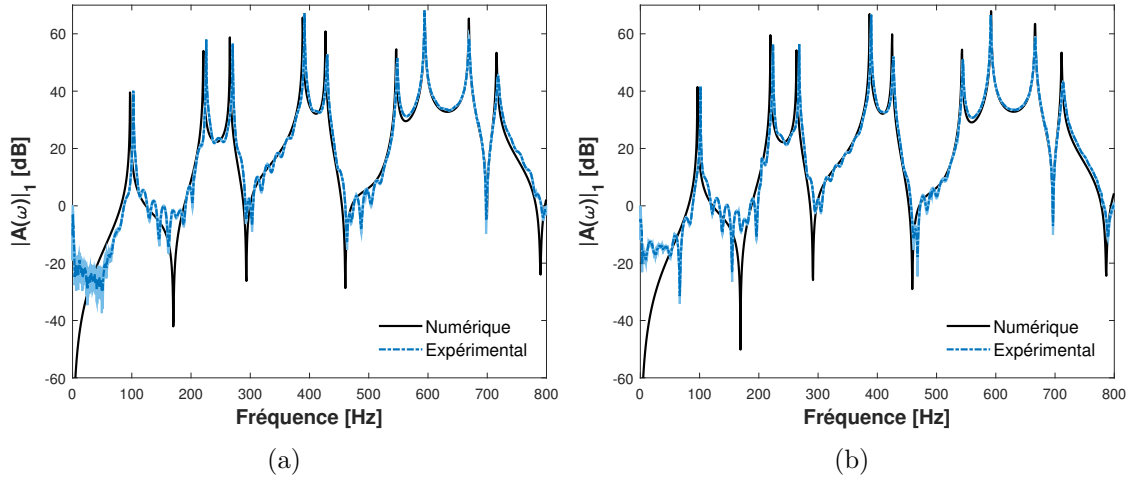


Figure 16: Comparaison de la FRF simulée à la FRF mesurée pour les configurations (a) 1 et (b) 2 de la mousse A.

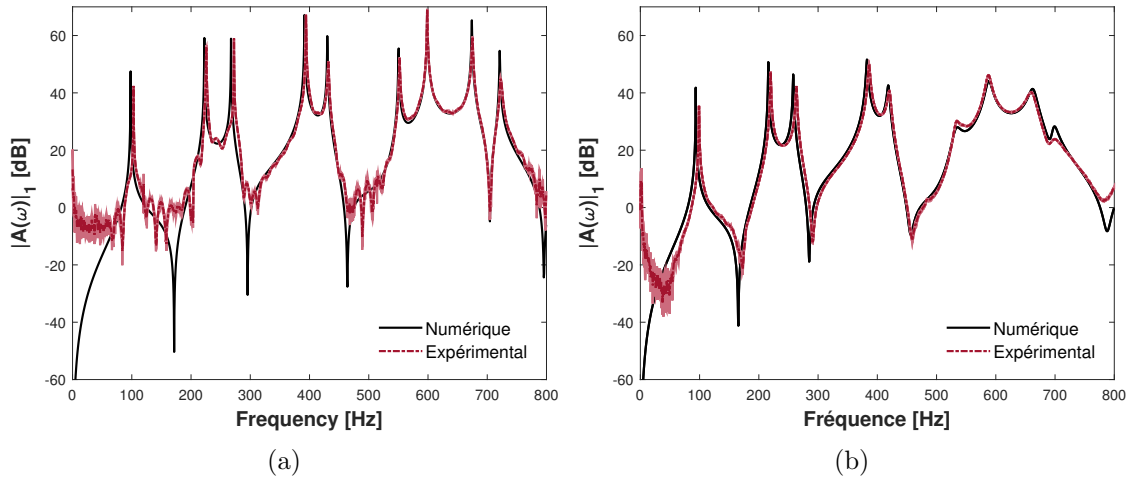


Figure 17: Comparaison de la FRF simulée à la FRF mesurée pour les configurations (a) 1 et (b) 2 de la mousse B.

fonctions de réponse en fréquence (FRF). L'équipement utilisé ainsi que les conditions d'essai sont similaires à ceux présentés au chapitre précédent. Ensuite, on estime les FRFs via les modèles des équations 6.12 et 6.14 en utilisant la méthode d'approximation modale. Puis, on estime les propriétés viscoélastiques du matériau poreux. Enfin, on valide le modèle estimé.

7.2. Méthode Inverse

La méthode inverse vise à déterminer les quatre paramètres $\theta = \{G_0, G_\infty, \tau, \alpha\}$ du modèle adopté pour décrire le comportement viscoélastique du matériau analysé (équation 8). Pour ce faire, on fait

la calibration du modèle par l'approche bayésienne afin de considérer les incertitudes des résultats expérimentaux. Ensuite, on vérifie et valide le modèle estimé.

Pour la calibration du modèle, chaque paramètre est décrit par une loi a priori uniforme, en considérant l'hypothèse d'une indépendance mutuelle. Puisqu'on considère que le bruit est additif, on définit une loi Gaussienne pour la fonction de vraisemblance. La variance est considérée ici comme une variable aléatoire décrite par une loi inverse-gamma. Deux étapes sont alors réalisées: la première porte sur l'estimateur du MAP, tandis que la seconde consiste à utiliser la méthode MCMC avec l'algorithme DRAM.

Pour la vérification et la validation, on propage les incertitudes dans le modèle calibré. On compare les FRFs mesurées et simulées puis on estime la différence entre les fréquences de résonance mesurées et simulées. Par ailleurs, on estime le FRAC (en anglais, *frequency response assurance criterion*).

Il convient de noter que les étapes de calibration et validation doivent utiliser des mesures différentes. Ainsi, on divise les résultats expérimentaux en deux ensembles de données pour évaluer leurs impacts sur l'estimation. Chaque ensemble de données S_{ijkl} est défini comme l'ensemble pour lequel la calibration utilise les FRF mesurées par les accéléromètres $\{ACi, ACj\}$ et pour lequel la validation utilise les FRFs mesurées par les accéléromètres $\{ACk, ACL\}$, où i, j, k, l in $\{1, 2, 3, 4\}$ et $i \neq j \neq k \neq l$. Les détails théoriques et pratiques d'implémentation sont donnés dans la thèse.

7.3. Résultats

On applique la méthode inverse pour déterminer les propriétés de deux matériaux poreux: la mousse de polyurethane à cellules fermées (matériau B), étudiée au chapitre 6, et un matériau poreux à base de caoutchouc recyclé (matériau C). Les tableaux 5 et 6 comparent les valeurs attendues et les intervalles de confiance à 95 % pour les matériaux B et C. On montre que les valeurs attendues varient selon ensemble de données lors de l'étape de calibration, mais les intervalles de confiance ont montré une bonne corrélation entre les estimations.

Sur les figures 18 et 19, on compare les résultats expérimentaux avec les enveloppes stochastiques générées après la propagation des incertitudes dans le modèle. On vérifie par cette comparaison que les modèles calibrés sont capables de prédire le comportement du système de façon satisfaisante. Les légères différences observées aux fréquences les plus élevées peuvent être corrélées avec la méthode de

RÉSUMÉ ÉTENDU

Table 5: Valeur attendue et intervalle de confiance (CI) à 95 % de chaque paramètre inconnu θ obtenus à partir de données du matériau B.

| Ensemble de données | $\mathbb{E}[G_0]$ 95 % CI | [Pa] | $\mathbb{E}[G_\infty]$ 95 % CI | [Pa] | $\mathbb{E}[\tau]$ 95 % CI | [s] | $\mathbb{E}[\alpha]$ 95 % CI |
|---------------------|------------------------------|---------------|-----------------------------------|---------------|-------------------------------|------------------|---------------------------------|
| S_{1234} | 1.09 [0.59, 1.89] | $\times 10^4$ | 2.66 [1.45, 4.42] | $\times 10^6$ | 4.42 [3.09, 5.88] | $\times 10^{-8}$ | 0.42 [0.35, 0.49] |
| S_{3412} | 1.21 [0.31, 2.31] | $\times 10^4$ | 1.92 [1.12, 3.37] | $\times 10^6$ | 4.53 [3.08, 5.95] | $\times 10^{-8}$ | 0.38 [0.32, 0.47] |

Table 6: Valeur attendue et intervalle de confiance (CI) à 95 % de chaque paramètre inconnu θ obtenus à partir de données du matériau C.

| Ensemble de données | $\mathbb{E}[G_0]$ 95 % CI | [Pa] | $\mathbb{E}[G_\infty]$ 95 % CI | [Pa] | $\mathbb{E}[\tau]$ 95 % CI | [s] | $\mathbb{E}[\alpha]$ 95 % CI |
|---------------------|------------------------------|---------------|-----------------------------------|---------------|-------------------------------|------------------|---------------------------------|
| S_{1234} | 1.90 [1.05, 2.79] | $\times 10^4$ | 2.36 [0.80, 9.10] | $\times 10^7$ | 1.93 [0.14, 9.56] | $\times 10^{-7}$ | 0.61 [0.53, 0.68] |
| S_{3412} | 2.03 [1.26, 2.94] | $\times 10^4$ | 2.22 [0.71, 9.04] | $\times 10^7$ | 1.24 [0.08, 9.33] | $\times 10^{-7}$ | 0.56 [0.51, 0.62] |

réduction modale utilisée pour le calcul des FRF.

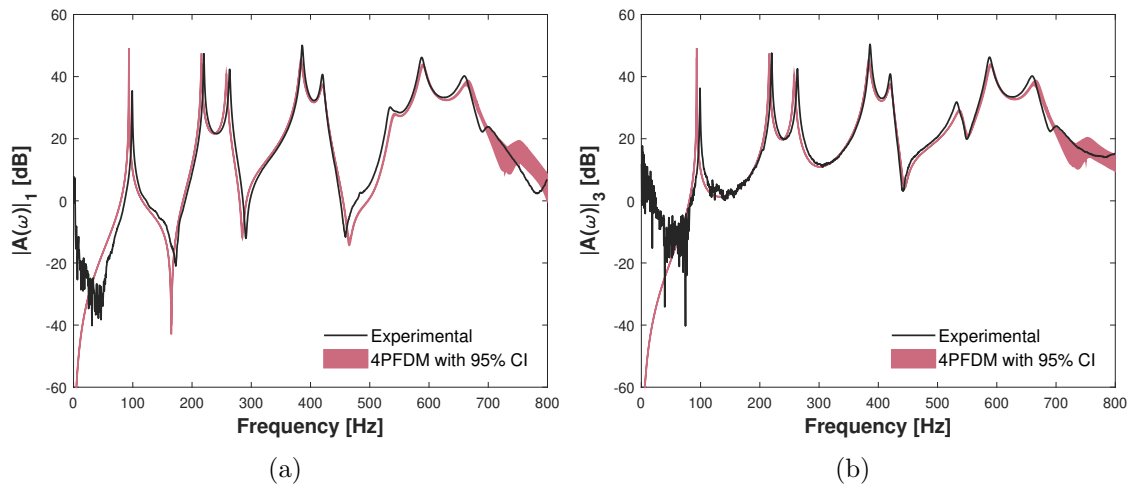


Figure 18: Propagation d'incertitude en tenant compte des résultats de l'ensemble de données S_{1234} du matériau B. (a) Étape de calibration - AC1 et (b) étape de validation - AC3.

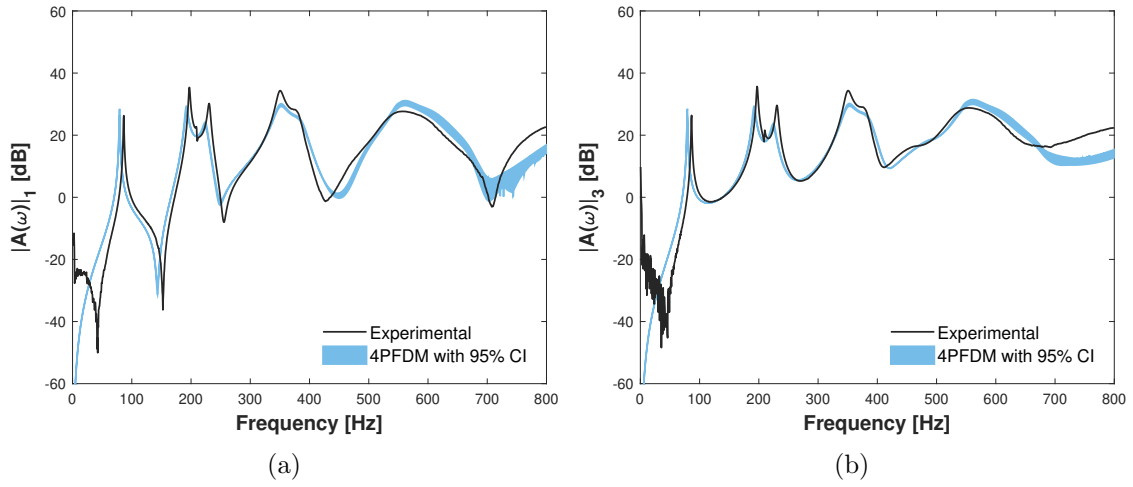


Figure 19: Propagation d'incertitude en tenant compte des résultats de l'ensemble de données S_{1234} du matériau C. (a) Étape de calibration - AC1 et (b) étape de validation - AC3.

De plus, dans le cas particulier du matériau B, on fait une comparaison entre les résultats estimés dans cette méthodologie avec les paramètres obtenus à partir d'un rhéomètre de torsion [1] (présentés au chapitre 6). Comme le montre la figure 20, on obtient un bon accord entre les FRFs générées à partir des valeurs obtenues par chaque méthode. Cela augmente la crédibilité de la méthodologie proposée.

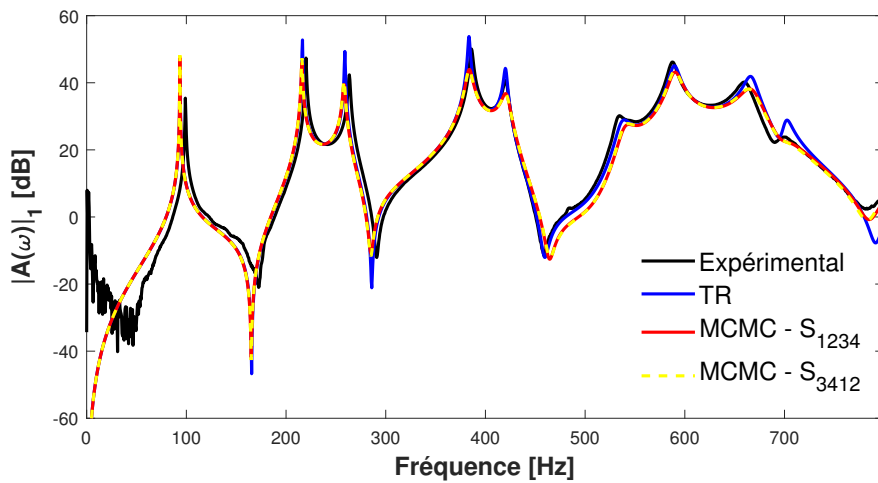


Figure 20: Comparaison entre les FRFs mesurée et simulées à partir de paramètres du DMA [1] et de la méthode inverse pour la localisation de AC1 pour le matériau B.

8. Conclusions et perspectives

Cette thèse examine deux problèmes principaux concernant la caractérisation et la modélisation des matériaux viscoélastiques et poro-viscoélastiques. Le premier problème a porté sur la technique de caractérisation DMA, tandis que le second a concerné de la dissipation de l'énergie mécanique provoquée par certains matériaux poreux en raison de leur viscoélasticité. Les principales réalisations sont énumérées ci-dessous.

Principales contributions reportées dans ce manuscrit de thèse

- Analyse de la répétabilité et de la reproductibilité des tests expérimentaux réalisés sur les modes de flexion des machines DMA.
- Analyse des incertitudes expérimentales des essais de flexion DMA dans la calibration des modèles viscoélastiques.
- Prédiction numérique du comportement cyclique des mousses polymères à partir d'un modèle à dérivée fractionnaire dans le domaine temporel.
- Développement et validation expérimentale d'un modèle élément finis 3D d'une structure recouverte d'une couche de matériau poreux, considérant uniquement la viscoélasticité du matériau poreux.
- Développement d'une méthode inverse par une approche bayésienne pour l'identification des propriétés viscoélastique des matériaux poreux.

Au-delà des résultats obtenus durant cette thèse, il reste toujours des problématique à aborder sur les sujets étudiés. Parmi les perspectives de travail mentionnées dans le manuscrit, les suivantes peuvent être soulignées:

Principales suggestions pour les travaux futurs

- la corrélation entre les modes de flexion de la DMA et les essais mécaniques (comme la traction et la flexion trois points) sur des machines universelles comme Instron;
- la modélisation des deux phases des matériaux poreux et de leurs effets de couplage en utilisant la théorie de Biot pour inclure d'autres mécanismes de dissipation tels que thermiques et visqueux visant à mieux décrire leur comportement à des fréquences plus élevées;
- l'analyse de la possibilité d'effectuer une caractérisation inverse des mousses polymères à des fréquences plus élevées.

Contents

| | |
|--|-----------|
| Acknowledgements | 5 |
| Résumé | 9 |
| Abstract | 11 |
| Résumé étendu | 13 |
| List of tables | 46 |
| List of figures | 56 |
| 1 Introduction | 57 |
| 1.1 Context | 58 |
| 1.2 Objectives | 60 |
| 1.3 Description of work environment | 61 |
| 1.4 Thesis outline | 62 |
| 1.5 Overview of the main contributions | 63 |
| I Theoretical Aspects | 67 |
| 2 Linear viscoelasticity | 71 |
| 2.1 Phenomenological aspects: relaxation, creep and hysteresis | 72 |

CONTENTS

| | | |
|----------|--|-----------|
| 2.2 | Boltzmann superposition principle | 74 |
| 2.3 | Dynamic response | 76 |
| 2.4 | Mechanical analogs | 77 |
| 2.4.1 | Maxwell and Kelvin-Voigt models | 78 |
| 2.4.2 | Standard linear solid | 79 |
| 2.4.3 | Generalized models | 80 |
| 2.5 | Fractional derivative models | 82 |
| 2.5.1 | Four-parameter fractional derivative model | 83 |
| 2.5.2 | Five-parameter fractional derivative model | 85 |
| 2.6 | Effects of time/frequency and temperature | 87 |
| 2.6.1 | General Aspects | 88 |
| 2.6.2 | Thermorheologically simple materials | 89 |
| 2.6.2.1 | Time-temperature superposition principle (TTSP) | 90 |
| 2.6.2.2 | Cole-Cole and Black diagrams | 92 |
| 3 | Model calibration & validation | 95 |
| 3.1 | Parameter estimation from a Bayesian perspective | 96 |
| 3.1.1 | Choice of the prior probability density function | 98 |
| 3.1.2 | Choice of the likelihood function | 98 |
| 3.1.3 | Posterior probability density function and point estimates | 100 |
| 3.2 | Markov chain monte carlo (MCMC) techniques | 101 |
| 3.2.1 | Metropolis-Hastings (MH) | 102 |
| 3.2.2 | Delayed rejection adaptive metropolis (DRAM) | 103 |
| 3.2.2.1 | Adaptive metropolis (AM) | 103 |
| 3.2.2.2 | Delayed rejection (DR) | 104 |
| 3.2.2.3 | DRAM: AM + DR | 106 |

CONTENTS

| | | |
|-----------|---|------------|
| 3.3 | Model Validation | 106 |
| 3.4 | Uncertainty quantification and propagation through Monte Carlo method | 108 |
| II | Dynamic Mechanical Analysis (DMA) | 111 |
| 4 | Complex modulus provided by dynamic mechanical analyzer (DMA) | 115 |
| 4.1 | Fundamentals | 116 |
| 4.1.1 | DMA principles | 116 |
| 4.1.2 | Mathematical formulation for complex modulus | 116 |
| 4.2 | Experimental set-up | 122 |
| 4.2.1 | Description of testing equipments | 122 |
| 4.2.2 | Material and samples manufacture | 124 |
| 4.3 | Study I: temperature-dependent complex modulus | 125 |
| 4.3.1 | Test conditions | 126 |
| 4.3.2 | Experimental results & discussion | 127 |
| 4.3.2.1 | Influence of testing equipment | 127 |
| 4.3.2.2 | Influence of operational mode | 131 |
| 4.3.2.3 | Discussion | 133 |
| 4.3.3 | Parametric study | 134 |
| 4.4 | Study II: temperature and frequency-dependent complex modulus | 141 |
| 4.4.1 | Test conditions | 142 |
| 4.4.2 | Experimental results & discussion | 142 |
| 4.4.2.1 | Influence of operational mode | 143 |
| 4.4.2.2 | Influence of testing equipment | 149 |
| 4.5 | Conclusion | 152 |
| 5 | Modeling the complex modulus within Bayesian framework | 155 |

CONTENTS

| | | |
|------------|---|------------|
| 5.1 | Methodology | 156 |
| 5.2 | Modeling | 156 |
| 5.3 | Results & discussion: identification of viscoelastic parameters | 157 |
| 5.3.1 | Description of calibration procedure | 157 |
| 5.3.2 | Model calibration | 159 |
| 5.4 | Conclusion | 167 |
| III | Poro-viscoelastic Materials | 169 |
| 6 | Damping performance of polymeric foams in the low-frequency range | 175 |
| 6.1 | Description of tested materials | 177 |
| 6.2 | Study I: cyclic loads | 178 |
| 6.2.1 | Description of numerical cases | 179 |
| 6.2.2 | Results & discussion of case 1: loading rates | 179 |
| 6.2.3 | Results & discussion of case 2: temperature | 182 |
| 6.3 | Study II: simply supported panels | 184 |
| 6.3.1 | Experiments | 185 |
| 6.3.1.1 | Description of testing equipment | 185 |
| 6.3.1.2 | Test conditions | 188 |
| 6.3.1.3 | Results | 188 |
| 6.3.2 | Finite element formulation | 193 |
| 6.3.2.1 | Structural problem | 194 |
| 6.3.2.2 | Governing equation and boundary conditions | 194 |
| 6.3.2.3 | Variational formulation | 195 |
| 6.3.2.4 | Finite element discretization | 196 |
| 6.3.3 | Numerical implementation and mesh convergence | 198 |

CONTENTS

| | | |
|----------|--|------------|
| 6.3.4 | Model validation & discussion | 200 |
| 6.3.4.1 | Comparison between experimental data and simulation: foam A . . . | 201 |
| 6.3.4.2 | Comparison between experimental data and simulation: foam B . . . | 204 |
| 6.3.4.3 | Discussion | 207 |
| 6.3.5 | Parametric study | 208 |
| 6.3.6 | Limitations of the model | 213 |
| 6.4 | Conclusion | 215 |
| 7 | Inverse characterization of viscoelastic properties of porous materials | 217 |
| 7.1 | Methodology | 219 |
| 7.2 | Experiments | 220 |
| 7.2.1 | Description of tested materials | 220 |
| 7.2.2 | Description of testing equipment and test conditions | 221 |
| 7.2.3 | Results | 222 |
| 7.3 | Modeling | 223 |
| 7.3.1 | Finite element formulation | 223 |
| 7.3.2 | Numerical implementation | 224 |
| 7.4 | Results & discussion: identification of viscoelastic parameters | 224 |
| 7.4.1 | Material B | 225 |
| 7.4.1.1 | Description of calibration and validation procedures | 225 |
| 7.4.1.2 | Model calibration | 228 |
| 7.4.1.3 | Model validation | 235 |
| 7.4.1.4 | Comparison with other techniques | 238 |
| 7.4.2 | Material C | 240 |
| 7.4.2.1 | Description of calibration and validation procedures | 240 |
| 7.4.2.2 | Model calibration | 243 |

CONTENTS

| | | |
|----------|--|------------|
| 7.4.2.3 | Model validation | 248 |
| 7.5 | Conclusion | 251 |
| 8 | Conclusions and perspectives | 255 |
| 8.1 | Dynamic mechanical analysis (DMA) | 256 |
| 8.1.1 | Achievements and outlook | 256 |
| 8.1.2 | Perspectives for future works | 257 |
| 8.2 | Poro-viscoelastic materials | 258 |
| 8.2.1 | Achievements and outlook | 258 |
| 8.2.2 | Perspectives for future works | 260 |
| | Bibliography | 261 |
| | Appendices | 276 |
| A | Fractional Calculus | 277 |
| A.1 | Fractional derivative | 277 |
| A.2 | Integration method for fractional differential equations | 278 |
| B | Complex modulus measured by PE machine | 281 |
| B.1 | Experimental results | 281 |
| B.2 | Modelling temperature and frequency effects | 285 |
| C | Identification of density ρ | 291 |
| C.1 | Description of experimental procedure | 291 |
| C.2 | Results | 292 |
| D | Identification of T_g of polymeric foams through DSC technique | 293 |
| D.1 | Description of testing equipment and test conditions | 293 |

CONTENTS

| | | |
|----------|---|------------|
| D.1.1 | Foam A | 294 |
| D.1.2 | Foam B | 295 |
| D.2 | Results | 295 |
| E | MIMO tests and experimental modal analysis | 297 |
| E.1 | Methodology | 297 |
| E.2 | Results | 299 |

CONTENTS

List of Tables

| | | |
|-----|---|-----|
| 4.1 | Technical characteristics of each DMA machine. | 124 |
| 4.2 | Samples' dimensions for the first case study, where L is the sample's length, w is the width and t is the thickness. | 125 |
| 4.3 | Samples' dimensions for the second case study, where L is the sample's length, w is the width and t is the thickness. | 125 |
| 4.4 | Testing parameters for the first case study, where t is thickness, S is the span, S/t is the span-to-thickness ratio and a is the amplitude. | 126 |
| 4.5 | Temperature Scans | 133 |
| 4.6 | Testing parameters for the second case study, where t is thickness, S is the span, S/t is the span-to-thickness ratio and a is the amplitude. | 142 |
| 4.7 | Empirical constants of WLF equation calibrated using measurements obtained by TA machine. | 148 |
| 4.8 | Comparison between the empirical constants of WLF equation calibrated using measured data from SC, DC and 3PT modes. | 150 |
| 5.1 | MAP results for the measurements subsets SC, DC and 3PT from TA machine. | 160 |
| 5.2 | MCMC results using DRAM algorithm for each data-set from TA machine. | 161 |
| 5.3 | Posterior mean value and 95% credibility interval (CI) of the unknown parameters θ for each data-set from TA machine. | 162 |

LIST OF TABLES

| | | |
|------|--|-----|
| 6.1 | Description of tested materials, where ν is the Poisson's ratio, ρ is the nominal density and T_g is the glass transition. | 178 |
| 6.2 | Fractional derivative model parameters of tested materials, where G_0 is the relaxed shear modulus, G_∞ is the unrelaxed shear modulus, τ is the relaxation time and α is the order of fractional derivative. | 178 |
| 6.3 | Empirical constants of WLF model extracted from the work of Henriques et al. [1]. . . | 183 |
| 6.4 | Description of each component of the experimental rig. | 186 |
| 6.5 | Locations of the applied force (F) and the four accelerometers (ACi, where $i \in \{1, 2, 3, 4\}$) placed on the bare panel side to measure the structure's response. | 187 |
| 6.6 | Comparison between the estimated natural frequencies (f_n) of configuration 1 and 2 of foam A. | 190 |
| 6.7 | Comparison between the estimated damping coefficients (ζ) of configuration 1 and 2 of foam A. | 190 |
| 6.8 | Comparison between the estimated natural frequencies (f_n) of configuration 1 and 2 of foam B. | 191 |
| 6.9 | Comparison between the estimated damping coefficients (ζ) of configuration 1 and 2 of foam B. | 192 |
| 6.10 | Description of finite element meshes of configurations 1 and 2. | 200 |
| 6.11 | Comparison between the initial and optimized properties for aluminum plate used for foam A. | 201 |
| 6.12 | Comparison between the experimental and numerical resonant frequencies obtained at the location of AC1 of configuration 1 used for foam A. | 202 |
| 6.13 | Comparison between the experimental and numerical resonant frequencies obtained at the location of AC1 for configuration 2 with foam A. | 204 |
| 6.14 | Comparison between the initial and optimized properties for aluminum plate used for foam B. | 204 |
| 6.15 | Comparison between the experimental and numerical resonant frequencies obtained at the location of AC1 of configuration 1 used for foam B. | 205 |

LIST OF TABLES

6.16 Comparison between the experimental and numerical resonant frequencies obtained at the location of AC1 of configuration 2 with foam B. 207

7.1 Description of tested materials, where ν is the Poisson’s ratio and ρ is the nominal density. 221

7.2 Definition of subsets S_{ijkl} used for model calibration and model validation of material B, where $i, j, k, l \in \{1, 2, 3, 4\}$ and $i \neq j \neq k \neq l$ 226

7.3 MAP results for the two measurement subsets S_{ijkl} , $i, j, k, l \in \{1, 2, 3, 4\}$ and $i \neq j \neq k \neq l$, of material B. 228

7.4 MCMC results using DRAM algorithm for the two measurement subsets S_{ijkl} , $i, j, k, l \in \{1, 2, 3, 4\}$ and $i \neq j \neq k \neq l$, of material B. 230

7.5 Posterior mean value and 95 % credibility interval of the unknown parameters θ for the two measurement subsets S_{ijkl} , $i, j, k, l \in \{1, 2, 3, 4\}$ and $i \neq j \neq k \neq l$, of material B. . . 231

7.6 Validation metric δf_r [%] for material B. 237

7.7 Comparison between the four parameters $\theta = \{G_0, G_\infty, \tau, \alpha\}$ estimated by different approaches for material B. 238

7.8 Comparison between the resonance frequencies from measured data and calibrated models by different approaches for material B. 240

7.9 Definition of subsets S_{ijkl} used for model calibration and model validation of material C, where $i, j, k, l \in \{1, 2, 3, 4\}$ and $i \neq j \neq k \neq l$ 241

7.10 MAP results for the two measurement subsets S_{ijkl} , $i, j, k, l \in \{1, 2, 3, 4\}$ and $i \neq j \neq k \neq l$, of material C. 243

7.11 MCMC results using DRAM algorithm for the two measurement subsets S_{ijkl} , $i, j, k, l \in \{1, 2, 3, 4\}$ and $i \neq j \neq k \neq l$, of material C. 245

7.12 Posterior mean value and 95 % credibility interval of the unknown parameters θ for the two measurement subsets S_{ijkl} , $i, j, k, l \in \{1, 2, 3, 4\}$ and $i \neq j \neq k \neq l$, of material C. . . 246

7.13 Validation metric δf_r [%] for material C. 250

B.1 Empirical constants of WLF equation calibrated using measurements obtained by PE machine. 283

LIST OF TABLES

| | | |
|-----|--|-----|
| B.2 | MAP results for the measurements subsets SC, DC and 3PT from PE machine. | 285 |
| B.3 | MCMC results using DRAM algorithm for each data set from PE machine. | 286 |
| B.4 | Posterior mean value and 95% credibility interval (CI) of the unknown parameters θ for each data set from PE machine. | 287 |
| C.1 | Estimated densities ρ [kg/m ³] for materials A, B and C, where $\mathbb{E}\{\rho\}$ is the mean value and σ_ρ is the corresponding standard deviation. | 292 |
| D.1 | Estimated glass transition temperature T_g [°C] for foams A and B, where $\mathbb{E}\{T_g\}$ is the mean value and σ_{T_g} is the corresponding standard deviation. | 296 |
| E.1 | Estimated natural frequencies (f_n) and damping coefficients (ζ) for each configuration 2 tested. | 300 |
| E.2 | Validation of the estimated modes for each configuration 2 tested. | 300 |

List of Figures

| | | |
|------|--|-----|
| 1.1 | Overview of the thesis. | 61 |
| 2.1 | Relaxation phenomenon. | 73 |
| 2.2 | Creep phenomenon. | 74 |
| 2.3 | Stress-strain curve for a linearly viscoelastic material, describing the hysteresis loop during a loading-unloading cycle. | 74 |
| 2.4 | The Boltzmann superposition principle. Each stress loading causes strain change independently. | 75 |
| 2.5 | Mechanical analogs. | 77 |
| 2.6 | Basic mechanical analogs. | 79 |
| 2.7 | Standard linear solid model. | 80 |
| 2.8 | Generalized Maxwell model (Weichert model). | 81 |
| 2.9 | Generalized Kelvin-Voigt model (Anelastic Displacement Fields, ADF). | 82 |
| 2.10 | Representation of the complex modulus of the four-parameter fractional derivative model. | 85 |
| 2.11 | Representation of the complex modulus of the five-parameter fractional derivative model. | 87 |
| 2.12 | Regions of viscoelastic behavior according to temperature changes. | 88 |
| 2.13 | Time-Temperature Superposition Principle (TTSP) [2]. | 92 |
| 4.1 | Stress $\sigma(t)$ and strain $\varepsilon(t)$ curves as function of time t of a linearly viscoelastic material under a dynamic loading. | 117 |
| 4.2 | Single Cantilever (SC) mode. | 118 |

LIST OF FIGURES

| | | |
|------|--|-----|
| 4.3 | Dual Cantilever (DC) mode. | 119 |
| 4.4 | Three-point bending (3PT) mode. | 119 |
| 4.5 | Clamping Correction Factor F_c for some values of L/t | 121 |
| 4.6 | Photograph of DMA PerkinElmer 8000. | 122 |
| 4.7 | Photograph of DMA TA Q800. | 123 |
| 4.8 | Photograph of DMA Netzsch 242 E Artemis. | 123 |
| 4.9 | Comparisons between complex modulus measured in SC mode. | 127 |
| 4.10 | Comparisons between complex modulus measured in DC mode. | 129 |
| 4.11 | Comparisons between complex modulus measured in 3PT mode. | 130 |
| 4.12 | Comparisons between complex modulus measured by PE machine using samples from set 1. | 131 |
| 4.13 | Comparisons between complex modulus measured by PE machine using samples from set 2. | 132 |
| 4.14 | Comparisons between complex modulus measured by TA machine. | 132 |
| 4.15 | Effects of geometry on complex modulus measured in SC mode. | 135 |
| 4.16 | Effects of geometry on complex modulus measured in DC mode. | 136 |
| 4.17 | Effects of geometry on complex modulus measured in 3PT mode. | 137 |
| 4.18 | Effects of stiffness on complex modulus. | 138 |
| 4.19 | Effects of Poisson's ratio on complex modulus measured by TA machine. | 139 |
| 4.20 | Comparison between the effects of a constant Poisson's ratio and a linear temperature-dependent Poisson's ratio on complex modulus measured by TA machine. | 140 |
| 4.21 | Effects of mathematical formulation on complex modulus. | 141 |
| 4.22 | Complex modulus measured in SC mode by TA machine. | 144 |
| 4.23 | Complex modulus measured in DC mode by TA machine. | 144 |
| 4.24 | Complex modulus measured in 3PT mode by TA machine. | 144 |

LIST OF FIGURES

| | | |
|------|---|-----|
| 4.25 | Comparisons between the temperature and frequency-dependent complex modulus measured in SC, DC and 3PT modes by TA machine. | 145 |
| 4.26 | Validation of thermo-rheological simple behavior considering measurements in SC mode by TA machine. | 146 |
| 4.27 | Validation of thermo-rheological simple behavior considering measurements in DC mode by TA machine. | 146 |
| 4.28 | Validation of thermo-rheological simple behavior considering measurements in 3PT mode by TA machine. | 147 |
| 4.29 | Horizontal shift coefficients $a_T(T, T_0)$ applied to the isotherms from measurements obtained by TA machine, shown in Figs. 4.22-4.24. The optimised coefficients are fitted by WLF equation. | 147 |
| 4.30 | Comparison between the horizontal shift coefficients $a_T(T, T_0)$ obtained for SC, DC and 3PT modes. The optimised coefficients (markers: *) are fitted by WLF equation (solid line: -). | 148 |
| 4.31 | Comparison between experimental master curves built at $T_0 = 70^\circ\text{C}$ considering measurements of complex modulus by TA machine. | 149 |
| 4.32 | Comparisons between the temperature and frequency-dependent complex modulus measured by TA and PE machines. | 150 |
| 4.33 | Comparison between experimental master curves built at $T_0 = 70^\circ\text{C}$ considering measurements of complex modulus in SC mode. | 151 |
| 4.34 | Comparison between experimental master curves built at $T_0 = 70^\circ\text{C}$ considering measurements of complex modulus in DC mode. | 151 |
| 4.35 | Comparison between experimental master curves built at $T_0 = 70^\circ\text{C}$ considering measurements of complex modulus in 3PT mode. | 152 |
| 5.1 | Schematic diagram of methodology employed to calibrate viscoelastic models considering measured data from DMA. | 156 |
| 5.2 | Convergence analysis for the 5PFDM using DRAM algorithm with each data-set from TA machine. | 160 |

LIST OF FIGURES

5.2 Convergence analysis for the 5PFDM using DRAM algorithm with each data-set from TA machine. 161

5.3 Posterior samples generated using DRAM algorithm with each data-set from TA machine. 163

5.4 PDFs for the parameters generated using DRAM algorithm with each data-set from TA machine. 163

5.4 PDFs for the parameters generated using DRAM algorithm with each data-set from TA machine. 164

5.5 Uncertainty propagation when considering $\theta \sim \pi(\theta|\mathbf{Y})$ for the data-set of SC mode from TA machine. 164

5.6 Uncertainty propagation when considering $\theta \sim \pi(\theta|\mathbf{Y})$ for the data-set of DC mode from TA machine. 165

5.7 Uncertainty propagation when considering $\theta \sim \pi(\theta|\mathbf{Y})$ for the data-set of 3PT mode from TA machine. 165

5.8 Comparison between the calibrated models from SC, DC, and 3PT modes of TA machine. 166

5.9 Comparison between the calibrated models from SC mode of TA and PE machines. . . 166

5.10 Comparison between the calibrated models from DC mode of TA and PE machines. . 167

5.11 Comparison between the calibrated models from 3PT mode of TA and PE machines. . 167

6.1 Optical microscope images of the cell structure of the two different foam materials. . . 177

6.2 Prescribed stress histories $\sigma_1(t)$ and $\sigma_2(t)$ for the study of rate effects in hysteresis cycles. 180

6.3 Strain responses obtained for each scenario at 20 °C. 180

6.4 Stress-strain responses obtained for each scenario at 20 °C. 181

6.5 Comparison between the stress-strain responses of load cases 1 and 2 at 20 °C. 182

6.6 Prescribed stress history $\sigma_3(t)$ for the study of temperature effects in hysteresis cycles. 183

6.7 Strain responses obtained for load case 3. 183

6.8 Comparison between stress-strain responses obtained for load case 3 for the study of temperature effects. 184

LIST OF FIGURES

6.9 Configurations of simply supported panels for the study of vibration damping performance. 185

6.10 Schematic diagram of the experimental rig. 185

6.11 Simply supported panel mounted in configuration 1. 186

6.12 Simply supported panel mounted in configuration 2. 187

6.13 Locations of the applied force and the accelerometers placed on the bare panel side. . . 188

6.14 Comparisons between the measured FRFs of configurations 1 and 2 of foam A. 189

6.15 Comparisons between the measured FRFs of configurations 1 and 2 of foam B. 191

6.16 Comparisons between the measured FRFs of configurations 1. 192

6.17 Comparisons between the measured FRFs of configurations 2 of foams A and B. 193

6.18 Description of the structural problem. 194

6.19 Finite element mesh for configuration 1. 199

6.20 Finite element mesh for configuration 2. 200

6.21 Comparisons between the FRFs obtained by experimental measurements and numerical simulations using optimized parameters of configuration 1 used for foam A. 202

6.22 Comparisons between the FRFs obtained by experimental measurements and numerical simulations of configuration 2 with foam A. 203

6.23 Comparisons between the FRFs obtained by experimental measurements and numerical simulations using optimized parameters of configuration 1 used for foam B. 205

6.24 Comparisons between the FRFs obtained by experimental measurements and numerical simulations of configuration 2 with foam B. 206

6.25 Frequency response function of configuration 2 with foam B considering the location of AC1. Performance of multi-modal approach. 208

6.26 Effects of the four model parameters (G_0 , G_∞ , τ and α) on the estimated FRF for configuration 2 with foam A considering the location of AC1. 209

6.27 Effects of model parameters on the estimated FRF for configuration 2 with foam B considering the location of AC1. 210

LIST OF FIGURES

6.28 Effects of material properties (ρ and ν) on the estimated FRF for configuration 2 with foam A considering the location of AC1. 211

6.29 Effects of material properties (ρ and ν) on the estimated FRF for configuration 2 with foam B considering the location of AC1. 211

6.30 Effects of geometry (L , w and t) on the estimated FRF for configuration 2 with foam A considering the location of AC1. 212

6.31 Effects of geometry (L , w and t) on the estimated FRF for configuration 2 with foam B considering the location of AC1. 213

6.32 Comparison between the experimental FRFs of configurations 2 with foams A and B measured by AC1 considering frequencies up to 1600 Hz. 214

6.33 Comparison between the FRFs obtained by experimental measurements and numerical simulations of configuration 2 with foam A considering the location of AC1 and frequencies up to 1600 Hz. 215

6.34 Comparison between the FRFs obtained by experimental measurements and numerical simulations of configuration 2 with foam B considering the location of AC1 and frequencies up to 1600 Hz. 215

7.1 Schematic diagram of methodology employed to inverse identify viscoelastic properties of porous materials. 219

7.2 Configurations of simply supported panels. 220

7.3 Optical microscope images of the structure of the two different porous materials. . . . 221

7.4 Comparisons between the measured FRFs of configurations 1 and 2 of material C. . . . 222

7.5 Finite element mesh adopted for the inverse method. 224

7.6 Selected points for calibration procedure in which $\Delta f = 1.5$ Hz. 226

7.7 Comparison between experimental data and model prediction using MAP estimate $\hat{\theta}_{MAP}$ for both measurement subsets S_{1234} and S_{3412} of material B. 229

7.8 Convergence analysis for the 4PFDM using DRAM algorithm of material B. 229

7.8 Convergence analysis for the 4PFDM using DRAM algorithm of material B. 230

LIST OF FIGURES

7.9 Posterior samples generated using DRAM algorithm for the 4PFDM of material B. 231

7.10 PDFs for the parameters of the 4PFDM of material B. 232

7.11 Uncertainty propagation when considering $\boldsymbol{\theta} \sim \pi(\boldsymbol{\theta}|\mathbf{Y})$ for measurement subset S_{1234} of material B. Frequency response functions computed for the two accelerometers AC1 and AC2 used in the calibration procedure. 233

7.12 Uncertainty propagation when considering $\boldsymbol{\theta} \sim \pi(\boldsymbol{\theta}|\mathbf{Y})$ for measurement subset S_{3412} of material B. Frequency response functions computed for the two accelerometers AC3 and AC4 used in the calibration procedure. 233

7.13 Comparison between experimental data and the calibrated model for measurement subset S_{1234} of material B. The frequency response function was computed through the direct method using the posterior mean value of the unknown parameters $\boldsymbol{\theta}$ 234

7.14 Comparison between experimental data and the calibrated model for measurement subset S_{3412} of material B. The frequency response function was computed through the direct method using the posterior mean value of the unknown parameters $\boldsymbol{\theta}$ 235

7.15 Uncertainty propagation when considering $\boldsymbol{\theta} \sim \pi(\boldsymbol{\theta}|\mathbf{Y})$ for measurement subset S_{1234} of material B. Frequency response functions computed for the two accelerometers AC3 and AC4 used in the validation procedure. 236

7.16 Uncertainty propagation when considering $\boldsymbol{\theta} \sim \pi(\boldsymbol{\theta}|\mathbf{Y})$ for measurement subset S_{3412} of material B. Frequency response functions computed for the two accelerometers AC1 and AC2 used in the validation procedure. 236

7.17 Absolute value of complex shear modulus, $|G^*(\omega)|$, of material B. Comparison between the calibrated models from TR measurements [1] and the proposed inverse characterization. 239

7.18 FRFs obtained for the location of AC1 for material B. Comparison between experimental data and model predictions using parameters obtained from TR measurements [1] and the ones from the proposed inverse characterization. 240

7.19 Selected points for model calibration procedure for material C. 242

LIST OF FIGURES

7.20 Comparison between experimental data and model prediction using MAP estimate $\hat{\theta}_{MAP}$ for both measurement subsets S_{1234} and S_{3412} of material C. 244

7.21 Convergence analysis for the 4PFDM using DRAM algorithm of material C. 244

7.21 Convergence analysis for the 4PFDM using DRAM algorithm of material C. 245

7.22 Posterior samples generated using DRAM algorithm for the 4PFDM of material C. . . 246

7.23 PDFs for the parameters of the 4PFDM of material C. 247

7.24 Uncertainty propagation when considering $\theta \sim \pi(\theta|Y)$ for measurement subset S_{1234} of material C. Frequency response functions computed for the two accelerometers AC1 and AC2 used in the calibration procedure. 248

7.25 Uncertainty propagation when considering $\theta \sim \pi(\theta|Y)$ for measurement subset S_{3412} of material C. Frequency response functions computed for the two accelerometers AC3 and AC4 used in the calibration procedure. 248

7.26 Uncertainty propagation when considering $\theta \sim \pi(\theta|Y)$ for measurement subset S_{1234} of material C. Frequency response functions computed for the two accelerometers AC3 and AC4 used in the validation procedure. 250

7.27 Uncertainty propagation when considering $\theta \sim \pi(\theta|Y)$ for measurement subset S_{3412} of material C. Frequency response functions computed for the two accelerometers AC1 and AC2 used in the validation procedure. 250

B.1 Complex modulus measured in SC mode by PE machine. 281

B.2 Complex modulus measured in DC mode by PE machine. 282

B.3 Complex modulus measured in 3PT mode by PE machine. 282

B.4 Validation of thermo-rheological simple behavior considering measurements in SC mode by PE machine. 282

B.5 Validation of thermo-rheological simple behavior considering measurements in DC mode by PE machine. 283

B.6 Validation of thermo-rheological simple behavior considering measurements in 3PT mode by PE machine. 283

LIST OF FIGURES

B.7 Horizontal shift coefficients $a_T(T, T_0)$ applied to the isotherms from measurements obtained by PE machine, shown in Figs. B.1-B.3. The optimised coefficients are fitted by WLF equation. 284

B.8 Comparison between experimental master curves built at $T_0 = 70$ °C considering measurements of complex modulus by PE machine. 284

B.9 Convergence analysis for the 5PFDM using DRAM algorithm with each data set from PE machine. 285

B.9 Convergence analysis for the 5PFDM using DRAM algorithm with each data set from PE machine. 286

B.10 Posterior samples generated using DRAM algorithm with each data set from PE machine. 287

B.11 PDFs for the parameters generated using DRAM algorithm with each data set from PE machine. 288

B.12 Uncertainty propagation when considering $\theta \sim \pi(\theta|Y)$ for the data-set of SC mode from PE machine. 289

B.13 Uncertainty propagation when considering $\theta \sim \pi(\theta|Y)$ for the data-set of DC mode from PE machine. 289

B.14 Uncertainty propagation when considering $\theta \sim \pi(\theta|Y)$ for the data-set of 3PT mode from PE machine. 290

B.15 Comparison between the calibrated models from SC, DC, and 3PT modes of PE machine. 290

C.1 Photograph showing the samples of materials A, B and C. They were cut by hand using a box cutter. 291

C.2 Photograph of the microgram scale (model ATX224 from SHIMADZU). 292

D.1 Photograph of DSC 200 F3 from Netzsch. 293

D.2 Photographs of the experimental set-up. 294

D.3 Photograph showing one of the samples of foam A inside the aluminum pan before it was closed. The sample was cut by hand using a box cutter. 295

LIST OF FIGURES

D.4 DSC scans. 296

E.1 Experimental mesh. 298

E.2 Averaged coherence function showing the quality of the FRF measurements performed
in each configuration 2 tested. 299

E.3 Averaged coherence function showing the quality of the FRF measurements performed
in each configuration 2 tested. 299

E.4 Auto-MAC with experimental modes for each configuration 2 tested. 300

Chapter 1

Introduction

This chapter gives some background to the work developed throughout this thesis. The context as well as the objectives are first specified. Then, a description of the practical organization of this thesis in the context of a “cotutelle” agreement between the Universidade Federal do Rio de Janeiro (UFRJ), Rio de Janeiro/RJ, and the Conservatoire National des Arts et Métiers (Cnam), Paris/France, is carried out. Finally, the structure of the present manuscript is introduced, followed by the main contributions achieved during this period.

Content

| | | |
|------------|---|-----------|
| 1.1 | Context | 58 |
| 1.2 | Objectives | 60 |
| 1.3 | Description of work environment | 61 |
| 1.4 | Thesis outline | 62 |
| 1.5 | Overview of the main contributions | 63 |

1.1 Context

The continuous search for new materials is a milestone in our history since the most historical periods. Its development provides significant economic and social improvements for society in general. It is inherent to the human being to always look forward to, create, explore something new to expand the limits of human effort and achievements.

Nowadays, different industries have pushed this evolution of materials. A great example is the transport industry, which invests significantly in the search for new materials that are lighter and more resistant, and that would help to reduce vibrations, gas emissions, and fuel consumption. Another example is the civil industry, which seeks materials that assure strength, resistance, flexibility, cost-effectiveness, and prevent corrosion.

Within this context, it is possible to highlight the increasing progress and use of materials known as viscoelastic. They have been widely applied as constrained or unconstrained layers in the most different structures for purposes of noise and vibration control [3–7]. Despite the achievements in this field, there are still improvements to be made concerning the prediction of material’s behavior, especially in terms of experimental characterization, model calibration and validation.

It is well-known that viscoelastic materials have both elastic and viscous characteristics [8–11]. They can benefit, for instance, from their dissipative properties without losing their ability to produce stable structures. Nevertheless, their response may vary considerably depending on the conditions to which they are subjected.

These materials are generally polymers whose properties can be adjusted/improved on their manufacturing process to better fit on a specific application. Some of their main features are the excellent combination of mechanical properties (e.g., damping and stiffness), durability, lightweight, relatively low cost, and thermal stability [4, 7, 12]. However, these properties may be affected by many operational and environmental factors such as temperature, time/frequency, humidity, pressure, preload, strain amplitude, and porosity [8, 13].

An appropriate characterization and careful modeling of viscoelastic properties become indispensable to obtain an accurate prediction of the mechanical behavior of these materials. These steps are of the utmost importance to the design and analysis of structures, to optimize projects, and to minimize their risks [7, 14].

With this in mind, several experimental methods have been developed and improved to measure the properties of such materials, especially as a function of temperature and time/frequency. Currently, it is even possible to measure them at the three scales, namely nano, micro and macroscopic, depending on the focus of the analysis and the intended use of these materials [15].

Among the techniques on the macroscale, in particular, it is possible to highlight the application of the one named Dynamic Mechanical Analysis (DMA). It has been widely used to characterize polymer-based materials mainly as a function of temperature and frequency. Aspects such as material's modulus, thermal transitions, and long-term behavior can be easily determined by only performing quick and simple tests [16]. Nevertheless, some inconsistencies can be found in literature [17, 18] and consequently, it deserves a closer inspection and study.

As for the modeling of the viscoelastic response, different approaches can be found in the literature as mechanical analogs [7, 10], internal variables [3, 19, 20], and fractional derivative models [7, 21–24]. The latter is appreciated for describing the behavior of these materials satisfactorily, with a limited number of parameters.

Regardless of the approach chosen, the adopted constitutive model presents a set of parameters that must be correctly estimated and validated. On several occasions, the process of model calibration is formulated based on inverse problems. This is because the direct determination of each material parameter can be costly, time-consuming, and even never achieved in practice.

In this framework, several techniques can be employed, ranging from deterministic to probabilistic ones [25–27]. To tackle model and experimental uncertainties, and noise measurements, Bayesian inference methods have been widely used, providing means of constructing stochastic models to describe the material's response and provide more complete information about the model parameters [14, 28, 29].

These constitutive models can be associated with numerical methods to simulate the material's response under different conditions, helping the design of various structures. Among the numerical tools, the Finite Element Method (FEM) has proven to be a very efficient one as it ensures a good compromise between accuracy and computational complexity. Nevertheless, it can be prohibitively costly in computational terms when dealing with large models and repeated routines such as optimization procedures and uncertainty propagation. This highlights the need for cost-efficient simulation tools.

This work contributes to filling some gaps in studies of viscoelastic materials, its characterization, and modeling. Initially, it is focused on the experimental technique DMA, mainly concerning the viscoelastic property known as the complex modulus measured by the flexural modes. The central idea is to provide insights regarding mathematical formulations, repeatability and reproducibility of experimental tests, and how measurement uncertainties affect model predictions. Then, it aims at exploring the viscoelasticity of some porous materials whose matrix is made by polymer. One of its goals is to propose a simplified model to describe their damping behavior, which results in a good trade-off between accuracy and computational time. Another goal is to propose an inverse characterization strategy through Bayesian inference based on the developed model.

1.2 Objectives

The objectives of this thesis are summarized in Fig. 1.1 and described below.

1. *To analyze the characterization technique Dynamic Mechanical Analysis.* This work contributes to filling the gap in studies about the divergences between the measurements performed in DMA machines, focusing on the three flexural modes available in these machines. It provides a theoretical background concerning the mechanisms of each operational mode with the corresponding mathematical formulations adopted in each DMA machine. The repeatability and reproducibility of the measurements are addressed. Comparisons between the estimated values for the modulus, the glass transition temperatures (T_g), and the long-term behavior are performed. The effects of geometric and mechanical parameters are analyzed. Furthermore, fractional derivative models are calibrated through the Bayesian framework to study the effects of DMA data in model predictions.
2. *To characterize and model the damping performance of polymeric foams.* This work contributes to assessing the capacity of two polymeric foams to dissipate mechanical energy through their viscoelastic properties. A fractional derivative model is adopted to describe their mechanical behavior. Model predictions in the time domain concerning their hysteretic behavior are given for different scenarios of loading and temperature. A FE model combined with the fractional derivative model is proposed to evaluate their capacity to damp structural vibrations in the low-frequency range. Experiments are carried out to validate the proposed model. The effects

1.3. DESCRIPTION OF WORK ENVIRONMENT

of some parameters on the system response are addressed.

3. *To inverse characterize the viscoelastic properties of porous materials.* The goal is to propose an experimental-numerical approach to inverse characterize viscoelastic properties of porous materials from a Bayesian perspective. A fractional derivative model is calibrated and validated for two different porous materials. Results are even compared with those obtained using other techniques.

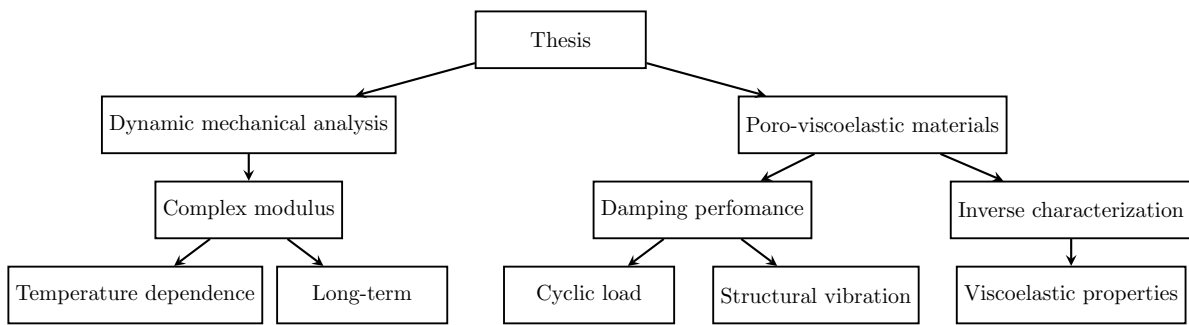


Figure 1.1: Overview of the thesis.

1.3 Description of work environment

This thesis was carried out within the scope of a joint supervision (“cotutelle” agreement) between the Laboratório de Acústica e Vibrações (LAVI) at UFRJ, Rio de Janeiro/Brazil, and the Laboratoire de Mécanique des Structures et des Systèmes Couplés (LMSSC) at Cnam, Paris/France. It can be divided into three parts corresponding to the periods spent in each institute: UFRJ/Cnam/UFRJ.

The first part of the thesis took place in the ‘home’ laboratories at UFRJ, in Rio de Janeiro. It consisted of taking the mandatory courses, doing the teaching internship, preparing for the Ph.D. qualifying exam, and investigating the characterization technique dynamic mechanical analysis. This investigation, in particular, led to the preparation of some articles for an international peer-reviewed journal and for some international conferences.

Following this first part, started a period entirely dedicated to the study of porous materials in the host laboratory at Cnam, in Paris. The initial investigations resulted in the development of several numerical codes related to finite element modeling, model reduction techniques, experimental modal analysis, inverse methods. This also led to the preparation of some articles for international

peer-reviewed journal and for some international conferences.

Finally, back to Rio de Janeiro, the study of porous materials was continued and a special attention was given to the inverse characterization through Bayesian approach.

1.4 Thesis outline

After this introduction, the thesis is divided in three main parts as follows.

Part I consists of presenting the theoretical background, which was the basis for the development of this thesis. It comprises Chapters 2 and 3.

- Chapter 2 provides a detailed description of the scientific fields related to the theory of linear viscoelasticity. It first presents the phenomenological aspects and the constitutive equations of viscoelastic materials. Then, it analyzes their dynamic response, bringing the concept of complex modulus. Afterward, it presents two approaches to model their macroscopic behavior, namely mechanical analogs and fractional derivative models. Finally, it discusses the effects of both time/frequency and temperature on the material's response.
- Chapter 3 is focused on the concepts of model calibration, model validation and uncertainty quantification. It first defines an inverse problem and formulates it in a Bayesian framework. Then, it reviews Markov chain Monte Carlo techniques, presenting some classical algorithms. Finally, it brings in the main concepts of model validation techniques and uncertainty quantification.

Part II, in turn, consists of the first main investigation of this thesis related to the characterization technique Dynamic Mechanical Analysis (DMA). It contains Chapters 4 and 5.

- Chapter 4 is dedicated to the investigation of the viscoelastic property known as complex modulus measured by DMA. It first introduces the concepts of complex modulus and how this property is mathematically formulated and measured in the three flexural modes. Then, it details the equipments used. Finally, two case studies are treated: one concerning the temperature dependence and other related to the long-term behavior.

1.5. OVERVIEW OF THE MAIN CONTRIBUTIONS

- Chapter 5 is concerned with the calibration of viscoelastic models to describe the complex modulus measured by DMA considering the Bayesian inference. It first describes the methodology adopted. Then, it presents the constitutive model chosen. Finally, it analyses the results obtained.

Part III consists of the second main investigation concerned with the damping behavior of porous materials in the low-frequency range. It comprises Chapters 6 and 7.

- Chapter 6 investigates experimentally and numerically the damping performance of two polymeric foams in both time and frequency domains. It first describes the studied foams, presenting their main features and the hypotheses assumed to model their behavior. Then, it discusses the first case study concerning the dissipation of mechanical energy due to cyclic loads. Finally, it talks about the second case study corresponding to their capacity to damp structural vibration in the low-frequency range.
- Chapter 7 treats the inverse characterization of the viscoelastic properties of two porous materials in a Bayesian framework. It first brings in the methodology adopted to assess the properties. Then, it details all the experimental set-up. Afterward, it presents the constitutive equation together with the finite element formulation. Finally, it discusses the results obtained by the proposed approach.

Finally, Chapter 8 brings the conclusive remarks together with perspectives for future works.

1.5 Overview of the main contributions

The main scientific contributions included in the present thesis can be highlighted with publications in international peer-reviewed journals and conference papers, and a book chapter.

- Published articles:

1. ORLANDINI, L.R.; HENRIQUES, I.R.; CASTELLO, D.A.; BORGES, L.A.; SOARES, B.G..
Dynamic mechanical characterization of epoxy-based thermosetting materials loaded with lignin.
Journal of the Brazilian Society of Mechanical Sciences and Engineering, v. 42, n. 8, 2020.

1.5. OVERVIEW OF THE MAIN CONTRIBUTIONS

2. HENRIQUES, I.R.; ROULEAU, L.; CASTELLO, D.A.; BORGES, L.A.; DEÜ, J.-F.. Viscoelastic behavior of polymeric foams: experiments and modeling. *Mechanics of Materials*, v. 148, 2020.
 3. HENRIQUES, I.R.; BORGES, L.A.; COSTA, M.F.; SOARES, B.G.; CASTELLO, D.A.. Comparisons of complex modulus provided by different DMA. *Polymer Testing*, v. 72, p. 394-406, 2018.
- Submitted/ To be submitted:
 1. HENRIQUES, I.R.; ROULEAU, L.; CASTELLO, D.A.; BORGES, L.A.; DEÜ, J.-F.. Modeling and experimental validation of damping performance of polymeric foams in the low-frequency range.
- International conferences:
 1. HENRIQUES, I.R.; ROULEAU, L.; BORGES, L.A.; M.F. COSTA; DEÜ, J.-F.; CASTELLO, D.A.. Comparisons of viscoelastic properties measured by different mechanical tests. 5th Brazilian Conference on Composite Materials, BCCM5, São Carlos, Brazil, 2020. (Accepted)
 2. HENRIQUES, I.R.; ROULEAU, L.; CASTELLO, D.A.; BORGES, L.A.; DEÜ, J.-F.. Experimental characterization and modeling of poroviscoelastic materials. 5th Brazilian Conference on Composite Materials, BCCM5, São Carlos, Brazil, 2020. (Accepted)
 3. ROULEAU, L.; HENRIQUES, I.R.; CASTELLO, D.A.; BORGES, L.A.; DEÜ, J.-F.. Inverse characterization of the damping performance of porous materials. Forum Acusticum, FA 2020, Lyon, France, 2020.
 4. HENRIQUES, I.R.; ROULEAU, L.; CASTELLO, D.A.; BORGES, L.A.; DEÜ, J.-F.. Damping performance of porous materials through dynamic analysis. Proceedings of 48th International Congress and Exposition on Noise Control Engineering, Internoise 2019, Madrid, Spain, 2019.
 5. HENRIQUES, I.R.; BORGES, L.A.; COSTA, M.; SOARES, B.G.; CASTELLO, D.A.. Differences between DMA modes and testing equipments. Proceedings of the 4th Brazilian Conference on Composite Materials, BCCM4, Rio de Janeiro, Brazil, 2018.

1.5. OVERVIEW OF THE MAIN CONTRIBUTIONS

6. HENRIQUES, I.R.; BORGES, L.A.; CASTELLO, D.A.; COSTA, M.; SOARES, B.G.. Comparison of complex modulus provided by three different dynamic mechanical analyzers. Proceedings of the 4th Brazilian Conference on Composite Materials, BCCM4, Rio de Janeiro, Brazil, 2018.
 7. HENRIQUES, I.R.; BORGES, L.A.; CASTELLO, D.A.; SOARES, B.G.; COSTA, M.. A critical analysis on the complex modulus provided by DMA. Proceedings of the 24th ABCM International Congress of Mechanical Engineering, COBEM 2017, Curitiba, Brazil, 2017.
- Book Chapter:
 1. HENRIQUES, I.R.; BORGES, L.A.; CASTELLO, D.A.. The mechanical behavior of viscoelastic materials in the frequency domain. In: Fleury A., Rade D., Kurka P. (eds) Proceedings of DINAME 2017. Lecture Notes in Mechanical Engineering. Springer, Cham, 2019.

1.5. OVERVIEW OF THE MAIN CONTRIBUTIONS

Part I

Theoretical Aspects

Introduction

The general objective of the first part of this thesis is to present the main concepts and theoretical background of the two theories utilized in this work. The first chapter introduces the essential concepts of linear viscoelasticity and its construction. It intends to facilitate the comprehension of viscoelastic materials behavior and the main tools and models used to characterize these materials. The second chapter focuses on the field of uncertainty quantification. It aims to introduce the main concepts and tools used herein to estimate and validate material parameters through this framework.

Chapter 2

Linear viscoelasticity

This chapter aims to present the theoretical background of linear viscoelasticity, highlighting the important aspects of the development of this work and its comprehension. It is organized as follows. Section 2.1 introduces viscoelastic materials and describes the three main characteristics of viscoelastic materials: creep, stress relaxation, and hysteresis. Section 2.2 presents the constitutive equations based on the Boltzmann superposition principle. Section 2.3 deals with the mechanical behavior of these materials when they are subjected to dynamic loads, bringing the concept of complex modulus. Section 2.4 presents an approach to describe the macroscopic behavior of viscoelastic materials based on mechanical analogs, introducing some classical models. Section 2.5 presents another approach to describe the macroscopic behavior based on fractional derivatives, focusing on the four-parameter and five-parameter models. Section 2.6 discusses the effects of time/frequency and temperature on the material's response. The special group of thermo-rheologically simple materials is defined and the time-temperature superposition principle is treated.

Content

| | | |
|------------|---|-----------|
| 2.1 | Phenomenological aspects: relaxation, creep and hysteresis | 72 |
| 2.2 | Boltzmann superposition principle | 74 |
| 2.3 | Dynamic response | 76 |
| 2.4 | Mechanical analogs | 77 |
| 2.4.1 | Maxwell and Kelvin-Voigt models | 78 |
| 2.4.2 | Standard linear solid | 79 |
| 2.4.3 | Generalized models | 80 |
| 2.5 | Fractional derivative models | 82 |
| 2.5.1 | Four-parameter fractional derivative model | 83 |
| 2.5.2 | Five-parameter fractional derivative model | 85 |
| 2.6 | Effects of time/frequency and temperature | 87 |
| 2.6.1 | General Aspects | 88 |
| 2.6.2 | Thermorheologically simple materials | 89 |

2.1 Phenomenological aspects: relaxation, creep and hysteresis

Linear viscoelastic materials are outside the scope of theories of elasticity and viscosity as they present both elastic and viscous properties. As a consequence, these materials have the capacity to both store and dissipate mechanical energy, being only able to recover some of the work done to deform them.

Furthermore, viscoelastic materials can be defined as materials with memory effects. It means that their current state of stress depends on the entire deformation history: both deformation path and deformation rates. Therefore, both stress and strain are time-dependent or frequency-dependent [9, 30].

Because of this time/frequency dependency, some phenomena are associated with viscoelastic materials depending on the excitation applied [8, 11]. The most commonly observed are relaxation, creep, and hysteresis as described below.

The relaxation phenomenon, also called as relaxation of stress, consists of the gradual decrease of stress with time (see Fig. 2.1a) under a constant deformation/strain (see Fig. 2.1b). This behavior is studied by imposing constant uniaxial deformation/strain on the material sample, initially non-deformed, and measuring the stress required to maintain that strain over time.

In other words, let the constant strain $\varepsilon(t)$ be a step function of magnitude ε_0 such as

$$\varepsilon(t) = \varepsilon_0 H(t), \quad (2.1)$$

where $H(t)$ is the unit Heaviside step function. Then, the stress history $\sigma(t)$ decreases with time and it is given by

$$\sigma(t) = \varepsilon_0 E(t), \quad (2.2)$$

where $E(t)$ is the relaxation modulus and it is a monotonically decreasing function of time.

2.1. PHENOMENOLOGICAL ASPECTS: RELAXATION, CREEP AND HYSTERESIS

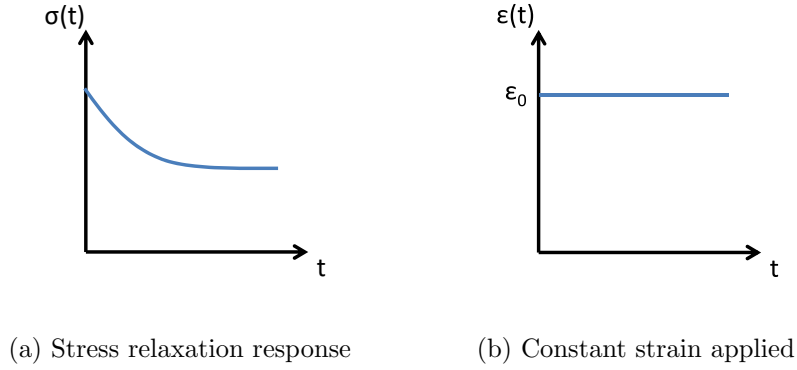


Figure 2.1: Relaxation phenomenon.

The creep phenomenon, also called as retardation of strain, consists of the gradual increase of strain with time (see Fig. 2.2a) under constant stress (see Fig. 2.2b). When this stress is released, the strain recovers or decreases progressively, sometimes even achieving zero. This phenomenon is studied by imposing constant uniaxial stress on the material sample, initially non-stressed, and measuring the strain required to maintain that stress over time.

In other words, let the constant stress $\sigma(t)$ be a step function of magnitude σ_0 such as

$$\sigma(t) = \sigma_0 H(t). \quad (2.3)$$

Then, the strain $\varepsilon(t)$ increases with time and it is expressed as

$$\varepsilon(t) = \sigma_0 J(t), \quad (2.4)$$

where $J(t)$ is the creep compliance and it is a monotonically increasing function of time.

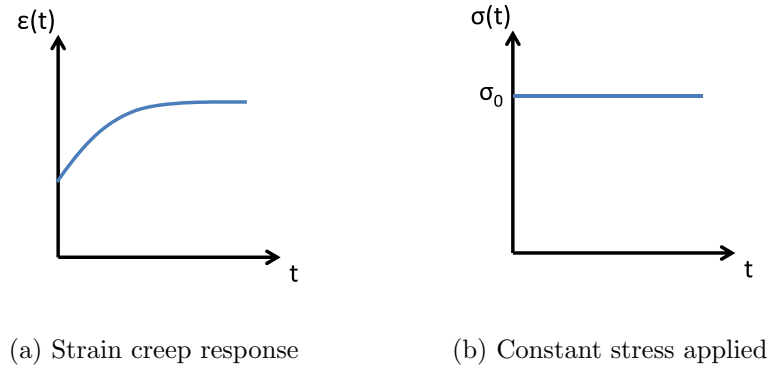


Figure 2.2: Creep phenomenon.

Finally, the hysteresis is observed in the stress-strain curve when a cyclic load is considered. As shown in Fig. 2.3, the loading and unloading curves do not coincide, forming a loop. The area inside this loop is called as hysteresis and it represents the energy lost during a cycle. This dissipation of mechanical energy depends on the excitation rate and temperature.

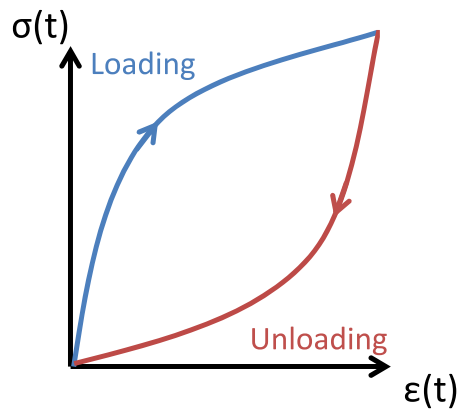


Figure 2.3: Stress-strain curve for a linearly viscoelastic material, describing the hysteresis loop during a loading-unloading cycle.

2.2 Boltzmann superposition principle

Under the hypothesis of small strains and isothermal mechanical processes, the constitutive equations of a linear viscoelastic material can be formulated based on the Boltzmann superposition principle

2.2. BOLTZMANN SUPERPOSITION PRINCIPLE

[9]. It establishes that the effect of a compound cause is the linear sum of the effects of the individual causes. Figure 2.4 illustrates, for example, this principle for the creep process. Each stress loading contributes independently to the strain of the material. The total creep is the linear sum of the creep strain caused by the stress loading history.

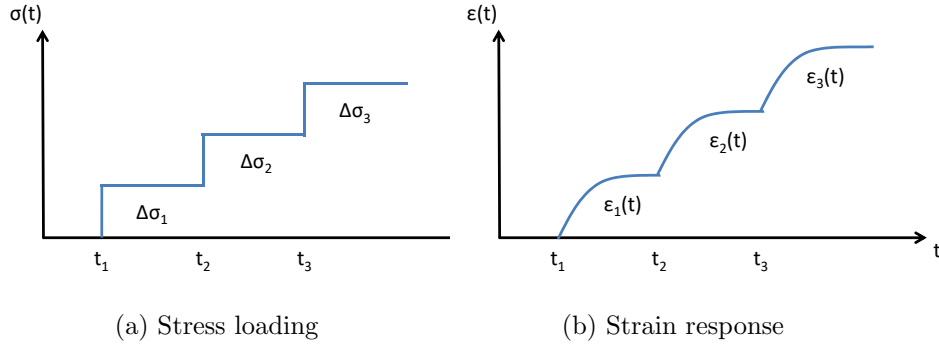


Figure 2.4: The Boltzmann superposition principle. Each stress loading causes strain change independently.

Therefore, if the strain history $\varepsilon(t)$ is specified, the one-dimensional constitutive equation is given by a convolution integral such as [9]

$$\sigma(t) = \int_{-\infty}^t E(t - \tau) \frac{d\varepsilon(\tau)}{d\tau} d\tau, \quad (2.5)$$

where $\sigma(t)$ is the stress component at time t , $E(t)$ is the relaxation modulus. Considering a zero strain history before the application of the loading and a step discontinuity at $t = 0$, Eq. 2.5 may be rewritten as

$$\sigma(t) = E(t)\varepsilon(0) + \int_0^t E(t - \tau) \frac{d\varepsilon(\tau)}{d\tau} d\tau, \quad (2.6)$$

where $\varepsilon(0)$ is the strain at $t = 0$.

Another way to express this stress-strain relation is obtained by reversing the roles of stress and strain. Therefore, for the case in which the stress history $\sigma(t)$ is specified, the one-dimensional constitutive equation is [9]

$$\varepsilon(t) = \int_{-\infty}^t J(t - \tau) \frac{d\sigma(\tau)}{d\tau} d\tau, \quad (2.7)$$

where $\varepsilon(t)$ is the strain component at time t and $J(t)$ is the creep compliance. Considering zero stress before the application of the loading and a step discontinuity at $t = 0$, Eq. 2.7 may be rewritten as

$$\varepsilon(t) = J(t)\sigma(0) + \int_0^t J(t - \tau) \frac{d\sigma(\tau)}{d\tau} d\tau. \quad (2.8)$$

2.3 Dynamic response

As viscoelastic materials are subjected to dynamic loads in several applications, it becomes interesting to investigate the behavior of these materials in this situation. Moreover, dynamic experiments are often more desired than static ones because they can measure viscoelastic response at shorter times in a more accurate way.

The stress-strain relation is now obtained by considering the excitation as a harmonic or sinusoidal steady-state one, also called as dynamic excitation. It is worthwhile mentioning that the term ‘dynamic’ here is not related to inertial effects or resonance [9].

Let the strain history be a sinusoidal function defined as

$$\varepsilon(t) = \varepsilon_0 e^{j\omega t}, \quad (2.9)$$

where $j = \sqrt{-1}$ is the imaginary number and ω is the angular frequency in radians per second.

The stress is also a sinusoidal function in time, if only the steady state form is considered. Thus, by the use of Fourier transform in Eq. 2.5, the one-dimensional constitutive equation becomes [9]

$$\tilde{\sigma}(j\omega) = E^*(\omega) \tilde{\varepsilon}(j\omega), \quad (2.10)$$

where $\tilde{q}(j\omega)$ denotes the Fourier transform of the variable $q(t)$, and $E^*(\omega) = \tilde{E}(j\omega) \times (j\omega)$ is the complex modulus that can be expressed in terms of its real and imaginary components such as

$$E^*(\omega) = E'(\omega) + jE''(\omega) = E'(\omega)(1 + j\eta(\omega)) \quad (2.11)$$

where $E'(\omega)$ is the real part known as storage modulus, $E''(\omega)$ is the imaginary part known as loss modulus, and $\eta(\omega) = E''(\omega)/E'(\omega)$ is known as loss factor. The storage modulus corresponds to the elastic response, representing the material’s ability to store energy. The loss modulus, in turn,

is associated with the viscous response, corresponding to the material's ability to dissipate energy. Finally, the loss factor represents how quickly material dissipates energy; it thus quantifies the damping capacity.

Another way of expressing the stress-strain relation shown in Eq. 2.10 is obtained by means of the complex exponential form. Therefore, Eq. 2.10 is rewritten as

$$\tilde{\sigma}(j\omega) = |E^*(\omega)|\varepsilon_0 e^{j(\omega t + \delta)}, \quad (2.12)$$

where $|E^*(\omega)|$ is the absolute value of $E^*(\omega)$ and $\delta = \tan^{-1}[E''(\omega)/E'(\omega)]$.

2.4 Mechanical analogs

The mechanical behavior of linear elastic material is usually modeled by a linear spring as shown in Fig. 2.5a. On the other hand, the behavior of a linear viscous fluid is usually described by a linear dashpot as shown in Fig. 2.5b. As the macroscopic behavior of viscoelastic materials involves aspects of both elastic solid and viscous fluid responses, models for viscoelastic materials are classically represented by the combination of springs and dashpots. This strategy of building mechanical models is called mechanical analogs.

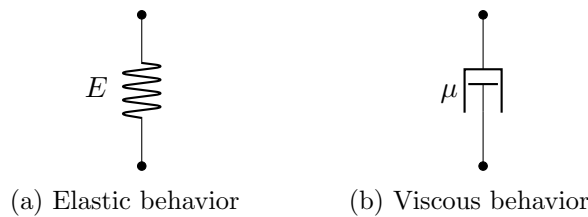


Figure 2.5: Mechanical analogs.

Mechanical analogs are phenomenological models. They cannot describe molecular or supramolecular mechanisms in the material, but only its macroscopic response [30]. Despite this, they are quite useful to predict the material's response to different loading situations and also to visualize how the viscoelastic behavior can arise [11].

There are many possible combinations of spring-dashpots, such as a spring connected in series/parallel to a dashpot, or several elements assembled in series/parallel, each one having its characteristics. Therefore, it is possible to characterize the response of many viscoelastic materials with

these models.

The constitutive equations are obtained through force analysis, geometrical considerations, and force-deformation relations of the structural elements. In this procedure, the mechanical elements are considered massless, inertia effects are neglected, and rheological concepts (stress and strain) are introduced once the force-deformation relation is well-defined [10].

Some examples of classical mechanical analogs are the Maxwell, the Kelvin-Voigt, the three-parameter, and generalized models. They are discussed in the next subsections in detail.

2.4.1 Maxwell and Kelvin-Voigt models

Maxwell model is one of the simplest model to describe the viscoelastic behavior [10]. It consists of a spring and a dashpot connected in series as shown in Fig. 2.6a. From force analysis, one can observe that the force is the same in both elements: $\sigma_{total}(t) = \sigma_s(t) = \sigma_d(t)$, where the subscripts s and d denote, respectively, spring and dashpot. From geometry, the total strain is the sum of the strains in each element: $\varepsilon_{total}(t) = \varepsilon_s(t) + \varepsilon_d(t)$. The constitutive equation for Maxwell model is then given by

$$\dot{\varepsilon}(t) = \frac{\dot{\sigma}(t)}{E} + \frac{\sigma(t)}{\mu}, \quad (2.13)$$

where E and μ are, respectively, the elastic modulus and the viscosity of the material.

For this model, the complex modulus shown in Eq. 2.11 can be written as

$$E^*(\omega) = \frac{jE\omega\mu}{E + j\omega\mu} = E \left[\frac{j\omega\tau}{1 + j\omega\tau} \right], \quad (2.14)$$

where $\tau = \mu/E$ is the relaxation time.

Another simple model to describe the viscoelastic behavior is called as Kelvin-Voigt model [10]. It connects a spring and a dashpot in parallel as shown in Fig. 2.6b. From the force analysis, it can be seen that the total force is the sum of the forces in each element, $\sigma_{total}(t) = \sigma_s(t) + \sigma_d(t)$. From geometry, the strain is the same in both elements, $\varepsilon_{total}(t) = \varepsilon_s(t) = \varepsilon_d(t)$. The constitutive equation is thus given by

$$\sigma(t) = E\varepsilon(t) + \mu\dot{\varepsilon}(t). \quad (2.15)$$

The corresponding complex modulus is expressed as

$$E^*(\omega) = E + j\omega\mu. \quad (2.16)$$

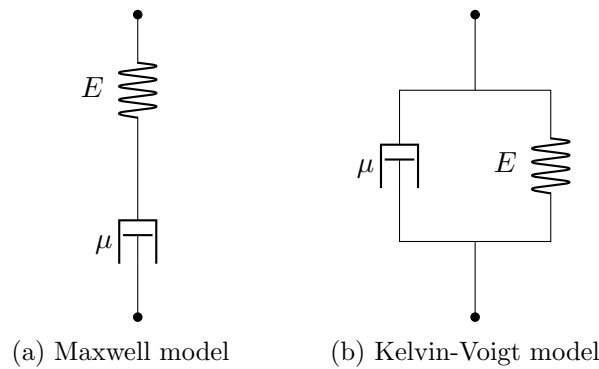


Figure 2.6: Basic mechanical analogs.

Due to the simplicity of these models, they do not describe perfectly the response of real viscoelastic materials to both stress and strain excitations. Maxwell model is only able to predict the relaxation phenomenon, whereas Kelvin-Voigt model can only predict the creep phenomenon. Hence, they can not independently model a viscoelastic material which can present both phenomena, as explained in Section 2.1. For this reason, some authors prefer to call them as a unit rather than models [30].

2.4.2 Standard linear solid

The simplest model that provides a good approximation for a real viscoelastic behavior contains three elements - two linear springs and a dashpot - and it is known as the three-parameter model or standard linear solid [10]. Figure 2.7 shows the two possible ways to construct this model: a Maxwell model connected in parallel to a linear spring (see Fig. 2.7a) and a Kelvin-Voigt model connected in series to a linear spring (see Fig. 2.7b).

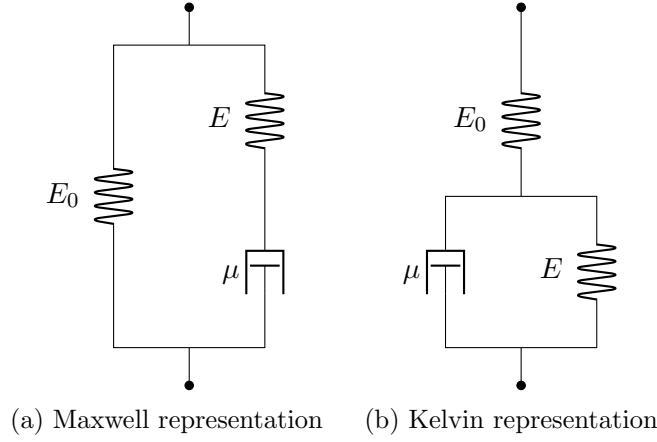


Figure 2.7: Standard linear solid model.

Both representations present the same form of constitutive equation [10]. For instance, let us focus on the Maxwell representation, also called as Zener model, to build the stress-strain relation. The subscript MM denotes the Maxwell element.

From the force analysis, the total force is the sum of the forces in each component, $\sigma_{total}(t) = \sigma_{MM}(t) + \sigma_s(t)$. From geometry, the total strain is the same in both components and so, $\varepsilon_{total}(t) = \varepsilon_{MM}(t) = \varepsilon_s(t)$. The constitutive equation for Zener model is thus given by

$$\sigma(t) + \frac{\mu}{E}\dot{\sigma}(t) = E_0\varepsilon(t) + \left[\frac{E + E_0}{E}\right]\mu\dot{\varepsilon}(t), \quad (2.17)$$

and the corresponding complex modulus is expressed as follows

$$E^*(\omega) = \frac{E_0 + E_\infty(j\omega\tau)}{1 + (j\omega\tau)}, \quad (2.18)$$

where E_0 is the relaxed modulus, corresponding to the value of the modulus at low frequencies, and $E_\infty = E_0 + E$ is the unrelaxed modulus, corresponding to the value of the modulus at high frequencies.

2.4.3 Generalized models

The three-parameter model can describe more realistically the behavior of viscoelastic materials once it can model relaxation and creep phenomena. However, it often fails to describe the behavior when these materials are, for example, subjected to dynamic loads. To overcome this issue, generalized models with a greater number of elements have been built.

2.4. MECHANICAL ANALOGS

At first, the more elements the model has, the more accurate it becomes to describe the behavior of real viscoelastic materials. Two standard generalizations of mechanical analogs are the generalized Maxwell and generalized Kelvin-Voigt models.

Figure 2.8 shows the generalized Maxwell model also known as Weichert model [31]. As can be seen, it consists of assembling a spring and N Maxwell models in parallel.

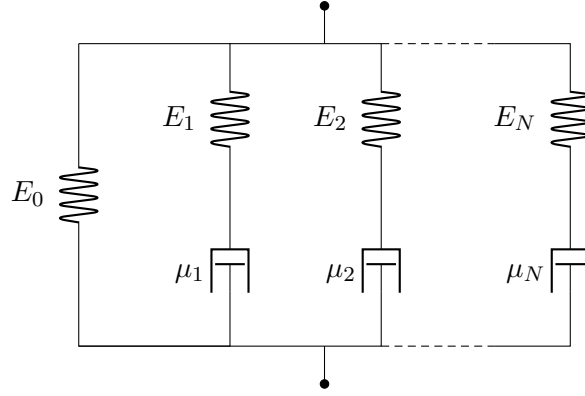


Figure 2.8: Generalized Maxwell model (Weichert model).

From force analysis, the total force is the sum of the forces in each component and so, $\sigma_{total}(t) = \sigma_s(t) + \sigma_{MM_1}(t) + \sigma_{MM_2}(t) + \dots + \sigma_{MM_N}(t)$. From geometry, the strain is the same in all components, i.e., $\varepsilon_{total}(t) = \varepsilon_s(t) = \varepsilon_{MM_1}(t) = \varepsilon_{MM_2}(t) = \dots = \varepsilon_{MM_N}(t)$. Therefore, the constitutive equation of this generalized Maxwell model is

$$\sigma(t) = \left[E_0 + \sum_{i=1}^N \frac{\partial/\partial t}{\frac{\partial/\partial t}{E_i} + \frac{1}{\mu_i}} \right] \varepsilon(t), \quad (2.19)$$

and the corresponding complex modulus is given by

$$E^*(\omega) = E_0 \left[1 + \sum_{i=1}^N \gamma_i \frac{j\omega\tau_i}{1 + j\omega\tau_i} \right], \quad (2.20)$$

where $E_\infty = E_0(1 + \sum_{i=1}^N \gamma_i)$ and τ_i is the relaxation time of the i^{th} element Maxwell model.

Figure 2.9 shows the generalized Kelvin-Voigt model, also called as Anelastic Displacement Fields (ADF) model [32]. As can be seen, it consists of a spring assembled in series to N Kelvin-Voigt models.

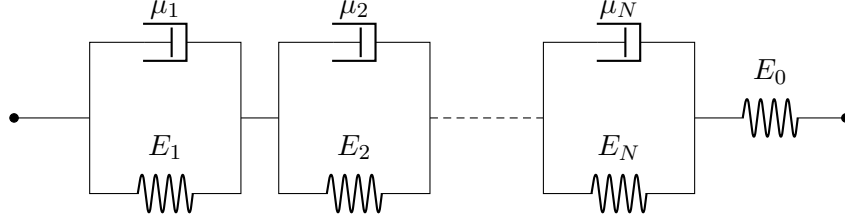


Figure 2.9: Generalized Kelvin-Voigt model (Anelastic Displacement Fields, ADF).

From force analysis, the total force is the same in all components and so, $\sigma_{total}(t) = \sigma_s(t) = \sigma_{MM_1}(t) = \sigma_{MM_2}(t) = \dots = \sigma_{MM_N}(t)$. From geometry, the strain is the sum of the strain in each component, i.e., $\varepsilon_{total}(t) = \varepsilon_s(t) + \varepsilon_{MM_1}(t) + \varepsilon_{MM_2}(t) + \dots + \varepsilon_{MM_N}(t)$. Therefore, the constitutive equation of this generalized Kelvin-Voigt model is

$$\varepsilon(t) = \left[\frac{1}{E_0} + \sum_{i=1}^N \frac{1}{E_i + \mu_i} \right] \sigma(t), \quad (2.21)$$

with the corresponding complex modulus given by

$$E^*(\omega) = E_0 \left[1 + \sum_{i=1}^N \Delta_i \frac{\omega^2 + j\omega\Omega_i}{\omega^2 + \Omega_i^2} \right], \quad (2.22)$$

where Ω_i is the inverse of relaxation time at a constant strain and Δ_i is the relaxation strength associated with i^{th} scalar modulus.

2.5 Fractional derivative models

Another way of modeling viscoelastic behavior is based on the use of fractional derivative operators. This approach was proposed by Bagley and Torvik [21], and it has proven to be more attractive than others to describe the dynamic behavior of various materials. Indeed, only a couple of parameters are needed to describe the variations of dynamic properties, which makes it suitable for vibration calculations. Some other advantages are the easy fitting of experimental measurements, the link between molecular theories and macroscopic behavior, the fulfillment of the second law of thermodynamics, and the prediction of hysteresis loops [33, 34].

The constitutive equations are thus built considering that the stress-strain relation is expressed as a fractional differential equation. The general form of the one-dimensional constitutive model based

on fractional operators in the time domain is given by [21]

$$\sigma(t) + \sum_{i=1}^n b_i D^{\beta_i}[\sigma(t)] = a_0 \varepsilon(t) + \sum_{k=1}^m a_k D^{\alpha_k}[\varepsilon(t)], \quad (2.23)$$

where a_i and b_i are material constants, β_i and α_k are the order of the fractional derivatives that must be within 0 and 1, and D^{α_k} and D^{β_i} are the Caputo fractional derivatives (see Appendix A for further details). The number of time derivatives m and n must satisfy the following thermodynamics restrictions: $m = n$ or $m = n + 1$.

Recalling that, the Fourier transform $F[\cdot]$ of the fractional derivative operator is given by

$$F\left[\frac{d^\alpha}{dt^\alpha} q(t)\right] = (j\omega)^\alpha \tilde{q}(j\omega), \quad (2.24)$$

Eq. 2.23 can be easily written in the frequency domain. Thus, applying Fourier transform on Eq. 2.23, the general form of the one-dimensional relationship between stress $\tilde{\sigma}(j\omega)$ and strain $\tilde{\varepsilon}(j\omega)$ is given by

$$\tilde{\sigma}(j\omega) + \sum_{i=1}^n b_i (j\omega)^{\beta_i} [\tilde{\sigma}(j\omega)] = a_0 \tilde{\varepsilon}(j\omega) + \sum_{k=1}^m a_k (j\omega)^{\alpha_k} [\tilde{\varepsilon}(j\omega)]. \quad (2.25)$$

The general form of complex modulus for a fractional derivative model is expressed as follows

$$E^*(\omega) = \frac{a_0 + \sum_{k=0}^m a_k (j\omega)^{\alpha_k}}{1 + \sum_{i=1}^n b_i (j\omega)^{\beta_i}}. \quad (2.26)$$

The complete thermodynamic analysis and the restrictions imposed on fractional derivative models are given by Bagley and Torvik [22], and Lion [23]. Detailed analysis of the use of fractional derivative operators and also historical information about this topic can be found in the reference book of Mainardi [24].

The fractional derivative models having four and five parameters are focused in sequence. The constitutive equations and the mathematical formulations of complex modulus are also highlighted.

2.5.1 Four-parameter fractional derivative model

The four-parameter fractional derivative model, also called as fractional Zener model, is the simplest fractional model to describe the dynamic behavior of real materials in a wide frequency range

2.5. FRACTIONAL DERIVATIVE MODELS

[21, 35]. The one-dimensional constitutive equation in the time domain for this model is derived from Eq. 2.23 and given by

$$\sigma(t) + \tau^\alpha \frac{d^\alpha \sigma(t)}{dt^\alpha} = E_0 \varepsilon(t) + E_\infty \tau^\alpha \frac{d^\alpha \varepsilon(t)}{dt^\alpha}, \quad (2.27)$$

where E_0 is the modulus at zero frequency, also known as relaxed modulus or static modulus of elasticity, E_∞ is the high frequency limit value of modulus, also known as unrelaxed modulus, τ is the relaxation time described by a power function [35]. According to Bagley and Torvik [22], these four parameters must obey the thermodynamic constraints shown in Eq. 2.28 to be physically meaningful.

$$E_\infty > E_0 \geq 0, \tau > 0 \text{ and } 0 < \alpha \leq 1. \quad (2.28)$$

By the use of Fourier transform, the constitutive equation shown in Eq. 2.27 can be written in the frequency domain as follows

$$[1 + \tau^\alpha (j\omega)^\alpha] \tilde{\sigma}(j\omega) = [E_0 + (E_\infty - E_0) \tau^\alpha (j\omega)^\alpha] \tilde{\varepsilon}(j\omega). \quad (2.29)$$

The corresponding complex modulus is thus defined as

$$E^*(\omega) = \frac{E_0 + E_\infty (j\omega\tau)^\alpha}{1 + (j\omega\tau)^\alpha}, \quad (2.30)$$

where the storage and loss moduli, and loss factor are, respectively, given by

$$E'(\omega) = \frac{E_0 + (E_\infty + E_0) \cos(\alpha\pi/2) (\omega\tau)^\alpha + E_\infty (\omega\tau)^{2\alpha}}{1 + 2\cos(\alpha\pi/2) (\omega\tau)^\alpha + (\omega\tau)^{2\alpha}}, \quad (2.31)$$

$$E''(\omega) = \frac{(E_\infty - E_0) \sin(\alpha\pi/2) (\omega\tau)^\alpha}{1 + 2\cos(\alpha\pi/2) (\omega\tau)^\alpha + (\omega\tau)^{2\alpha}} \quad (2.32)$$

and

$$\eta(\omega) = \frac{(E_\infty - E_0) \sin(\alpha\pi/2) (\omega\tau)^\alpha}{E_0 + (E_\infty - E_0) \cos(\alpha\pi/2) (\omega\tau)^\alpha + E_\infty (\omega\tau)^{2\alpha}}. \quad (2.33)$$

Finally, some points should be highlighted concerning the effects of these four parameters (α, E_0, E_∞ and τ) and the variations of complex modulus as outlined by Pritz [35]. From Eqs. 2.31 to 2.33, it can be seen that storage modulus increases from E_0 to E_∞ as frequency increases, while the slope

2.5. FRACTIONAL DERIVATIVE MODELS

of the storage modulus curve at the inflection point is affected by the value of α : the smaller α , the smaller the slope is. Both loss modulus and loss factor curves have only one symmetric peak related to frequency. The slope of the increase and decrease of these curves, respectively, below and above the peak is influenced by α . Furthermore, the frequency at which the maximum loss modulus occurs is given by $1/\tau$.

Figure 2.10 illustrates these effects for the absolute value of complex modulus, $|E^*(\omega)|$, and loss factor, $\eta(\omega)$. The following parameters were considered constant $E_0 = 10^4$ Pa, $E_\infty = 10^6$ Pa and $\tau = 10^{-8}$ s, while parameter α varied from 0.3 to 0.7.

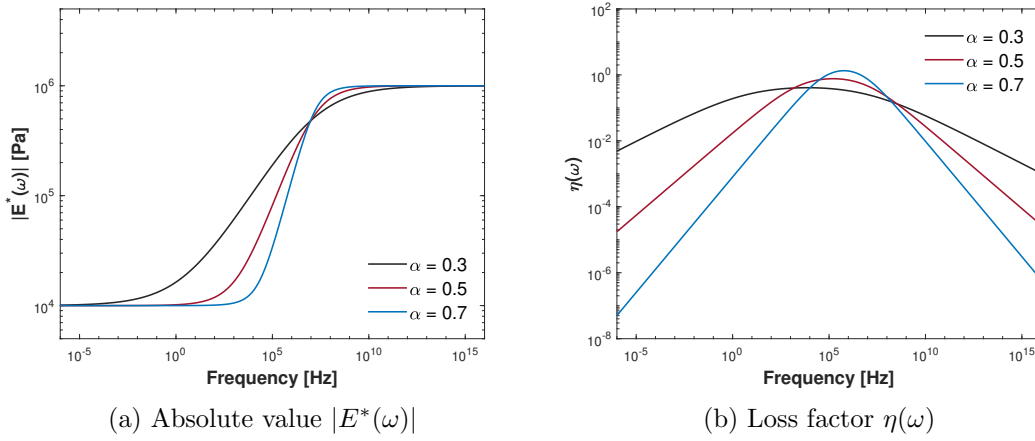


Figure 2.10: Representation of the complex modulus of the four-parameter fractional derivative model.

2.5.2 Five-parameter fractional derivative model

As previously mentioned, the four-parameter fractional derivative model is effective to describe the frequency dependence of a viscoelastic property. However, this model is only able to predict symmetric loss peak, which is not always the case: some materials have shown loss modulus and loss factor curves flattening after the peak. As a result, Pritz [36] proposed the introduction of a fifth parameter β into the model aiming at overcoming this issue.

In this way, the five-parameter fractional derivative model, also referred to as the five-parameter fractional derivative Zener model, allows the prediction of an asymmetrical loss peak and a better description of high-frequency behavior [36]. The one-dimensional constitutive equation in the time domain for this model is given by

2.5. FRACTIONAL DERIVATIVE MODELS

$$\sigma(t) + \tau^\beta \frac{d^\beta \sigma(t)}{dt^\beta} = E_0 \varepsilon(t) + E_0 \tau^\beta \frac{d^\beta \varepsilon(t)}{dt^\beta} + (E_\infty - E_0) \tau^\alpha \frac{d^\alpha \varepsilon(t)}{dt^\alpha}. \quad (2.34)$$

where β is the order of the fractional derivative introduced to describe the flattening of curve after the peak. It must be within 0 and 1.

It should be pointed out that, even though some parameters appear in both Eqs. 2.27 and 2.34, they do not necessarily signify the same thing. The parameter E_∞ is related to the high-frequency behavior, but it is not anymore the limit value. The parameter τ , in turn, is also the relaxation time described by a power function, but its value is different from the one of the four-parameter model. Furthermore, these five parameters must obey the thermodynamic constraints shown in Eq. 2.35 to be physically meaningful [36].

$$E_\infty \geq E_0 \geq 0, \tau > 0 \text{ and } 0 < \beta < \alpha \leq 1. \quad (2.35)$$

By the use of Fourier transform on Eq. 2.34, the relationship between stress and strain is written in frequency domain such as

$$[1 + \tau^\beta (j\omega)^\beta] \tilde{\sigma}(j\omega) = [E_0 + E_0 \tau^\beta (j\omega)^\beta + (E_\infty - E_0) \tau^\alpha (j\omega)^\alpha] \tilde{\varepsilon}(j\omega), \quad (2.36)$$

leading to the following complex modulus

$$E^*(\omega) = E_0 + \frac{(E_\infty - E_0)(j\omega\tau)^\alpha}{1 + (j\omega\tau)^\beta}, \quad (2.37)$$

where the storage and loss moduli, and loss factor are, respectively, given by

$$E'(\omega) = E_0 + (E_\infty - E_0) \frac{\cos(\alpha\pi/2)(\omega\tau)^\alpha + \cos[(\alpha - \beta)\pi/2](\omega\tau)^{\alpha+\beta}}{1 + 2\cos(\beta\pi/2)(\omega\tau)^\beta + (\omega\tau)^{2\beta}} \quad (2.38)$$

$$E''(\omega) = (E_\infty - E_0) \frac{\sin(\alpha\pi/2)(\omega\tau)^\alpha + \sin[(\alpha - \beta)\pi/2](\omega\tau)^{\alpha+\beta}}{1 + 2\cos(\beta\pi/2)(\omega\tau)^\beta + (\omega\tau)^{2\beta}} \quad (2.39)$$

and

$$\eta(\omega) = \frac{(E_\infty/E_0 - 1) \{ \sin(\alpha\pi/2)(\omega\tau)^\alpha + \sin[(\alpha - \beta)\pi/2] \} (\omega\tau)^{\alpha+\beta}}{1 + 2\cos(\beta\pi/2)(\omega\tau)^\beta + (\omega\tau)^{2\beta} + (E_\infty/E_0 - 1) \{ \cos(\alpha\pi/2)(\omega\tau)^\alpha + \cos[(\alpha - \beta)\pi/2] \} (\omega\tau)^{\alpha+\beta}}. \quad (2.40)$$

2.6. EFFECTS OF TIME/FREQUENCY AND TEMPERATURE

Finally, some points should be highlighted concerning the effects of these five parameters and the variations of complex modulus as outlined by Pritz [36]. From Eqs. 2.38 to 2.40, it can be seen that storage modulus monotonically increases from E_0 , but does not have an upper limit. Both loss modulus and loss factor curves increase after a slight decrease after the peak. The slope of both storage and loss moduli curves is determined by the value of $\alpha - \beta$. Furthermore, the low-frequency behavior of loss modulus and loss factor curves is influenced by α , whereas the high-frequency one is affected by β .

Figure 2.11 illustrates these effects for the absolute value of complex modulus, $|E^*(\omega)|$, and loss factor, $\eta(\omega)$. The following parameters were considered constant $E_0 = 10^4$ Pa, $E_\infty = 10^6$ Pa, $\tau = 10^{-8}$ s and $\alpha = 0.5$, while parameter β varied from 0.05 to 0.45.

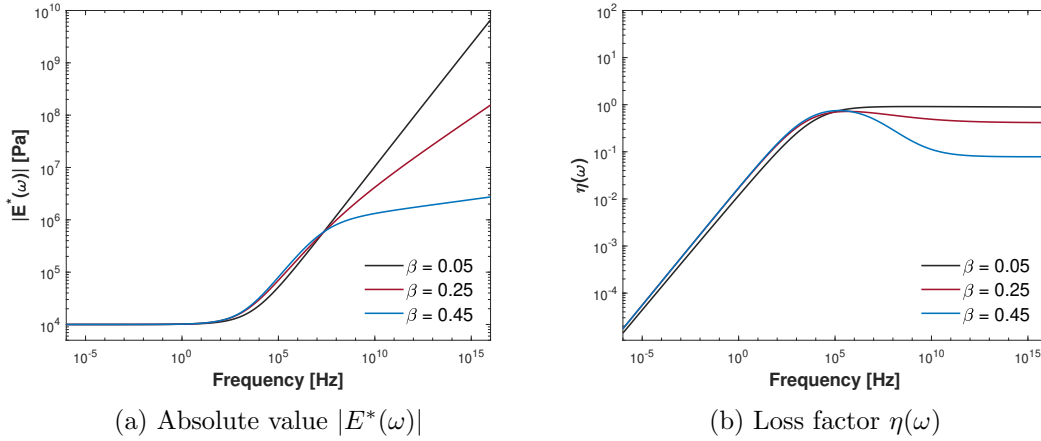


Figure 2.11: Representation of the complex modulus of the five-parameter fractional derivative model.

2.6 Effects of time/frequency and temperature

The time/frequency and temperature dependencies of viscoelastic materials are crucial to characterize their behavior as they can change drastically their mechanical response. Hence, this section focus on the physical phenomena that influence these dependencies and how they lead to the general behavior of these materials.

2.6.1 General Aspects

The temperature dependence is a consequence of the microstructure of viscoelastic materials. In the particular case of amorphous polymers, this microstructure is composed of entangled long chains of molecules that, depending on the composition and temperature, can have different types of bonds between themselves. In general, more cross-linked molecules indicate a higher strength of the material, while less entangled molecules indicate a more viscous behavior.

Figure 2.12 illustrates the temperature dependence of a typical viscoelastic mechanical property. At low temperatures, the amorphous regions of a polymer are in the glassy state. In this state, the molecules are frozen in place: they may be able to vibrate slightly, but they do not have any segmental motion in which portions of the molecule wiggle around. It makes the material usually hard, rigid, and brittle. If the polymer is heated, it will eventually reach its glass transition. In this region, portions of the molecules can start to wiggle around allowing some movement between chains, which, in turn, raise the influence of viscous behavior. Note that the transition does not occur at a single temperature. As the temperature increases, the polymer reaches its rubbery state. In this state, molecules easily slide between each other, providing a soft movement and lowering the stiffness of the material. It makes the material usually soft and flexible. If the temperature rises above the rubbery state, the material can gradually transit to a liquid state, where there is no more entanglement between molecules, and intermolecular bonds are weak.

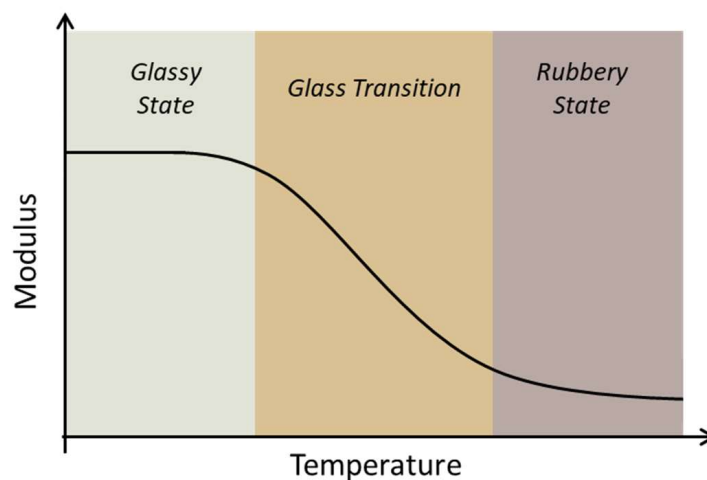


Figure 2.12: Regions of viscoelastic behavior according to temperature changes.

Another important feature is the time/frequency dependence. This dependency may have great impacts on material properties. Its effects are similar to what happens with temperature changes. Over long enough time periods, or small enough frequencies, the viscoelastic material becomes softer and more fluid-like, passing through transitions, due to molecular arrangements.

Nevertheless, sometimes this effect may be almost undetectable depending on the time scale. A way to verify its influence is through the dimensionless number known as Deborah Number [8, 13]. This number compares the time that the material takes to respond to an excitation and the time of the experiment as defined in Eq. 2.41.

$$n_D = \frac{\tau_{rex}}{\tau_{exp}} \quad (2.41)$$

where τ_{rex} is the time scale of the material rearrangements and τ_{exp} is the experimental time scale.

In Eq. 2.41, when $n_D \rightarrow \infty$, the relaxation time is much greater than the experimental time leading to a pure elastic behavior. On the other hand, when $n_D \rightarrow 0$, the relaxation time is too low in comparison to the experimental time leading to a pure viscous behavior. Indeed, a more fluid-like material needs less time to flow than a solid-like material when subjected to the same loading rate. When Deborah number is between these limits, the viscoelastic behavior emerges. Polymers, in particular, have $n_D \approx 1$, being called as viscoelastic materials *par excellence*.

2.6.2 Thermorheologically simple materials

Viscoelastic materials are time (t) (or frequency (ω)) and temperature (T) dependent. In this regard, a viscoelastic function can be written according to both dependencies; for example, the relaxation modulus can be denoted by $E(t, T)$ instead of just $E(t)$ as well as the complex modulus can be represented by $E^*(\omega, T)$ instead of $E^*(\omega)$. Therefore, in rheological studies, these dependencies may need to be accounted for.

There is a special group of viscoelastic materials known as Thermo-rheologically Simple Materials [37] that presents mechanical properties with particular temperature dependence. For them, all relaxation times have the same temperature dependence, i.e., time and temperature dependences can be considered as the same phenomenon.

Changes in temperature stretch or shrink the effective time scale [8, 11]. In other words, changes

in temperature cause relaxation modulus to be shifted to the right or left when plotted against time (or frequency) on a log scale. But, the short-term $E(t \rightarrow 0)$ and the long-term $E(t \rightarrow \infty)$ of relaxation modulus remain the same, regardless of temperature.

Such materials obey the Time-Temperature Superposition Principle (TTSP) [37] and can be experimentally identified through Cole-Cole [38] and Black [39] diagrams. These concepts are explained in the next subsections.

2.6.2.1 Time-temperature superposition principle (TTSP)

Time-Temperature Superposition Principle (TTSP), also known as Method of Reduced Variables, is an empirical principle that is valid for most polymers in the linear regime as well as in nonlinear regime when close to their transition region. It classically determines that a single master curve that covers many decades of time or frequency can be obtained by applying horizontal a_T and vertical b_T shift factors to isotherms just above or below the reference temperature T_0 [8, 9, 37].

The generated master curve enables one to have more information about material behavior than the curves of the original data. They expand the available time range which is usually restricted due to instrument limitations [40]. Hence, TTSP becomes an important procedure to predict the viscoelastic behavior over a very long-time regime just by measuring it at a set of temperatures $\{T_1, T_2, \dots, T_N\}$.

From a molecular point of view [8, 40], TTSP implies that there is an equivalence between viscoelastic properties measured at a temperature T and time t , and those measured at a reference temperature T_0 and reduced time t_R .

From the mathematical point of view, this principle is expressed as

$$E(t, T) = b_T E(t_R, T_0), \quad (2.42)$$

where t is the time at which the material reaches a particular response at temperature T , $t_R = t/a_T(T, T_0)$ is the reduced time, and a_T and b_T are the shift factors that depend on the material and on T_0 .

Furthermore, this principle can also be expressed in the frequency domain by the use of Fourier transform in Eq. 2.42. In this case, it is known as frequency-temperature superposition principle (FTSP) [14]. Thus, Eq. 2.42 becomes

$$E^*(\omega, T) = b_T E^*(\omega_R, T_0), \quad (2.43)$$

where $\omega_R = \omega \times a_T(T, T_0)$ is the reduced angular frequency in radians per second.

The horizontal shift factor a_T describes the relationship between relaxation time and temperature and is described by different models in literature [8, 41, 42]. For temperatures closer to glass transition ($T_g < T < T_g + 100^\circ\text{C}$), one of the main models used is the empirical relationship known as the Williams-Landel-Ferry (WLF) equation proposed by Williams et al. [43]. It assumes that the fractional free volume of polymers increases with temperature, and it is defined as

$$\log a_T(T, T_0) = -\frac{C_1(T - T_0)}{C_2 + (T - T_0)}, \quad (2.44)$$

where T is the temperature in Kelvin and, C_1 and C_2 are empirical constants that depend on the material and the reference temperature T_0 , which have an order of magnitude of 10 and 100K, respectively [8]. When the reference temperature chosen for the analyses corresponds to the glass transition one, C_1 and C_2 are the universal constants that Ferry has proposed and whose values are, respectively, 17.44 and 51.6 K [8].

The vertical shift factor b_T , on the other hand, describes the thermal expansion effects of the material, having a lower temperature dependence in comparison to the horizontal shift factor. It is usually modeled through the Bueche-Rouse theory [44]. This theory assumes that the material property is proportional to the product of the density ρ and the temperature T . As temperature changes, the thermal expansion effects modify the density of the material. The vertical shift factor b_T is thus given by [41]

$$b_T(T, T_0) = \frac{T_0 \rho_0}{T \rho}, \quad (2.45)$$

where ρ_0 is the density at temperature T_0 .

To illustrate this idea of applying shift factors into isotherm curves, Fig. 2.13 shows the methodology behind this principle. The symbol E is adopted to denote any viscoelastic property. First, experimental measurements are carried out, and the material property is determined as a function of frequency at different temperatures (see Fig. 2.13a). Afterward, the horizontal shift factors a_T are

applied to the isotherm curves (see Fig. 2.13b). Finally, the vertical factors b_T are applied to obtain the final master curve (see Fig. 2.13c), which has a greater frequency window than the original curves.

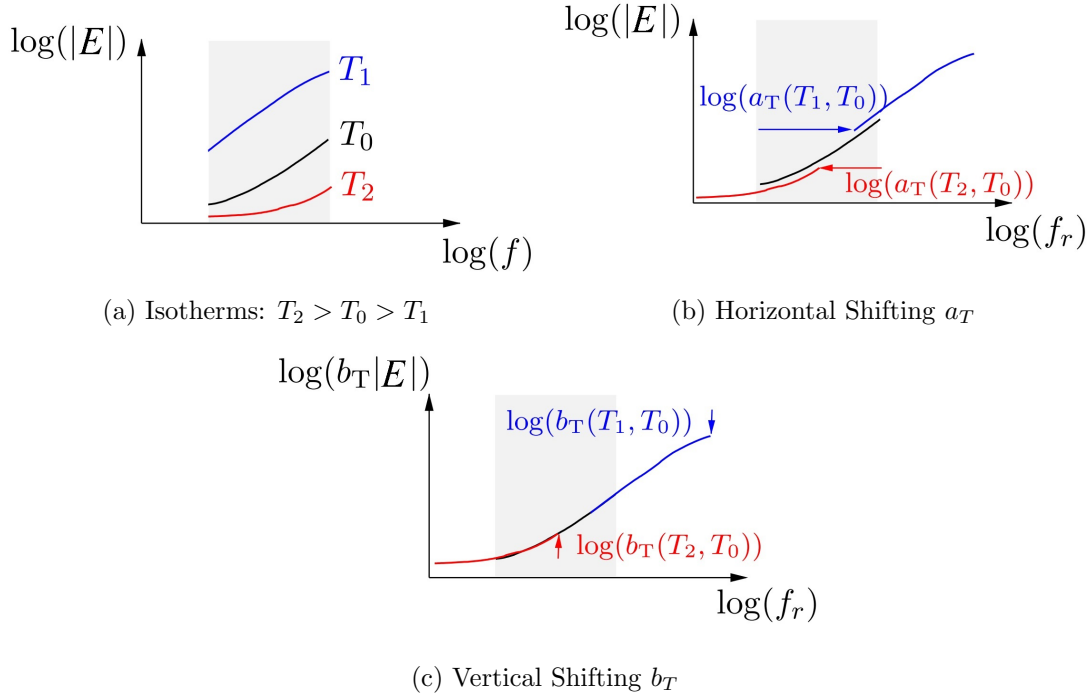


Figure 2.13: Time-Temperature Superposition Principle (TTSP) [2].

2.6.2.2 Cole-Cole and Black diagrams

In some cases, thermo-rheological simplicity can not be expected such as if the material passes through a phase transformation, if it burns or decomposes, if it has a multiplicity of relaxation mechanisms, or if it is composed by different phases with different temperature dependencies [11, 40]. Two simple ways to check the validity of this assumption and the applicability of TTSP are through the Cole-Cole Diagram [38] and the Black Space [39].

The so-called Cole-Cole Diagram is obtained by plotting the imaginary part of the material modulus against the real one in a double logarithmic scale, for example, $E''(\omega, T) \times E'(\omega, T)$. The Black Space or Wicket Plot, on the other hand, is determined by plotting loss factor against modulus amplitude, such as $\eta(\omega) \times |E^*(\omega, T)|$.

In both diagrams, the hypothesis of thermo-rheological simple behavior is validated when all data obtained at different frequencies and temperatures lie close to one single curve. As stated by Dae Han

2.6. EFFECTS OF TIME/FREQUENCY AND TEMPERATURE

and Kim [38], these diagrams must fall on a continuous circular arc; in which a circular arc with a particular shape is obtained for each temperature analyzed.

Furthermore, they can also identify the need for vertical shifting when a slight temperature dependence is exhibited. In this situation, parallel isotherms are observed in the diagrams [2].

2.6. EFFECTS OF TIME/FREQUENCY AND TEMPERATURE

Chapter 3

Model calibration & validation

This chapter aims to present theoretical aspects of the Bayesian framework for inverse problems and model validation techniques, highlighting the important aspects related to this work and its comprehension. It is organized as follows. Section 3.1 first defines an inverse problem and then discusses its concepts from a Bayesian perspective. Section 3.2 deals with Markov chain Monte Carlo techniques, which are commonly employed to solve a stochastic inverse problem, and presents classical algorithms. Section 3.3 introduces the main concepts of model validation techniques, focusing on the approaches adopted herein.

Content

| | | |
|------------|--|------------|
| 3.1 | Parameter estimation from a Bayesian perspective | 96 |
| 3.1.1 | Choice of the prior probability density function | 98 |
| 3.1.2 | Choice of the likelihood function | 98 |
| 3.1.3 | Posterior probability density function and point estimates | 100 |
| 3.2 | Markov chain monte carlo (MCMC) techniques | 101 |
| 3.2.1 | Metropolis-Hastings (MH) | 102 |
| 3.2.2 | Delayed rejection adaptive metropolis (DRAM) | 103 |
| 3.3 | Model Validation | 106 |
| 3.4 | Uncertainty quantification and propagation through Monte Carlo method | 108 |

3.1 Parameter estimation from a Bayesian perspective

Nowadays, the formalism of inverse problems is quite useful in engineering due to their capacity to indirectly identify system parameters by analysing its response. According to Alifanov, ‘*solution of an inverse problem entails determining unknown causes based on observation of their effects*’. This is in contrast with direct problem where causes are given and the effects are unknown and to be determined. Therefore, inverse problems techniques are powerful tools to determine initial conditions, boundary conditions and other system parameters from a set of measurements [25, 26, 45].

Let us consider a mathematical model f , that is used to describe a physical system \mathbb{S} , which has a certain set of inputs $\mathbf{x} \in \mathfrak{R}^{N_x}$ and a set of measured outputs $\mathbf{y} \in \mathfrak{R}^{N_y}$ that may have noise. Also, consider that the model f has a set of parameters $\boldsymbol{\theta} \in \mathfrak{R}^{N_\theta}$ that may be inaccurate. In other words, model parameters may not be completely known. In this regard, the system’s measured response \mathbf{y} can be expressed as follows:

$$\mathbf{y} = f(\boldsymbol{\theta}, \mathbf{x}, \mathbf{e}) \tag{3.1}$$

where $f : \mathfrak{R}^{N_\theta} \times \mathfrak{R}^{N_x} \rightarrow \mathfrak{R}^{N_y}$ is the model mathematical operator and $\mathbf{e} \in \mathfrak{R}^{N_x}$ is related to model inaccuracies and noise. The symbols N_x , N_y and N_θ denote the number of inputs (dimension of the vector \mathbf{x}), observables quantities (dimension of the vector \mathbf{y}) and unknown parameters (dimension of the vector $\boldsymbol{\theta}$), respectively.

The inverse problem consists of determining the set of parameters $\boldsymbol{\theta}$ given the system’s measured response \mathbf{y} and the set of input variables \mathbf{x} . That is, one would say that the objective of this kind of problem is to find the most suitable unknown parameters $\boldsymbol{\theta}$ which provide minimum distance between measurement \mathbf{y} and predictions $f(\boldsymbol{\theta}, \mathbf{x})$ according to some metric previously defined by the user.

An important point is that inverse problems are often considered as ill-posed. They do not satisfy any postulate of Hadamard [46]: the conditions of existence, uniqueness, and stability concerning the input data. Besides, they are also considered to be non-local and/or non-causal, leading to abrupt changes of its solutions by small variations on the data set [26].

Various numerical techniques are used to solve this kind of problem for parameter estimation [27]. One may cite, for instance, Tikhonov regularization, gradient-based methods, nonlinear regressions,

and the Bayesian approach. The latter, however, presents some advantages over the classical methods, mainly because it allows to add prior information about the set of parameters $\boldsymbol{\theta}$ and to quantify the uncertainties about them. For this reason, this statistical framework is adopted herein and its main aspects are described in the next paragraphs.

In a Bayesian framework, all unknown quantities and measurements are considered as random variables. The uncertainty about each random variable is modeled through its probability density function (PDF), which describes the current state of knowledge or the prior on this parameter. Further, the solution of the inverse problem is also modelled in terms of a PDF, called posterior distribution. Henceforth, the following notation is used: $\pi(\theta)$ represents the PDF of a random variable θ , $\pi(\theta, y)$ represents the joint PDF of the random variables θ and y , $\pi(\theta|y)$ represent the conditional PDF of θ given y , and $\pi(\boldsymbol{\theta})$ represents the PDF of a random vector $\boldsymbol{\theta}$.

Therefore, the objective of the inverse problem through a Bayesian perspective is not anymore the search for a set of unknown parameters $\boldsymbol{\theta}$ but to extract all possible information about them consistently with (i) the set of measured data \mathbf{y} , (ii) the mathematical model f , and (iii) the information about $\boldsymbol{\theta}$ before the measurement acquisition. The problem thus tries to find a probability density function for $\boldsymbol{\theta}$ given the available data \mathbf{y} .

From a mathematical point of view, the relation between the random variables \mathbf{y} , $\boldsymbol{\theta}$ and \mathbf{x} relies on Bayes' theorem, also referred as *Bayes' theorem of inverse problems* [25, 26], as

$$\pi(\boldsymbol{\theta}|\mathbf{y}) = \frac{\pi(\mathbf{y}|\boldsymbol{\theta})\pi_0(\boldsymbol{\theta})}{\pi(\mathbf{y})} \quad (3.2)$$

where $\pi(\boldsymbol{\theta}|\mathbf{y})$ is the posterior probability density function of the model parameters, $\pi(\mathbf{y}|\boldsymbol{\theta})$ is the likelihood function, $\pi_0(\boldsymbol{\theta})$ is the prior model adopted for the unknown parameters $\boldsymbol{\theta}$, and $\pi(\mathbf{y})$ is the probability density function of measured data \mathbf{y} given by

$$\pi(\mathbf{y}) = \int_{\mathfrak{R}^{N_\theta}} \pi(\boldsymbol{\theta}, \mathbf{y}) d\boldsymbol{\theta}. \quad (3.3)$$

In practice, the marginal density $\pi(\mathbf{y})$ is hardly available since it requires a large number of experiments to get some information about it. Fortunately, this PDF plays the role of a scaling constant and has often little influence [26]. Hence, Eq. 3.2 becomes

$$\pi(\boldsymbol{\theta}|\mathbf{y}) \propto \pi(\mathbf{y}|\boldsymbol{\theta})\pi_0(\boldsymbol{\theta}). \quad (3.4)$$

Generally speaking, one would say that, from Eq. 3.4, the procedure to solve a Bayesian inverse problem can be divided into three main steps. The first one is to estimate the prior PDF $\pi_0(\boldsymbol{\theta})$ based on all the knowledge of the parameters already obtained. The second one is to obtain a likelihood function $\pi(\mathbf{y}|\boldsymbol{\theta})$ which describes the relationship between model parameters and experimental data. Finally, the third is to develop a method to obtain the posterior PDF $\pi(\boldsymbol{\theta}|\mathbf{y})$.

Therefore, it becomes quite important to comprehend the components of Eq. 3.4 as they are the base for solving inverse problems from a Bayesian perspective [25, 26].

3.1.1 Choice of the prior probability density function

One crucial step in this framework is the choice of the prior probability density function $\pi_0(\boldsymbol{\theta})$, which is often the most challenging endeavor as well. The major difficulty with finding an adequate prior PDF lies in the essence of the prior information about the parameters $\boldsymbol{\theta}$.

In general terms, the prior PDF $\pi_0(\boldsymbol{\theta})$ is the initial guess of parameter distribution, reflecting the uncertainty related to the parameters $\boldsymbol{\theta}$. Indeed, it can be seen as a measure of the knowledge a priori of the user on the parameters to identify.

The prior model may be built exploring all the information available about $\boldsymbol{\theta}$ before measurements. One often makes use of data from previous experiments, data from manufacturer catalogs, or empirical data obtained from people working in the field. There are many possible choices to priors distribution such as Gaussian, uniform, or chi-squared distributions [25, 26]. However, if there is no reliable knowledge of the parameters, it is recommended to adopt a non-informative prior, i.e., a uniform density distribution with its range encompassing all possible values.

3.1.2 Choice of the likelihood function

The most straightforward step in statistical inversion is often the choice of the likelihood function $\pi(\mathbf{y}|\boldsymbol{\theta})$. This function incorporates the knowledge about the model, the noise, and the modeling uncertainties.

Generally speaking, the conditional PDF $\pi(\mathbf{y}|\boldsymbol{\theta})$ is the likelihood of obtaining the results \mathbf{y} given

3.1. PARAMETER ESTIMATION FROM A BAYESIAN PERSPECTIVE

a set of parameters $\boldsymbol{\theta}$. It reflects the uncertainty related to the measured data \mathbf{y} , and it can be seen as a measure of the fidelity of the model to the measured data.

The specification of the likelihood function depends on the hypotheses about the distribution of noise. Different formulations can be used to model it [26]. Assuming that the noise \mathbf{e} is modeled as an additive and considered to be iid, Eq. 3.1 can be rewritten as:

$$\mathbf{y} = f(\boldsymbol{\theta}, \mathbf{x}) + \mathbf{e}, \quad (3.5)$$

in which the expected value $\mathbb{E}[\mathbf{e}] = 0$ and the constant variance $\sigma^2 = \mathbb{E}[(\mathbf{y} - \mathbb{E}[\mathbf{y}])^2]$.

Then, the likelihood function $\pi(\mathbf{y}|\boldsymbol{\theta})$ can be expressed as follows

$$\pi(\mathbf{y}|\boldsymbol{\theta}) = \pi_{noise}(\mathbf{y} - f(\boldsymbol{\theta}, \mathbf{x})|\boldsymbol{\theta}) \quad (3.6)$$

where $\pi_{noise}(\mathbf{y} - f(\boldsymbol{\theta}, \mathbf{x})|\boldsymbol{\theta})$ is the probability density of the additive noise \mathbf{e} evaluated in $\mathbf{y} - f(\boldsymbol{\theta}, \mathbf{x})$.

Furthermore, if one assumes that this additive noise follows, for example, a Gaussian distribution with zero mean and a covariance matrix Σ such as

$$\mathbf{e} \sim N(\mathbf{0}, \Sigma), \quad (3.7)$$

the likelihood is expressed as [25, 26]

$$\pi(\mathbf{y}|\boldsymbol{\theta}) = \frac{1}{(2\pi)^{N_y} |\Sigma|^{1/2}} \exp\left\{ -\frac{1}{2} [\mathbf{y} - f(\boldsymbol{\theta}, \mathbf{x})]^T \Sigma^{-1} [\mathbf{y} - f(\boldsymbol{\theta}, \mathbf{x})] \right\}. \quad (3.8)$$

Finally, the covariance matrix Σ can be defined as a diagonal covariance matrix such as

$$\Sigma = \begin{bmatrix} \sigma_1^2 & 0 & \dots & 0 \\ 0 & \sigma_2^2 & \dots & 0 \\ \vdots & \vdots & \ddots & 0 \\ 0 & 0 & \dots & \sigma_{N_y}^2 \end{bmatrix} \quad (3.9)$$

where σ_i^2 is the standard deviation of the i^{th} set of measured data \mathbf{y}_i . Moreover, if one does not know this deviation, it is possible to consider it as an additional random parameter to be estimated [25].

3.1.3 Posterior probability density function and point estimates

The posterior probability density function $\pi(\boldsymbol{\theta}|\mathbf{y})$ represents the probability of observing the parameters $\boldsymbol{\theta}$ given the measured data \mathbf{y} . Alternatively, it can be seen as the measure of knowledge about the parameters $\boldsymbol{\theta}$ after performing measurements to obtain \mathbf{y} .

From this posterior PDF, one may readily compute some point estimates to define the most likely values of the parameters $\boldsymbol{\theta}$ based on concepts of mean, median, or mode. In this context, different ways can be found in the literature based on Bayesian ideas. Among them, it is possible to highlight three estimators: the maximum likelihood $\hat{\boldsymbol{\theta}}_{ML}$, the maximum a posteriori $\hat{\boldsymbol{\theta}}_{MAP}$ and the mean of the posterior distribution $\mathbb{E}_{\boldsymbol{\theta}|\mathbf{y}}(\boldsymbol{\theta})$ as described next.

The maximum likelihood (ML) $\hat{\boldsymbol{\theta}}_{ML}$ is one of the most popular estimates. It is defined as the parameter value that is most likely to create the measured data \mathbf{y} given by

$$\hat{\boldsymbol{\theta}}_{ML} = \arg \max_{\boldsymbol{\theta} \in \mathfrak{R}^{N_{\theta}}} \pi(\mathbf{y}|\boldsymbol{\theta}). \quad (3.10)$$

The maximum a posteriori (MAP) $\hat{\boldsymbol{\theta}}_{MAP}$, also referred as posterior mode, is another popular estimates. It is defined as the parameter value that maximizes the posterior PDF $\pi(\boldsymbol{\theta}|\mathbf{y})$ such as

$$\hat{\boldsymbol{\theta}}_{MAP} = \arg \max_{\boldsymbol{\theta} \in \mathfrak{R}^{N_{\theta}}} \pi(\boldsymbol{\theta}|\mathbf{y}). \quad (3.11)$$

It should be pointed out that when the prior $\pi_0(\boldsymbol{\theta})$ is defined by a uniform distribution, the maximum a posteriori is equivalent to the maximum likelihood, i.e. $\hat{\boldsymbol{\theta}}_{MAP} = \hat{\boldsymbol{\theta}}_{ML}$. Also, both estimators require the application of an optimization technique such as gradient-based methods.

Finally, the mean of the posterior distribution $\mathbb{E}_{\boldsymbol{\theta}|\mathbf{y}}(\boldsymbol{\theta})$ is another common point estimate defined as

$$\mathbb{E}_{\boldsymbol{\theta}|\mathbf{y}}(\boldsymbol{\theta}) = \int_{\mathfrak{R}^{N_{\theta}}} \boldsymbol{\theta} \pi(\boldsymbol{\theta}|\mathbf{y}) d\boldsymbol{\theta}, \quad (3.12)$$

for which one has to solve an integration on a high-dimensional space $\mathfrak{R}^{N_{\theta}}$.

Nevertheless, a closed-form analytical expression for this posterior PDF is seldom available. The mathematical operator $f(\boldsymbol{\theta}, \mathbf{x})$ is often non-linear and this PDF $\pi(\boldsymbol{\theta}|\mathbf{y})$ is defined in a high-dimensional space. One of the most efficient ways to explore it is through sampling based techniques such as the Markov Chain Monte Carlo Techniques (MCMC), which are adopted in this work. Their basics aspects

are described in the next section. For more information, one may cite the reference books by Kim et al. [47], Smith [25], Kaipio and Somersalo [26].

3.2 Markov chain monte carlo (MCMC) techniques

Markov Chain Monte Carlo (MCMC) techniques are general computational approaches that have been widely employed in different areas to explore the posterior probability function based on the ideas of Monte Carlo integration and Markov chains. They are considered to be conceptually simple, easy to be implemented, and explore more efficiently the whole space of parameters when dealing with large dimensions [25, 26].

Markov chains are sequences of S -valued random variables that satisfy the Markov property which states that the probability of future states only depends on the present state. They are stochastic processes such that the past and future states are independent of each other. Further, they are described by three elements: a state-space S , an initial distribution, and a transition or Markov kernel [25].

The central idea behind MCMC is to design a Markov chain $\boldsymbol{\theta} = \{\boldsymbol{\theta}^{(1)}, \boldsymbol{\theta}^{(2)}, \dots, \boldsymbol{\theta}^{(M)}\}$ whose stationary distribution is exactly the one that we are interested in sampling from, often referred as target distribution $\bar{\pi}(\boldsymbol{\theta})$. The samples are generated sequentially so that the sample distribution $\boldsymbol{\theta}^{(j)}$ depends only on the last generated sample $\boldsymbol{\theta}^{(j-1)}$.

When dealing with inverse problems, the target distribution is the posterior probability density function, i.e. $\bar{\pi}(\boldsymbol{\theta}) = \pi(\boldsymbol{\theta}|\mathbf{y})$, which can always be approximated by the method regardless of how it is initialized. However, depending on initialization, the method can present a transient behavior before converging to the solution. Hence, the influence of this transient period should be eliminated from the Markov chain by removing the initial samples, which is also called as burn-in period.

The Markov chain generated $\{\boldsymbol{\theta}^{(1)}, \boldsymbol{\theta}^{(2)}, \dots, \boldsymbol{\theta}^{(M)}\}$ is considered to be homogeneous, irreducible and aperiodic. From this chain, it is thus possible to determine any statistical parameter according to the interest of the researcher, such as, for example, mean, variance, kurtosis.

There are several MCMC methods to achieve this goal. The main differences between them are associated with convergence rates and also with the acceptance rate of the Markov chain [26]. The basic aspects and implementation characteristics of some classical algorithms are presented next.

3.2.1 Metropolis-Hastings (MH)

One of the simplest and most used algorithm to solve inverse problems within the Bayesian approach is the Metropolis-Hastings (MH) algorithm proposed by Metropolis et al. [48] and modified by Hastings [49].

The method starts with an initial sample $\boldsymbol{\theta}^{(0)}$ which is used to generate a candidate $\boldsymbol{\theta}^{(*)}$ from a proposal distribution $\pi(\boldsymbol{\theta}^{(*)}|\boldsymbol{\theta}^{(j-1)})$, which can be symmetric such as $\pi(\boldsymbol{\theta}^{(*)}|\boldsymbol{\theta}^{(j-1)}) = \pi(\boldsymbol{\theta}^{(j-1)}|\boldsymbol{\theta}^{(*)})$ or nonsymmetric. Afterwards, the candidate $\boldsymbol{\theta}^{(*)}$ is accepted or rejected with probability equal to Hastings ratio such as

$$\alpha_{MH} = \min \left\{ 1, \frac{\pi(\boldsymbol{\theta}^{(*)}|\mathbf{y}) \pi(\boldsymbol{\theta}^{(j-1)}|\boldsymbol{\theta}^{(*)})}{\pi(\boldsymbol{\theta}^{(j-1)}|\mathbf{y}) \pi(\boldsymbol{\theta}^{(*)}|\boldsymbol{\theta}^{(j-1)})} \right\}, \quad (3.13)$$

where $\pi(\boldsymbol{\theta}^{(i)}|\mathbf{y})$ is the target distribution as shown in Eq. 3.2.

To decide if the candidate is accepted or not, the probability α_{MH} is compared with another random sample value u generated from a uniform distribution on the set $[0, 1]$. If $u < \alpha_{MH}$, the sample is accepted, becoming the new value of the chain $\boldsymbol{\theta}^{(j)} = \boldsymbol{\theta}^{(*)}$. However, if $u > \alpha_{MH}$, the candidate is rejected and so, the value of the chain is thus not modified $\boldsymbol{\theta}^{(j)} = \boldsymbol{\theta}^{(j-1)}$. It is important to notice that, if the parameter $\alpha_{MH} \geq 1$, the procedure always accepts the proposal, but if $\alpha_{MH} < 1$, there is still a chance to the value be accepted. This property of accepting better cases and occasionally worst cases ensures that the chain will converge to the values where the likelihood has high density, but it will still visit the whole state space.

Another important point is the choice of the proposal function since it affects the exploration of the parameter space and the convergence of the algorithm. A small step-size in the proposal transition yields a poor exploration of the parameter space and slow convergence. A large step-size, on the other hand, can lead to low acceptance rates, which indicates that the chain moves slowly and can sometimes stagnate. The acceptance rate must be thus verified over the sampling process in order to ensure that convergence is achieved. Reasonable values of acceptance ratio are within 0.1 and 0.5 [25].

Algorithm 1 summarizes the classical formulation of Metropolis-Hastings algorithm [25, 26].

Algorithm 1 Metropolis-Hastings Algorithm

```

1: Set the number of chain elements M
2: Determine the initial sample  $\boldsymbol{\theta}^{(0)}$  and the initial covariance matrix  $\Sigma_0$ 
3: for  $j = 1$  to M do
4:   Sample a candidate  $\boldsymbol{\theta}^{(*)}$  from a proposal distribution  $\pi(\boldsymbol{\theta}^{(*)}|\boldsymbol{\theta}^{(j-1)})$ 
5:   Sample a random number  $u$  from a uniform distribution:  $u \sim U(0,1)$ 
6:   Calculate the acceptance ratio  $\alpha_{MH}$  given by Eq. 3.13
7:   if  $u < \alpha(\boldsymbol{\theta}^{(*)}|\boldsymbol{\theta}^{(j-1)})$  then
8:     accept  $\boldsymbol{\theta}^{(*)}$  and set  $\boldsymbol{\theta}^{(j)} = \boldsymbol{\theta}^{(*)}$ 
9:   else
10:    reject  $\boldsymbol{\theta}^{(*)}$  and set  $\boldsymbol{\theta}^{(j)} = \boldsymbol{\theta}^{(j-1)}$ 
11:   end if
12: end for

```

3.2.2 Delayed rejection adaptive metropolis (DRAM)

One of the main concerns of Metropolis-Hastings algorithm is related to convergence rates. Regardless the choice of the proposal distribution function, the method does not incorporate any additional information during the sampling process and chain generation. This may lead to slow convergence rate and a high computational cost.

Bearing this in mind, Haario et al. [50] proposed the Delayed Rejection Adaptive Metropolis (DRAM) algorithm aiming at improving the efficiency of MCMC methods. It combines the main characteristics of the Adaptive Metropolis (AM) [51] and Delayed Rejection (DR) [52] algorithms, while retaining the Markovian property and reversibility of the Markov chains.

The basic aspects of the AM, DR and DRAM algorithms are thus detailed in the next subsections.

3.2.2.1 Adaptive metropolis (AM)

The Adaptive Metropolis (AM) algorithm proposed by Haario et al. [51] is the first adaptive MCMC algorithm. It aims to adapt the Gaussian proposal distribution function considering the sample path of the Markov chain. Somehow, it tries to overcome an issue of the method as one has to build a proposal PDF based on the support domain and the dimension of the target PDF which are not yet known before the inference process.

The basic idea behind the AM algorithm is to tune the covariance matrix Σ of the proposal PDF based on the past states of the chain $\{\boldsymbol{\theta}^{(j-k)}, \dots, \boldsymbol{\theta}^{(j-1)}, \boldsymbol{\theta}^{(j)}\}$ that have already been accepted in the MH algorithm. This approach, however, affects the Markovian properties of the chain, only keeping

the ergodicity properties of the samples [51].

The updating routine is quite straightforward. A strictly positive definite initial covariance matrix Σ_0 is chosen based on the prior knowledge. During an initial non-adaptative period denoted by j_0 , this covariance matrix held constant is used to compute the states of the chain so that $\Sigma = \Sigma_0$. After this period, the covariance matrix Σ is updated considering the past states of the chain such as

$$\Sigma_j = s_p \text{cov}(\boldsymbol{\theta}^0, \boldsymbol{\theta}^1, \dots, \boldsymbol{\theta}^{j-1}) + \epsilon \mathbb{I}_p, \quad (3.14)$$

where s_p is a scale factor related to the dimension p of the parameter space, $\epsilon \geq 0$ is a constant value that may be small, and \mathbb{I}_p denotes the p -dimensional identity matrix. The scale factor s_p is often taken to be $s_p = 2.38^2/p$. According to Gelman et al. [53], this value can optimize the mixing properties of MH when dealing with Gaussian distributions. Furthermore, the term $\epsilon \mathbb{I}_p$ ensures that Σ_j is positive definite and for many practical cases, one often sets $\epsilon = 0$.

A recursive formula can be used to estimate this updated covariance matrix in order to reduce the computational cost [25, 50]. Therefore, Eq. 3.14 becomes

$$\Sigma_{j+1} = \frac{j-1}{j} \Sigma_j + \frac{s_p}{j} [j \bar{\boldsymbol{\theta}}^{(j-1)} (\bar{\boldsymbol{\theta}}^{(j-1)})^T - (j+1) \bar{\boldsymbol{\theta}}^{(j)} (\bar{\boldsymbol{\theta}}^{(j)})^T + \boldsymbol{\theta}^{(j)} (\boldsymbol{\theta}^{(j)})^T + \epsilon \mathbb{I}_p] \quad (3.15)$$

where $\bar{\boldsymbol{\theta}}^{(j+1)}$ is the sample mean computed recursively such as

$$\bar{\boldsymbol{\theta}}^{(j+1)} = \frac{j}{j+1} \bar{\boldsymbol{\theta}}^{(j)} + \frac{1}{j+1} \boldsymbol{\theta}^{(j)}. \quad (3.16)$$

It is worthwhile mentioning that this algorithm can be improved if adaptation period occurs at prescribed intervals of length j_0 .

3.2.2.2 Delayed rejection (DR)

The Delayed Rejection (DR) algorithm aims to improve the efficiency of MCMC estimates regarding asymptotic variance ordering. It proposes a strategy to build a sequence of alternative candidates $\boldsymbol{\theta}^{(*n)}$, $n = 1, \dots, n_s$, if the first generate candidate $\boldsymbol{\theta}^{(*1)}$ is rejected. As the acceptance probability of this new stage candidate is estimated, the reversibility of the Markov chain is kept.

This process of delaying rejection can be performed for a fixed or random number of stages (n_s)

working on an iterative process. In doing so, however, one may increase significantly the computational time. For instance, Mira [52] and Haario et al. [50] both propose 3 stages ($n_s = 3$), whereas Smith [25] proposes 2 stages ($n_s = 2$). According to Haario et al. [50], the first stage enables a more global exploration.

As a result, the DR algorithm acts as a partial local adaptation of the proposal. It maintains the Markovian properties and reversibility in each new state of the Markov chain [50, 52].

The method is quite straightforward. It takes into account the first probability of acceptance α_1 corresponding to the MH process according to Eq. 3.13. If the first candidate $\boldsymbol{\theta}^{(*1)}$ is rejected, a second one $\boldsymbol{\theta}^{(*2)}$ is thus sampled from a second proposal distribution $\pi_2(\boldsymbol{\theta}^{(*2)}|\boldsymbol{\theta}^{(j-1)}, \boldsymbol{\theta}^{(*1)})$ and a new acceptance probability is calculated as follows

$$\alpha_2(\boldsymbol{\theta}^{(*2)}|\boldsymbol{\theta}^{(j-1)}, \boldsymbol{\theta}^{(*1)}) = \min \left\{ 1, \frac{\pi(\boldsymbol{\theta}^{(*2)}|\mathbf{y})\pi(\boldsymbol{\theta}^{(*1)}|\boldsymbol{\theta}^{(*2)})\pi_2(\boldsymbol{\theta}^{(j-1)}|\boldsymbol{\theta}^{(*2)}, \boldsymbol{\theta}^{(*1)})[1 - \alpha_{MH}(\boldsymbol{\theta}^{*1}|\boldsymbol{\theta}^{(*2)})]}{\pi(\boldsymbol{\theta}^{(j-1)}|\mathbf{y})\pi(\boldsymbol{\theta}^{(*1)}|\boldsymbol{\theta}^{(j-1)})\pi_2(\boldsymbol{\theta}^{(*2)}|\boldsymbol{\theta}^{(j-1)}, \boldsymbol{\theta}^{(*1)})[1 - \alpha_{MH}(\boldsymbol{\theta}^{*1}|\boldsymbol{\theta}^{(j-1)})]} \right\}. \quad (3.17)$$

If this second candidate $\boldsymbol{\theta}^{(*2)}$ is rejected, the iterative process can be stopped keeping the current state $\boldsymbol{\theta}^{(j)} = \boldsymbol{\theta}^{(j-1)}$ or can compute a third new stage. The recursive relations to construct the candidates $\boldsymbol{\theta}^{(*i)}$ and the corresponding probabilities $\alpha_i(\boldsymbol{\theta}^{(*i)}, \dots, \boldsymbol{\theta}^{(*)}, \boldsymbol{\theta}^{(j-1)})$ can be found in the works of Mira [52] and Haario et al. [51].

Finally, some points should be noted. This algorithm ensures a smaller rejection rate as a result of the smaller asymptotic variance of the samples of the chain. The proposal PDF, for the j^{th} stage, may be calculated according to

$$\pi_r(\boldsymbol{\theta}^{(*r)}|\boldsymbol{\theta}^{(j-1)}, \boldsymbol{\theta}^{(*r-1)}) \sim N(\boldsymbol{\theta}^{j-1}, \gamma_s^r \boldsymbol{\Sigma}_r^{j-1}), \quad (3.18)$$

where $\gamma_s < 1$ is the shrinkage factor which increases mixing. for example, Haario et al. [50] consider $\gamma_s = \frac{1}{10}$ and Smith [25] consider $\gamma_s = \frac{1}{5}$. Further, the covariance matrix $\boldsymbol{\Sigma}_r$ shown in Eq. 3.18 can be updated following some adaptive algorithm such as AM.

3.2.2.3 DRAM: AM + DR

DRAM algorithm combines the two complementary approaches DR and AM to modify the proposal function aiming at increasing the convergence rate of the stationary PDF and improving the acceptance ratio. DR method consists of a mechanism to modify the proposal PDF aiming at improving mixing, leading to temporary modifications. AM method, on the other hand, is addressed to adapt the proposal PDF using the information learned about the posterior, which results in permanent changes.

Algorithm 2 summarizes the classical formulation of Delayed Rejection Adaptive Metropolis method [25, 26].

Algorithm 2 Delayed Rejection Adaptive Metropolis Algorithm

```

1: Set the number of chain elements M
2: Determine the initial sample  $\theta^{(0)}$  and the initial covariance matrix  $\Sigma_0$ 
3: for  $j = 1$  to M do
4:   Sample a candidate  $\theta^{(*)}$  from a proposal distribution  $\pi(\theta^{(*)}|\theta^{(j-1)})$ 
5:   Sample a random number  $u$  from a uniform distribution:  $u \sim U(0, 1)$ 
6:   Calculate the acceptance ratio  $\alpha_{MH}$  given by Eq. 3.13
7:   if  $u < \alpha(\theta^{(*)}|\theta^{(j-1)})$  then
8:     accept  $\theta^{(*)}$  and set  $\theta^{(j)} = \theta^{(*)}$ 
9:   else
10:    Sample a second candidate  $\theta^{(*2)}$  from a proposal distribution  $\pi_2(\theta^{(*2)}|\theta^{(j-1)}, \theta^{(*)})$ 
11:    Sample a random number  $u$  from a uniform distribution:  $u \sim U(0, 1)$ 
12:    Calculate the acceptance ratio  $\alpha_2$  given by Eq. 3.17
13:    if  $u < \alpha_2(\theta^{(*2)}|\theta^{(j-1)}, \theta^{(*)})$  then
14:      accept  $\theta^{(*2)}$  and set  $\theta^{(j)} = \theta^{(*2)}$ 
15:    else
16:      reject  $\theta^{(*2)}$  and set  $\theta^{(j)} = \theta^{(j-1)}$ 
17:    end if
18:  end if
19:  if  $j > j_0$  then
20:    update the covariance matrix  $\Sigma_j$  given by Eq. 3.14
21:  else
22:     $\Sigma_j = \Sigma_{j-1}$ 
23:  end if
24: end for

```

3.3 Model Validation

The process of model calibration alone cannot guarantee the accuracy of prediction when the system is submitted to different scenarios and conditions, regardless of the calibration technique adopted [20]. Efforts shall be made to validate the calibrated models. In this context, the field of verification and

3.3. MODEL VALIDATION

validation (V&V) [54, 55] appeared to study and quantify how accurate a model prediction is to the actual system behavior.

Comprehensive information about the verification and validation (V&V) field applied to the analysis of computational models can be found in the reports by AIAA [54] and by ASME [55] and in the reference book of [56]. According to Borges et al. [20], V&V comprises seven steps as:

1. enlightening position on the use of the model;
2. experiment design and measurement;
3. model calibration based on parameter estimation;
4. judgment of the model predictions based on new experimental data;
5. judgment of the model predictions in an environment which provides data more complex than the one used in the process of model calibration;
6. make model improvements depending on the results obtained in item 5;
7. going back to item 3 depending on the results obtained in items 5 and 6.

Within a V&V program, it is clear that model calibration is one of the main steps, and another main point is related to the analysis of the predictive capacity of the model. This assessment is done employing model validation techniques.

Model validation is a process of determining the degree to which a model is an accurate representation of the real world from the perspectives of the intended uses of the model [54, 57]. In other words, model validation aims at evaluating the predictive capability of a numerical model for its intended use [55].

This process of judging the model accuracy is accomplished by performing quantitative comparisons between experimental data and model predictions for a scenario different from the one used for model calibration. According to Schwer [58], three basic elements of validation assessment are:

1. items to be compared;
2. manner in which to make the comparison;

3. determination of accuracy;

in which these last two items are often done through validation metrics.

Generally speaking, validation metrics provide a mathematical measure of the agreement between numerical simulations and experimental measurements. They often estimate the difference between these two results in a way that zero is achieved if they are equivalent. Furthermore, they should incorporate the uncertainties associated with the numerical and experimental outcomes to better evaluate the confidence level of the model.

In this context, the formulation and assessment of validation metrics have been attracted to the focus of many kinds of research. Indeed, several metrics applied to different applications can be found in literature such as [12, 14, 20, 29, 57–61], to cite a few. A typical one, for example, is a quantification metric that is defined as the magnitude of the difference between the experimental and numerical outcomes normalized by dividing this difference by measurement.

Concerning the uncertainties, Oberkampf and Barone [57] pointed out that a functional form of the metric is not absolute, nor unique, and so, both measurement and model uncertainties should be included to evaluate the reliability of model predictions. They can be classified either as random variables or unknown quantities. In the context of the present work, uncertainties are considered to be random variables.

3.4 Uncertainty quantification and propagation through Monte Carlo method

Uncertainty quantification and propagation evaluate the impact of uncertainties of a set of parameters $\boldsymbol{\psi} \in \mathfrak{R}^{N_p}$ on the system's response $\boldsymbol{y} \in \mathfrak{R}^{N_y}$. It increases the confidence level of the predictions as well as better estimations of risks related to specific design choices.

In general terms, uncertainty quantification (UQ) is an inverse analysis that consists of analytically or numerically measuring uncertainties over a set of parameters $\boldsymbol{\psi}$ according to the available data of a system and its error. Such quantification can be done either in the form of error bounds or probability distribution functions. Uncertainty propagation (UP), on the other hand, is a forward study that consists of mapping the uncertainty in the parameters $\boldsymbol{\psi}$ to uncertainty on the model predictions \boldsymbol{y} [62].

3.4. UNCERTAINTY QUANTIFICATION AND PROPAGATION THROUGH MONTE CARLO METHOD

Within a Bayesian perspective, the uncertainties of a set of parameters $\boldsymbol{\psi}$ are modeled as random variables, and as a result, they are described by a PDF $\pi(\boldsymbol{\psi})$. Hence, all informations about the uncertainties of model predictions can be extracted from the joint PDF $\pi(\mathbf{y}, \boldsymbol{\psi})$ as follows

$$\pi(\mathbf{y}) = \int_{D_{\boldsymbol{\psi}}} \pi(\mathbf{y}, \boldsymbol{\psi}) d\boldsymbol{\psi} = \int_{D_{\boldsymbol{\psi}}} \pi(\mathbf{y}|\boldsymbol{\psi})\pi(\boldsymbol{\psi}) d\boldsymbol{\psi}. \quad (3.19)$$

However, as can be seen in Eq. 3.19, one has to compute a multidimensional integral to assess the uncertainties, which is a difficult task to use conventional integration methods. Accordingly, sampling techniques such as Monte Carlo (MC) are commonly employed as they can provide a simpler and more robust solution.

The Monte Carlo method is a step-wise procedure. First, a certain number of samples n_s are drawn from a PDF that describes the informations about the parameters $\boldsymbol{\psi}^{(n_s)}$. Then, the deterministic problem is calculated using each one of these drafted samples, leading to n_s model predictions. Finally, from the PDFs of the outputs, one may be able to compute all statistics such as the expected value and the variance, respectively, expressed in Eqs. 3.20a and 3.20b.

$$\mathbb{E}[\mathbf{y}] = \frac{1}{n_s} \sum_{r=1}^{n_s} \mathbf{y}_r, \quad (3.20a)$$

$$\mathbb{V}[\mathbf{y}] = \sum_{r=1}^{n_s} \frac{(\mathbf{y}_r - \mathbb{E}[\mathbf{y}])^2}{n_s - 1}. \quad (3.20b)$$

This approach enables one to have, in a simple way, a much richer knowledge of a system's response, only requiring the solutions of a deterministic model. Besides, the propagation of the PDFs from input quantities through the model leads to a PDF for its response.

Furthermore, it is important to emphasize that the solution obtained is an approximation of the desired response, as only an infinite amount of simulations would provide a perfect PDF. Hence, precision depends on the number of samples considered, and convergence criteria need to be implemented to evaluate the minimum number of samples which guarantees that the method produces a stable solution.

3.4. UNCERTAINTY QUANTIFICATION AND PROPAGATION THROUGH MONTE CARLO METHOD

Part II

Dynamic Mechanical Analysis (DMA)

Introduction

Dynamic Mechanical Analysis (DMA) has become a powerful technique in the field of rheology by enabling one to identify and characterize the material's properties primarily as a function of temperature and frequency. It often provides more information about the material's behavior than techniques based solely on static tests [16].

In this regard, DMA has become widely used in several areas to study the various aspects of a material. The traditional applications are concerned with the identification of thermal transitions and how some parameters affect the material's behavior [5, 63–75], to mention a few. Recently, the use of DMA has been expanded to other research areas such as crack healing [76], the spatial distribution of material properties [77], and mechanical properties of heterogeneous materials [78, 79].

Despite the vast range of applications and its potential, the absolute values of the modulus and temperatures related to phase transitions are well-known to show divergences between samples, loading clamps and testing parameters [18, 67, 69, 80–93]. Difficulty in correlating DMA measurements to other experimental techniques have also been reported in literature [18, 67, 87, 94–98].

For these reasons, some standards suggest that the generated data only indicates relative values according to Lee-Sullivan and Dykeman [82]. Also, DMA results are often referred to as valuable only for purposes of quality control, research, development, and establishment of optimum processing conditions as reported by Deng et al. [87].

Few researches in the literature, however, explore these divergences. Mathematical formulations for estimating the complex modulus in each operational mode are usually not examined. Parametric studies, therefore, are also not done. Furthermore, the differences inherent to different commercial equipment are also not commonly investigated.

Aiming to fill this gap, this second part of the thesis is dedicated to the study of the complex

modulus measured by the flexural modes (single and dual cantilever, and three-point bending) existing in three DMA equipment. It is divided into two chapters.

The first chapter evaluates theoretically and experimentally the effects of both operational modes and machines on the complex modulus. First, a theoretical study is carried out about this technique, focusing on the mechanisms of each test and the mathematical formulations proposed by each equipment. Then, experimental tests are carried out to assess the temperature-dependent complex modulus. Special attention is given to the reproducibility and repeatability of the tests. Next, a parametric study is carried out to analyze the impacts that are caused by the different formulations and hypotheses adopted. After that, more experimental tests are performed, but this time to evaluate the frequency and temperature-dependent complex modulus. Special efforts are devoted to generating the experimental master curves to study long-term behavior identified by the different tests.

The second chapter aims to calibrate fractional derivative models through the Bayesian approach to evaluate the impact of experimental uncertainties identified in the preceding chapter on the predictions of numerical models. First, the methodology adopted is briefly described. Then, the constitutive model is presented, giving the justification for its choice. Afterward, the results of the calibration procedure are discussed. The effects of different data-sets are studied.

Objectives of Part II

To sum up, the main objectives of the second part of this thesis regarding the characterization technique DMA are:

- gather the mathematical formulations of complex modulus adopted by different DMA manufacturers;
- investigate the effects of the flexural modes and testing equipment on the measurements;
- analyze the reproducibility and repeatability of the tests;
- study the long-term behavior;
- calibrate fractional derivative models through Bayesian approach to assess the impacts of the experimental variability on model predictions.

Chapter 4

Complex modulus provided by dynamic mechanical analyzer (DMA)

This chapter consists of an investigation of the complex modulus measured by a dynamic mechanical analyzer (DMA). The main objective is to assess the impacts of different flexural modes and testing equipment on the estimates of this viscoelastic property.

It is organized as follows. First, Section 4.1 provides a discussion of the DMA principles and the mathematical formulation of each mode provided by each DMA machine. Then, Section 4.2 describes the experimental apparatus design in detail. Next, Section 4.3 presents the first case study concerning these effects on the temperature-dependent complex modulus (Henriques et al. [17]). Afterward, Section 4.4 discusses the second case study concerning these effects on the long-term behavior (Henriques et al. [99]). Finally, Section 4.5 outlines the main conclusions drawn from these studies.

Content

| | | |
|------------|--|------------|
| 4.1 | Fundamentals | 116 |
| 4.1.1 | DMA principles | 116 |
| 4.1.2 | Mathematical formulation for complex modulus | 116 |
| 4.2 | Experimental set-up | 122 |
| 4.2.1 | Description of testing equipments | 122 |
| 4.2.2 | Material and samples manufacture | 124 |
| 4.3 | Study I: temperature-dependent complex modulus | 125 |
| 4.3.1 | Test conditions | 126 |
| 4.3.2 | Experimental results & discussion | 127 |
| 4.3.3 | Parametric study | 134 |
| 4.4 | Study II: temperature and frequency-dependent complex modulus | 141 |
| 4.4.1 | Test conditions | 142 |
| 4.4.2 | Experimental results & discussion | 142 |
| 4.5 | Conclusion | 152 |

4.1 Fundamentals

This section introduces the theoretical aspects related to the DMA technique and the complex modulus estimated by it.

4.1.1 DMA principles

The DMA operation mechanism consists of applying a sinusoidal force to a sample and measuring its deformation, or applying a sinusoidal deformation and measuring its force, or even applying a constant force/deformation and measuring its creep/relaxation modulus. The material's response can be characterized as a function of temperature, frequency, time, stress, or a combination of these control parameters, depending on the intended use of the material. Based on these measurements, DMA can determine some material's properties [16, 87].

The material modulus reported over the test is a complex quantity that enables one to better analyze the material's behavior, as explained in Section 2.3. It may represent shear, tensile or flexural modulus, depending on the chosen operational mode.

It is worthwhile mentioning that the complex modulus measured in DMA is not the same as Young's modulus of the classic Hooke's law from the theory of elasticity. When testing an elastic material under a uniaxial state of stresses, Young's modulus is estimated by the computation of the slope of a stress-strain curve in the linear region. As for the complex modulus of a viscoelastic material, when a uniaxial state of stresses holds, its estimation demands the material's response to an oscillatory excitation [16].

4.1.2 Mathematical formulation for complex modulus

First, let's consider that a sample is being tested in a mode such that the uniaxial stress state holds. Second, let's consider the use of dynamic stress to deform a sample, i.e., sinusoidal stress is being applied to a sample and its deformation is being measured. This oscillatory stress can be expressed as

$$\sigma(t) = \sigma_0 \sin(\omega t), \tag{4.1}$$

with σ_0 as the amplitude. Consequently, the strain history $\varepsilon(t)$ can be given by

$$\varepsilon(t) = \varepsilon_0 \sin(\omega t + \delta), \quad (4.2)$$

with ε_0 as the amplitude of the strain history and δ as the phase angle between the applied stress $\sigma(t)$ and the response $\varepsilon(t)$. Figure 4.1 shows the oscillatory stress and the strain response.

The one-dimensional stress-strain relation in the frequency domain is thus given by [9]

$$\tilde{\sigma}(\omega) = E^*(\omega)\tilde{\varepsilon}(\omega) \quad (4.3)$$

where $E^*(\omega)$ is the complex modulus defined in Eq. 2.11.

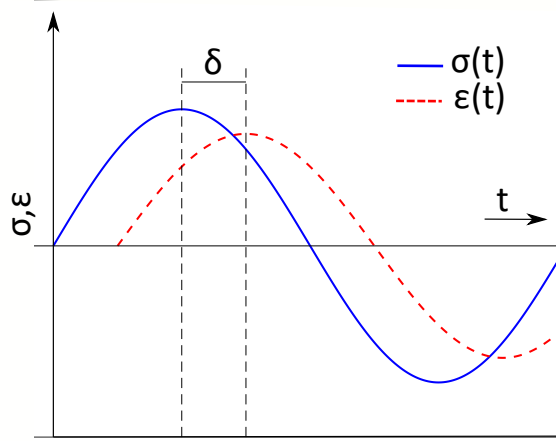


Figure 4.1: Stress $\sigma(t)$ and strain $\varepsilon(t)$ curves as function of time t of a linearly viscoelastic material under a dynamic loading.

From the measurements of the force, the displacement, and the phase angle, DMA determines each component of the complex modulus. This estimate also depends on the sample geometry, operational mode, and boundary conditions. As one seeks to analyze and scrutinize the estimates provided by DMA, it is required to describe the physical mechanism and the mathematical formulation associated with each operational mode.

Nevertheless, many works reported differences between operational modes, indicating some inconsistencies regarding complex modulus estimates. It can be problematic for standardization, especially on modes that should provide estimates for the same material property. In this regard, single cantilever, dual cantilever, and three-point bending modes are of special importance as they are the

4.1. FUNDAMENTALS

bending clamps in DMA, measuring thus flexural modulus. In this work, these three modes are chosen to be analyzed.

Single cantilever (hereinafter referred to as SC) mode consists of a sample anchored on one end by a stationary clamp and attached to a moveable clamp on the other one. Through this moveable clamp, a controlled force is applied by the motor. In this mode, it is important to emphasize that the span (S) between these two clamps may vary as the moveable clamp can present a minor lateral movement, and as a result, it should be measured before each test. The basic characteristics of this mode as well as the equivalent mechanical model are represented in Fig. 4.2.

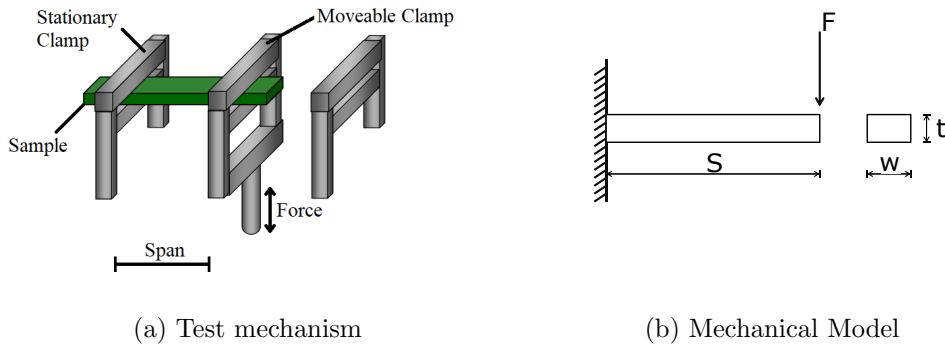


Figure 4.2: Single Cantilever (SC) mode.

Dual cantilever (hereinafter referred to as DC) mode, in turn, consists of a sample anchored on both ends by stationary clamps. The moveable clamp, which applies the motor force, is placed at the midpoint of the sample. The span (S) is now fixed and considered as the distance between the fixed clamps. Fig. 4.3 shows the mechanism and the equivalent mechanical model for this operational mode.

In both SC and DC modes, the sample is fixed in the apparatus (more precisely, in both ends and the middle for DC, and both ends for SC) and so, it is usually considered not to deform in this clamped region. Nevertheless, it seems that this condition is never achieved in practice. DMA samples often have their ends deformed after tests due to clamping in SC and DC modes. The clamping ends introduce shear deformation to the sample and so, this effect should be taken into account when elaborating strategies to compute the material modulus.

Finally, three-point bending (hereinafter referred to as 3PT) mode consists of a sample that is

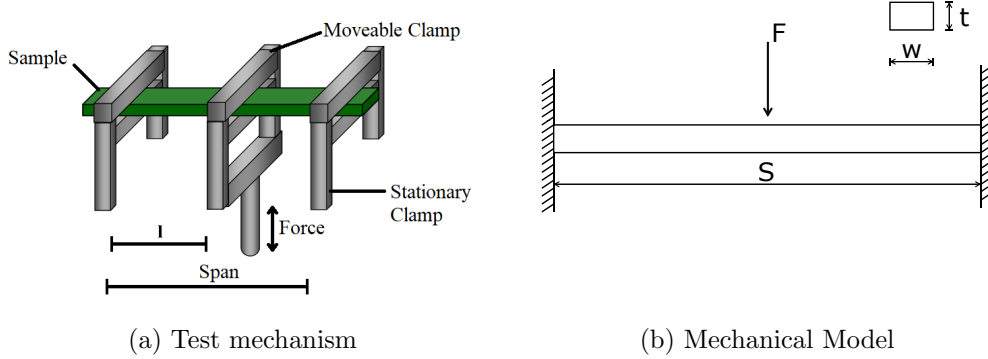


Figure 4.3: Dual Cantilever (DC) mode.

only supported at both ends by stationary clamps, as shown in Fig. 4.4. The controlled force is applied at the midspan through the moveable clamp, and the span (L) is fixed being considered as the distance between the supports. But, unlike SC and DC modes, the sample is free to move as it is only supported. Additionally, this mode is often considered as a pure mode of deformation because there is no clamping effect.

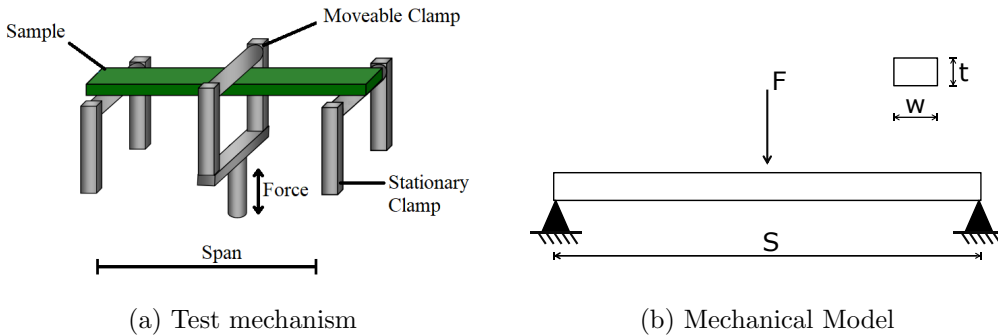


Figure 4.4: Three-point bending (3PT) mode.

Concerning the process of building mechanical models for the operational modes, one must rely on the theory of linear elasticity [100] and the theory of linear viscoelasticity [9]. The model complexity may vary from one dimensional to three-dimensional formulations depending on the hypotheses adopted, which should reflect both the physical conditions of the mechanical apparatus and the physical behavior of the sample during the tests.

As for the DMA manufacturers, they also adopt some hypotheses that are appropriate to their

4.1. FUNDAMENTALS

equipment and the model formulation is implicitly written within their software that is used to provide estimates for the modulus. In this work, three DMA machines that are commonly found in the market were used, namely: PerkinElmer 8000, TA Q800, and Netzsch 242 E Artemis. Each manufacturer presents its unique characteristics.

Regarding the mathematical formulation of these three modes, PerkinElmer 8000 (hereinafter referred to as PE) considers a small shear correction taking into account a constant Poisson's ratio. This constant Poisson's ratio is considered to be between $\nu = 0.33$ and $\nu = 0.5$ as these values are commonly related to, respectively, the glassy region and the rubbery region. In this work, it is considered $\nu = 0.35$. Hence, the absolute value of complex modulus is determined for SC, DC, and 3PT modes through Eqs. 4.4, 4.5 and 4.6 as shown below.

$$|E_{SC}^*(\omega)|_{PE} = K_s \frac{S^3}{12I} \left[1 + 2.9 \left(\frac{t}{S} \right)^2 \right], \quad (4.4)$$

$$|E_{DC}^*(\omega)|_{PE} = K_s \frac{l^3}{24I} \left[1 + 2.9 \left(\frac{t}{l} \right)^2 \right], \quad (4.5)$$

$$|E_{3PT}^*(\omega)|_{PE} = K_s \frac{S^3}{48I} \left[1 + 2.9 \left(\frac{t}{S} \right)^2 \right], \quad (4.6)$$

where K_s is the measured stiffness given by the ratio between the force applied to the sample (F) and the displacement amplitude (a), l is the distance between the fixed clamp and the moveable clamp, S is the total span, I is the inertia moment, and t is the sample's thickness.

DMA TA Q800 (hereinafter referred to as TA) also assumes a shear correction based on a constant Poisson's ratio. In this work, it is assumed a constant value of $\nu = 0.35$ as adopted in the PE machine. Additionally, TA introduces an extra term called clamping correction factor (F_c) to consider the deformation of the sample within the clamped regions in both SC and DC modes. Therefore, the absolute value of complex modulus for SC, DC, and 3PT modes can be estimated, respectively, by Eqs. 4.7, 4.8 and 4.9 as shown next.

$$|E_{SC}^*(\omega)|_{TA} = \frac{1}{F_c} K_s \frac{S^3}{12I} \left[1 + 2.4(1 + \nu) \left(\frac{t}{S} \right)^2 \right], \quad (4.7)$$

$$|E_{DC}^*(\omega)|_{TA} = \frac{1}{F_c} K_s \frac{S^3}{24I} \left[1 + 2.4(1 + \nu) \left(\frac{2t}{S} \right)^2 \right], \quad (4.8)$$

$$|E_{3PT}^*(\omega)|_{TA} = K_s \frac{S^3}{6I} \left[1 + 0.6(1 + \nu) \left(\frac{2t}{S} \right)^2 \right], \quad (4.9)$$

where ν is the Poisson's ratio. The clamping correction factor F_c is determined through Eq. 4.10 and is shown in Fig. 4.5 as a function of S/t . Note that the influence of this term in the absolute value of complex modulus can vary depending on the value of S/t : as S/t increases, F_c reaches an asymptotic value between 0.9 and 1.

$$F_c = 0.7616 - 0.02719 \sqrt{\left(\frac{S}{t} \right)} + 0.1083 \ln \left(\frac{S}{t} \right). \quad (4.10)$$

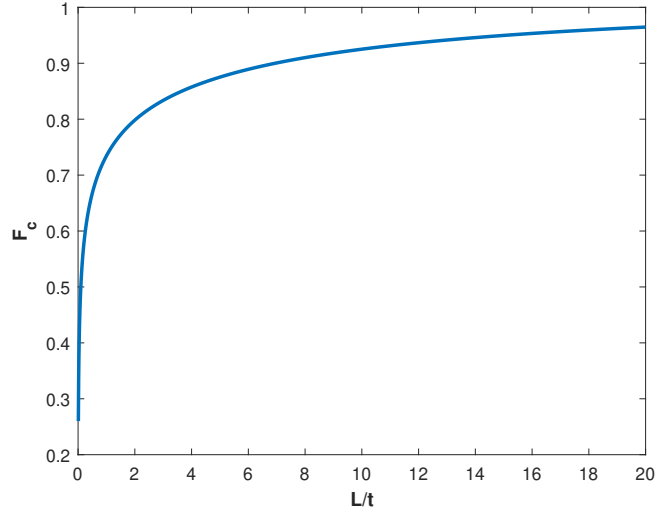


Figure 4.5: Clamping Correction Factor F_c for some values of L/t

Finally, the mathematical formulation of Netzsch 242 E Artemis (hereinafter referred to as NET) does not take into account the influence of Poisson's ratio in the modulus. It formulates the absolute value of complex modulus for SC, DC, and 3PT modes, respectively, as shown in Eqs. 4.11, 4.12 and 4.13.

$$|E_{SC}^*(\omega)|_{NET} = \frac{F}{a} \frac{S^3}{12I}, \quad (4.11)$$

$$|E_{DC}^*(\omega)|_{NET} = \frac{F}{a} \frac{S^3}{192I}, \quad (4.12)$$

$$|E_{3PT}^*(\omega)|_{NET} = \frac{F}{a} \frac{S^3}{48I}. \quad (4.13)$$

4.2 Experimental set-up

This section is devoted to detail all the experimental set-up adopted in this work to measure the complex modulus.

4.2.1 Description of testing equipments

As previously mentioned, three DMA machines from different manufacturers were used herein to perform dynamic tests to measure the complex modulus $E^*(\omega)$ of a viscoelastic material: PerkinElmer 8000 (PE), TA Q800 (TA), and Netzsch 242 E Artemis (NET). They were available, respectively, at Laboratório de Acústica e Vibrações (LAVI), Instituto de Macromoléculas Professora Eloisa Mano (IMA) and Laboratório de Processamento e Caracterização de Materiais (LPCM) of UFRJ.

These machines are all made of four basic components: force motor, displacement sensor, sample holder, and furnace, as shown in Figs. 4.6-4.8. Force motor provides the control of all forces required to the sample. The displacement sensor is the detection system, and it tracks any changes in the sample. In TA, it consists of a high resolution linear optical encoder. In PE and NET, on the other hand, it consists of an LVDT system. Sample holders enable one to perform different modes of operation. The clamps have a high stiffness to minimize the compliance, and they also have a low mass for fast temperature equilibration. The furnace provides temperature control during the tests. In TA and NET, it is an automatic furnace. In PE, it is a manual one. The main difference between an automatic and a manual furnace is the setup time.

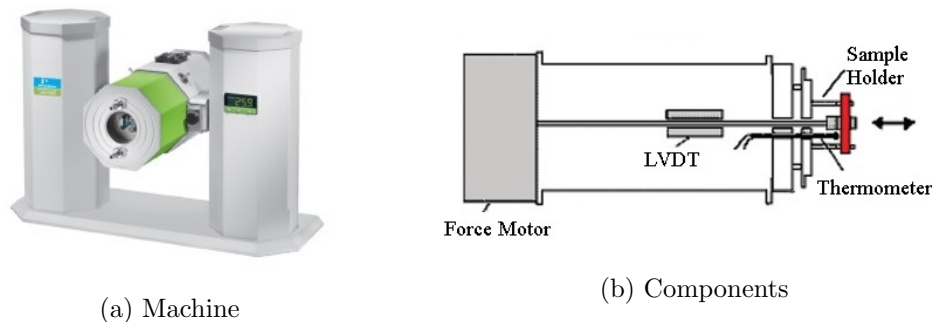


Figure 4.6: Photograph of DMA PerkinElmer 8000.

4.2. EXPERIMENTAL SET-UP

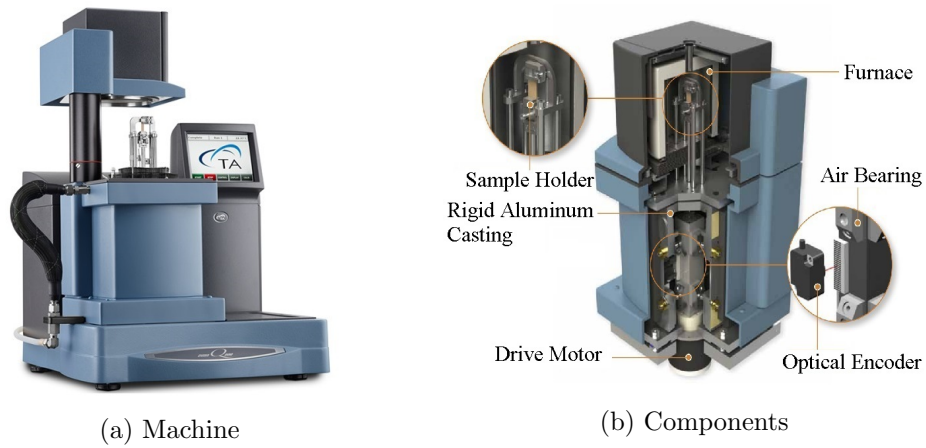


Figure 4.7: Photograph of DMA TA Q800.

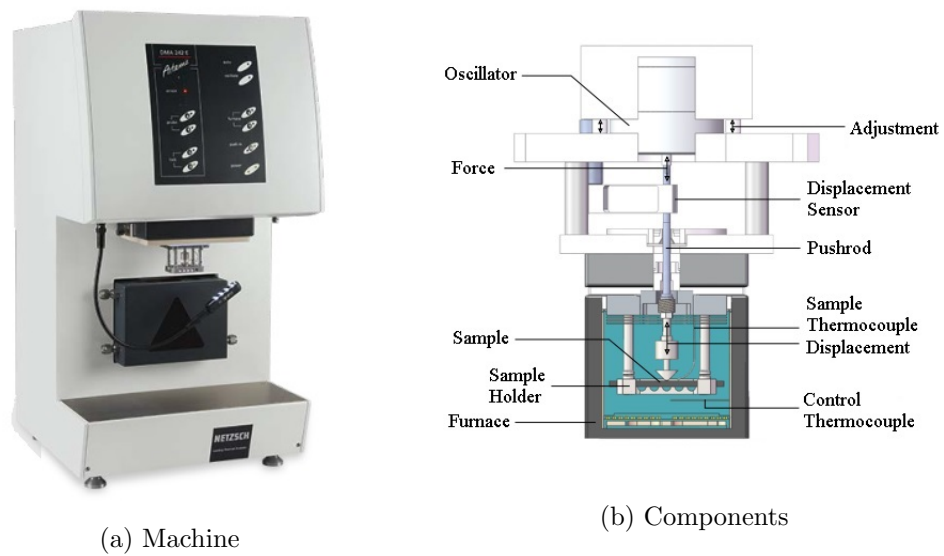


Figure 4.8: Photograph of DMA Netzsch 242 E Artemis.

Finally, Tab. 4.1 presents a comparison of the operational range of each DMA machine used in this work.

4.2. EXPERIMENTAL SET-UP

Table 4.1: Technical characteristics of each DMA machine.

| Characteristics | NET | PE 8000 | TA Q800 |
|---|-------------|-------------|--------------------|
| Temperature Range [°C] | -170 to 600 | -190 to 400 | -150 to 600 |
| Heating Scanning Range [°C/min] | 0.01 to 20 | 0 to 20 | 0.1 to 20 |
| Frequency Range [Hz] | 0.01 to 100 | 0 to 600 | 0.01 to 200 |
| Frequency Resolution [Hz] | | 0.001 | |
| Displacement Range [μm] | ± 240 | ± 1000 | ± 0.5 to 10000 |
| Displacement Resolution [μm] | 0.0005 | 0.001 | 0.001 |
| Force Range [N] | 24 | ± 10 | ± 18 |
| Force Resolution [N] | 0.0005 | 0.002 | 0.00001 |

4.2.2 Material and samples manufacture

An epoxy resin (ER) based on bisphenol A, whose trade name is Araldite LY 1564 BR, was purchased from Maxepoxi (São Paulo, Brazil). This ER has an epoxide equivalent weight of 161-173 g/eq and a viscosity at 25 °C of 1200-1400 mPa.s. The curing agent based on cycloaliphatic amines, whose trade name is Aradur 2963 BR, was also purchased from Maxepoxi (São Paulo, Brazil). It has a density of 1 g/cm³ and a viscosity at 25 °C of 30-70 mPa.s.

Two batches of material, one for each case study, were prepared strictly following the same procedure. The epoxy resin and the curing agent were first mixed in a stoichiometric proportion of 48 *phr* related to the ER as indicated by the manufacturer, aiming at providing the best mechanical performance. Then, the system was put on an ultrasonic bath for 15 min to reduce air bubbles. Afterward, the mixture was poured in silicone rubber molds with appropriate dimensions and cured at room temperature for 24 h. A post-curing step was carried out at 60 °C for 8 h. Finally, the samples were demolded and superficially sanded in both sides using super fine sandpaper to remove superficial defects and to meet the required dimensions.

Samples' dimensions varied according to DMA machine and case study as shown on Tables 4.2 and 4.3, where L is the sample's length, w is the width and t is the thickness. It is noteworthy that two sets of samples with different geometries were manufactured for tests performed using the PE machine in the first case study. Furthermore, they were all stored under the same conditions before testing to certify that the results can be comparable.

4.3. STUDY I: TEMPERATURE-DEPENDENT COMPLEX MODULUS

Table 4.2: Samples' dimensions for the first case study, where L is the sample's length, w is the width and t is the thickness.

| DMA | Mode | L [mm] | w [mm] | t [mm] |
|------------|------|------------------|------------------|-----------------|
| PE - Set 1 | SC | 35.00 \pm 0.05 | 12.29 \pm 0.04 | 3.20 \pm 0.01 |
| | DC | 52.50 \pm 0.05 | 10.04 \pm 0.15 | 3.21 \pm 0.01 |
| | 3PT | 52.50 \pm 0.05 | 10.16 \pm 0.04 | 3.20 \pm 0.01 |
| PE - Set 2 | SC | 25.0 \pm 0.05 | 7.02 \pm 0.08 | 1.93 \pm 0.09 |
| | DC | 50.00 \pm 0.05 | 6.89 \pm 0.01 | 2.06 \pm 0.04 |
| | 3PT | 50.00 \pm 0.05 | 6.93 \pm 0.08 | 2.02 \pm 0.01 |
| TA | SC | 35.00 \pm 0.05 | 12.47 \pm 0.02 | 3.20 \pm 0.01 |
| | DC | 60.00 \pm 0.05 | 11.91 \pm 0.03 | 3.20 \pm 0.02 |
| | 3PT | 60.00 \pm 0.05 | 12.27 \pm 0.07 | 3.23 \pm 0.06 |
| NET | 3PT | 60.00 \pm 0.05 | 9.88 \pm 0.14 | 3.16 \pm 0.01 |

Table 4.3: Samples' dimensions for the second case study, where L is the sample's length, w is the width and t is the thickness.

| DMA | Mode | L [mm] | w [mm] | t [mm] |
|-----|------|------------------|------------------|-----------------|
| PE | SC | 25.00 \pm 0.05 | 7.01 \pm 0.08 | 2.05 \pm 0.01 |
| | DC | 52.00 \pm 0.05 | 9.85 \pm 0.18 | 3.23 \pm 0.02 |
| | 3PT | 52.00 \pm 0.05 | 9.79 \pm 0.16 | 3.21 \pm 0.01 |
| TA | SC | 35.00 \pm 0.05 | 12.11 \pm 0.04 | 3.17 \pm 0.03 |
| | DC | 60.00 \pm 0.05 | 11.98 \pm 0.23 | 3.16 \pm 0.01 |
| | 3PT | 60.00 \pm 0.05 | 12.09 \pm 0.07 | 3.17 \pm 0.02 |

4.3 Study I: temperature-dependent complex modulus

In Study I, the effects of the flexural modes and testing equipment on the temperature-dependent complex modulus are investigated. Experimental tests were first carried out using SC, DC, and 3PT modes in three DMA machines. Then, the measurement results were compared to study the influence of both operational mode and testing equipment on the measured value of the modulus and also on the glass transition temperature T_g . The repeatability of each type of test was also analyzed. Finally, numerical analyses considering the sensitivity of the modulus to material and model parameters such as Poisson's ratio and geometry were performed.

4.3.1 Test conditions

Dynamics tests were performed in SC, DC, and 3PT modes in all three DMA machines, namely PE, TA, and NET. They were all carried out in similar conditions to obtain reliable results. Besides, mechanical calibrations were carried out before each set of tests of each operational mode.

A temperature scan technique was employed. After an isotherm of 30 min at 25 °C, the temperature varied from 25 to 90 °C with a heating rate of 2 °C/min at a constant frequency of 1 Hz. The strain amplitude was set to 50 μm to ensure that the linear viscoelastic hypothesis holds. As 3PT is a tensioning clamp, a force track was set to 120 % which means that the static force was 120 % of the dynamic force along with the test.

As Menard [16] recommends, three samples were used on each test to reduce the risks of abnormalities due to the fabrication or experimental errors. The normal statistics of sampling and data analysis were performed. Hence, all experimental results are presented as the mean of these three samples together with the corresponding standard deviation.

Testing parameters are summarized on Table 4.4, where t is thickness, S is the span, S/t is the span-to-thickness ratio and a is the amplitude. It is worth recalling that tests were performed in PE machine considering two sets of samples with different geometries and spans to also evaluate the influence of the sample's geometry in the measurements.

Table 4.4: Testing parameters for the first case study, where t is thickness, S is the span, S/t is the span-to-thickness ratio and a is the amplitude.

| DMA | Mode | t [mm] | S [mm] | S/t | a [mm] | Force Track [%] |
|------------|------|----------|----------|-------|----------|-----------------|
| PE - Set 1 | SC | 3.2 | 17.2 | 5.4 | 50 | - |
| | DC | 3.2 | 40.0 | 12.5 | 50 | - |
| | 3PT | 3.2 | 45.0 | 14.1 | 50 | 120 |
| PE - Set 2 | SC | 2.0 | 12.2 | 6.1 | 50 | - |
| | DC | 2.0 | 20.0 | 10.0 | 50 | - |
| | 3PT | 2.0 | 35.0 | 17.5 | 50 | 120 |
| TA | SC | 3.2 | 17.5 | 5.5 | 50 | - |
| | DC | 3.2 | 35.0 | 10.9 | 50 | - |
| | 3PT | 3.2 | 50.0 | 15.6 | 50 | 120 |
| NET | 3PT | 3.2 | 40.0 | 12.5 | 50 | 120 |

4.3.2 Experimental results & discussion

SC, DC, and 3PT modes were performed in PE, TA, and NET machines using the same test conditions in temperature scan. This section presents a comparative analysis of the experimental results to assess the effects of testing equipment and operational modes, followed by a discussion part.

4.3.2.1 Influence of testing equipment

SC mode was performed in two DMA machines, PE and TA, using the same test conditions. In PE, tests were carried out for two sets of samples with different geometries. The measurement results for storage and loss moduli are shown in Fig. 4.9.

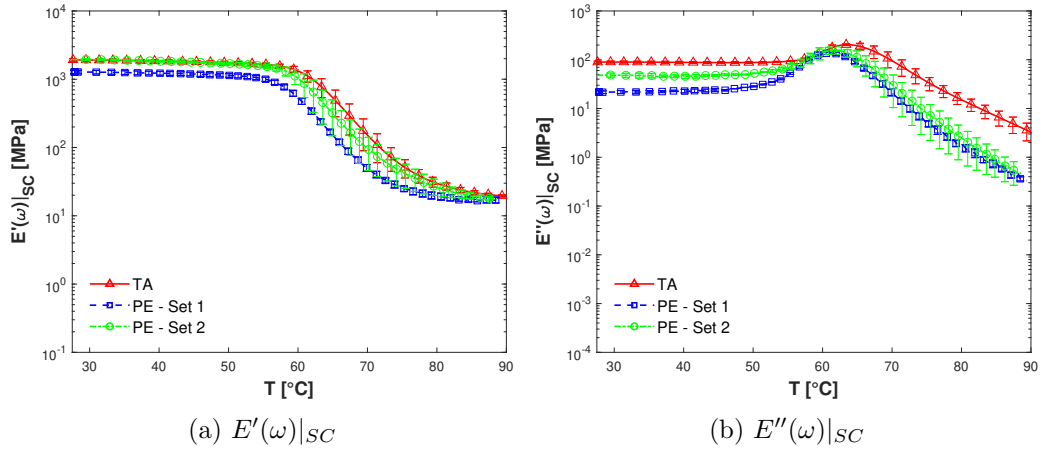


Figure 4.9: Comparisons between complex modulus measured in SC mode.

It can be noted the classical three regions of viscoelastic behavior [8, 101] in both DMA results. Storage modulus decreased with temperature. This decrease was even more rapid as the material approached its glass transition due to the large scale molecular movement and its softening. Then, it reached a plateau as the temperature was further increased. Loss modulus, in turn, increased slightly up to approximately 65 °C and from there, it suddenly decreased with the increase in temperature.

It can also be observed by the low amplitudes of the standard deviations that the DMA machines provided good results when performing tests using the same test conditions and testing parameters in the same machine, especially in the glassy state. In other words, the repeatability was quite good. At 30 °C, for example, the results of storage modulus from TA samples were within 4.4%, from PE Set 1 samples were within 5.9% and from PE Set 2 samples were within 3.1%. The results for glass

4.3. STUDY I: TEMPERATURE-DEPENDENT COMPLEX MODULUS

transition temperatures (T_g), here considered as the peak of loss modulus curves, were also very similar, being 1.42 °C for TA samples the largest standard deviation observed.

However, when SC tests were performed with different geometries in the same machine as was the case of PE Set 1 and PE Set 2, the measurement results of storage modulus had a poor agreement. This difference, however, decreased as temperature increased. In the glassy state, the results from PE Set 2 were almost 53 % higher than the ones from PE Set 1. In the rubbery state, PE Set 2 was only 8 % higher. The measurement results of loss modulus, in turn, had a poor agreement at low temperatures but after approximately 55 °C, this difference decreased significantly. For instance, at low temperatures, PE Set 2 was almost twice as high as PE Set 1. This difference reduced to 5 % at around 58 °C and to 2 % at around 90 °C. Besides, the glass transition was identified at a lower temperature for PE Set 1.

Comparing the results provided by these two machines in this operational mode, only the averages from PE Set 2 and TA had a reasonable agreement for storage modulus in both glassy and rubbery states. PE Set 2 was within 98 % of TA at low temperatures and almost 90 % at high temperatures. It was somewhat surprising considering the testing parameters used. As shown in Tab. 4.4, PE Set 2 and TA had different values for the sample's thickness, span and, span-to-thickness ratios. However, the average results for loss modulus showed TA having higher values in all temperature range. In fact, its peak value was 56 % higher than the one of PE Set 1 and 18 % than the one of PE Set 2. Despite these differences in terms of moduli magnitude, temperatures related to the onset point of storage modulus and to the peak point of loss modulus had a small variation up to 5 °C. In particular, the average result of T_g was 61.2 °C for PE Set 1, 61.8 °C for PE Set 2, and 63.9 °C for TA. The difference between the highest and lowest T_g 's was 4.5 °C (see Tab. 4.5).

DC mode was also performed in PE and TA machines. Test conditions were the same and two sets of samples were also tested in PE. Figure 4.10 shows the average results with the corresponding standard deviations.

As in SC mode, it can be noticed the three regions of viscoelastic behavior [8, 101]. The repeatability among samples from the same set was also good. In fact, DC results had lower standard deviations than SC results. For comparison, TA samples were within 2.4 %, PE Set 1 within 1.2 %, and PE Set 2 samples within 2.5 % at 30 °C.

4.3. STUDY I: TEMPERATURE-DEPENDENT COMPLEX MODULUS

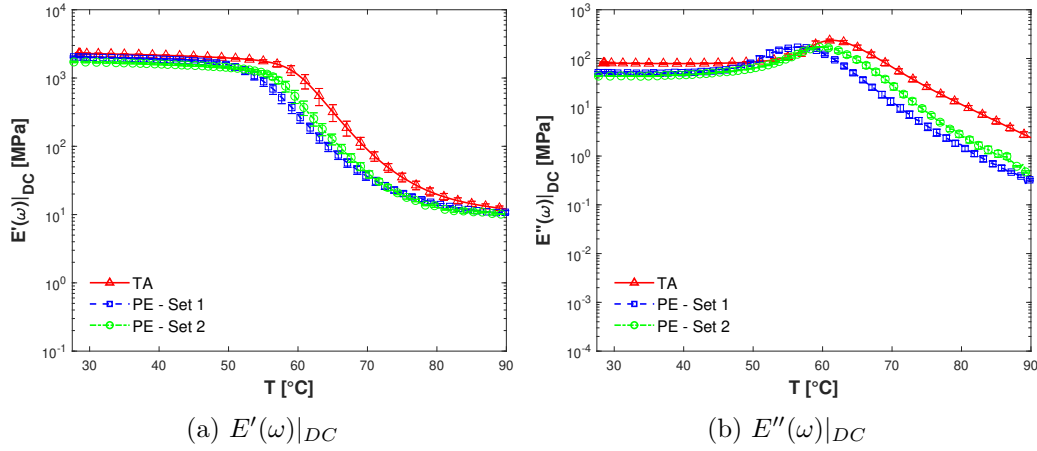


Figure 4.10: Comparisons between complex modulus measured in DC mode.

Comparing the measurements performed in PE machine, once again the sample's geometry affected them. PE Set 1 and PE Set 2 had a poor agreement for storage modulus, especially in both glassy state and glass transition region. At low temperatures, PE Set 1 was approximately 18 % higher than PE Set 2. However, during the glass transition, PE Set 2 was the one higher, being, for example, 46 % higher at 65 °C. Their loss modulus curves, in turn, had almost identical shapes with their peaks presenting nearly the same value: PE Set 1 was around 2 % higher than PE Set 2. They differed by only a shift on temperature due to the different T_g .

Comparing the values measured by these two machines, TA provided higher values for both storage and loss moduli for all temperature range tested. For storage modulus, the greatest discrepancies were observed during the glass transition. At 65 °C, for example, TA was almost four times PE Set 1 and three times PE Set 2. For loss modulus, on the other hand, the greatest discrepancies were observed after the transition. Indeed, the peak value of loss modulus in TA was 47 % higher than PE Set 2. As for the glass transition temperature, the average result of T_g was 56.4 °C for PE Set 1, 59.3 °C for PE Set 2, and 61.6 °C for TA. The difference between the highest and lowest T_g 's was 7.2 °C (see Tab. 4.5).

Finally, 3PT mode was performed in three DMA machines, PE, TA, and NET. Tests were carried out using similar conditions in these machines and two sets of samples were investigated in PE. Figure 4.11 shows the average results with the corresponding standard deviations.

As SC and DC modes, the three regions of viscoelastic behavior can be seen. However, the

4.3. STUDY I: TEMPERATURE-DEPENDENT COMPLEX MODULUS

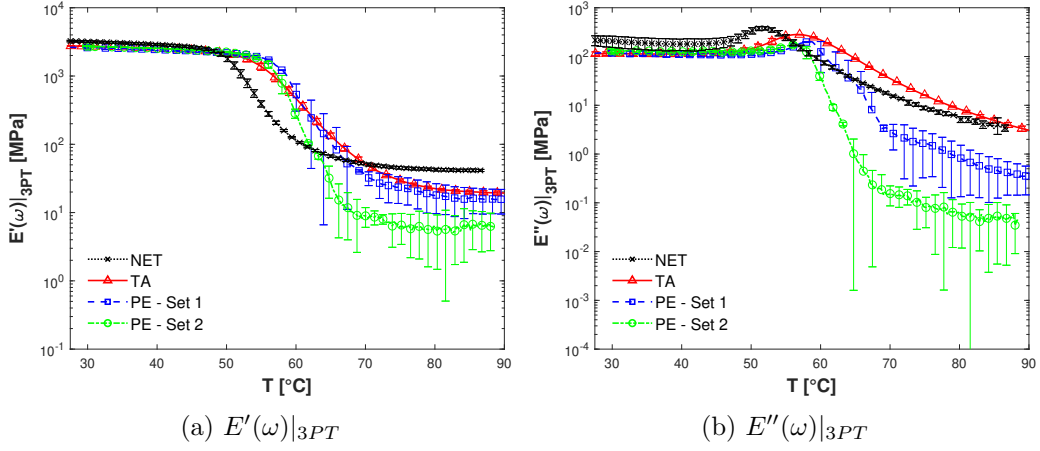


Figure 4.11: Comparisons between complex modulus measured in 3PT mode.

repeatability varied according to the region and also to the machine. From the results of the storage modulus, it can be observed that all DMA machines had good repeatability on the glassy state. At 30 °C, for instance, TA samples were within 1 %, NET samples within 0.03 %, PE set 1 within 4 %, and PE set 2 within 2 %. However, at the end of the glass transition and also in the rubbery state, PE results had bad repeatability. For instance, PE Set 1 and PE Set 2 samples were within, respectively, 110 % and 64 % at 65 °C, and 46 % and 72 % at 80 °C. The other machines had good repeatability on the rubbery state as NET samples were within a 0.04 % range and TA samples within a 9.5 % range. The same behavior of storage modulus can be noted for the loss modulus.

It is worthwhile mentioning that these large deviations in 3PT mode have also been reported in the literature [16, 79, 91, 102]. They are commonly associated with the fact that the sample is only supported and so, there is a possible loss of contact between the sample and the sensor due to the low stiffness of the material or even the slippage of the sample.

Unlike SC and DC modes, the results from the PE machine had a good agreement in the glassy state, regardless of the sample's dimensions and testing parameters. For example, PE Set 2 was only 4.7 % higher than PE Set 1 at 30 °C. However, the results began to be inconsistent as temperature increased, especially at the end of the glass transition. PE Set 1 was almost four times PE Set 2 at 65 °C.

Comparing the values among DMA machines, NET provided a higher storage and loss moduli in the glassy state. In the rubbery state, NET presented a higher storage modulus but its loss modulus

4.3. STUDY I: TEMPERATURE-DEPENDENT COMPLEX MODULUS

stayed below TA. The onset point of storage modulus and the peak of loss modulus were identified at a lower temperature in NET measurements, indicating that the glass transition happened first in this DMA machine. The average value of T_g was around 51.6 °C for NET, 58.6 °C for PE Set 1, 56.9 °C for PE Set 2, and 57 °C for TA. The difference between the highest and the lowest was approximately 7.7 °C (see Tab. 4.5).

Nonetheless, it was surprising that the results of TA and both sets of PE showed a good agreement, especially for storage modulus in the glassy state, regardless of the sample's dimensions. From Tab. 4.4, one can note that only PE Set 1 and TA had similar values for both sample's thickness and span-to-thickness ratios.

4.3.2.2 Influence of operational mode

Another way to evaluate these experimental results is to compare the ones provided by the same machine to study the influence of operational mode. Figures 4.12 to 4.14 show the average results with the corresponding standard deviations for both storage and loss moduli obtained in PE and TA machines.

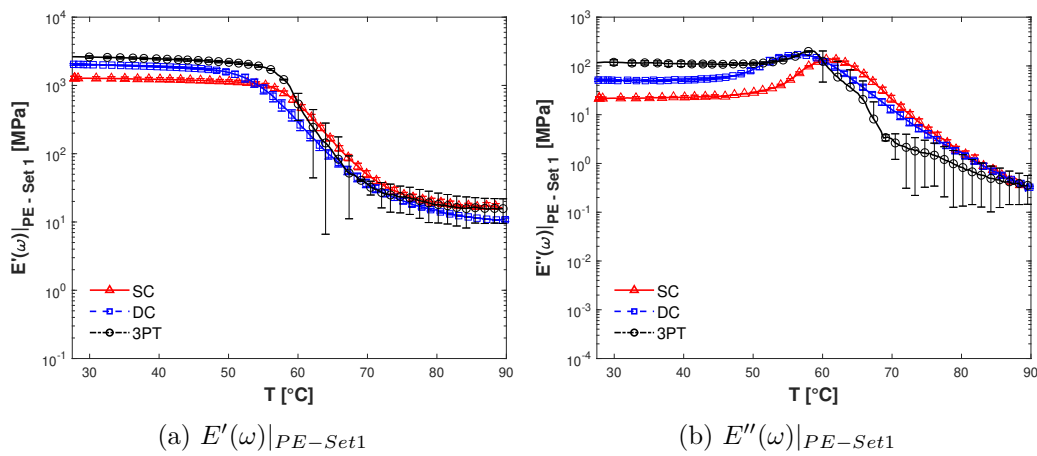


Figure 4.12: Comparisons between complex modulus measured by PE machine using samples from set 1.

4.3. STUDY I: TEMPERATURE-DEPENDENT COMPLEX MODULUS

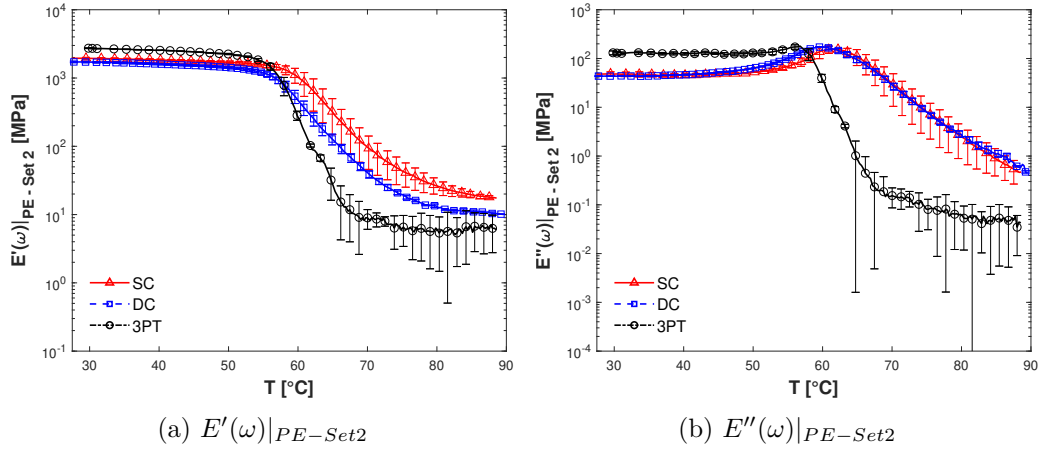


Figure 4.13: Comparisons between complex modulus measured by PE machine using samples from set 2.

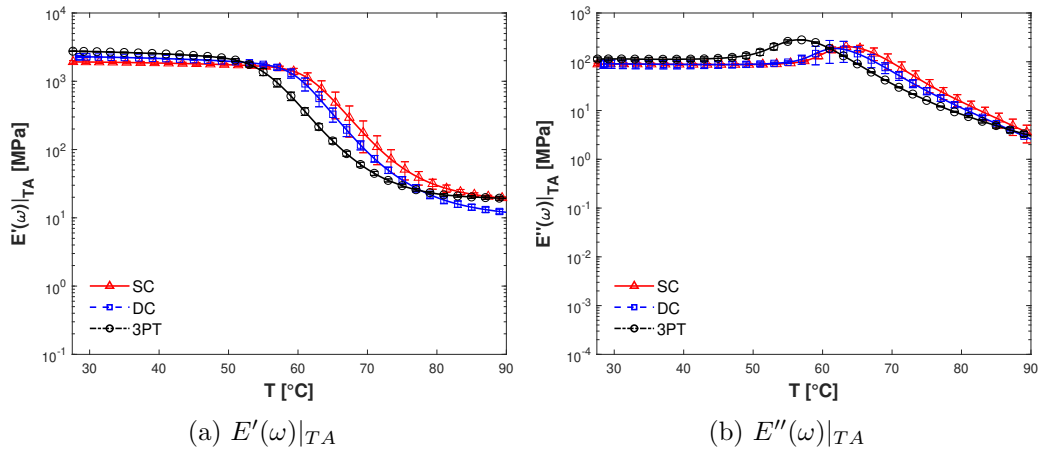


Figure 4.14: Comparisons between complex modulus measured by TA machine.

It can be observed that the measured modulus indeed depended on the operational mode in both DMA machines. This indicates inconsistencies on the DMA machines as the moduli are material parameters, being only dependent on the material tested [9, 103]. Therefore, they should not change between types of tests that measures the same property.

In both PE and TA machines, 3PT mode provided the highest values during the glassy state, while SC gave the highest ones in the rubbery state. Nevertheless, the differences between the results of both SC and DC modes decreased as the material passed its glass transition. From TA results for storage modulus, for example, 3PT mode was almost 42 % higher than SC mode and 19 % than DC mode at 30 °C, while SC mode was almost 51 % higher than DC mode and 33 % than 3PT mode at

4.3. STUDY I: TEMPERATURE-DEPENDENT COMPLEX MODULUS

80 °C.

Moreover, SC mode identified higher values for T_g as highlighted in Tab. 4.5. For instance, in the TA machine, the T_g observed in SC mode was around 4 % higher than the one in DC mode and 13 % than the one in 3PT mode. This difference may be related to the position of the sensor concerning the sample. The sensor is fixed in the apparatus, near to the moveable clamp of the system, and as a consequence, the position of the sensor concerning the sample is different when one changes the operational mode. In SC mode, the sensor is near the end of the sample. In DC and 3PT modes, on the other hand, the sensor is near the middle of the sample. The heat radiation in the furnace is also another influential factor [83, 90, 96].

Table 4.5: Temperature Scans

| DMA Machine | PE - Set 1 | PE - Set 2 | TA | NET |
|-------------|------------------|------------------|------------------|------------------|
| SC | 61.21 ± 0.34 | 61.80 ± 0.60 | 63.99 ± 1.42 | - |
| DC | 56.44 ± 1.03 | 59.30 ± 0.39 | 61.59 ± 0.99 | - |
| 3PT | 51.57 ± 0.52 | 56.86 ± 0.50 | 58.63 ± 0.11 | 56.95 ± 0.56 |

4.3.2.3 Discussion

To sum up, although the same material was being tested, the modulus' estimates varied according to both the operational mode and the DMA manufacturer. From the physical point of view, this should not occur as the same physical property was being estimated during all those tests. The key point here is that the material modulus has a very clear physical meaning as it is a constitutive parameter that relates stress and strain in the frequency domain as can be seen in the reference books by Christensen [9], Lakes [11], Wineman and Rajagopal [10], and Drodzdov [103]. Therefore, the discrepancies observed in the modulus estimates deserve further investigations.

Although literature [87, 91] suggests that instrumentation compliance, sample's geometry, stiffness, and span-to-thickness ratio may influence DMA results, it is possible to observe that these influences depend on the operational mode. In SC mode, the measurement results obtained by the PE machine showed that the changes of sample's stiffness and dimensions, and span-to-thickness ratios modified "the estimate of the material's modulus" provided by DMA. But it was possible to find reasonable agreement in some results of storage modulus from two machines even though the testing parameters were different. In DC mode, on the other hand, there is no agreement in the results even for the

4.3. STUDY I: TEMPERATURE-DEPENDENT COMPLEX MODULUS

ones provided by the same machine, indicating a great dependency on the testing parameters and instrumentation compliance. Finally, in 3PT mode, the results of storage modulus from two machines presented some consistency for the temperature range investigated, despite the differences in the geometry and instrumentation compliance.

Therefore, it seems that the effects of sample's geometry, stiffness, and span-to-thickness ratios are only relevant for SC and DC modes as changes in these parameters modified the estimated material's modulus even when using the same DMA machine. As previously mentioned in Section 4.1.2, both SC and DC modes have some clamp conditions and these may affect the measurements. The shear deformation and thermal stresses, for example, may be larger than expected.

When comparing DMA results from different machines, however, one should keep in mind that each testing equipment has its mathematical formulation for complex modulus as explained in Section 4.1.2. Therefore, small variations in the modulus' estimate from different DMA machines are quite expected to happen. For example, in SC and DC modes, only the mathematical formulation of TA introduced an extra factor (F_c) to reduce the clamping effects, but its influence depends on the ratio S/t as illustrated in Fig. 4.5. In this work, $1/F_c$ was around 1.14 in both SC and DC modes, increasing 14% the modulus measured. Moreover, NET does not consider the effects of Poisson's ratio in these three operational modes.

4.3.3 Parametric study

As the experimental measurements evidenced some deviations, a parametric study was carried out to assess the effects of geometric and mechanical parameters and temperature. In each analysis, only one parameter, shown in Eqs. 4.4 to 4.13, was varied, while the others were considered to be constant.

The influence of the geometric parameters (S , w , and t) was first evaluated for each operational mode. Accordingly, a constant value was chosen for the stiffness K_s , and only one geometric parameter was varied while the others remained constants. Figures 4.15 to 4.17 show the theoretical influence of the geometric parameters. The absolute value of complex modulus is directly proportional to the span, but it is inversely proportional to both sample's thickness and width in all cases. 3PT mode has the greatest dependence on the sample's thickness and width, whereas SC mode on the span.

4.3. STUDY I: TEMPERATURE-DEPENDENT COMPLEX MODULUS

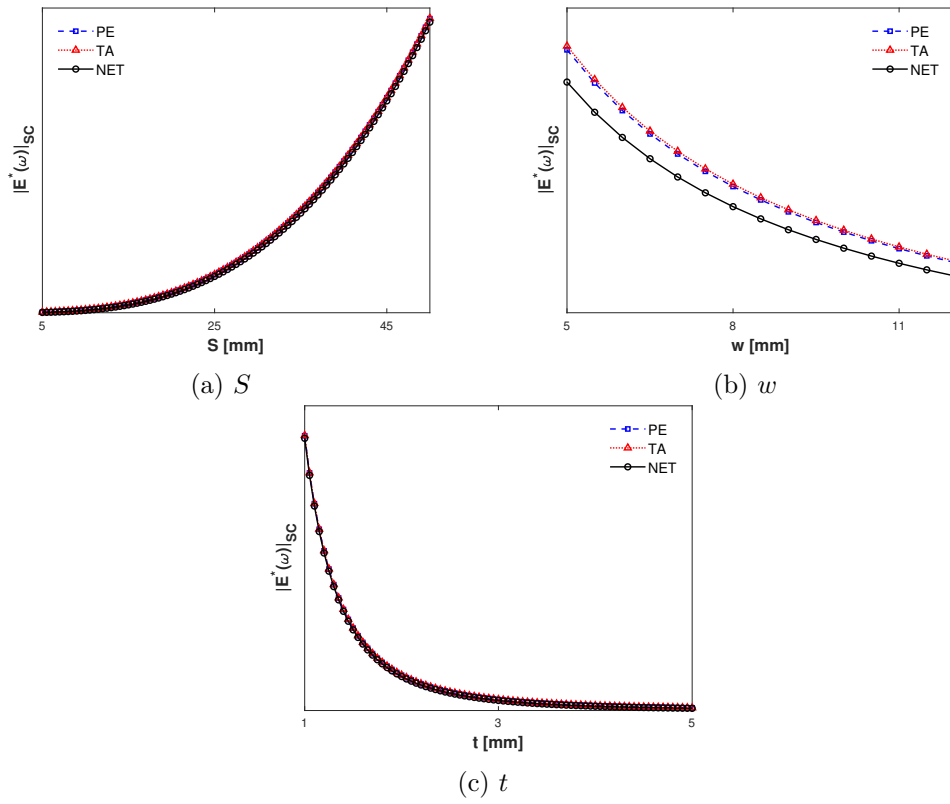


Figure 4.15: Effects of geometry on complex modulus measured in SC mode.

4.3. STUDY I: TEMPERATURE-DEPENDENT COMPLEX MODULUS

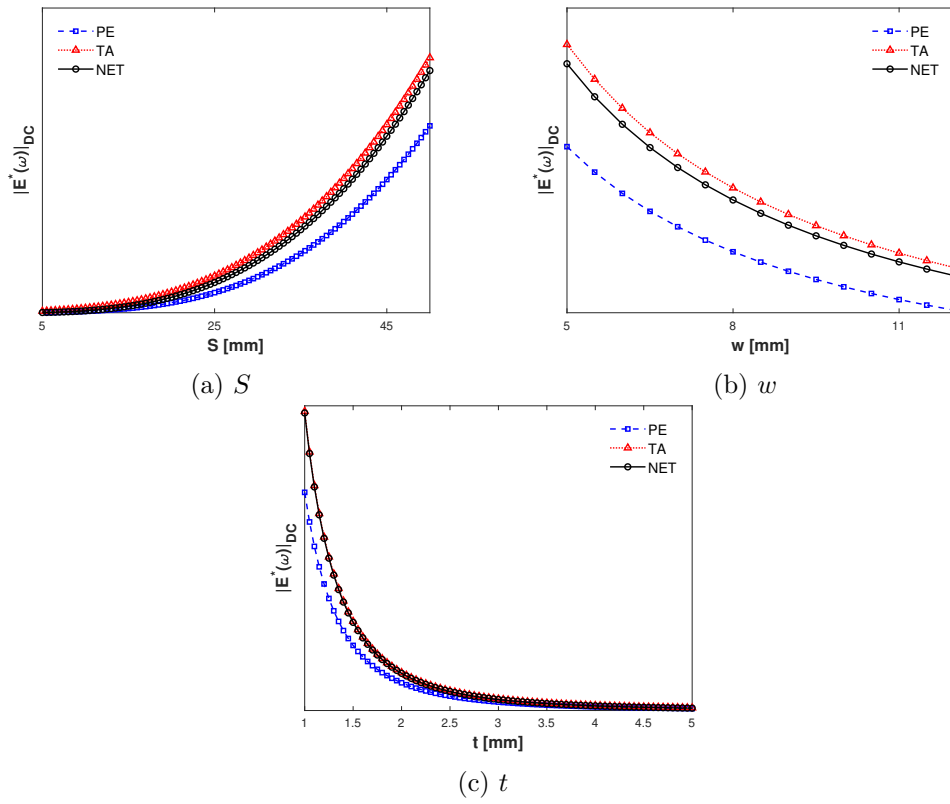


Figure 4.16: Effects of geometry on complex modulus measured in DC mode.

4.3. STUDY I: TEMPERATURE-DEPENDENT COMPLEX MODULUS

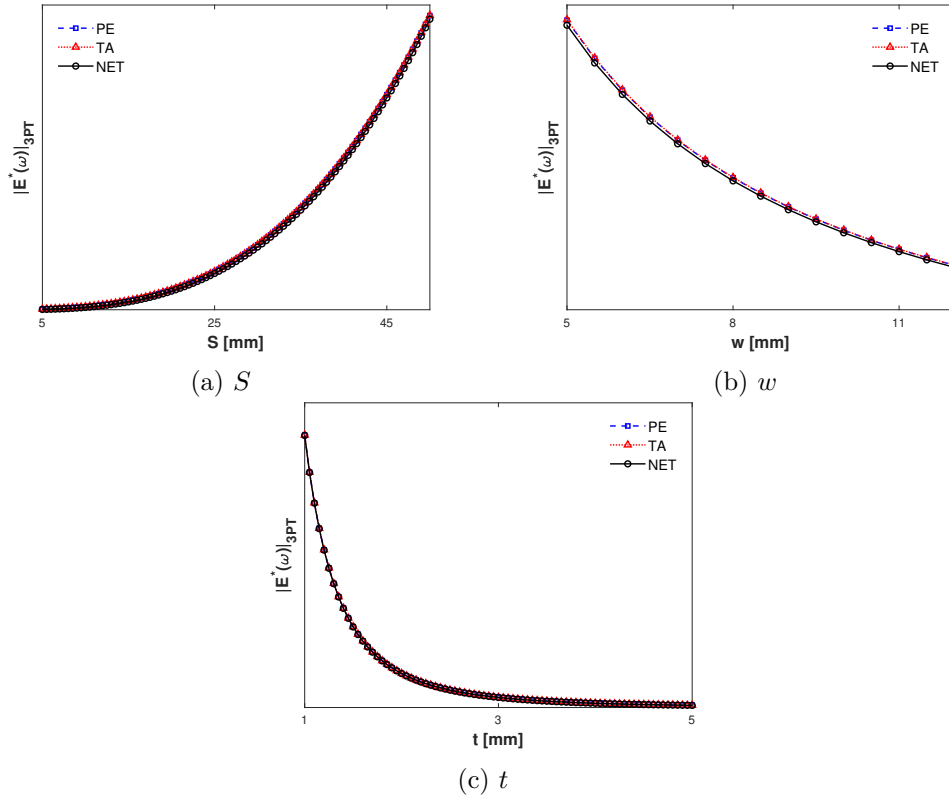


Figure 4.17: Effects of geometry on complex modulus measured in 3PT mode.

Afterward, the influence of the measured stiffness (K_s) is analyzed. For this, the parameters (S , w , t , ν) were the same in all formulations and kept constant. Figure 4.18 shows the absolute value of complex modulus as a function of the measured stiffness for all three modes. It can be seen that the estimated modulus increased with the increase of the material's stiffness and also that TA provided the highest values. The difference between them increased with the measured stiffness. DC mode presented the greatest variations up to 76% between TA and PE, whereas 3PT mode had the lowest ones up to 11% between TA and NET when considering the entire range from 0 to 0.5 $0.5 \text{ N}/\mu\text{m}$. Hence, 3PT is the mode with the least sensibility to the different formulations and should be the most consistent when comparing different machines while DC mode should be the least consistent, for the available data in this work.

4.3. STUDY I: TEMPERATURE-DEPENDENT COMPLEX MODULUS

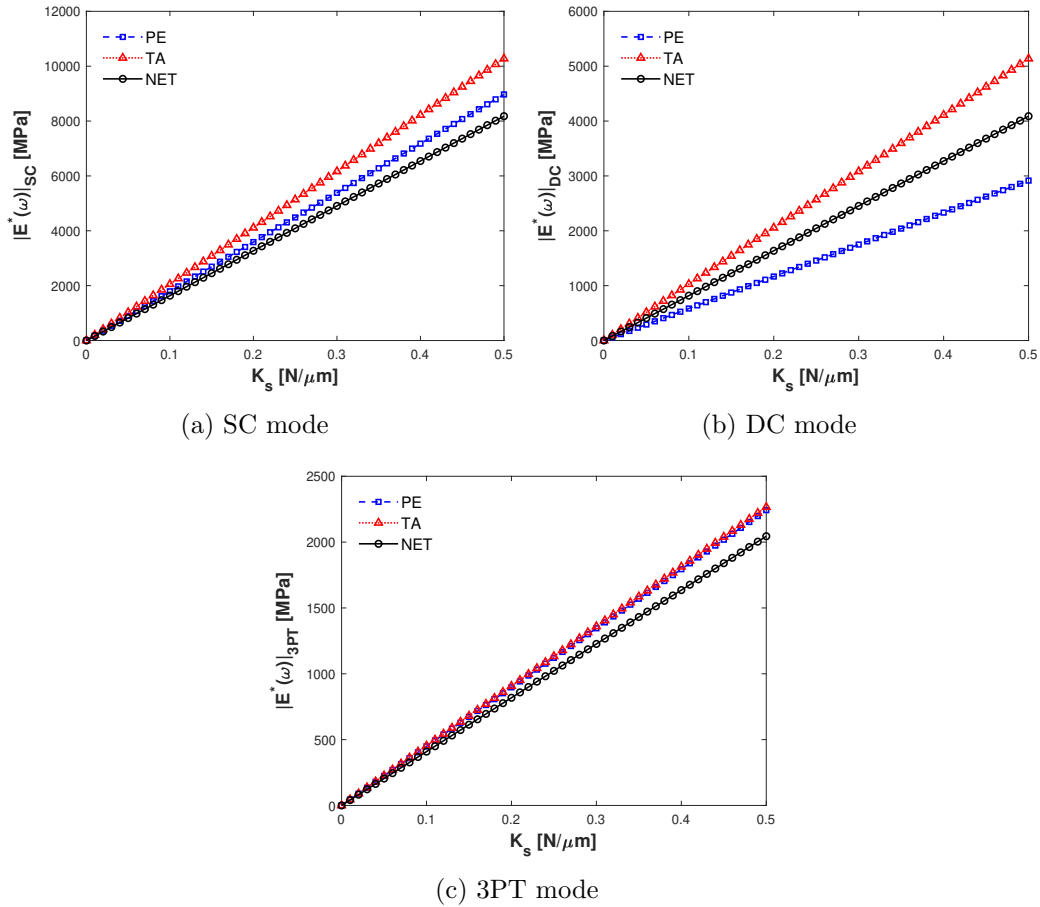


Figure 4.18: Effects of stiffness on complex modulus.

Then, the effects of Poisson's ratio were examined. In some DMA machines, this property is assumed to be constant in their mathematical formulation. However, in viscoelastic materials, Poisson's ratio is considered to be temperature- and frequency-dependent [104–107]. Indeed, it usually increases with temperature and decreases with frequency. Pandini and Pegoretti [107], for example, showed that 0.5 instead of 0.35 would be more appropriate for two differently cross-linked epoxy resins in the rubbery region.

In this regard, let consider the mathematical formulation provided by TA machine shown in Eqs. 4.7 to 4.9 to investigate how the variation of Poisson's ratio can affect the measured modulus by each operational mode. Considering that the applied force, the displacement amplitude, the span and the sample's geometry are the same in SC, DC, and 3PT modes, Fig. 4.19 shows the absolute value of complex modulus as a function of Poisson's ratio.

4.3. STUDY I: TEMPERATURE-DEPENDENT COMPLEX MODULUS

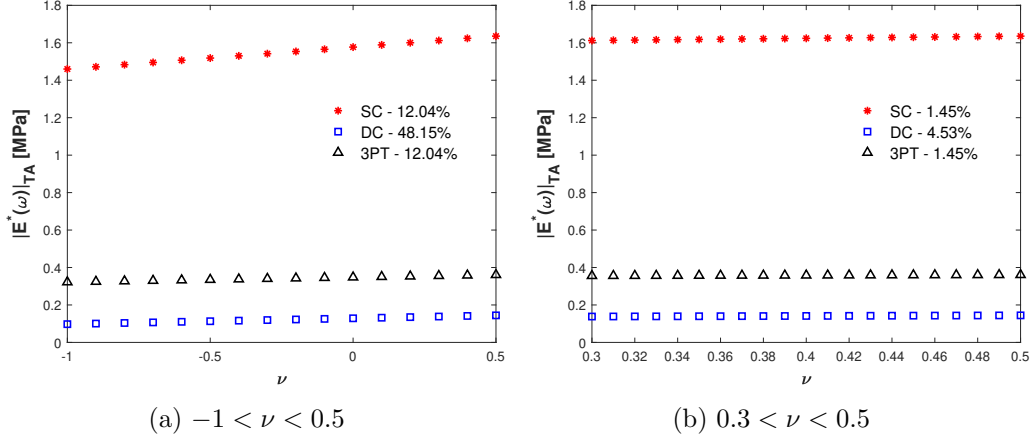


Figure 4.19: Effects of Poisson's ratio on complex modulus measured by TA machine.

It can be observed that modulus increased with the increase of Poisson's ratio, being DC mode the one presenting the greatest dependence. Considering the entire range from -1 to 0.5 (see Fig. 4.19a), the modulus increased approximately 48% in DC, whereas 12% in SC and 3PT. When considering the range from 0.3 to 0.5 (see Fig. 4.19b), this variation reduced to 5% in DC and 1% in SC and 3PT. Therefore, depending on the material, the assumption of a constant Poisson's ratio does not lead to great changes.

To further explore the relevance of Poisson's ratio dependence on temperature in these measurements, a comparative plot was traced using Eqs. 4.7, 4.8 and 4.9 considering the hypotheses of a constant Poisson's ratio and a temperature-dependent Poisson's ratio, which varies linearly from 0.35 to 0.5 according to temperature. The linear model proposed is expressed as follows

$$\nu(T) = 0.35 + 0.15 \left[\frac{(T - T_i)}{(T_F - T_i)} \right], \quad (4.14)$$

where T_i is the initial temperature and T_F is the final temperature. Figure 4.20 shows the results obtained for each operational mode, suggesting that the effect of varying Poisson's ratio is neglectable on modulus measurements for all three modes.

4.3. STUDY I: TEMPERATURE-DEPENDENT COMPLEX MODULUS

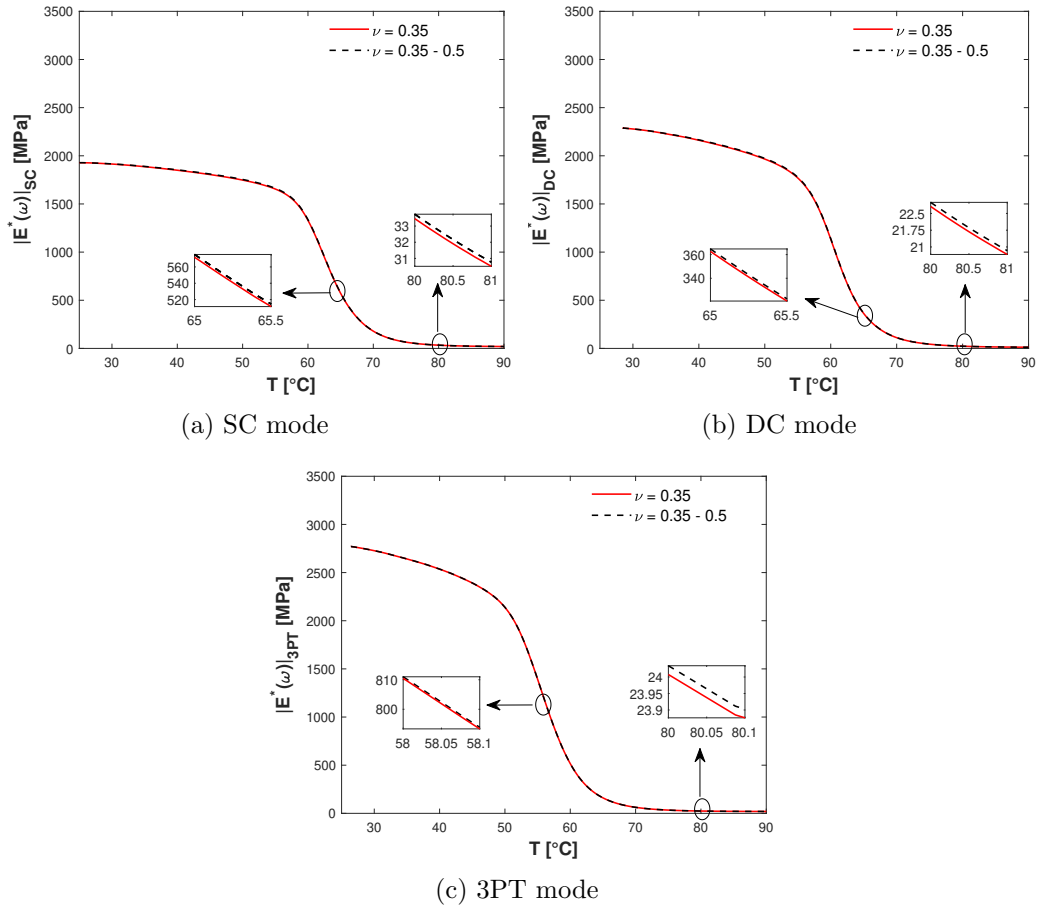


Figure 4.20: Comparison between the effects of a constant Poisson's ratio and a linear temperature-dependent Poisson's ratio on complex modulus measured by TA machine.

Finally, the influence of temperature on each model provided by Eqs. 4.4 to 4.13 was analyzed by setting the parameters K_s , S , w , and t to the same values obtained by the TA machine in each mode. Figure 4.21 compares the differences between each mathematical formulation as temperature increased. As suggested by the previous results shown in Fig. 4.18, the mathematical formulation from TA provided the highest estimates for all three modes. The differences between the formulations are more noticeable in DC results. On the other hand, 3PT mode had almost the same value for all formulations.

4.4. STUDY II: TEMPERATURE AND FREQUENCY-DEPENDENT COMPLEX MODULUS

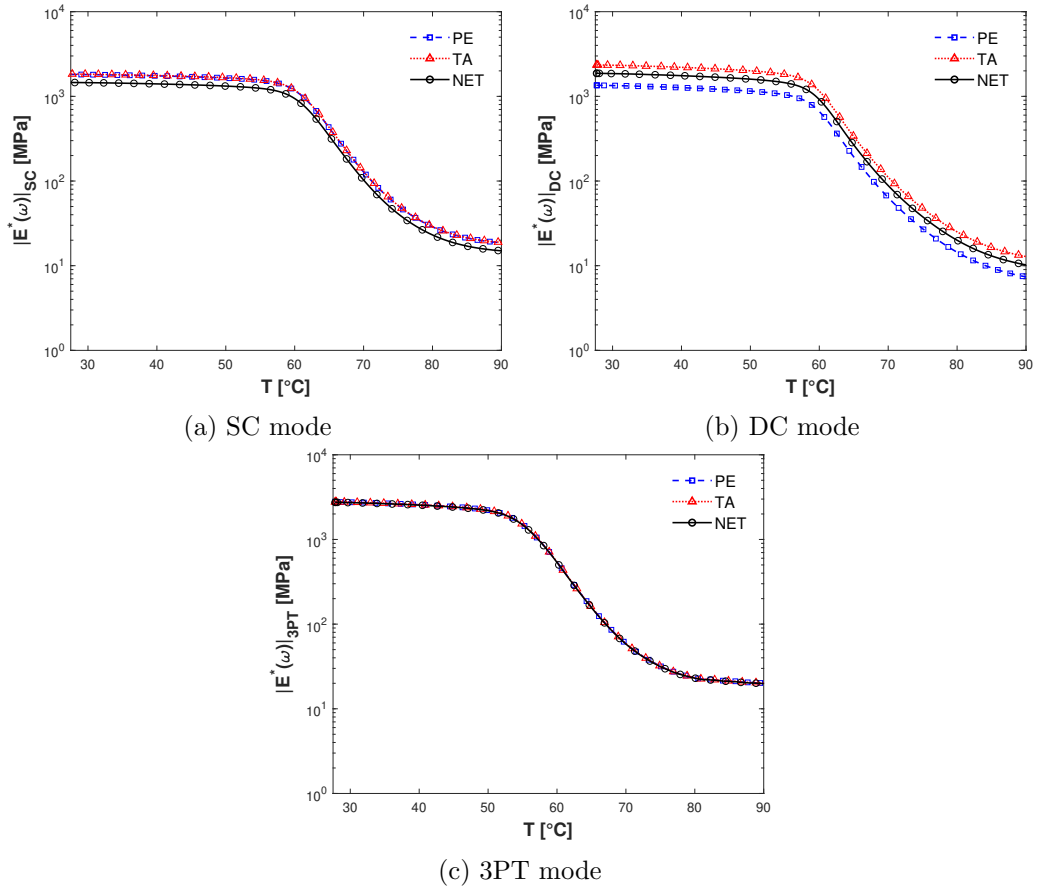


Figure 4.21: Effects of mathematical formulation on complex modulus.

4.4 Study II: temperature and frequency-dependent complex modulus

In Study II, the effects of the flexural modes and testing equipment on the temperature and frequency-dependent complex modulus were investigated. The objectives of this work were twofold. The first one was to observe how both temperature and frequency dependencies were experimentally measured in DMA tests using all flexural modes. The second one was to assess the effects of these modes and testing equipment on the long-term behavior of viscoelastic materials. For these purposes, experimental measurements were first carried out in SC, DC, and 3PT modes. The repeatability of each type of test was also analyzed. The hypothesis of thermo-rheological simple behavior was then validated, allowing the application of the time-temperature superposition principle to generate experimental master curves.

4.4. STUDY II: TEMPERATURE AND FREQUENCY-DEPENDENT COMPLEX MODULUS

4.4.1 Test conditions

Dynamics tests were performed in SC, DC, and 3PT modes only in PE and TA machines. They were all carried out in similar conditions in order to obtain reliable results. Furthermore, mechanical calibrations were carried out prior to each set of tests of each operational mode.

Temperature-frequency scan technique was employed. Frequency sweeps from 1 to 100 Hz were carried out at fourteen temperatures from 25 to 90 °C. Isotherms were maintained for 5 min every 5 °C and the heating rate was 2 °C/min. The strain amplitude was set to 10 μm to remain in the linear viscoelastic regime. The force track for 3PT tests was again set to 120 %.

Similarly to Study I, at least two samples were used on each test to reduce the risks of abnormalities due to fabrication or experimental errors. The normal statistics of sampling and data analysis were performed. Hence, all experimental results are presented as the mean of these samples together with the corresponding standard deviation.

Testing parameters are summarized on Table 4.6, where t is thickness, S is the span, S/t is the span-to-thickness ratio and a is the amplitude. Only one set of samples were tested in each operational mode in each machine.

Table 4.6: Testing parameters for the second case study, where t is thickness, S is the span, S/t is the span-to-thickness ratio and a is the amplitude.

| DMA | Mode | t [mm] | S [mm] | S/t | a [μm] | Force Track [%] |
|-----|------|----------|----------|-------|-----------------------|-----------------|
| PE | SC | 2.0 | 12.2 | 6.1 | 10 | - |
| | DC | 3.2 | 30.0 | 9.4 | 10 | - |
| | 3PT | 3.2 | 35.0 | 10.9 | 10 | 120 |
| TA | SC | 3.2 | 17.5 | 5.5 | 10 | - |
| | DC | 3.2 | 35.0 | 10.9 | 10 | - |
| | 3PT | 3.2 | 50.0 | 15.6 | 10 | 120 |

4.4.2 Experimental results & discussion

SC, DC, and 3PT modes were performed in PE and TA machines using the same test conditions in temperature and frequency scans. This section discusses the experimental results to observe the influences of operational mode and testing equipment.

4.4.2.1 Influence of operational mode

As the complex modulus showed similar behavior in the measurements performed through PE and TA machines, the conclusions were quite similar. For this reason, only the experimental results obtained by the TA machine were analyzed and discussed next. The results from the PE machine can be found in Appendix B.

Figures 4.22 to 4.24 show the experimental results obtained in SC, DC and 3PT modes, respectively. It can be noted that all of them identified the classical viscoelastic response associated with thermosetting resins [8]. That is, the mechanical behavior of these polymers was directly affected by temperature and frequency. The increase in temperature caused a decrease in the modulus. The increase in frequency, in turn, caused an increase in the modulus and also in the glass transition temperature (T_g). These effects are associated with the molecular rearrangements of polymer chains and relaxation phenomena.

From Figs. 4.22a, 4.23a and 4.24a, the storage modulus was almost constant with frequency and temperature between 25 and 50 °C. It indicates that the system was in the glassy state, presenting thus lower molecular mobility and higher resistance to strain. Between 55 and 90 °C, on the other hand, this modulus decreased with an increase in temperature but increased with an increase in frequency. It suggests that the system was in the glass transition region, presenting higher molecular mobility and lower resistance to strain.

Furthermore, all tests had good repeatability as the standard deviations presented low amplitude levels on the full analyzed range. 3PT provided the highest amplitudes, but they were less than 10 %. A similar pattern was observed in the measurement results in the works of Henriques et al. [17] and McAninch et al. [91] for epoxy systems.

Comparing the results from these three flexural modes, however, 3PT presented the highest estimates for both storage and loss moduli in all range of frequency and temperature, whereas SC presented the lowest ones. Figure 4.25 directly compares the values measured for storage modulus at, for example, 25 and 70 °C to highlight the differences. Considering the applied frequency equal to 10 Hz, 3PT was 32 % (respectively 44 %) higher than SC and 21 % (respectively 41 %) higher than DC at 25 °C (respectively 70 °C).

These variations due to changes in operational mode can also be observed in the work of Feng

4.4. STUDY II: TEMPERATURE AND FREQUENCY-DEPENDENT COMPLEX MODULUS

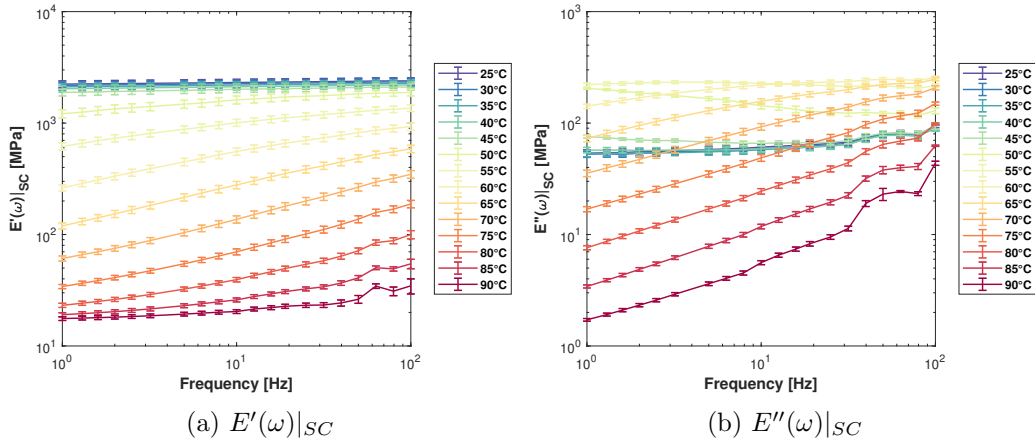


Figure 4.22: Complex modulus measured in SC mode by TA machine.

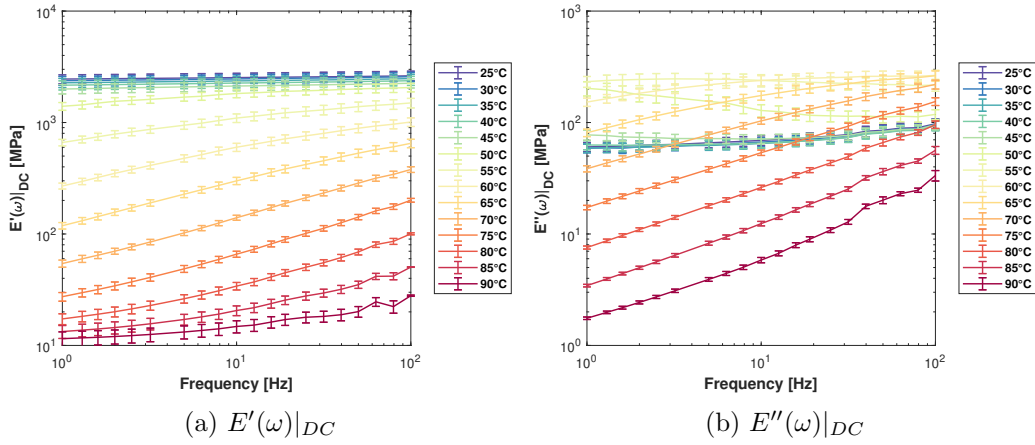


Figure 4.23: Complex modulus measured in DC mode by TA machine.

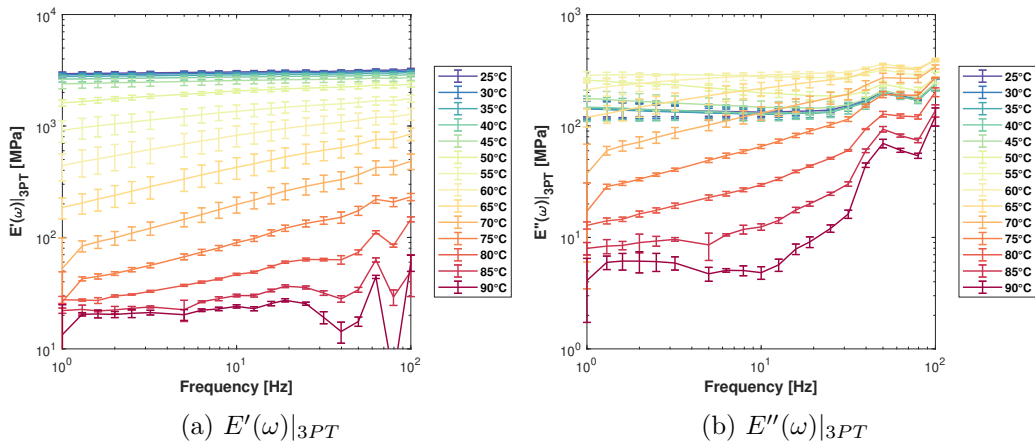


Figure 4.24: Complex modulus measured in 3PT mode by TA machine.

4.4. STUDY II: TEMPERATURE AND FREQUENCY-DEPENDENT COMPLEX MODULUS

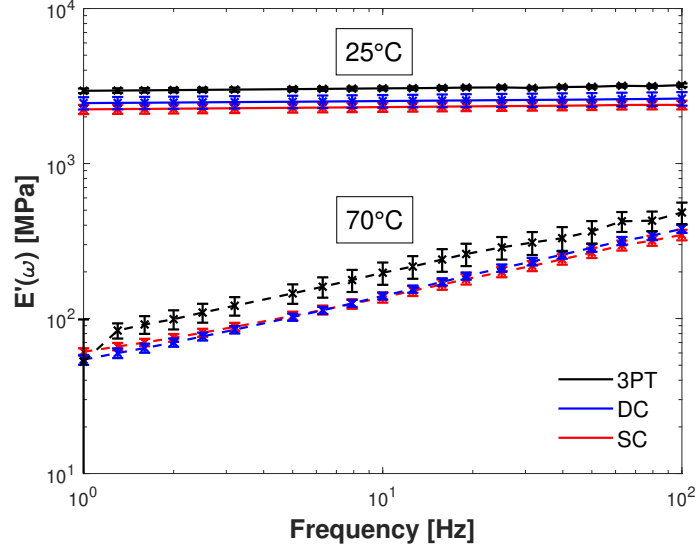


Figure 4.25: Comparisons between the temperature and frequency-dependent complex modulus measured in SC, DC and 3PT modes by TA machine.

and Guo [93]. Even though the testing parameters were different from this work, the results therein also showed 3PT having the highest modulus in the temperature and frequencies investigated for epoxy-based composites.

Despite the differences in the values of both storage and loss moduli, the Cole-Cole diagram and Black Space were built to verify if the thermo-rheological simple behavior could be identified in the measured data provided by all three modes. Figures 4.26 to 4.28 show that all $E'(\omega) \times E''(\omega)$ and $\eta(\omega) \times |E^*(\omega)|$ curves in double logarithmic scales at different temperatures fall on a continuous circular arc, fulfilling thus the requirements of thermo-rheological simplicity. Nevertheless, some points from the measurements deviated from the curves at high frequencies and temperatures, especially in 3PT mode, and they are associated with experimental difficulties such as, for example, resonance phenomena [5, 108] and sample slippage [17].

As the material met the assumption of thermo-rheological simple behavior, the time-temperature superposition principle was employed to generate master curves. In this regard, the temperature chosen as reference for this procedure was $T_0 = 70^\circ\text{C}$, and only the measurement points related to the temperature range 55 to 90°C were considered. It should be pointed out that only horizontal shifting was considered as neither the Cole-Cole diagram nor Black space evidenced a need for vertical shifting

4.4. STUDY II: TEMPERATURE AND FREQUENCY-DEPENDENT COMPLEX MODULUS

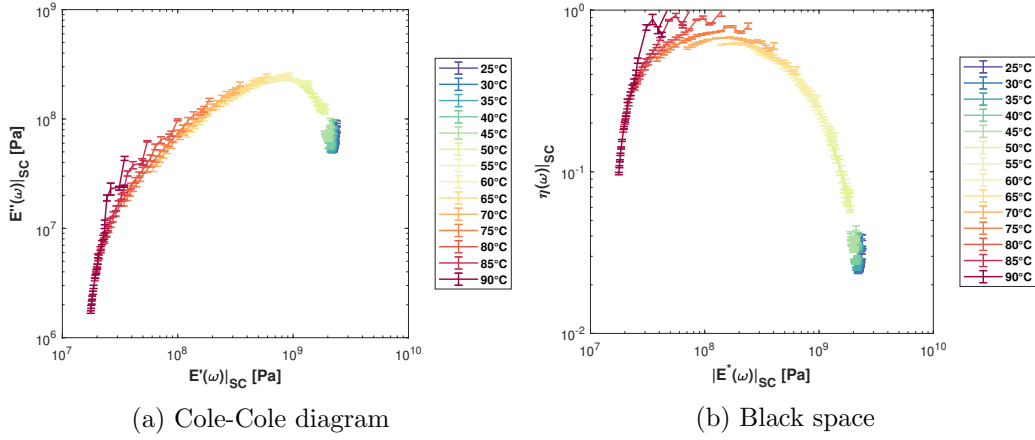


Figure 4.26: Validation of thermo-rheological simple behavior considering measurements in SC mode by TA machine.

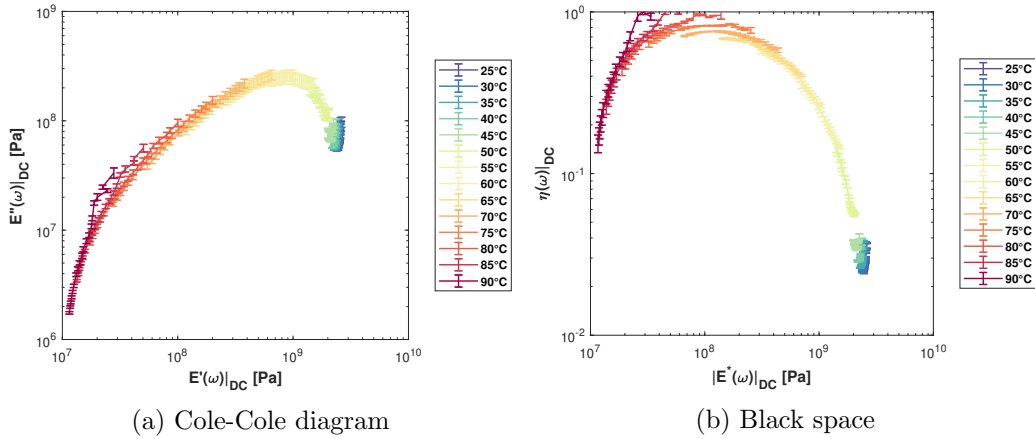


Figure 4.27: Validation of thermo-rheological simple behavior considering measurements in DC mode by TA machine.

[2].

The horizontal shift factors were first computed for all samples of SC, DC, and 3PT modes using the optimized method proposed by Rouleau et al. [2]. Afterward, they were fitted by the WLF equation to certify the consistency of their values. Figure 4.29 compares the factors obtained by each method, showing a good agreement for all three modes. Table 4.7 presents the empirical constants C_1 and C_2 that led to a good fit with the optimized shift coefficients.

4.4. STUDY II: TEMPERATURE AND FREQUENCY-DEPENDENT COMPLEX MODULUS

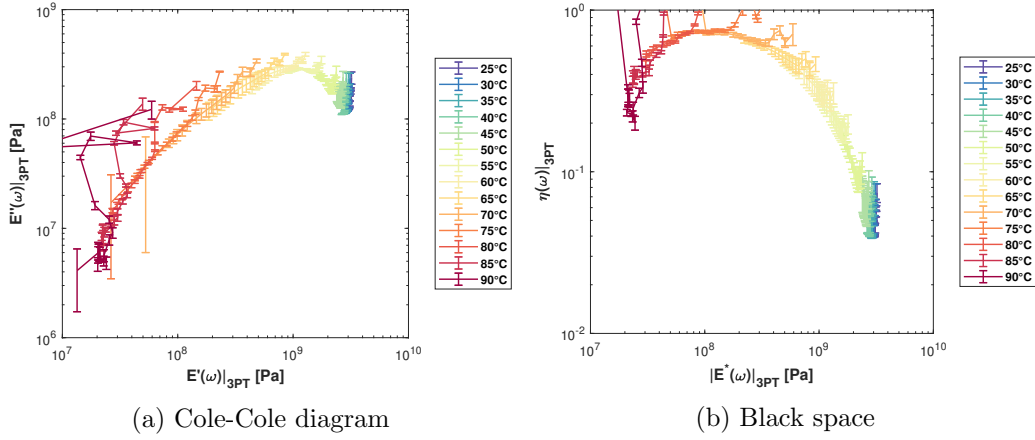


Figure 4.28: Validation of thermo-rheological simple behavior considering measurements in 3PT mode by TA machine.

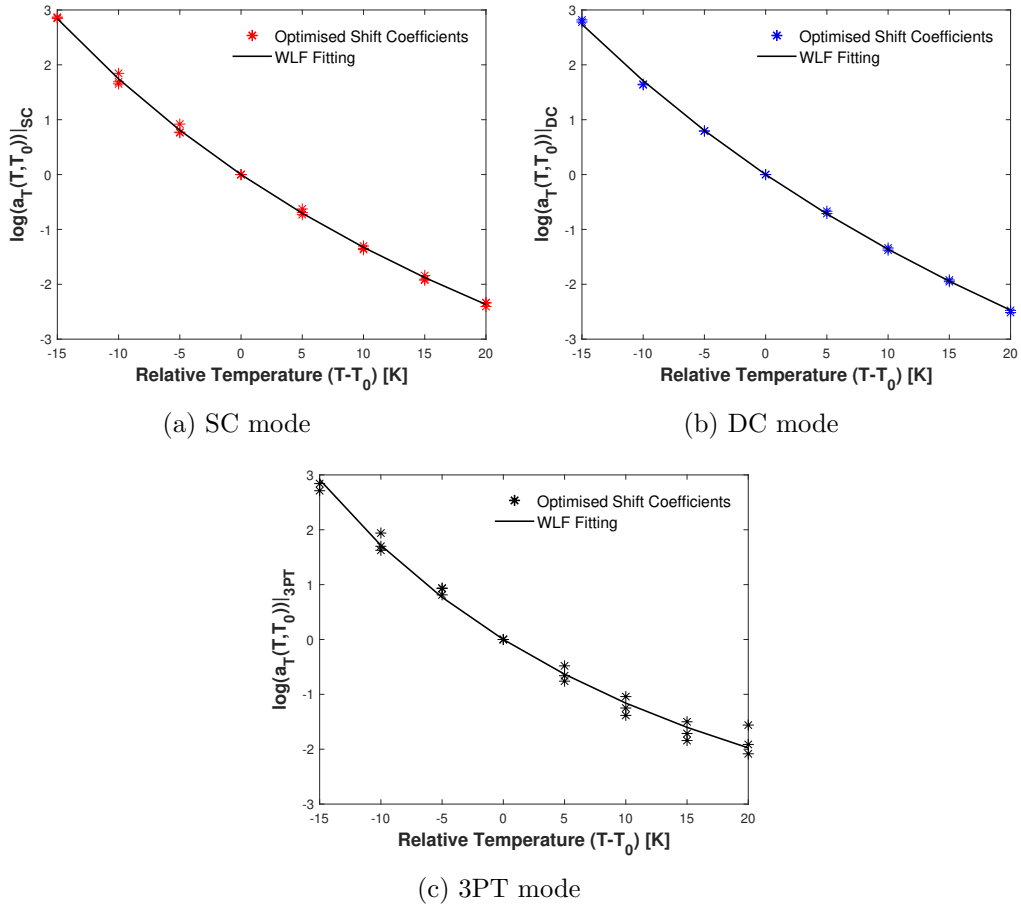


Figure 4.29: Horizontal shift coefficients $a_T(T, T_0)$ applied to the isotherms from measurements obtained by TA machine, shown in Figs. 4.22-4.24. The optimised coefficients are fitted by WLF equation.

4.4. STUDY II: TEMPERATURE AND FREQUENCY-DEPENDENT COMPLEX MODULUS

Table 4.7: Empirical constants of WLF equation calibrated using measurements obtained by TA machine.

| Constants | SC mode | DC mode | 3PT mode |
|-----------|------------------|------------------|------------------|
| C_1 | 11.14 ± 0.32 | 13.41 ± 0.45 | 7.69 ± 1.83 |
| C_2 [K] | 73.97 ± 5.42 | 88.47 ± 2.27 | 54.87 ± 9.14 |

To better compare the effects of operational mode in these estimates, Fig. 4.30 directly compares the results obtained in each test. It can be observed a slight difference among them, especially at higher temperatures. As a consequence, the fitting parameters C_1 and C_2 of the WLF equation shown in Tab. 4.7 were not the same, but they were very close to each other. This fact is coherent with the concepts of these empirical constants once they depend on the material and the reference temperature, not on the operational mode [8]. Moreover, Arzoumanidis and Liechti [109] also observed a similar pattern when estimating these parameters using measured data from tensile and shear tests.

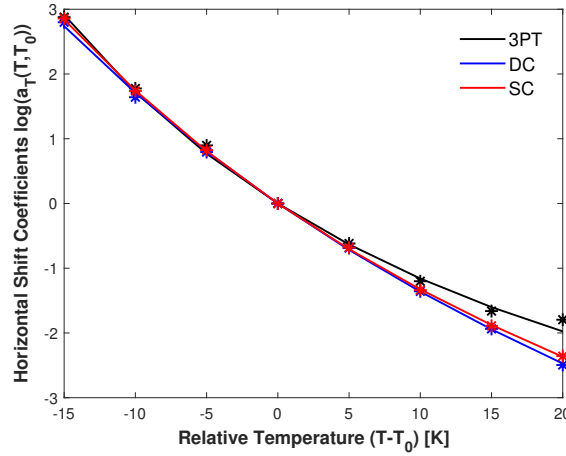


Figure 4.30: Comparison between the horizontal shift coefficients $a_T(T, T_0)$ obtained for SC, DC and 3PT modes. The optimised coefficients (markers: *) are fitted by WLF equation (solid line: -).

Finally, each isotherm was shifted according to the corresponding shift factor $a_T(T, T_0)$, and the experimental master curves were generated at the reference temperature $T_0 = 70^\circ\text{C}$ as shown in Fig. 4.31. The moduli behavior is predicted over a large frequency range up to about 10^5Hz . From the curve of storage modulus $E'(\omega)$, one can thus infer the long-term behavior of the material [8]. From the curve of loss factor $\eta(\omega)$, in turn, one can assess the damping capacity of the material.

Comparing these master curves, it can be seen that 3PT provided, in general, the highest values for

4.4. STUDY II: TEMPERATURE AND FREQUENCY-DEPENDENT COMPLEX MODULUS

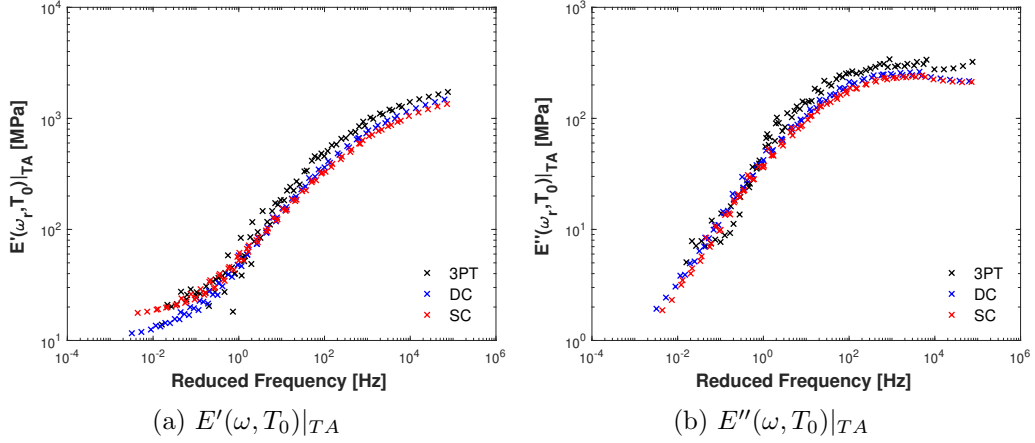


Figure 4.31: Comparison between experimental master curves built at $T_0 = 70\text{ }^\circ\text{C}$ considering measurements of complex modulus by TA machine.

both storage and loss moduli, as already suggested by previous results. When analyzing the response along with the frequency, however, it is possible to observe similar material's behavior regardless of the modality test performed.

From Fig. 4.31a, all curves of storage modulus $E'(\omega)$ followed the same pattern where the three regions of viscoelastic behavior could be identified. The modulus initially had approximately a constant value in the low frequencies. Afterward, it increased significantly with the frequency until it reached a new plateau at high frequencies. Moreover, the beginning and end of the slope of the curves of the three tests happened at similar frequencies.

From Fig. 4.31b, all curves obtained for the loss modulus $E''(\omega)$ also showed three regions of behavior. Initially, it increased significantly with the frequency until reaching a maximum value, and from this point, it presented a slight decay toward a constant value. Moreover, the peak happened almost at the same frequency in the three tests.

4.4.2.2 Influence of testing equipment

As previously mentioned, the temperature and frequency-dependent complex modulus was measured in three flexural modes by two DMA machines. Figure 4.32 compares the results from these two testing equipment at three selected temperatures $T = \{25\text{ }^\circ\text{C}, 60\text{ }^\circ\text{C}, 90\text{ }^\circ\text{C}\}$. Similar to Study I, their influence on experimental measurements depended on the operational mode and also on the test temperature. The TA machine estimated a higher modulus for most temperatures and frequencies,

4.4. STUDY II: TEMPERATURE AND FREQUENCY-DEPENDENT COMPLEX MODULUS

especially in DC mode. These differences are quite similar for the other temperatures; hence, they have not been shown here.

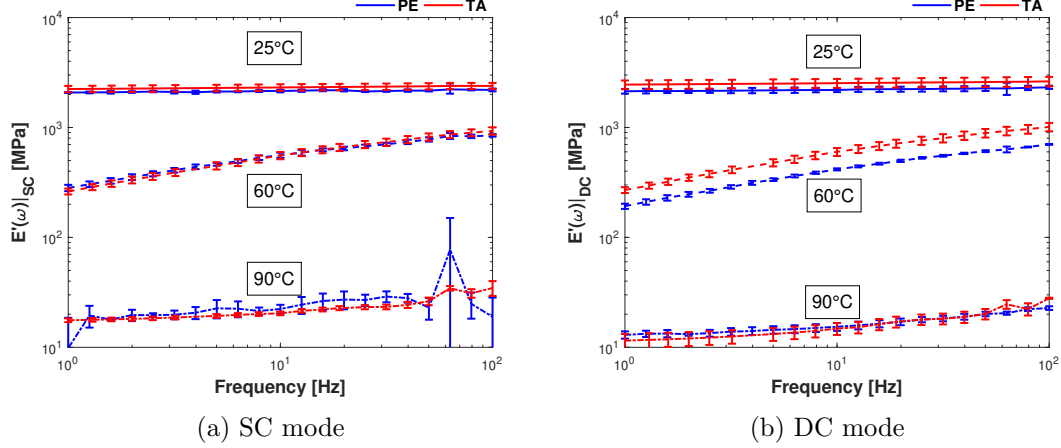


Figure 4.32: Comparisons between the temperature and frequency-dependent complex modulus measured by TA and PE machines.

Table 4.8 compares the results of the empirical constants C_1 and C_2 obtained in the different tests performed on the two machines. DC mode was the one most affected by testing equipment, whereas 3PT was the one less affected.

Table 4.8: Comparison between the empirical constants of WLF equation calibrated using measured data from SC, DC and 3PT modes.

| Mode | Constants | PE machine | TA machine |
|------|-----------|------------------|------------------|
| SC | C_1 | 8.52 | 11.14 ± 0.32 |
| | C_2 [K] | 57.6 | 73.97 ± 5.42 |
| DC | C_1 | 9.31 ± 0.47 | 13.41 ± 0.45 |
| | C_2 [K] | 63.36 ± 4.14 | 88.47 ± 2.27 |
| 3PT | C_1 | 7.65 ± 0.58 | 7.69 ± 1.83 |
| | C_2 [K] | 54.15 ± 0.47 | 54.87 ± 9.14 |

Finally, Figs. 4.33 to 4.35 compare the experimental master curves obtained, respectively, in the tests performed in SC, DC, and 3PT modes by the two testing equipment. As can be seen, all master curves built using measured data from the TA machine presented the highest values for both storage and loss moduli. A similar pattern was observed in the first study case (see Section 4.3), in which the moduli was only measured as a function of temperature.

4.4. STUDY II: TEMPERATURE AND FREQUENCY-DEPENDENT COMPLEX MODULUS

Nevertheless, a similar material behavior can be noted in the curves regardless of the testing equipment. This suggests a small influence of the machine in identifying the relaxation time of the material.

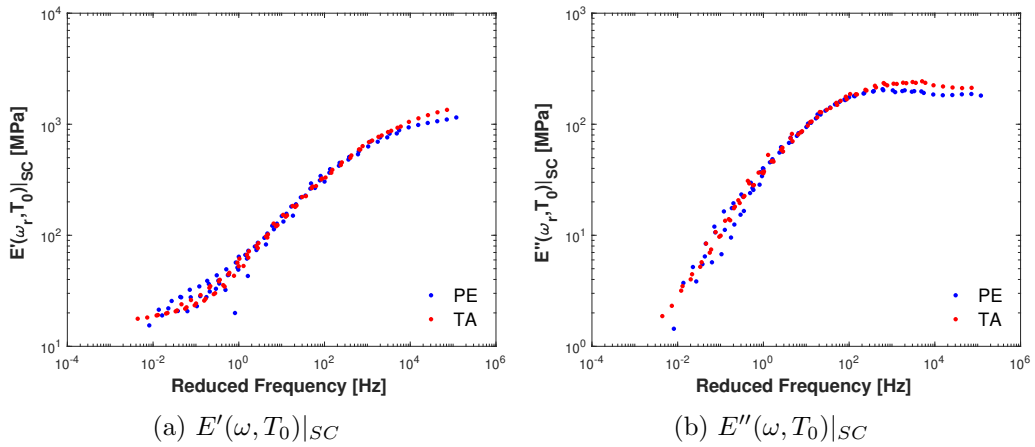


Figure 4.33: Comparison between experimental master curves built at $T_0 = 70^\circ\text{C}$ considering measurements of complex modulus in SC mode.

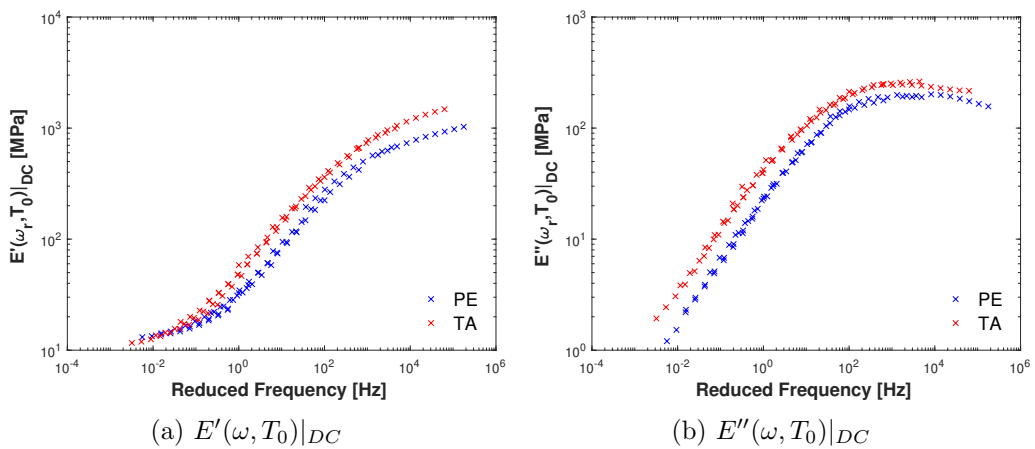


Figure 4.34: Comparison between experimental master curves built at $T_0 = 70^\circ\text{C}$ considering measurements of complex modulus in DC mode.

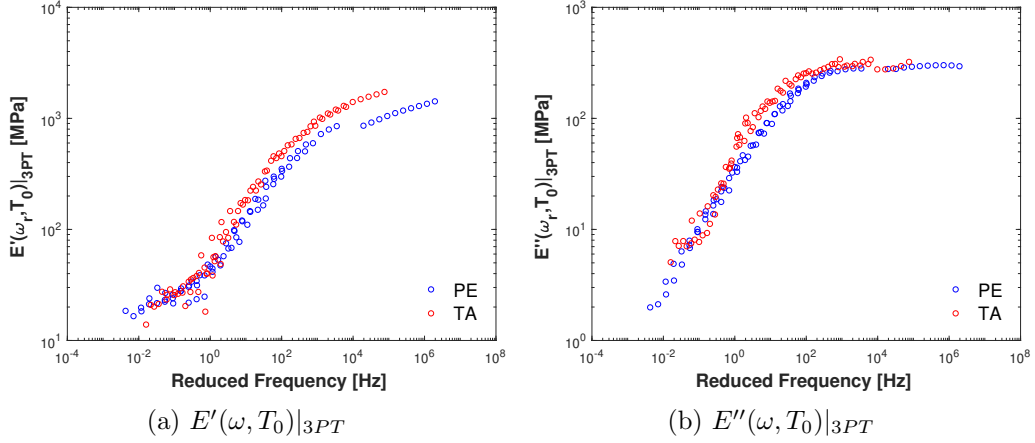


Figure 4.35: Comparison between experimental master curves built at $T_0 = 70^\circ\text{C}$ considering measurements of complex modulus in 3PT mode.

4.5 Conclusion

This chapter presented an inter-laboratory study about the complex modulus measured by the flexural modes existing in DMA machines. It was divided into two parts: (i) theoretical analysis and (ii) experimental tests. The main results achieved may be described as follows.

The first part related to theoretical aspects explained the key features of each operational mode, such as mechanism and mathematical formulation. It highlighted that SC and DC modes may present clamping effects and that each DMA machine has its model assumptions. Consequently, some discrepancies among estimates from different machines may happen even if the test conditions are the same.

The second part consisted of two experimental investigations concerning how this modulus is measured only as a function of temperature and as a function of both temperature and frequency. It aimed to evaluate the effects of operational modes and testing equipment on the values of the moduli, on the glass transition temperature and also on the long-term behavior. Moreover, it also addressed the repeatability and reproducibility of the tests.

The experimental results showed that DMA measurements can vary among modes and machines. Although the repeatability of the tests was reasonable, the reproducibility was quite poor. These uncertainties, however, varied according to the region of viscoelastic behavior. Furthermore, SC and

4.5. CONCLUSION

DC modes indeed suffered from clamping effects as the ends of the samples deformed after the tests, and they were the most affected by the sample's geometry and DMA machine. 3PT mode, on the other hand, was found to be the one more reliable among the flexural modes, and it provided the highest estimates.

It is worth recalling that these findings cannot be generalized to other viscoelastic materials but draw attention of common issues when dealing with this technique. Moreover, it emphasized the need for revision of the current standards to define new procedures for the measurement of this property, which is widely used to describe the material's behavior.

4.5. CONCLUSION

Chapter 5

Modeling the complex modulus within Bayesian framework

This chapter is concerned with the calibration of fractional derivative models within the Bayesian framework for a viscoelastic material considering experimental data acquired by the three flexural modes in a DMA machine. The main objective is to study the effects of uncertainties inherent to DMA measurements carried out in different set-ups on model predictions. In this regard, it could provide insights about the reliability of models calibrated from DMA data. It is organized as follows. First, Section 5.1 provides a brief description of the methodology adopted for modeling the complex modulus. Then, Section 5.2 details the mathematical formulation adopted to model material's behavior. Afterward, Section 5.3 shows and discusses the calibrated models. Finally, Section 5.4 presents the concluding remarks.

Content

| | | |
|------------|--|------------|
| 5.1 | Methodology | 156 |
| 5.2 | Modeling | 156 |
| 5.3 | Results & discussion: identification of viscoelastic parameters | 157 |
| 5.3.1 | Description of calibration procedure | 157 |
| 5.3.2 | Model calibration | 159 |
| 5.4 | Conclusion | 167 |

5.1 Methodology

This section outlines the methodology adopted to model the complex modulus measured by DMA machine aiming at observing the effects of both operational mode and machine on the model parameters and consequently, on its predictions. Figure 5.1 schematic illustrates this approach which was mainly divided into three main steps. The first step comprised the tests performed using SC, DC, and 3PT modes in two DMA machines and the attainment of experimental master curves. The second one, in turn, involved the description of the material behavior using a fractional derivative model. Finally, the third main step was concerned with the model calibration procedure through the Bayesian framework.

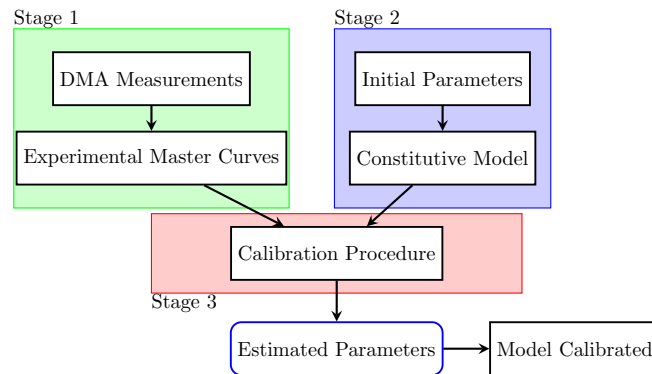


Figure 5.1: Schematic diagram of methodology employed to calibrate viscoelastic models considering measured data from DMA.

An important point to mention is that the experimental data used for the calibration of the models corresponded to the results presented in the second case study of the preceding chapter. A complete description of the machines and material can be found in Section 4.2 of Chapter 4, and the results obtained in Section 4.4. For the sake of conciseness of this chapter, they are not reported herein.

5.2 Modeling

Once an experimental master curve is built, one can calibrate viscoelastic models to provide predictions of the material's response when applied in structures and submitted to the most varied loading conditions, for example, in finite element simulations. Different constitutive models can be found in literature as introduced in Chapter 2. It was adopted herein the five-parameter fractional derivative

5.3. RESULTS & DISCUSSION: IDENTIFICATION OF VISCOELASTIC PARAMETERS

model (5PFDM), explained in subsection 2.5.2 of Chapter 2, to describe the viscoelastic behavior of the investigated material. Accordingly, the complex modulus $E^*(\omega)$ was expressed as follows

$$E^*(\omega) = E_0 + \frac{(E_\infty - E_0)(j\omega\tau)^\alpha}{1 + (j\omega\tau)^\beta}, \quad (5.1)$$

where E_0 and E_∞ are, respectively, the relaxed and unrelaxed moduli, τ is the relaxation time, and α and β are the orders of the fractional derivative model. These five parameters $\boldsymbol{\theta} = \{E_0, E_\infty, \tau, \alpha, \beta\}$ must respect the thermodynamic restrictions given by Eq. 2.35 and be determined by inverse techniques.

It is worth highlighting the reasons why this model was chosen. In general, fractional models have been able to describe the dynamic behavior of different viscoelastic materials along with frequency. The model with five parameters, in particular, can depict the asymmetry evidenced in the peaks of the experimental master curves of the loss modulus and the loss factor, in addition to the slight increase of the module at the highest frequencies. Besides, Orlandini et al. [74] recently calibrated this model satisfactorily for epoxy-based materials.

5.3 Results & discussion: identification of viscoelastic parameters

This section presents the results of the calibration of the models adopted to describe the long-term viscoelastic behavior. To this end, a probabilistic approach based on Bayesian inference, explained in Chapter 3, was considered to assess information about the posterior probability density function $\pi(\boldsymbol{\theta}|\mathbf{Y})$ of the model parameters $\boldsymbol{\theta} = \{E_0, E_\infty, \tau, \alpha, \beta\}$ that define the fractional model given by Eq. 5.1.

5.3.1 Description of calibration procedure

As previously mentioned, the measured data \mathbf{Y} comprised the experimental master curves built at $T_0 = 70^\circ\text{C}$ in the Chapter 4 for complex modulus $E^*(\omega_r, T_0)$. The unknown parameter vector was defined as $\boldsymbol{\theta} = \{E_0, E_\infty, \tau, \alpha, \beta\}^T$. However, as these parameters vary several orders of magnitude, they were normalized $\boldsymbol{\theta}_s = \{p_1, p_2, p_3, p_4, p_5\}^T$ to improve the performance of the inverse method [25] as

5.3. RESULTS & DISCUSSION: IDENTIFICATION OF VISCOELASTIC PARAMETERS

$$p_1 = E_0 \times 10^{-7} [\text{Pa}], \quad (5.2a)$$

$$p_2 = E_\infty \times 10^{-9} [\text{Pa}], \quad (5.2b)$$

$$p_3 = \tau \times 10^3 [\text{s}], \quad (5.2c)$$

$$p_4 = \alpha, \quad (5.2d)$$

$$p_5 = \beta. \quad (5.2e)$$

It is worth mentioning that the scale set for parameters E_0 and E_∞ were chosen according to the values obtained for storage modulus in the lower and higher frequencies, respectively, as shown in Fig. 4.31. The scale set for parameter τ was based on the results presented in the work of Orlandini et al. [74] for a similar epoxy system.

All data-set obtained for each DMA equipment has been split into three different subsets (SC, DC and 3PT) to quantify the effects of operational mode on the model updating process and consequently, on the model parameters. For each one, a specific structure was adopted.

Initially, the complex modulus of the i^{th} sample was organized in a N-dimensional vector $\mathbf{E}^*|_{S_i} = \{E^*(\omega_1, T_0)|_{S_i}, \dots, E^*(\omega_N, T_0)|_{S_i}\}^T$. Afterward, this vector was separated into its real $\Re[\mathbf{E}^*|_{S_i}]$ and imaginary $\Im[\mathbf{E}^*|_{S_i}]$ parts to consider both elastic and viscous effects in the process, and also to avoid issues when building the covariance matrix. Finally, a statical analysis was carried out to estimate the mean value and standard deviation of each part. Accordingly, the measured data \mathbf{Y} corresponded to a 2N-dimensional vector defined as follows

$$\mathbf{Y} = \{\Re[\tilde{\mathbf{E}}] \Im[\tilde{\mathbf{E}}]\}^T \quad (5.3)$$

where $\Re[\tilde{\mathbf{E}}]$ and $\Im[\tilde{\mathbf{E}}]$ are the average results for the real and imaginary parts, respectively.

For the model calibration step using Bayesian inference, one must define the likelihood function $\pi(\mathbf{Y}|\boldsymbol{\theta})$ and the prior distribution $\pi_0(\boldsymbol{\theta})$ of each unknown parameter, as shown in Eq. 3.4. In this work, the likelihood function $\pi(\mathbf{Y}|\boldsymbol{\theta})$ was defined by the distribution of the additive error as shown in Eq. 3.6, whereupon it was considered $\mathbf{e} \sim N(\mathbf{0}, \boldsymbol{\Sigma})$. A diagonal empirical covariance matrix $\boldsymbol{\Sigma}$, as shown in Eq. 3.9, was built with the maximum variance found from the experimental measurements, i.e., $\sigma_i^2 = \sigma_{max}^2$.

5.3. RESULTS & DISCUSSION: IDENTIFICATION OF VISCOELASTIC PARAMETERS

Concerning the prior distributions $\pi_0(\boldsymbol{\theta})$, a uniform prior distribution is herein assumed for the unknown parameters $\boldsymbol{\theta} = \{E_0, E_\infty, \tau, \alpha, \beta\}^T$ as there is no reliable knowledge of them. Every random variable was constructed under the hypothesis that they were mutually independent. Moreover, the marginal prior for the variable θ was defined to be within the set D_θ such as

$$D_{p_1} = \{p_1 \in \mathbb{R} | 0 < p_1 < 10\}, \quad (5.4a)$$

$$D_{p_2} = \{p_2 \in \mathbb{R} | 0 < p_2 < 10\}, \quad (5.4b)$$

$$D_{p_3} = \{p_3 \in \mathbb{R} | p_3 > 0\}, \quad (5.4c)$$

$$D_{p_4} = \{p_4 \in \mathbb{R} | 0 < p_4 < 1\}, \quad (5.4d)$$

$$D_{p_5} = \{p_5 \in \mathbb{R} | 0 < p_5 < 1\}. \quad (5.4e)$$

Finally, the values for parameters α and β were chosen following the thermodynamics constraints explained in subsection 2.5.2 of Chapter 2.

After setting all parameters and distributions, the calibration of the model started. Firstly, a deterministic analysis was done to assess the maximum a posteriori estimate $\hat{\boldsymbol{\theta}}_{MAP}$ shown in Eq. 3.11. Then, the approximate posterior covariance matrix is determined as $\hat{\Sigma} \approx (\mathbf{J}^T \boldsymbol{\Sigma} \mathbf{J})^{-1}$, where the operator \mathbf{J} is related to the model Jacobian evaluated at $\hat{\boldsymbol{\theta}}_{MAP}$. Finally, the posterior distribution of the unknown parameters $\pi(\boldsymbol{\theta} | \mathbf{Y})$ was explored with the DRAM algorithm. In the AM method, the adaptation occurred at prescribed intervals of length $j_0 = 100$ with a Gaussian candidate distribution. In the DR method, three stages were considered in which $\gamma_s = \{1/5, 1/4, 1/3\}$. A total number of $N_{MC} = 200000$ samples was considered.

5.3.2 Model calibration

The calibrations performed using measured data from TA and PE machines showed similar behavior, thus leading to similar conclusions. Hence, only the results generated from the TA machine are analyzed and discussed next. The results from the PE machine can be found in Appendix B.

As a starting-point, a MAP estimator was carried out to find an optimum point $\hat{\boldsymbol{\theta}}_{MAP}$ to start the MCMC sampling process. This is done to reduce the computational cost of the estimation. The results achieved for each unknown parameter are shown in Tab. 5.1.

5.3. RESULTS & DISCUSSION: IDENTIFICATION OF VISCOELASTIC PARAMETERS

Table 5.1: MAP results for the measurements subsets SC, DC and 3PT from TA machine.

| Subset | E_0 [Pa] | E_∞ [Pa] | τ [s] | α | β |
|-----------|--------------------|--------------------|-----------------------|----------|---------|
| Initial | 1.00×10^7 | 1.00×10^9 | 0.50×10^{-3} | 0.5 | 0.5 |
| MAP - SC | 0.78×10^7 | 1.13×10^9 | 0.33×10^{-3} | 0.46 | 0.40 |
| MAP - DC | 0.16×10^7 | 1.21×10^9 | 0.40×10^{-3} | 0.47 | 0.42 |
| MAP - 3PT | 0.51×10^7 | 1.03×10^9 | 1.58×10^{-3} | 0.54 | 0.46 |

Figure 5.2 compares the results obtained for SC, DC, and 3PT modes using the DRAM algorithm, evidencing the well-mixing samples and that the stationarity of the posterior distributions has been reached. The convergence was monitored by computing the cumulative mean in the Markov chain of all the parameters. From these means, it is possible to infer that both parameters E_0 and τ were more affected by the set of measured data, that is, by the operational modes. Finally, Tab. 5.2 summarizes the analyses of the MCMC samples, showing that the acceptance rate values were consistent [25].

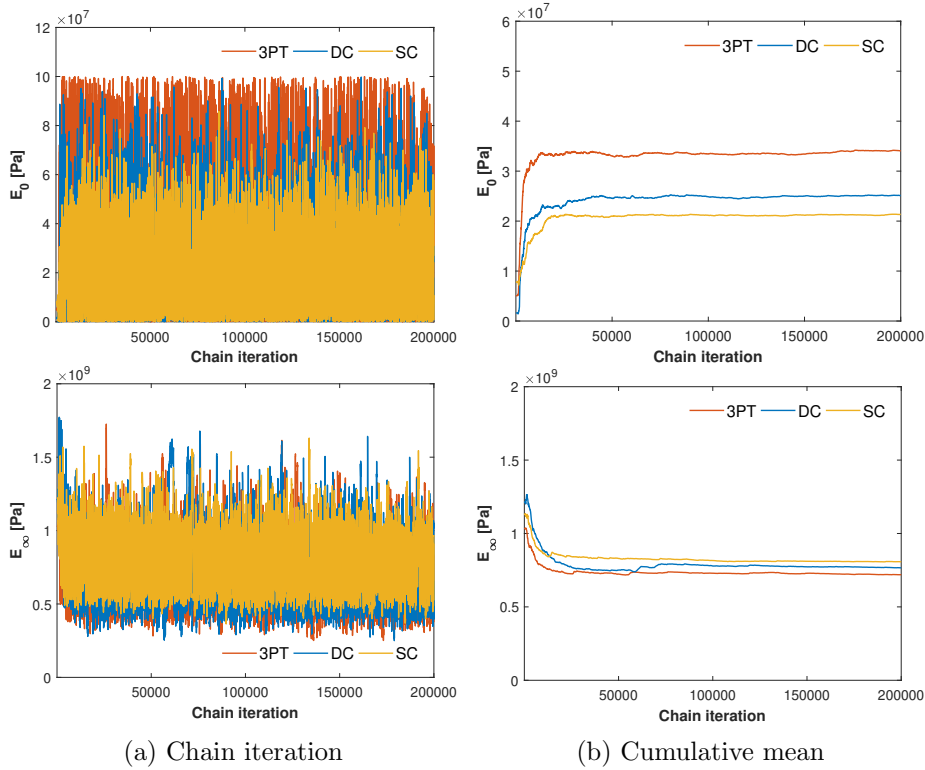


Figure 5.2: Convergence analysis for the 5PFDM using DRAM algorithm with each data-set from TA machine.

5.3. RESULTS & DISCUSSION: IDENTIFICATION OF VISCOELASTIC PARAMETERS

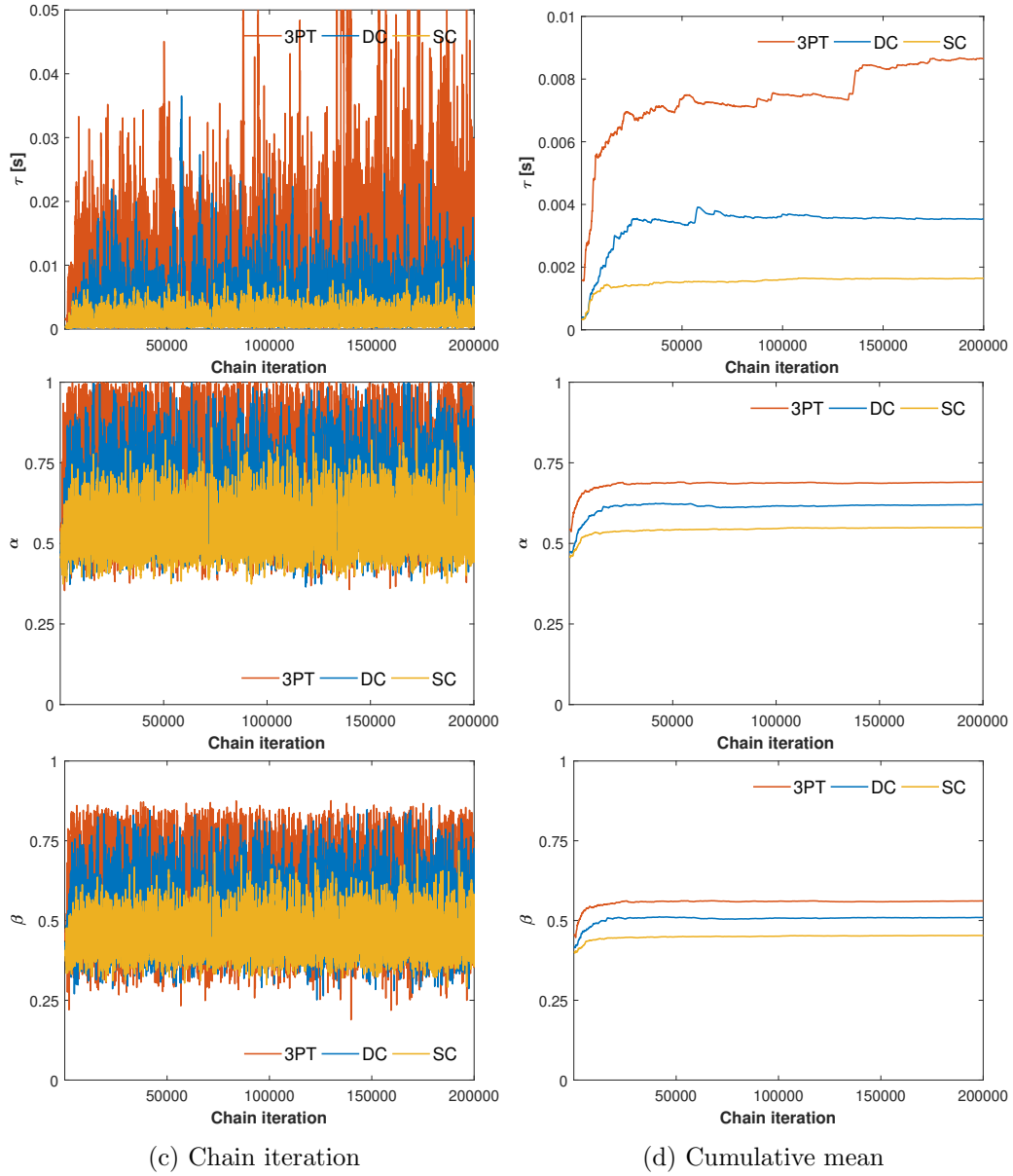


Figure 5.2: Convergence analysis for the 5PFDM using DRAM algorithm with each data-set from TA machine.

Table 5.2: MCMC results using DRAM algorithm for each data-set from TA machine.

| Mode | Total samples | Burn-in | Acceptance rate |
|------|---------------|---------|-----------------|
| SC | 200000 | 150000 | 38.95 |
| DC | 200000 | 150000 | 26.40 |
| 3PT | 200000 | 175000 | 39.68 |

5.3. RESULTS & DISCUSSION: IDENTIFICATION OF VISCOELASTIC PARAMETERS

After discarding the samples from the burn-in period, Monte Carlo approximations were computed for the posterior mean $\mathbb{E}[\theta]$ and 95 % credibility interval (CI) of each model parameter θ as shown in Tab. 5.3. It is possible to observe that the mean value of these estimates varied according to the operational mode, but their credibility intervals were quite close to each other. Furthermore, both parameters E_0 and τ were indeed the ones most affected by the operational mode.

Table 5.3: Posterior mean value and 95 % credibility interval (CI) of the unknown parameters θ for each data-set from TA machine.

| Mode | $\mathbb{E}[E_0]$ [$\times 10^7$ Pa] | $\mathbb{E}[E_\infty]$ [$\times 10^9$ Pa] | $\mathbb{E}[\tau]$ [$\times 10^{-3}$ s] | $\mathbb{E}[\alpha]$ | $\mathbb{E}[\beta]$ |
|------|---------------------------------------|--|--|----------------------|---------------------|
| | 95 % CI | 95 % CI | 95 % CI | 95 % CI | 95 % CI |
| SC | 2.19 | 0.80 | 1.68 | 0.55 | 0.46 |
| | [0.11, 5.26] | [0.48, 1.24] | [0.21, 5.24] | [0.44, 0.72] | [0.36, 0.59] |
| DC | 2.54 | 0.75 | 3.43 | 0.63 | 0.51 |
| | [0.13, 6.74] | [0.40, 1.30] | [0.27, 13.26] | [0.44, 0.89] | [0.36, 0.74] |
| 3PT | 3.43 | 0.71 | 8.64 | 0.70 | 0.57 |
| | [0.14, 8.57] | [0.39, 1.26] | [0.64, 35.56] | [0.49, 0.96] | [0.38, 0.80] |

Once the mapping between the random vector θ and the model prediction was non-linear, the samples could have some level of linear correlation. For this reason, scatter plots were built, as shown in Fig. 5.3. It can be seen little or no correlation between the parameters, which endorses the independence hypothesis adopted for all random variables when building the prior PDFs.

Figure 5.4 shows the marginal posterior PDFs computed for each unknown parameter θ . It can be seen that the PDFs for both E_0 and τ deviate from a Gaussian distribution. These parameters were the most affected by the data-set, i.e., by the operational mode: the posterior mean and the 95 % credibility interval varied significantly, as evidenced in Tab. 5.3.

5.3. RESULTS & DISCUSSION: IDENTIFICATION OF VISCOELASTIC PARAMETERS

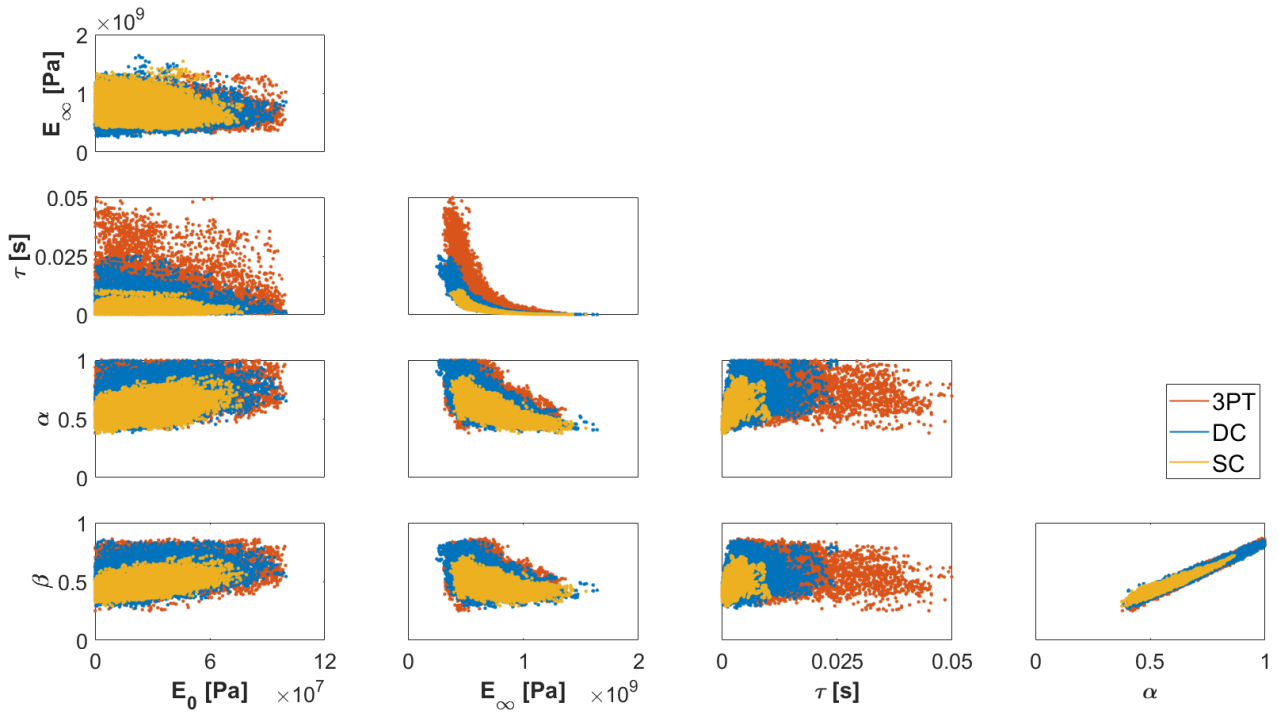


Figure 5.3: Posterior samples generated using DRAM algorithm with each data-set from TA machine.

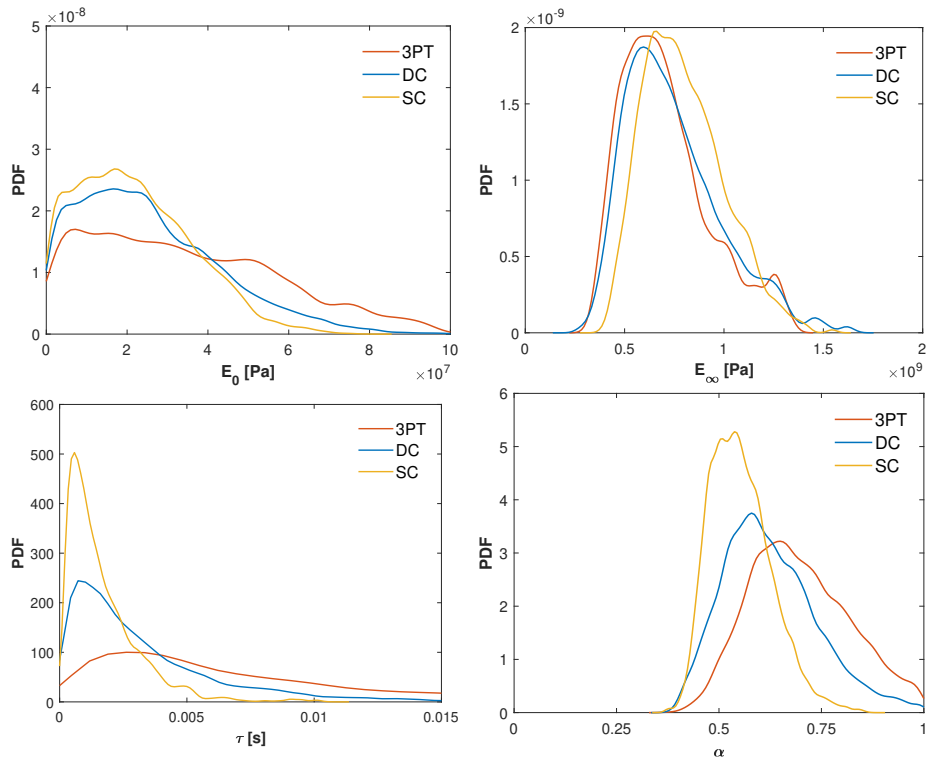


Figure 5.4: PDFs for the parameters generated using DRAM algorithm with each data-set from TA machine.

5.3. RESULTS & DISCUSSION: IDENTIFICATION OF VISCOELASTIC PARAMETERS

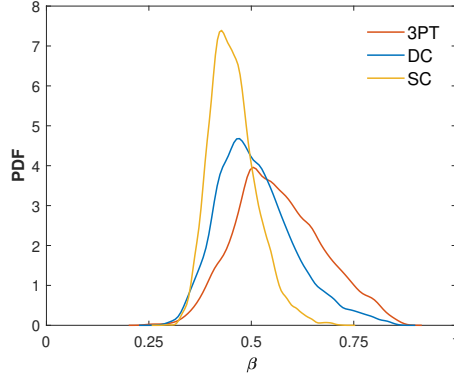


Figure 5.4: PDFs for the parameters generated using DRAM algorithm with each data-set from TA machine.

Finally, the uncertainty propagation from the model parameters $\theta \sim \pi(\theta|\mathbf{Y})$ to the complex modulus $E^*(\omega)$ was done for all data-sets. All samples $\{\theta^{(1)}, \dots, \theta^{(N_{mc})}\}$ from the posterior distribution $\pi(\theta|\mathbf{Y})$ were considered as input to the forward problem in order to guarantee mean square convergence.

Figures 5.5 to 5.7 show the results of this uncertainty propagation. They graphically compare the 95% credibility interval of the calibrated 5PFDM models and the experimental master curves. It is possible to note that the credibility intervals were initially large, but they decreased with the increase of frequency. Furthermore, all calibrated models had a good agreement with the experimental data.

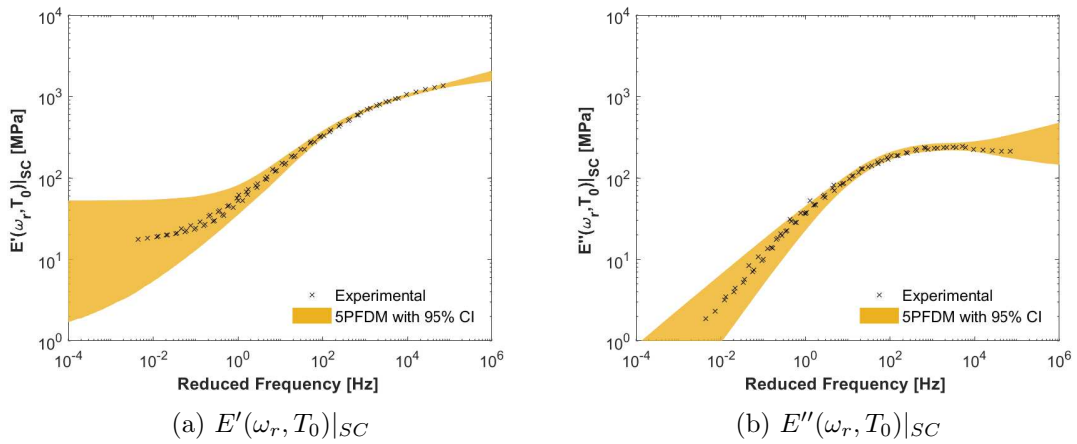


Figure 5.5: Uncertainty propagation when considering $\theta \sim \pi(\theta|\mathbf{Y})$ for the data-set of SC mode from TA machine.

5.3. RESULTS & DISCUSSION: IDENTIFICATION OF VISCOELASTIC PARAMETERS

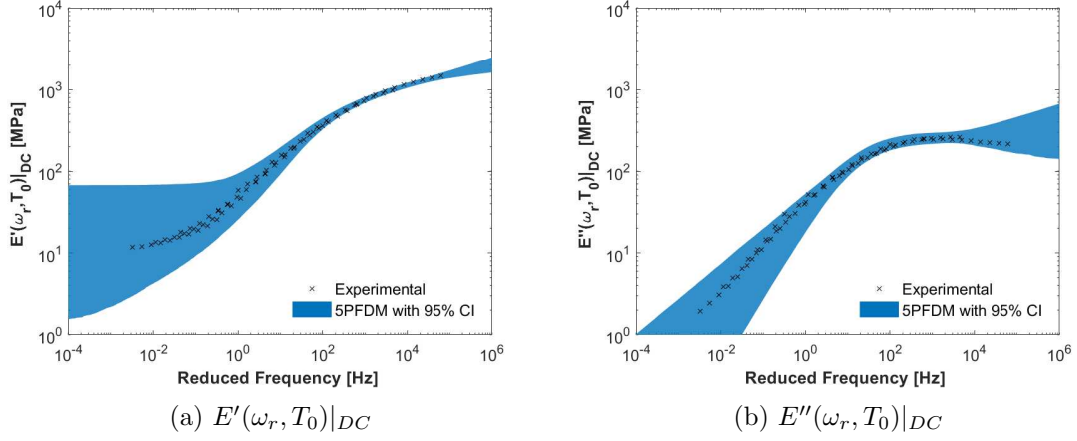


Figure 5.6: Uncertainty propagation when considering $\theta \sim \pi(\theta|\mathbf{Y})$ for the data-set of DC mode from TA machine.

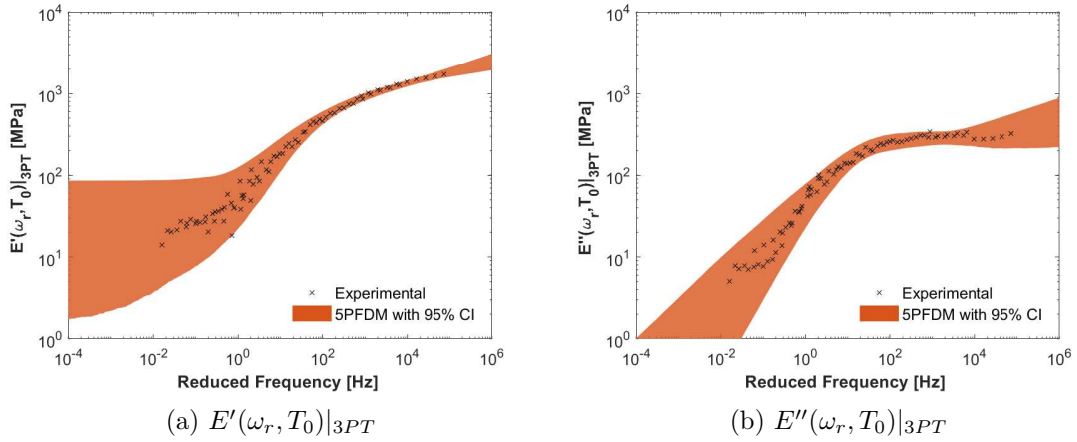


Figure 5.7: Uncertainty propagation when considering $\theta \sim \pi(\theta|\mathbf{Y})$ for the data-set of 3PT mode from TA machine.

To study the effects of operational modes on model predictions, Fig. 5.8 compares all three calibrated models obtained using measured data from SC, DC, and 3PT modes. It can be seen the 3PT mode had the highest uncertainties, especially at low frequencies. Additionally, the posterior mean value may differ between the tests. However, when considering the uncertainties related to the estimates, a good agreement can be found.

5.3. RESULTS & DISCUSSION: IDENTIFICATION OF VISCOELASTIC PARAMETERS

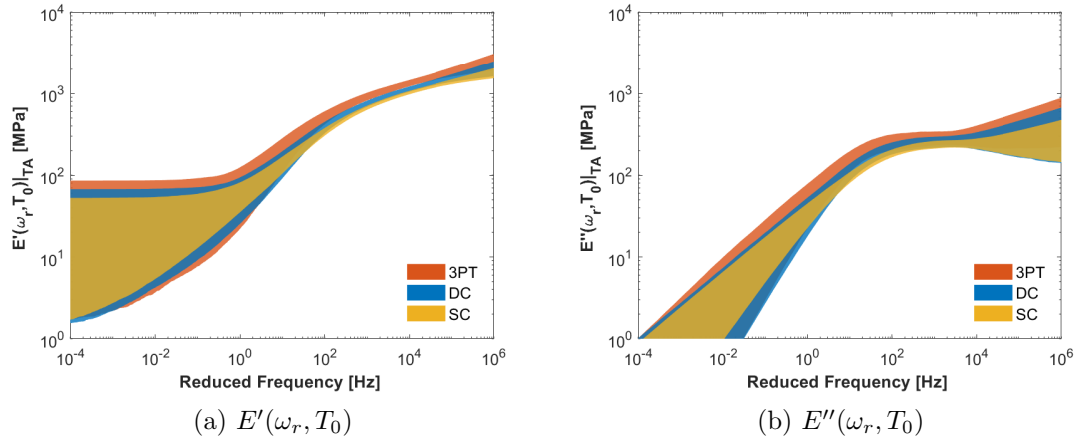


Figure 5.8: Comparison between the calibrated models from SC, DC, and 3PT modes of TA machine.

To analyze the effects of testing equipment on the predictions of material's behavior, Figs. 5.9 to 5.11 show all calibrated models for each operational mode tested in PE and TA machines. They graphically compare the 95% credibility intervals achieved. It can be observed that the highest uncertainties were associated with the models calibrated from the data-sets of the TA machine. A good agreement can be observed, however, in the low frequencies when taking into account the uncertainties.

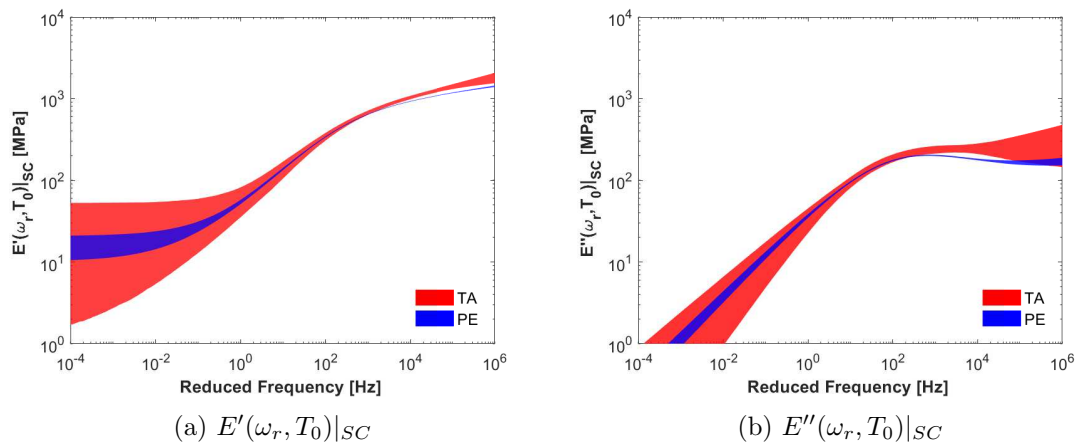


Figure 5.9: Comparison between the calibrated models from SC mode of TA and PE machines.

5.4. CONCLUSION

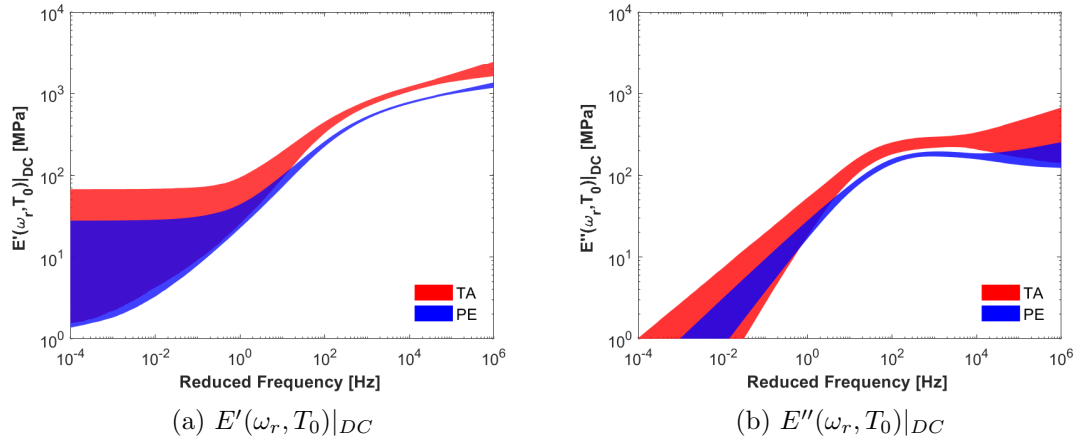


Figure 5.10: Comparison between the calibrated models from DC mode of TA and PE machines.

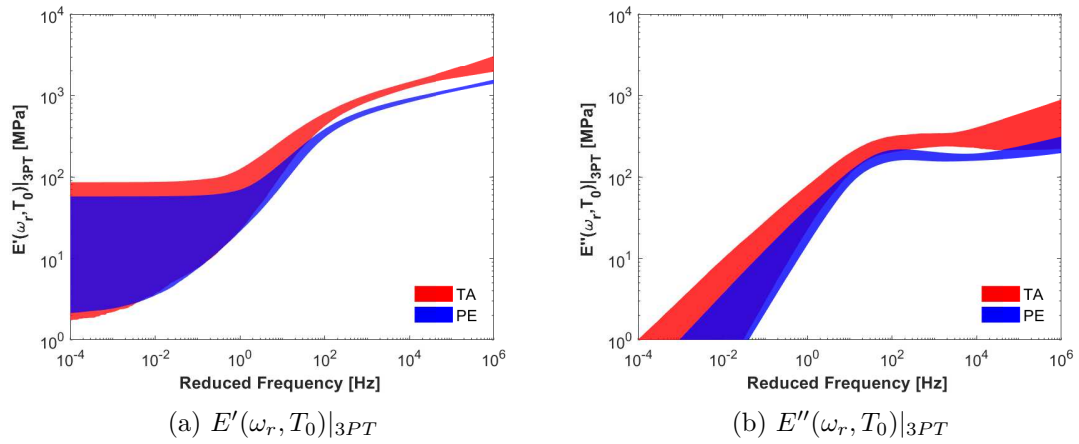


Figure 5.11: Comparison between the calibrated models from 3PT mode of TA and PE machines.

5.4 Conclusion

This chapter presented the calibration of fractional derivative models to describe the viscoelastic behavior identified by the different flexural tests of DMA. The main goal was to assess the impacts of different data-sets in the model's predictions, taking into account the uncertainties related to the measurements and model assumptions.

The results evidenced that operational modes and testing equipment can indeed influence the estimated parameters in different amounts. Consequently, numerical predictions performed from them are also affected, leading to divergences between model and reality. However, the effects of these un-

5.4. CONCLUSION

knowns can be minimized and better understood when considering the uncertainties on the parameter estimation.

After performing the uncertainty propagation on the forward problem, the predictions provided by the different sets of parameters displayed good agreement to experiments. It reaffirmed the robustness of the method to acquire the system's parameters, highlighting the importance of taking into account the uncertainties in parameter estimation to have better predictions of the material's behavior.

Part III

Poro-viscoelastic Materials

Introduction

Over the past few years, porous materials have been widely used for noise and vibration control in several applications such as civil, aerospace, and automotive industries. Their energy dissipation mechanisms have been proved useful for sound absorption and damping purposes. Thus, the characterization and modeling of their material properties are essential for predictive analyses of their acoustics and mechanical behavior.

Generally speaking, porous materials are composed of a matrix and a porous space filled by fluid, usually air. Their behavior depends on the composition of both phases in addition to the fluid-structure interactions that may happen [110, 111]. Nevertheless, depending on the conditions they are subjected to, only one material phase is relevant. For example, the fluid-phase of polymeric foams usually has a negligible role either under vacuum conditions or in the low-frequency range [85, 112–117].

Different approaches can be found in literature to describe their behavior such as Biot theory [118–120], equivalent fluid representation and equivalent solid description [121–123]. Each one with its own hypotheses, models, numerical and analytical methods of solution, and challenges. For instance, when the hypothesis of solid viscoelastic material is adopted, it is quite common to use fractional models to describe their properties as a function of frequency [1, 124–128].

From an experimental point of view, many efforts have been made to develop and improve measurement methods to assess their characteristics in the last years. Jaouen et al. [124] reviewed some techniques concerned with the characterization of elastic and damping features, classifying them as quasi-static or dynamic methods. Egab et al. [129] analyzed experimental techniques related to the identification of physical properties such as porosity, while also performing an investigation on the existing modeling theories. Recently, Bonfiglio et al. [98] examined some methods regarding the viscoelastic properties of poroelastic media used in vibroacoustic applications.

Efforts have also been made to characterize these materials by inverse methods. Since direct measurement of all material properties often requires different testing equipment, it could be troublesome in some sense to rely on them. In this context, Renault et al. [130] proposed an approach to inverse estimate the elastic properties from beam bending vibrations. Chazot et al. [28] proposed a method to extract the elastic and acoustical parameters from standing wave tube tests. Bonfiglio and Pompoli [131] reviewed some inverse techniques to estimate physical properties from acoustical tests, to mention a few.

Bearing all this in mind, the third part of this thesis aims to explore the damping performance of some porous materials, in particular an open-cell foam, a closed-cell foam and a granular material, through the viscoelasticity inherent in their matrices. It is divided into two chapters.

The first chapter aims to examine the mechanical energy dissipation of two polymeric foams when subjected to cyclic loads (study I) and structural vibrations (study II) from fractional derivative models calibrated using experimental data of a torsional rheometer. Initially, an approach to numerically predict their behavior in cyclic loads is proposed. The effects of the loading rate and temperature are investigated. Then, the capacity of these materials to damp structural vibrations is analyzed. Finally, a finite element model considering only the viscoelasticity of the matrix is proposed and validated. The influences of geometry and mechanical properties are studied.

The second chapter proposes a strategy to inverse characterize the viscoelastic properties of porous materials through the Bayesian approach. More specifically, it aims to calibrate and validate fractional derivative models for the complex shear modulus. Initially, the method is applied and validated for a polymeric foam previously studied in the first chapter. Then, it is used to characterize a granular material that, to the author's best knowledge, has not yet been modeled in the literature.

Objectives of Part III

To sum up, the main goals of the third part of this thesis concerning porous materials are:

- evaluate the mechanical energy dissipation through viscoelastic properties;
- propose an approach to predict the response of polymeric foams to cyclic loads;
- develop and validate a finite element model considering only the viscoelasticity of the matrix whose properties are described by a fractional derivative model;

-
- propose a numerical-experimental method to calibrate and validate viscoelastic models for porous materials, relying on the Bayesian framework.

Chapter 6

Damping performance of polymeric foams in the low-frequency range

This chapter analyses the dissipation of mechanical energy of two polymeric foams with different viscoelastic behavior in both time and frequency domains. The goal is to relate viscoelastic properties measured through a torsional rheometer with their damping performance in the low-frequency dynamic applications. In this way, it could help designing damping solutions based on foams. For instance, the time-domain response of foams to loading-unloading cycles is of interest when studying shock and vibration isolation during shipping and transportation in packaging applications. The frequency-domain response, in turn, is of interest when investigating the potential use of foam layers as passive damping of structures.

It should be highlighted that both studies here described neglected the air-skeleton interactions since they were carried out in the low-frequency range. As a result, the investigated foams were considered as monophasic viscoelastic solids with frequency-dependent properties. From a physical point of view, in closed-cell foams, the pressure caused by the presence of air in the pores contributes to the material's stiffness. In open-cell foams, on the other hand, the air can escape when the material is under loading conditions. However, the airflow does not have a great influence when the material is subjected to quasi-static conditions or excited in the low-frequency range [11]. Furthermore, the intrinsic mechanical dissipation related to the viscoelastic solid skeleton has been pointed out to play a major role in the analyzed low-frequency range [122].

It is organized as follows. First, Section 6.1 provides a complete description of the polymeric foam materials herein investigated. Then, Section 6.2 presents the investigation on the mechanical energy dissipation when these materials are subjected to cyclic loads in the time domain (Henriques et al. [1]). Afterward, Section 6.3 focuses on the study of their damping performance when they are subjected to structural vibrations in the low-frequency range (Henriques et al. [128]). Finally, Section 6.4 summarizes the main contributions.

Content

| | | |
|------------|--|------------|
| 6.1 | Description of tested materials | 177 |
| 6.2 | Study I: cyclic loads | 178 |

| | | |
|------------|---|------------|
| 6.2.1 | Description of numerical cases | 179 |
| 6.2.2 | Results & discussion of case 1: loading rates | 179 |
| 6.2.3 | Results & discussion of case 2: temperature | 182 |
| 6.3 | Study II: simply supported panels | 184 |
| 6.3.1 | Experiments | 185 |
| 6.3.2 | Finite element formulation | 193 |
| 6.3.3 | Numerical implementation and mesh convergence | 198 |
| 6.3.4 | Model validation & discussion | 200 |
| 6.3.5 | Parametric study | 208 |
| 6.3.6 | Limitations of the model | 213 |
| 6.4 | Conclusion | 215 |

6.1 Description of tested materials

In this chapter, two different polymeric foams were investigated aiming at exploring the variety of porous materials commonly employed on the passive control of noise and vibration. One of them was made of melamine resin, a thermosetting polymer, having open cells (hereinafter referred to as foam A), and the other was made of polyurethane, also a thermosetting polymer, having closed cells (hereinafter referred to as foam B). Both foams were air-saturated materials being highly porous and soft such that inertial, elastic, and viscous coupling effects were weaker.

Figure 6.1 shows optical microscope images of their cell structures. Foam A has a very filigree structure with very small cells and thin cell walls in white. Foam B, on the other hand, has closed cells with solid membranes; it is possible to observe some of these cells open as a consequence of the cross-sectional cut. Additionally, both foams exhibit uniformly distributed cells.

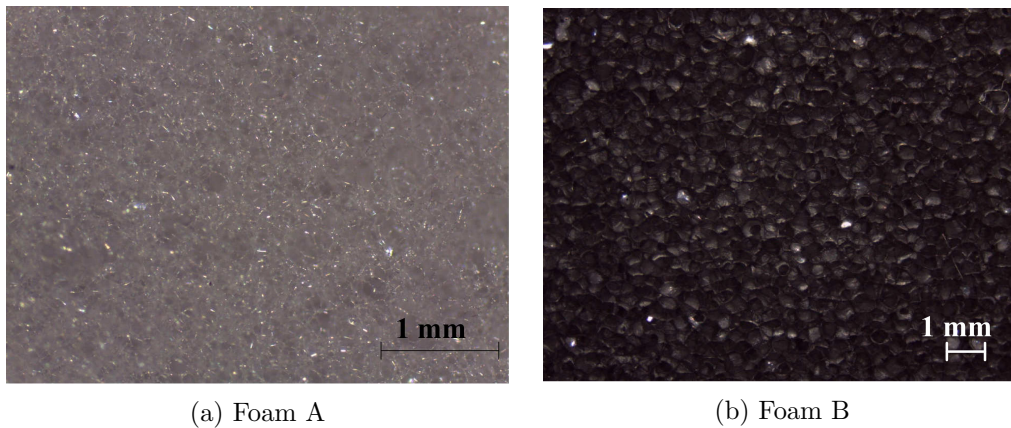


Figure 6.1: Optical microscope images of the cell structure of the two different foam materials.

These foams were industrially produced and their manufacturing processes are not known. Nevertheless, they were part of the five porous materials characterized in an interlaboratory campaign of Bonfiglio et al. [98] on the dynamic elastic properties of poroelastic media. From the measurement results presented therein, these two particular foams can be modeled as homogeneous and almost isotropic with a constant and real-valued Poisson's ratio. As a consequence, all foam's mechanical moduli had the same frequency dependence. This feature of foams has also been evidenced in previous experimental works such as Mariez et al. [132], Jaouen et al. [124] and Etchessahar et al. [116].

Table 6.1 presents the nomenclature adopted as well as selected properties for the development of

6.2. STUDY I: CYCLIC LOADS

this work, whereby the foams are sorted by density. Cell type, Poisson's ratio ν and density ρ were extracted from the work of Bonfiglio et al. [98]. It should be highlighted that the value of Poisson's ratio is a representative one chosen from the experimental results presented in [98]. The values for the densities ρ 's were verified (see Appendix C for details). The glass transition temperature T_g was determined by a differential scanning calorimetry (DSC) following the standard DIN EN ISO 11357-2:2014-07 (see Appendix D for details).

Table 6.1: Description of tested materials, where ν is the Poisson's ratio, ρ is the nominal density and T_g is the glass transition.

| Foam | Material base | Cell type | ν | ρ [kg/m ³] | T_g [°C] |
|-------------|----------------------|------------------|-------|-----------------------------|------------|
| A | melamine | open | 0.30 | 10 | n/a |
| B | polyurethane | closed | 0.35 | 48 | -35.5 |

Moreover, Henriques et al. [1] have recently characterized and modeled their complex shear modulus $G^*(\omega)$. They first performed dynamic tests in a torsional rheometer at different temperatures and frequencies. Then, they calibrated a four-parameter fractional derivative model for each foam material considering a reference temperature of 20 °C. Table 6.2 shows the four parameters estimated therein whose values were considered in this work.

Table 6.2: Fractional derivative model parameters of tested materials, where G_0 is the relaxed shear modulus, G_∞ is the unrelaxed shear modulus, τ is the relaxation time and α is the order of fractional derivative.

| Foam | G_0 [Pa] | G_∞ [Pa] | τ [s] | α |
|-------------|--------------------|--------------------|-----------------------|----------|
| A | 4.79×10^4 | 8.63×10^4 | 1.32×10^{-1} | 0.43 |
| B | 1.31×10^4 | 2.11×10^6 | 4.70×10^{-8} | 0.30 |

6.2 Study I: cyclic loads

In Study I, the dissipation of mechanical energy of two polymeric foams was numerically investigated in the time domain. Firstly, a one-dimensional cyclic loading was prescribed to the material. Then, the constitutive equation adopted to describe the viscoelastic behavior was numerically integrated, obtaining the material's response. Finally, hysteresis curves were obtained to quantify the amount of energy lost. The simulations were carried out considering different loading rates and dif-

ferent temperatures.

6.2.1 Description of numerical cases

One of the phenomena observed in viscoelastic materials is a hysteresis in a stress-strain curve when a cyclic loading is applied, as explained in Section 2.1 of Chapter 2. The amount of dissipated energy during a loading-unloading cycle may even vary according to loading rate and temperature [8, 11].

Aiming at determining the time domain behavior of these materials when prescribing a loading-unloading stress history $\sigma(t)$, two numerical cases were carried out considering one-dimensional transient analyses. The first case consisted of evaluating the effects of the loading rate on the material's response, while the second one consisted of assessing the impacts of the temperature.

Both analyses assumed the polymeric foams as isotropic homogeneous viscoelastic materials. Their mechanical behavior was described using the four-parameter fractional derivative model calibrated by Henriques et al. [1], as introduced in Section 6.1. Therefore, the one-dimensional relationship between their stress $\sigma(t)$ and strain $\varepsilon(t)$ in the time domain was given by

$$\sigma(t) + \tau^\alpha \frac{d^\alpha \sigma(t)}{dt^\alpha} = G_0 \varepsilon(t) + G_\infty \tau^\alpha \frac{d^\alpha \varepsilon(t)}{dt^\alpha}, \quad (6.1)$$

whose model parameters $\{G_0, G_\infty, \tau, \alpha\}$ are presented in Tab. 6.2 for each foam material considering a reference temperature of 20 °C. Nevertheless, these model parameters can be assessed at any desired temperature as the investigate materials presented thermo-rheological simple behavior [1].

Since Eq. 6.1 does not have an analytical solution, the numerical approach based on triangular strip matrices proposed by Podlubny [133] was implemented in MATLAB[®] software to solve the numerical cases (see Appendix A for further details). The reader is referred to Podlubny [133] and Podlubny et al. [134] for additional details.

6.2.2 Results & discussion of case 1: loading rates

Figure 6.2 shows the two prescribed stress histories applied to the materials to analyze the effects of loading rates considering a reference temperature of 20 °C. For both situations, three linear loading-unloading cycles (sawtooth behavior) were performed in a way that both excitation frequency and

6.2. STUDY I: CYCLIC LOADS

maximum stress level successively increased. The complete first loading-unloading cycle takes 0.5 s ($\times 10^{-3}$) with a maximum stress level of 1 Pa . The second one, in turn, takes 1.0 s ($\times 10^{-3}$) with a maximum level of 2 Pa . The third cycle, finally, takes 1.5 s ($\times 10^{-3}$) with a maximum level of 3 Pa . Note that the difference between these two stress histories relied on the very distinct time scales, about 10^0 s in the first case and 10^{-3} s in the second one.

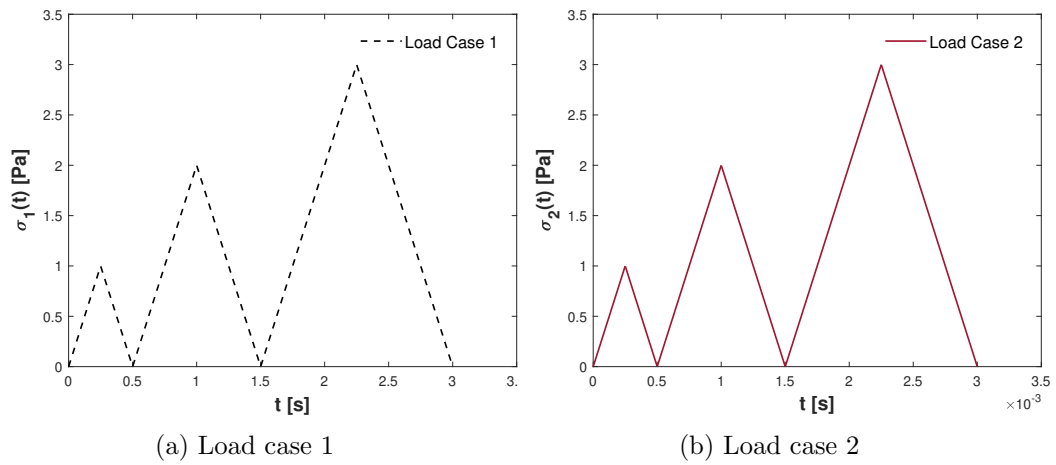


Figure 6.2: Prescribed stress histories $\sigma_1(t)$ and $\sigma_2(t)$ for the study of rate effects in hysteresis cycles.

Figure 6.3 shows the strain responses given by each foam for both loading cases. They were obtained by integrating the constitutive equation expressed in Eq. 6.1 through the algorithm proposed by Podlubny [133].

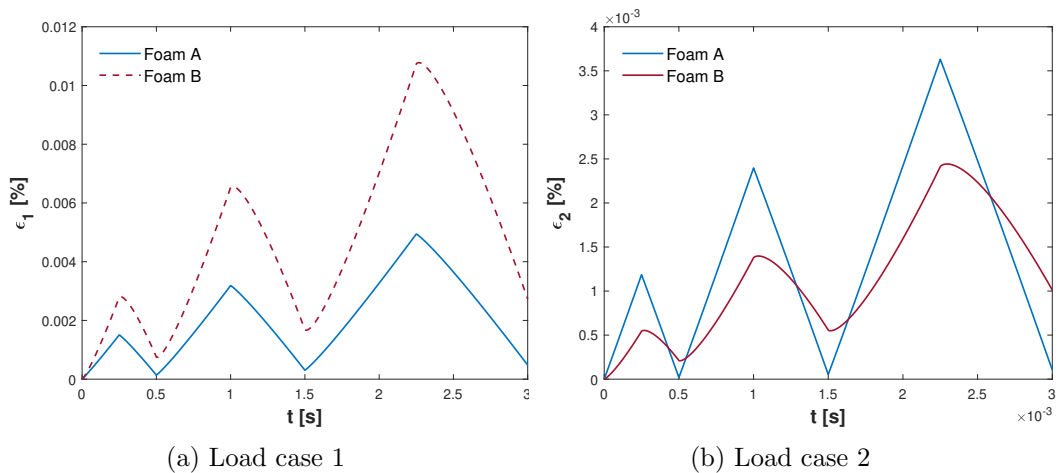


Figure 6.3: Strain responses obtained for each scenario at $20\text{ }^\circ\text{C}$.

6.2. STUDY I: CYCLIC LOADS

In both scenarios, foam A showed a behavior very close to elastic. It deformed almost linearly during loading and returned almost completely to its original shape also linearly during unloading, especially for load case 2. Foam B, in turn, showed a dissipative behavior. It deformed during loading, but it was not able to return to its original shape after each unloading; it retained some of the strain.

Figure 6.4 shows the stress-strain curves obtained for the two load cases. It is possible to observe hysteresis loops in all scenarios and also, a permanent strain at the end of each cycle. This is even more evident for foam B.

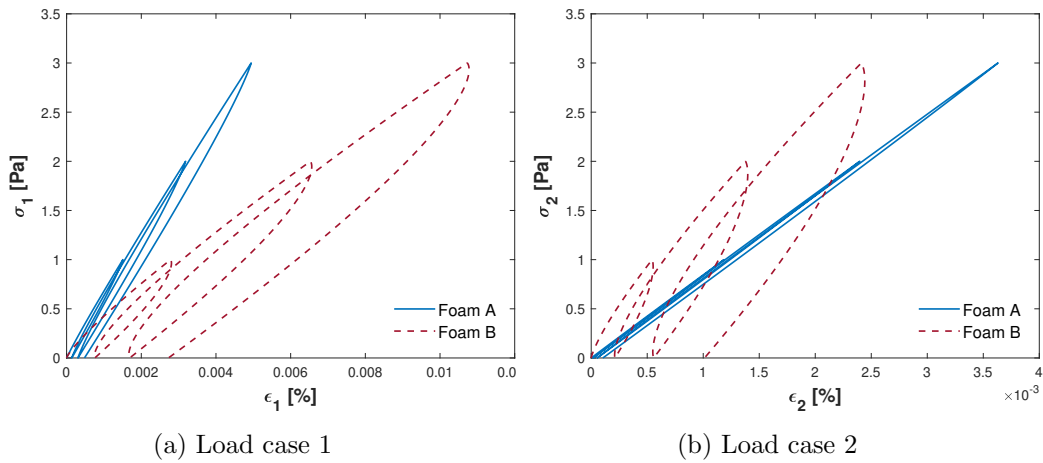


Figure 6.4: Stress-strain responses obtained for each scenario at 20 °C.

Furthermore, for the first load case, foam A required more force to achieve the same amount of strain than foam B. For the second load case, on the other hand, foam A deformed more easily. This comparison supports the idea that foam B has more energy dissipation capacity than foam A. These results are consistent with the strong viscoelastic behavior identified for foam B by Henriques et al. [1].

Finally, Fig. 6.5 compares the effects of loading rate for each foam. The dissipation of mechanical energy is indeed dependent upon the stress applied and its rate for both foams. The higher the maximum stress level, the greater the percentage of dissipation per cycle. Additionally, they all exhibit a lower energy loss in the second load case whose stress rate was 10^3 times higher than the first case. This means that aspects of elastic behavior were more predominant than the viscous ones, especially for foam A.

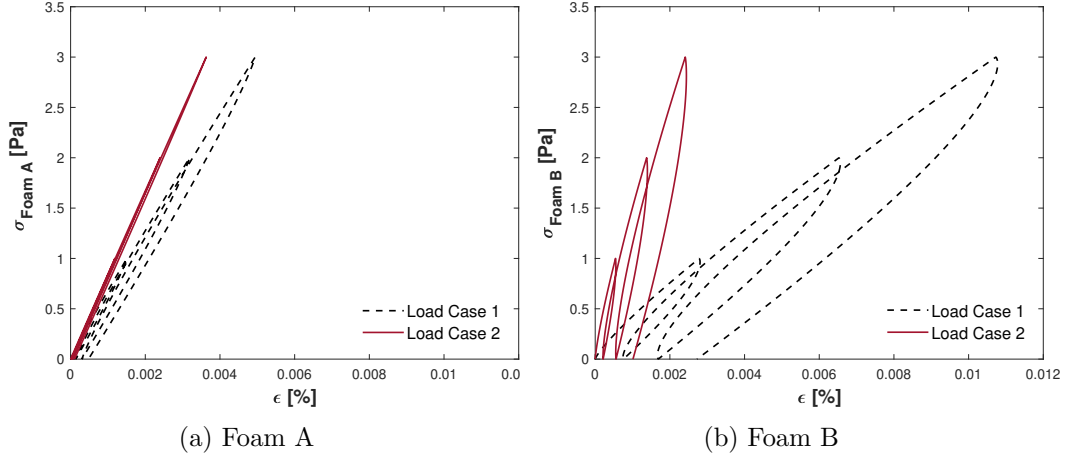


Figure 6.5: Comparison between the stress-strain responses of load cases 1 and 2 at 20 °C.

6.2.3 Results & discussion of case 2: temperature

As the investigated materials present thermo-rheological simple behavior, the influence of temperature can be taken into account through the horizontal $a_T(T, T_0)$ and vertical $b_T(T, T_0)$ shift factors from the time-temperature superposition principle. This is because the complex shear modulus $G^*(\omega)$ can be predicted for any temperature once models for these factors have been previously calibrated.

Figure 6.6 shows the prescribed stress history $\sigma_3(t)$ applied to the materials to assess the effects of temperature. Only one cycle of loading-unloading was considered with a time scale of the order of 10^0 s. Moreover, the complete loading-unloading cycle takes 2.5 s with a maximum stress level of 5 Pa.

The strain responses were thus estimated by combining the WLF model (see Eq. 2.44) of the horizontal shift factor $a_T(T, T_0)$ calibrated by Henriques et al. [1] and the constitutive equation shown in Eq. 6.1. Table 6.3 recalls the empirical constants C_1 and C_2 found therein for each foam material, which were needed to estimate $a_T(T, T_0)$ and consequently, the complex shear modulus $G^*(\omega)$ and the corresponding model parameters $\{G_0, G_\infty, \tau, \alpha\}$ at the desired temperature.

Figure 6.7 shows the responses obtained at four temperatures $T = \{-10\text{ °C}, 0\text{ °C}, 10\text{ °C}, 20\text{ °C}\}$. It can be seen that the strain increased with the increase in temperature. For example, the maximum deformation found was 0.0060 (resp. 0.0018) at -10 °C and 0.0083 (resp. 0.0185) at 20 °C for foam A (resp. foam B). These features can be related to molecular motion of polymer chains: as temperature increases, the mobility of the chains increases, which means that the material can deform more easily.

6.2. STUDY I: CYCLIC LOADS

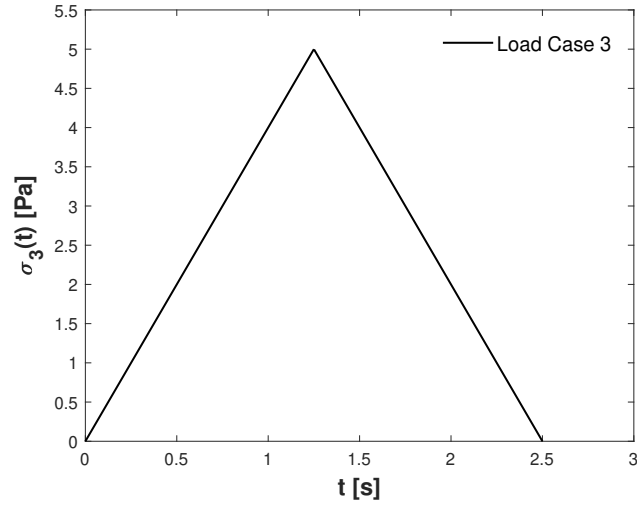


Figure 6.6: Prescribed stress history $\sigma_3(t)$ for the study of temperature effects in hysteresis cycles.

Table 6.3: Empirical constants of WLF model extracted from the work of Henriques et al. [1].

| Foam | C_1 | C_2 [K] |
|------|-------|-----------|
| A | 9.80 | 115.08 |
| B | 17.99 | 153.03 |

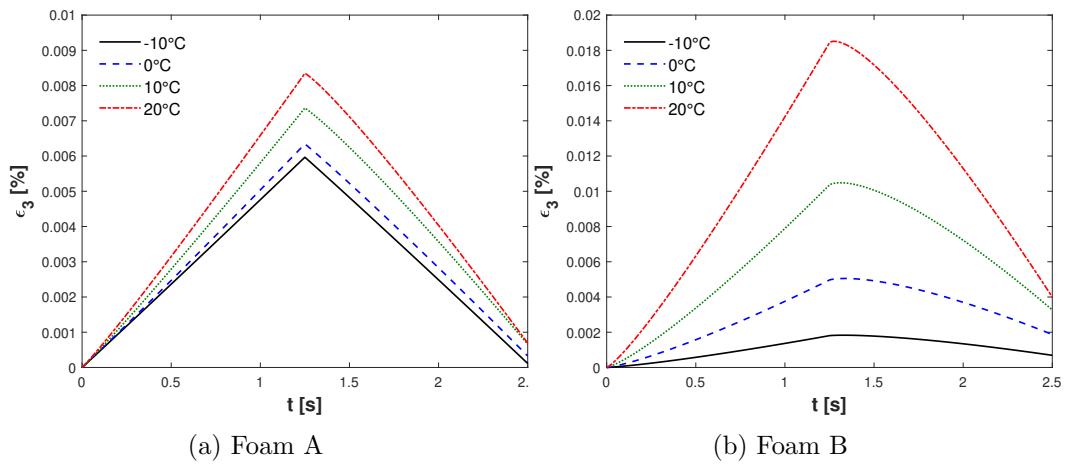


Figure 6.7: Strain responses obtained for load case 3.

Figure 6.8 compares the stress-strain curves obtained for each temperature. For both materials, the energy loss increased significantly by varying the temperature from -10°C to 20°C : the dissipation

6.3. STUDY II: SIMPLY SUPPORTED PANELS

increased almost 7 times for foam A and 4 times for foam B. As in load cases 1 and 2, foam B presents a better capacity to dissipate energy than foam A at all analyzed temperatures.

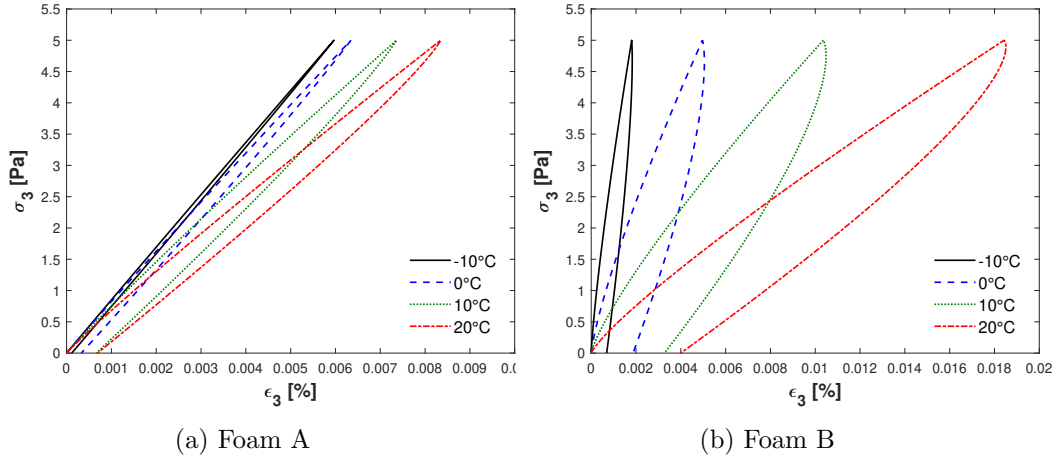


Figure 6.8: Comparison between stress-strain responses obtained for load case 3 for the study of temperature effects.

6.3 Study II: simply supported panels

In Study II, the damping behavior of the two polymeric foams was experimentally and numerically investigated in the frequency domain. The objectives of this work were twofold. The first goal was to experimentally study if the polymeric foams could be used as free-layer damping treatment to reduce structural vibrations significantly. The second one was to evaluate if the four-parameter fractional derivative model calibrated using measured data from a torsional rheometer [1] could be used on a FE model to predict damping effects with a relevant precision in the low-frequency range.

For these purposes, vibration tests were performed on simply supported panels mounted in two different structural configurations, as shown in Fig. 6.9, to better evaluate the impacts of the foam layers on the system dynamics. Then, finite element simulations were carried out considering only the viscoelasticity of the skeleton whose properties were previously characterized through torsion tests. Afterward, comparisons between the measured frequency response functions (FRFs) and those predicted from the simulations were done to assess the validity of the model assumptions. Finally, numerical analyses considering the sensitivity of the FRFs to the foams material parameters were performed.

6.3. STUDY II: SIMPLY SUPPORTED PANELS

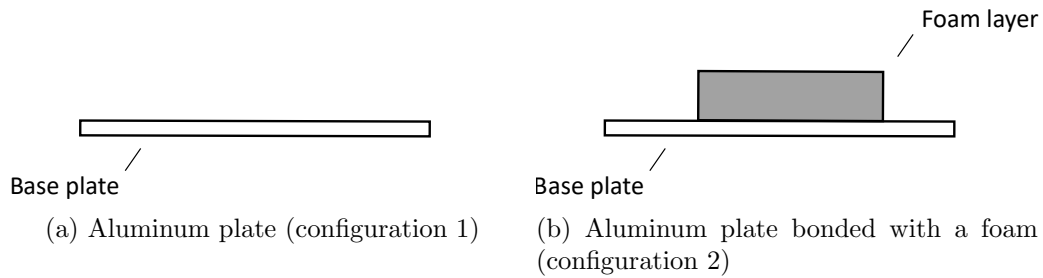


Figure 6.9: Configurations of simply supported panels for the study of vibration damping performance.

6.3.1 Experiments

This section describes the experimental set-up and discusses the corresponding measurement results. All the experiments were performed at Laboratoire de Mécanique des Structures et des Systèmes Couplés (LMSSC) of Cnam.

6.3.1.1 Description of testing equipment

The experimental rig chosen to measure the frequency response function (hereinafter referred to as FRF) for the two configurations under study is schematically shown in Fig. 6.10. It was composed of suspended panels mounted on a specific frame to approximate simply supported conditions [135], four accelerometers, an impact hammer, and a PC equipped with M+P VibPilot-E hardware and M+P Analyzer software for signal acquisition and export data. A description of each component is shown in Table 6.4. Furthermore, the post-processing was performed in MATLAB[®] software.

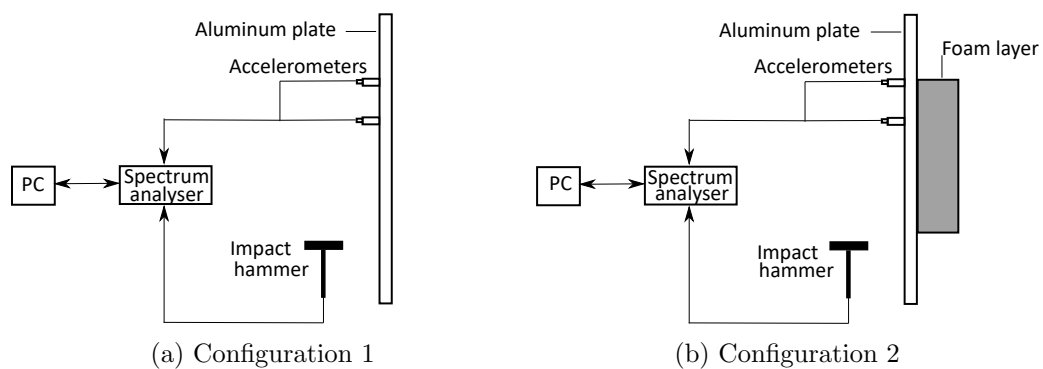


Figure 6.10: Schematic diagram of the experimental rig.

6.3. STUDY II: SIMPLY SUPPORTED PANELS

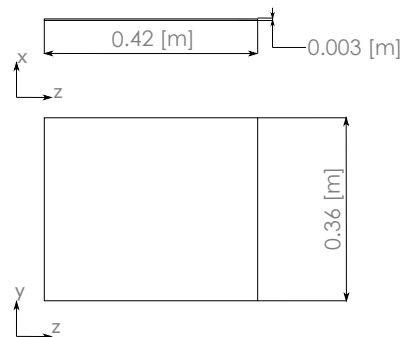
Table 6.4: Description of each component of the experimental rig.

| Equipment | Model | Serial | Sensitivity |
|-----------------|------------|----------|--------------|
| Impact Hammer | IH-02 | 611756 | 2.52 [mV/N] |
| Accelerometer 1 | PCB352C22 | LW214512 | 10.46 [mV/g] |
| Accelerometer 2 | PCB352C22 | LW214395 | 10.73 [mV/g] |
| Accelerometer 3 | PCB352C22 | LW214393 | 10.61 [mV/g] |
| Accelerometer 4 | PCB352C22 | LW214397 | 10.70 [mV/g] |
| M+P Hardware | VibPilot-E | B170105 | - |

The simply supported panel of configuration 1 consisted of a rectangular aluminum plate with dimensions $0.003 \text{ m} \times 0.360 \text{ m} \times 0.420 \text{ m}$ (see Fig. 6.11) mounted on a steel frame, following the description of assembly given by Robin et al. [135]. The panel of configuration 2, on the other hand, was obtained by gluing a free-layer of foam material with dimensions $0.025 \text{ m} \times 0.200 \text{ m} \times 0.200 \text{ m}$ centered on the back of the aluminum plate from configuration 1 (see Fig. 6.12). This bonding was done by a spray adhesive model Foam Fast 74 from 3M, which allowed to extend an approximately uniform layer without influencing the system's mass and stiffness. It is worth mentioning that each foam studied had its aluminum plate and steel frame to reduce experimental issues related to the gluing process and assembly. The layers of foam materials have been cut off from the same small-sized block of the material used in the work of Henriques et al. [1] to limit the potential effects of spatial heterogeneity and manufacturing process.



(a) Photograph of experimental configuration



(b) Schematic diagram

Figure 6.11: Simply supported panel mounted in configuration 1.

6.3. STUDY II: SIMPLY SUPPORTED PANELS

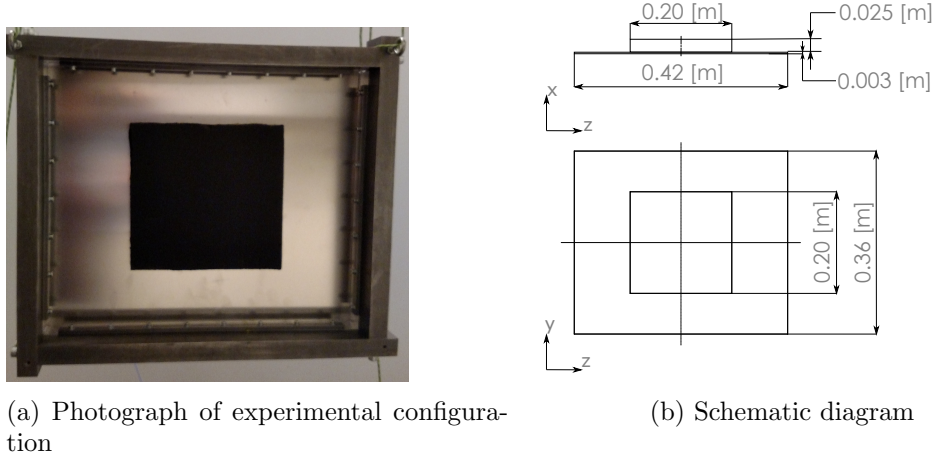


Figure 6.12: Simply supported panel mounted in configuration 2.

The impact hammer was used to apply a point force (hereinafter referred to as F) to excite the panel. The four accelerometers (hereinafter referred to as AC_i , where i denotes the corresponding number) were glued on the bare panel side through beeswax in different locations to measure the structure's response. Since each accelerometer weighted approximately 0.5 g , it was assumed to not affect the response of the panel. Both hammer and accelerometers were connected to M+P VibPilot-E hardware, which, in turn, was connected to a computer.

The positions of the force applied and the accelerometers are detailed on Tab. 6.5 and can be seen in Fig. 6.13.

Table 6.5: Locations of the applied force (F) and the four accelerometers (AC_i , where $i \in \{1, 2, 3, 4\}$) placed on the bare panel side to measure the structure's response.

| Coordinates | F | AC1 | AC2 | AC3 | AC4 |
|-------------|------|------|------|------|------|
| y [m] | 0.08 | 0.28 | 0.14 | 0.08 | 0.30 |
| z [m] | 0.08 | 0.08 | 0.18 | 0.34 | 0.32 |

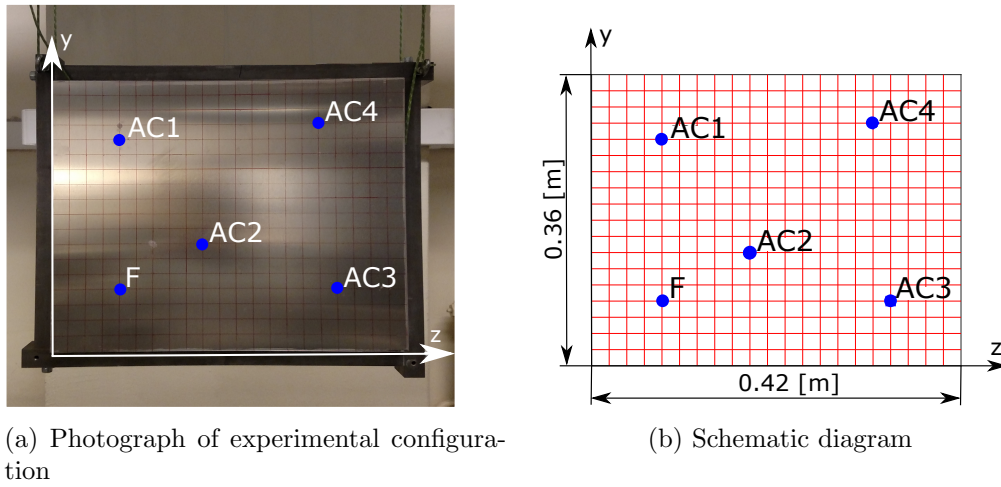


Figure 6.13: Locations of the applied force and the accelerometers placed on the bare panel side.

6.3.1.2 Test conditions

A SIMO (Single-Input, Multiple-Output) analysis was performed on each structural configuration aiming at evaluating how the free-layer of foam affects the system dynamics. Each structure was excited by a point force and the system’s response was measured by the four accelerometers simultaneously. The measurements were recorded up to 800 Hz, with a frequency resolution of 0.5 Hz, at ambient conditions (room temperature and in the presence of air). Each FRF was determined from the measured input and output based on averaging three measurements in the complex domain at each frequency.

It is important to highlight that each structure was tested ten times to verify the repeatability of the measurements and to perform statistical analysis. Hence, all experimental results are presented as the mean of these ten measurements together with the confidence interval of 95 %.

6.3.1.3 Results

Aiming at evaluating the damping performance of two polymeric foams, the frequency response functions (FRFs) of suspended panels mounted on a specific frame to approximate simply supported conditions were experimentally measured in the low-frequency range. For each foam analyzed, two configurations were assembled, as shown in Figs. 6.11 and 6.12.

Figure 6.14 compares all measured FRFs of configurations 1 and 2 of foam A. It is possible to

6.3. STUDY II: SIMPLY SUPPORTED PANELS

observe that both configurations presented almost similar behavior as the amplitude and resonant frequencies of the FRFs were nearly the same. That is, the addition of foam A on the aluminum plate did not change the structure's response significantly. Consequently, this foam is not attractive to damp structural vibrations. Furthermore, the repeatability of the tests performed in each configuration was quite good as the confidence intervals were very narrow.

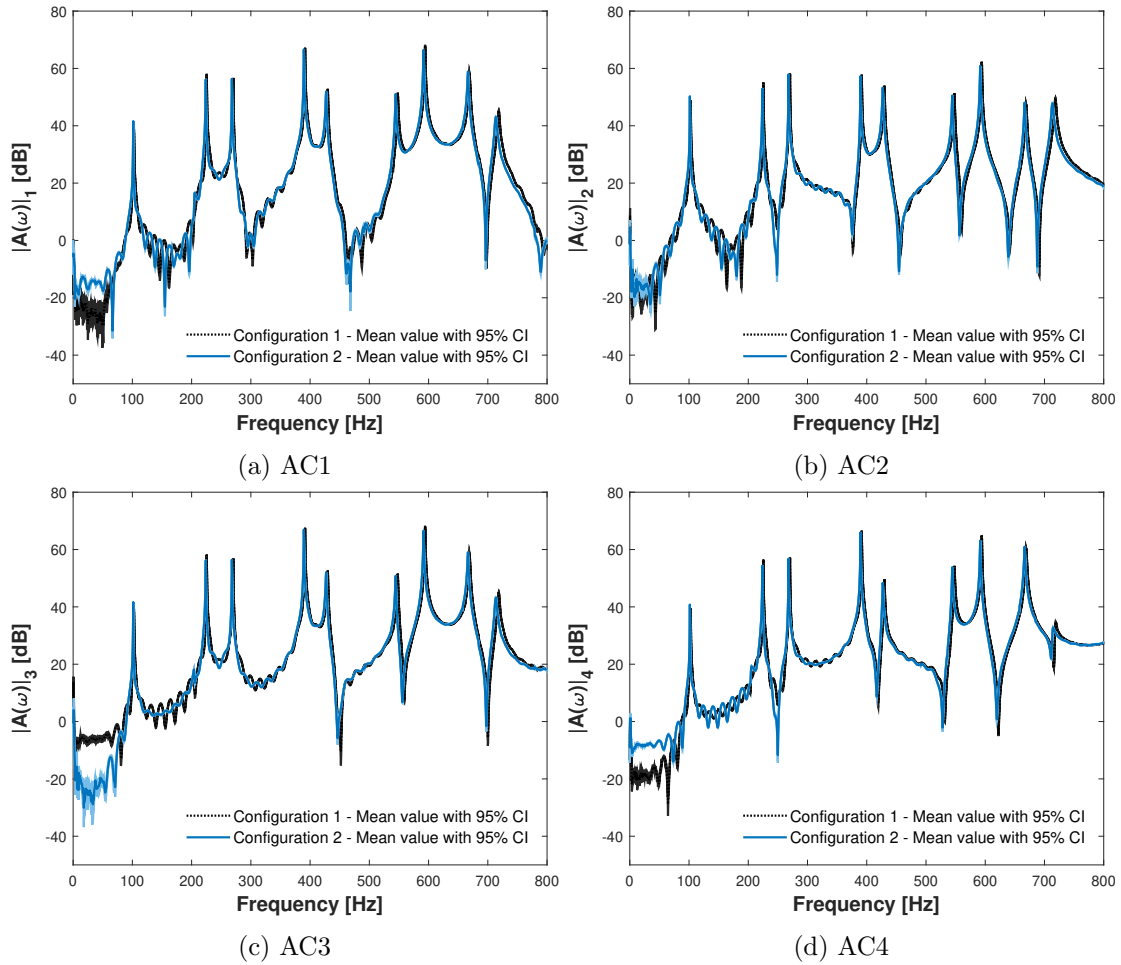


Figure 6.14: Comparisons between the measured FRFs of configurations 1 and 2 of foam A.

To quantify the effects of the addition of foam A on the structure, an experimental modal analysis (EMA) was carried out to extract the natural frequencies (f_n) and damping coefficients (ζ) of each structure tested. This modal parameter extraction was done in each measured FRF in the form of acceptance by an in-house program based on SDOF extraction techniques [136, 137]. Initially, the parameters f_n and ζ were assessed using a least-square solution as described in Brandt [137]. Then,

6.3. STUDY II: SIMPLY SUPPORTED PANELS

the parameters were estimated using the Circle-fit method [136] to validate the previous results.

Table 6.6 and 6.7, respectively, show the empirical mean of both natural frequencies (f_n) in Hz and damping coefficient (ζ) in %. As expected, the results of configurations 1 and 2 of foam A were quite similar, evidencing that this foam did not have much effect on the system's response.

Table 6.6: Comparison between the estimated natural frequencies (f_n) of configuration 1 and 2 of foam A.

| Configuration | 1 | 2 | 3 | 4 | 5 | 6 | 7 | 8 | 9 |
|---------------|--------|--------|--------|--------|--------|--------|--------|--------|--------|
| 1 [Hz] | 102.73 | 225.71 | 270.33 | 391.67 | 429.74 | 548.03 | 594.22 | 669.25 | 718.88 |
| 2 [Hz] | 101.41 | 223.80 | 268.14 | 389.62 | 427.05 | 544.42 | 591.55 | 666.51 | 714.09 |

Table 6.7: Comparison between the estimated damping coefficients (ζ) of configuration 1 and 2 of foam A.

| Configuration | 1 | 2 | 3 | 4 | 5 | 6 | 7 | 8 | 9 |
|---------------|------|------|------|------|------|------|------|------|------|
| 1 [%] | 0.07 | 0.02 | 0.05 | 0.05 | 0.13 | 0.11 | 0.05 | 0.13 | 0.23 |
| 2 [%] | 0.11 | 0.07 | 0.05 | 0.05 | 0.13 | 0.11 | 0.07 | 0.14 | 0.27 |

Figure 6.15 presents the results obtained of configurations 1 and 2 of foam B. It can be seen that the addition of foam B modified the responses via mass and damping. It decreased both resonant frequencies and magnitude of resonance peaks, while increased the width of the resonant peaks. These differences got more evident as frequency increased.

From the measurements obtained by AC1 shown in Fig. 6.15a, for example, the first peak in the FRFs of configurations 1 and 2 was, respectively, identified at 103 Hz and 99 Hz with magnitude of 42 dB and 35 dB, while the fifth peak was observed at 432 Hz and 420 Hz with corresponding amplitudes of 51 dB and 41 dB.

Therefore, foam B has the potential to be applied as a layer in damping treatments to reduce structural vibrations. An important point worth mentioning is that the addition of this foam did not significantly increase the mass of the structure, only about 5 %, which makes its application even more attractive. Furthermore, the repeatability of the tests performed in each configuration was quite good as the confidence intervals were narrow.

An experimental modal analysis was also performed on these structures to quantify the effects of

6.3. STUDY II: SIMPLY SUPPORTED PANELS

the addition of foam B on the system. The modal parameter extraction techniques were similar to those used in the analysis of the configurations of foam A.

Tables 6.8 and 6.9 present the results obtained in this stage. It can be seen that the impact of foam B was clear and significant: configuration 2 had lower natural frequencies and higher damping coefficients. These results reinforce the idea of using foam B to damp structural vibrations.

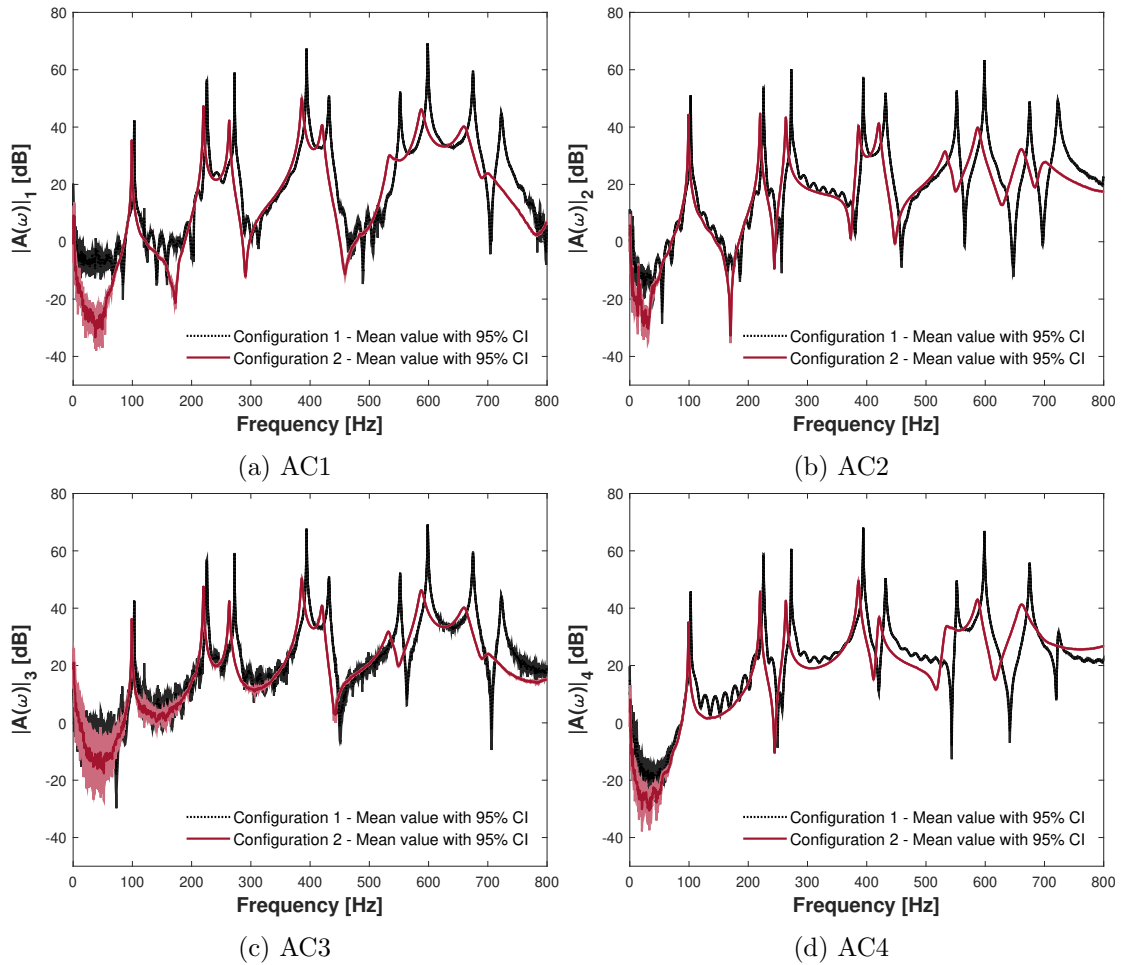


Figure 6.15: Comparisons between the measured FRFs of configurations 1 and 2 of foam B.

Table 6.8: Comparison between the estimated natural frequencies (f_n) of configuration 1 and 2 of foam B.

| Configuration | 1 | 2 | 3 | 4 | 5 | 6 | 7 | 8 | 9 |
|---------------|--------|--------|--------|--------|--------|--------|--------|--------|--------|
| 1 [Hz] | 103.44 | 225.75 | 272.58 | 394.16 | 431.81 | 552.02 | 598.67 | 674.98 | 723.33 |
| 2 [Hz] | 99.10 | 219.94 | 263.50 | 386.13 | 420.38 | 533.06 | 587.46 | 660.41 | |

6.3. STUDY II: SIMPLY SUPPORTED PANELS

Table 6.9: Comparison between the estimated damping coefficients (ζ) of configuration 1 and 2 of foam B.

| Configuration | 1 | 2 | 3 | 4 | 5 | 6 | 7 | 8 | 9 |
|---------------|------|------|------|------|------|------|------|------|------|
| 1 [%] | 0.08 | 0.03 | 0.03 | 0.04 | 0.14 | 0.13 | 0.05 | 0.11 | 0.22 |
| 2 [%] | 0.27 | 0.22 | 0.34 | 0.38 | 0.62 | 1.24 | 0.82 | 1.08 | 1.52 |

It is important to note that, even though different aluminum frames and plates were used to build each configuration 1, their responses were approximately the same as indicated by the results of the modal analysis performed on each one (see Tabs. 6.6 to 6.9). Figure 6.16 below also highlights the good reproducibility and repeatability of the tests. However, the small differences observed indicate that, for the numerical simulations, a model updating procedure should be conducted to find the properties that better describe the test conditions of each plate.

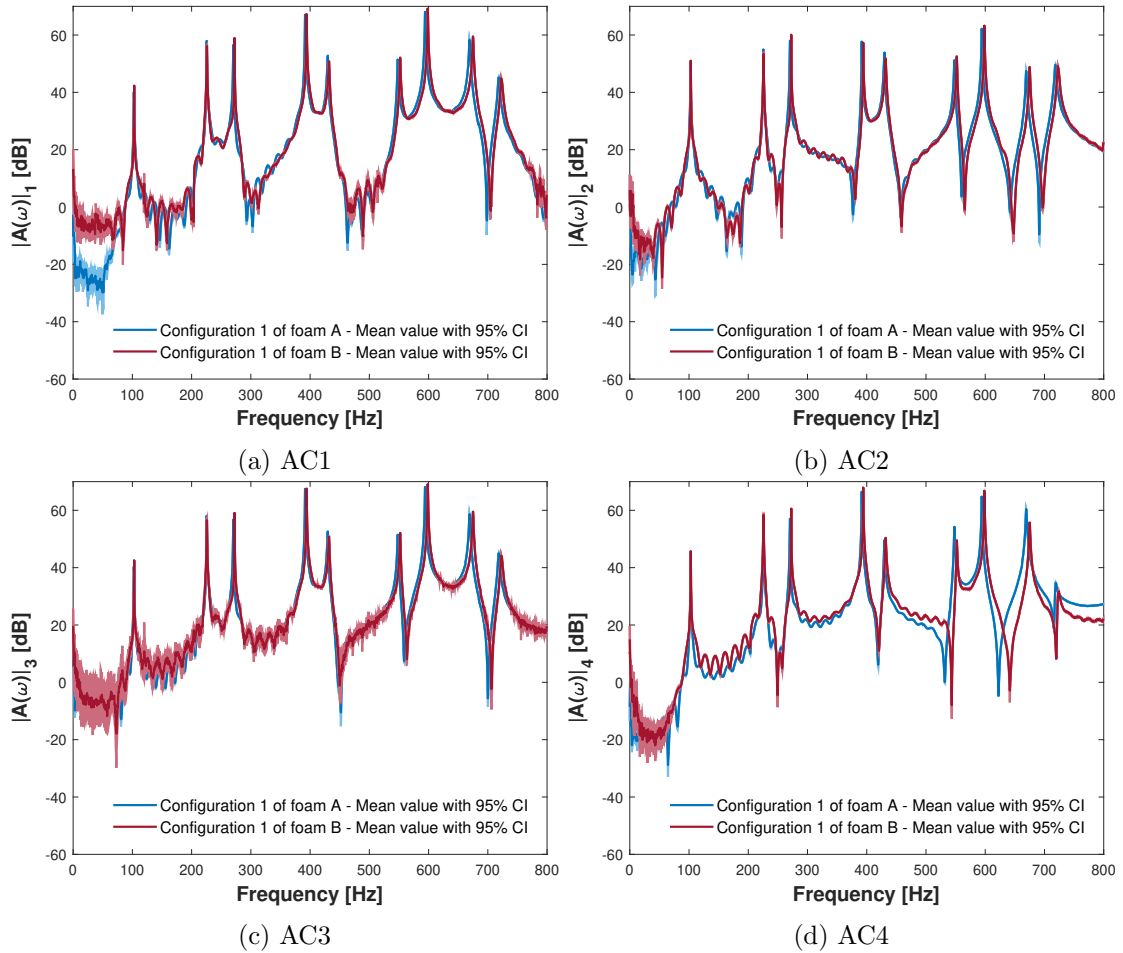


Figure 6.16: Comparisons between the measured FRFs of configurations 1.

6.3. STUDY II: SIMPLY SUPPORTED PANELS

As the main difference among the configurations 2 under analyses was indeed the type of foam material, one may conclude that foam B has a greater damping capacity than foam A from the results presented above. To further compare the performance of these two materials, the FRFs obtained for each one are traced in Fig. 6.17. One can observe that the width of the resonant peaks are wider and the amplitudes are smaller, especially after about 250 Hz. This agrees well with the results of Study I and the work of Henriques et al. [1].

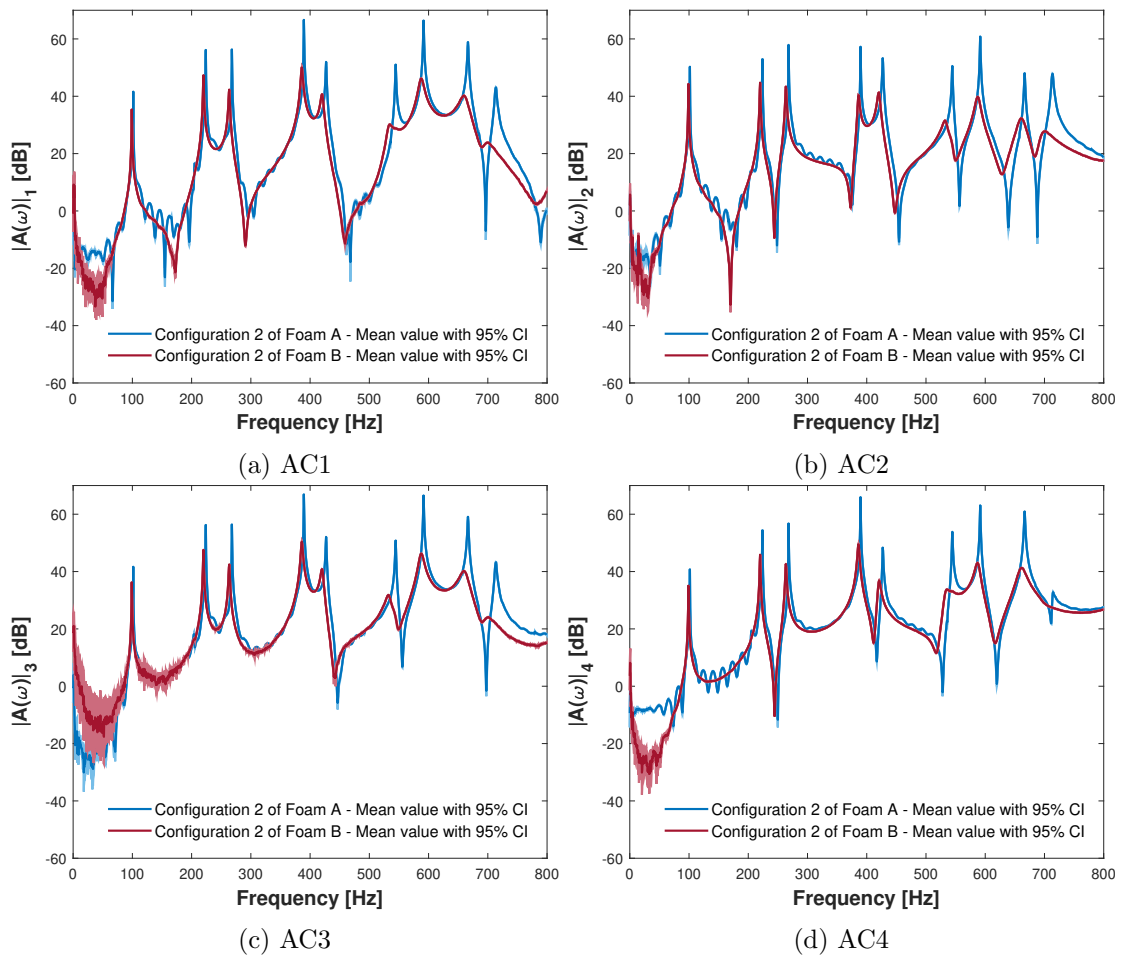


Figure 6.17: Comparisons between the measured FRFs of configurations 2 of foams A and B.

6.3.2 Finite element formulation

This section presents the finite element models adopted to solve the structural problems in the frequency domain.

6.3.2.1 Structural problem

Figure 6.18 shows the description and notations of a general structural problem. The solid structure occupies the domain denoted by Ω^S . It is described by the variable displacement \mathbf{u}^S . Moreover, its boundary is separated into contours of:

- imposed Dirichlet boundary condition: Γ_1^S
- prescribed Neumann boundary condition: Γ_2^S

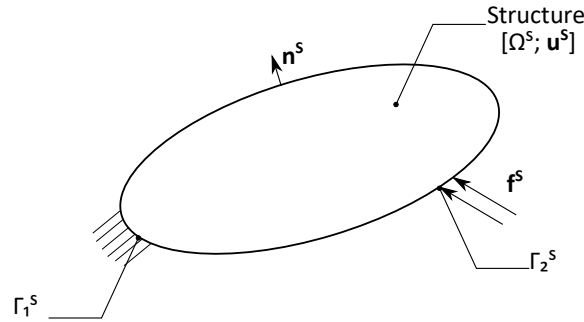


Figure 6.18: Description of the structural problem.

Next, the finite element formulation is presented considering a steady state time-harmonic response of the $e^{j\omega t}$.

6.3.2.2 Governing equation and boundary conditions

The structural domain is governed by the elastodynamic linearized equation at a angular frequency ω as follows

$$\nabla \cdot \boldsymbol{\sigma}^S + \rho_S \omega^2 \mathbf{u}^S = 0 \text{ in } \Omega^S, \quad (6.2)$$

where ρ_S is the structure mass density, \mathbf{u}^S denotes the displacement vector field and $\boldsymbol{\sigma}^S$ denotes the Cauchy stress tensor. Assuming Hooke's law and using Voigt notation, this stress tensor $\boldsymbol{\sigma}^S$ can be related to the strain tensor $\boldsymbol{\varepsilon}^S$ such as

$$\begin{bmatrix} \sigma_{11} \\ \sigma_{22} \\ \sigma_{33} \\ \sigma_{12} \\ \sigma_{13} \\ \sigma_{23} \end{bmatrix} = \begin{bmatrix} \lambda + 2\mu & \lambda & \lambda & 0 & 0 & 0 \\ \lambda & \lambda + 2\mu & \lambda & 0 & 0 & 0 \\ \lambda & \lambda & \lambda + 2\mu & 0 & 0 & 0 \\ 0 & 0 & 0 & \mu & 0 & 0 \\ 0 & 0 & 0 & 0 & \mu & 0 \\ 0 & 0 & 0 & 0 & 0 & \mu \end{bmatrix} \begin{bmatrix} \varepsilon_{11}^S \\ \varepsilon_{22}^S \\ \varepsilon_{33}^S \\ 2\varepsilon_{12}^S \\ 2\varepsilon_{13}^S \\ 2\varepsilon_{23}^S \end{bmatrix}, \quad (6.3)$$

where λ and μ are the Lamé coefficients, and the strain tensor $\boldsymbol{\varepsilon}^S$ is defined as

$$\boldsymbol{\varepsilon}^S = \frac{1}{2}[(\nabla \mathbf{u}^S) + (\nabla \mathbf{u}^S)^T]. \quad (6.4)$$

It is worth mentioning that, if the structure is composed of a viscoelastic material, Lamé coefficients are complex and frequency-dependent denoted by $\lambda^*(\omega)$ and $\mu^*(\omega)$. Consequently, both stress and strain tensors become complex and frequency-dependent such as $\boldsymbol{\sigma}^{S*}(\omega)$ and $\boldsymbol{\varepsilon}^{S*}(\omega)$ by means of Fourier transform.

Concerning the boundary conditions of this problem, a prescribed displacement \mathbf{u}_d is applied to the external boundary Γ_1^S of Ω^S and a prescribed harmonic force \mathbf{f}^S is applied to the external boundary Γ_2^S of Ω , respectively, given by

$$\begin{cases} \mathbf{u}^S = \mathbf{u}_d = 0 \text{ on } \Gamma_1^S \end{cases} \quad (6.5a)$$

$$\begin{cases} \boldsymbol{\sigma}^S \cdot \mathbf{n}^S = \mathbf{f}^S \text{ on } \Gamma_2^S. \end{cases} \quad (6.5b)$$

6.3.2.3 Variational formulation

The derivation of the variational formulation is done by means of the test-function method. Let $C_{\mathbf{u}^S}$ be the admissible space of regular functions \mathbf{u}^S in Ω^S . Let $\delta \mathbf{u}^S$ be a frequency-independent test function, associated with the displacement field \mathbf{u}^S , belonging to the admissible space $C_{\mathbf{u}^S}^* = \{\delta \mathbf{u}^S \in C_{\mathbf{u}^S} | \delta \mathbf{u}^S = \mathbf{0} \text{ in } \Gamma_1^S\}$. Multiplying Eq. 6.2 by $\delta \mathbf{u}^S \in C_{\mathbf{u}^S}^*$ and applying a Green's formula leads to

$$\int_{\Omega^S} (\nabla \cdot \boldsymbol{\sigma}^S) \cdot \delta \mathbf{u}^S d\Omega^S + \rho \omega^2 \int_{\Omega^S} \mathbf{u}^S \cdot \delta \mathbf{u}^S d\Omega^S - \int_{\Gamma_2^S} (\boldsymbol{\sigma}^S \cdot \mathbf{n}^S) \cdot \delta \mathbf{u}^S dS = \mathbf{0}, \quad \forall \delta \mathbf{u}^S \in C_{\mathbf{u}^S}^*. \quad (6.6)$$

Applying the conditions expressed in Eqs. 6.5a and 6.5b into Eq. 6.6, the final variational form reads

$$\int_{\Omega^S} \boldsymbol{\sigma}^S : \nabla(\delta \mathbf{u}^S) d\Omega^S - \rho_S \omega^2 \int_{\Omega^S} \mathbf{u}^S \cdot \delta \mathbf{u}^S d\Omega^S = \int_{\Gamma_1^S} \mathbf{f}^S \cdot \delta \mathbf{u}^S dS, \forall \delta \mathbf{u}^S \in C_{\mathbf{u}^S}^*. \quad (6.7)$$

6.3.2.4 Finite element discretization

Discretizing the structural domain Ω^S into n_e classical finite elements and interpolating the macroscopic field \mathbf{u}^S in terms of the nodal displacement variable \mathbf{U}^S yields, for the e^{th} element,

$$\mathbf{u}^{S^e} = \mathbb{N}_{\mathbf{u}^S}^e \mathbf{U}^{S^e}, \quad (6.8)$$

where $\mathbb{N}_{\mathbf{u}^S}^e$ is the corresponding shape function.

Equation 6.7 is then discretized by means of finite element method and the following matrix equation for a general structural problem is obtained

$$[\mathbb{K}^S - \omega^2 \mathbb{M}^S] \mathbf{U}^S(\omega) = \mathbf{F}^S(\omega), \quad (6.9)$$

where $\mathbf{U}^S(\omega)$ and $\mathbf{F}^S(\omega)$ are, respectively, the displacement and load vectors at angular frequency ω , and \mathbb{K}^S and \mathbb{M}^S are, respectively, the global stiffness and real mass matrices given by

$$\mathbb{K}^S = \sum_{k=1}^{N_e} \int_{\Omega^{S^e}} \mathbb{B}_{\mathbf{u}^S}^{eT} \mathbb{C} \mathbb{B}_{\mathbf{u}^S}^e d\Omega^{S^e} \quad (6.10a)$$

$$\mathbb{M}^S = \sum_{k=1}^{N_e} \int_{\Omega^{S^e}} \mathbb{N}_{\mathbf{u}^S}^{eT} \rho_S \mathbb{N}_{\mathbf{u}^S}^e d\Omega^{S^e}, \quad (6.10b)$$

where \mathbb{C} is the constitutive matrix of the material, $\mathbb{B}_{\mathbf{u}^S}^e = \mathbb{D}_{\mathbf{u}^S} \mathbb{N}_{\mathbf{u}^S}^e$ is the discrete gradient matrix and $\mathbb{D}_{\mathbf{u}^S}$ is the gradient operator defined by

$$\mathbb{D}_{\mathbf{u}^S} = \begin{bmatrix} \partial/\partial x & 0 & 0 \\ 0 & \partial/\partial y & 0 \\ 0 & 0 & \partial/\partial z \\ 0 & \partial/\partial z & \partial/\partial y \\ \partial/\partial z & 0 & \partial/\partial x \\ \partial/\partial y & \partial/\partial x & 0 \end{bmatrix}. \quad (6.11)$$

The first structural configuration consisted of a mono-layer panel made of aluminum as shown in Fig. 6.9a. The system was thus modeled under the hypothesis of homogeneous linear isotropic elastic

6.3. STUDY II: SIMPLY SUPPORTED PANELS

material with structural damping. In this sense, Eq. 6.9 becomes

$$[(1 + j\eta)\mathbb{K}_E - \omega^2\mathbb{M}_E]\mathbf{U}^S(\omega) = \mathbf{F}^S(\omega), \quad (6.12)$$

where \mathbb{K}_E and \mathbb{M}_E are, respectively, the stiffness and mass matrices related to the elastic component and η is its structural loss factor. Accordingly, the constitutive matrix \mathbb{C} was defined as

$$\mathbb{C} = \frac{E}{(1 - 2\nu)(1 + \nu)} \begin{bmatrix} (1 - \nu) & \nu & \nu & 0 & 0 & 0 \\ \nu & (1 - \nu) & \nu & 0 & 0 & 0 \\ \nu & \nu & (1 - \nu) & 0 & 0 & 0 \\ 0 & 0 & 0 & \frac{(1 - 2\nu)}{2} & 0 & 0 \\ 0 & 0 & 0 & 0 & \frac{(1 - 2\nu)}{2} & 0 \\ 0 & 0 & 0 & 0 & 0 & \frac{(1 - 2\nu)}{2} \end{bmatrix}. \quad (6.13)$$

The second configuration, in turn, was a two-layered panel made of aluminum and a foam material as shown in Fig 6.9b. It thus involved an elastic structure bonded to a homogeneous linear isotropic viscoelastic component whose properties were frequency-dependent. In this respect, Eq. 6.9 is then rewritten as follows

$$[\mathbb{K}_E + G^*(\omega)\mathbb{K}_V^0 - \omega^2(\mathbb{M}_E + \mathbb{M}_V)]\mathbf{U}^S(\omega) = \mathbf{F}^S(\omega), \quad (6.14)$$

where \mathbb{K}_V^0 is the stiffness matrix related to the viscoelastic component and computed for a unit shear modulus, \mathbb{M}_V is the mass matrix of the viscoelastic component, and $G^*(\omega)$ is the complex shear modulus of the viscoelastic material modeled herein by the four-parameter fractional derivative model (see subsection 2.5.1 of Chapter 2) shown in Eq. 6.15.

$$G^*(\omega) = \frac{G_0 + G_\infty(j\omega\tau)^\alpha}{1 + (j\omega\tau)^\alpha}, \quad (6.15)$$

where G_0 and G_∞ are, respectively, the relaxed and unrelaxed shear moduli, τ is the relaxation time and α is the order of the fractional derivative model.

It is worth noting that the hypotheses of isotropy and constant Poisson's ratio were also adopted for the foams as detailed in Section 6.1. In this way, all foam's mechanical moduli were independent of the direction and also had the same frequency dependence. For example, the complex modulus $E^*(\omega)$

can be estimated by the relationship between the Poisson's ratio and the complex shear modulus $G^*(\omega)$ such as

$$E^*(\omega) = 2(1 + \nu)G^*(\omega), \quad (6.16)$$

which leads to the following three-dimensional constitutive matrix

$$\mathbb{C}^*(\omega) = G^*(\omega) \begin{bmatrix} \frac{2(1-\nu)}{1-2\nu} & \frac{2\nu}{1-2\nu} & \frac{2\nu}{1-2\nu} & 0 & 0 & 0 \\ \frac{2\nu}{1-2\nu} & \frac{2(1-\nu)}{1-2\nu} & \frac{2\nu}{1-2\nu} & 0 & 0 & 0 \\ \frac{2\nu}{1-2\nu} & \frac{2\nu}{1-2\nu} & \frac{2(1-\nu)}{1-2\nu} & 0 & 0 & 0 \\ \frac{2\nu}{1-2\nu} & \frac{2\nu}{1-2\nu} & \frac{2(1-\nu)}{1-2\nu} & 0 & 0 & 0 \\ 0 & 0 & 0 & 1 & 0 & 0 \\ 0 & 0 & 0 & 0 & 1 & 0 \\ 0 & 0 & 0 & 0 & 0 & 1 \end{bmatrix}. \quad (6.17)$$

6.3.3 Numerical implementation and mesh convergence

An in-house program using GMSH [138] and MATLAB[®] software was developed to build the geometries and related meshes, and also to compute the frequency response functions (FRFs) through the direct or model reduction methods [139]. It is worth mentioning that the codes were validated from a comparative analysis with simulations performed with NASTRAN[®] software.

For both FE models, the structure was modeled with three-dimensional finite elements, more specifically the 20-node hexahedral element. This type of element has quadratic shape functions and allows the numerical models to show a good capacity of describing the important physical mechanisms [140].

The FE model of configuration 1, shown in Eq. 6.12, was first developed and validated. The following properties were considered for the aluminum plate: Young's modulus $E = 69$ GPa, Poisson's ratio $\nu = 0.35$, mass density $\rho = 2700$ kg/m³ and structural loss factor $\eta = 0.001$. Only one layer mesh in the thickness was generated and different element sizes were considered. Based on some numerical tests, the finite element mesh was set with 1512 elements and 32931 degrees of freedom as detailed in Tab. 6.10 and graphically illustrated in Fig. 6.19.

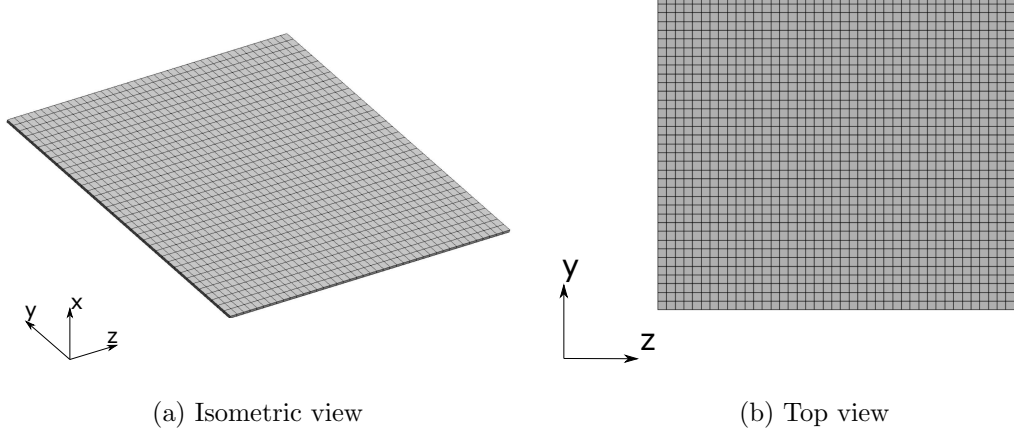


Figure 6.19: Finite element mesh for configuration 1.

After validation and convergence of numerical results, a model updating routine was implemented in MATLAB[®] software to estimate the properties (E , ν , ρ , and η) of each aluminum plate that best describe the experimental conditions. It consisted of the minimization of a squared error cost function defined as follows

$$CF(\boldsymbol{\theta}) = \sum_{i=1}^{N_f} [\mathbf{Y}(\omega_i) - f(\boldsymbol{\theta}, \omega_i)]^2 \quad (6.18)$$

where $\boldsymbol{\theta} = \{E, \nu, \rho, \eta\}$ is the vector of the properties to be estimated, ω_i is the i^{th} measured frequency, N_f is the total number of frequencies, \mathbf{Y} is the vector of the experimental data, $f(\boldsymbol{\theta}, \omega)$ is the vector of model predictions.

It is worth mentioning that the FRFs were computed using the multi-model approach [139] in this optimization routine. The optimization was done with the help of the MATLAB[®] function *fminsearchbnd*. Also, a specific organization was adopted to the experimental vector \mathbf{Y} as

$$\mathbf{Y} = \{\Re[\mathbf{F}\tilde{\mathbf{R}}\mathbf{F}|_{AC1}]; \cdots; \Re[\mathbf{F}\tilde{\mathbf{R}}\mathbf{F}|_{AC4}]; \Im[\mathbf{F}\tilde{\mathbf{R}}\mathbf{F}|_{AC1}]; \cdots; \Im[\mathbf{F}\tilde{\mathbf{R}}\mathbf{F}|_{AC4}]\}^T, \quad (6.19)$$

where $\Re[\tilde{\mathbf{a}}]$ and $\Im[\tilde{\mathbf{a}}]$ are, respectively, the real and imaginary parts of a complex vector $\tilde{\mathbf{a}}$.

This full characterization eliminates imprecisions on the properties of the aluminum plates, which were not previously measured, and minimizes the effects of the flexibility of the blades linking the

6.3. STUDY II: SIMPLY SUPPORTED PANELS

plate to the steel frame built around it [141]. Hence, it allows us to focus only on the characterization of the free-layer of foam material of configuration 2.

The FE model of configuration 2, shown in Eq. 6.14, was thus implemented for each structure tested. For the aluminum plate, the properties considered were those obtained by the optimization procedure described above. For the foam layer, in turn, the properties considered are shown in Tabs. 6.1 and 6.2 in Section 6.1. Only one layer mesh was generated to the aluminum plate, whereas different quantities of layers mesh were generated to the foam material. Different element sizes were also considered. The mesh with 2712 elements and 48429 degrees of freedom converged to the proper response as detailed in Tab. 6.10 and graphically represented in Fig. 6.20.

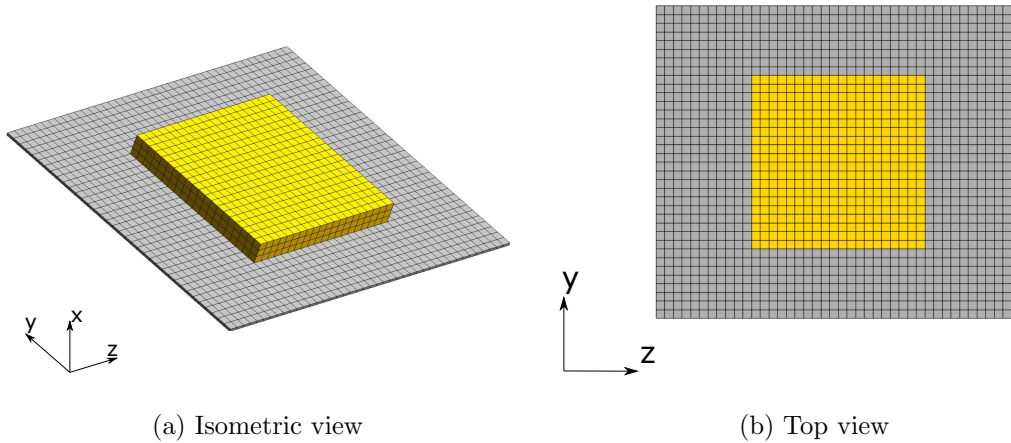


Figure 6.20: Finite element mesh for configuration 2.

Table 6.10: Description of finite element meshes of configurations 1 and 2.

| Configuration | Elements | Number of nodes | Degrees of freedom |
|---------------|--|-----------------|--------------------|
| 1 | $1 \times 36 \times 42$ | 10977 | 32931 |
| 2 | $1 \times 36 \times 42$ $3 \times 20 \times 20$ | 16143 | 48429 |

6.3.4 Model validation & discussion

This section compares the experimental measurements with the simulated responses for the two structural configurations under study. This verifies the possibility of correctly predicting their me-

chanical behavior with the adopted methodology and FE formulation.

6.3.4.1 Comparison between experimental data and simulation: foam A

As previously explained, the FE model of configuration 1 used for foam A was first implemented, followed by a model updating routine to find the material's properties (E , ρ , ν , η) of the aluminum plate. Table 6.11 compares the initial parameters with the ones estimated in this routine.

Table 6.11: Comparison between the initial and optimized properties for aluminum plate used for foam A.

| | E [GPa] | ν | ρ [kg/m ³] | η [%] |
|-----------|-----------|--------|-----------------------------|------------|
| Initial | 69.000 | 0.3500 | 2700 | 0.10 |
| Optimized | 70.914 | 0.3386 | 2800 | 0.11 |

Figure 6.21 compares the experimental FRFs with the simulated ones computed through the direct method considering the optimized parameters shown in Tab. 6.11 of the aluminum plate. It is shown that the model had, on the whole, a good agreement with the experimental results. Even though it underestimated the resonant frequencies, the biggest difference between the experimental and numerical values was less than 6% in the first excitation mode. Table 6.12 shows the resonant frequencies (f_r) identified at the location of AC1, where the relative discrepancy δf_r was calculated as

$$\delta f_r^i = \frac{|f_{r-exp}^i - f_{r-sim}^i|}{f_{r-exp}^i} \times 100\%, \quad (6.20)$$

where f_{r-exp}^i and f_{r-sim}^i correspond, respectively, to the i^{th} measured and simulated resonant frequency.

6.3. STUDY II: SIMPLY SUPPORTED PANELS

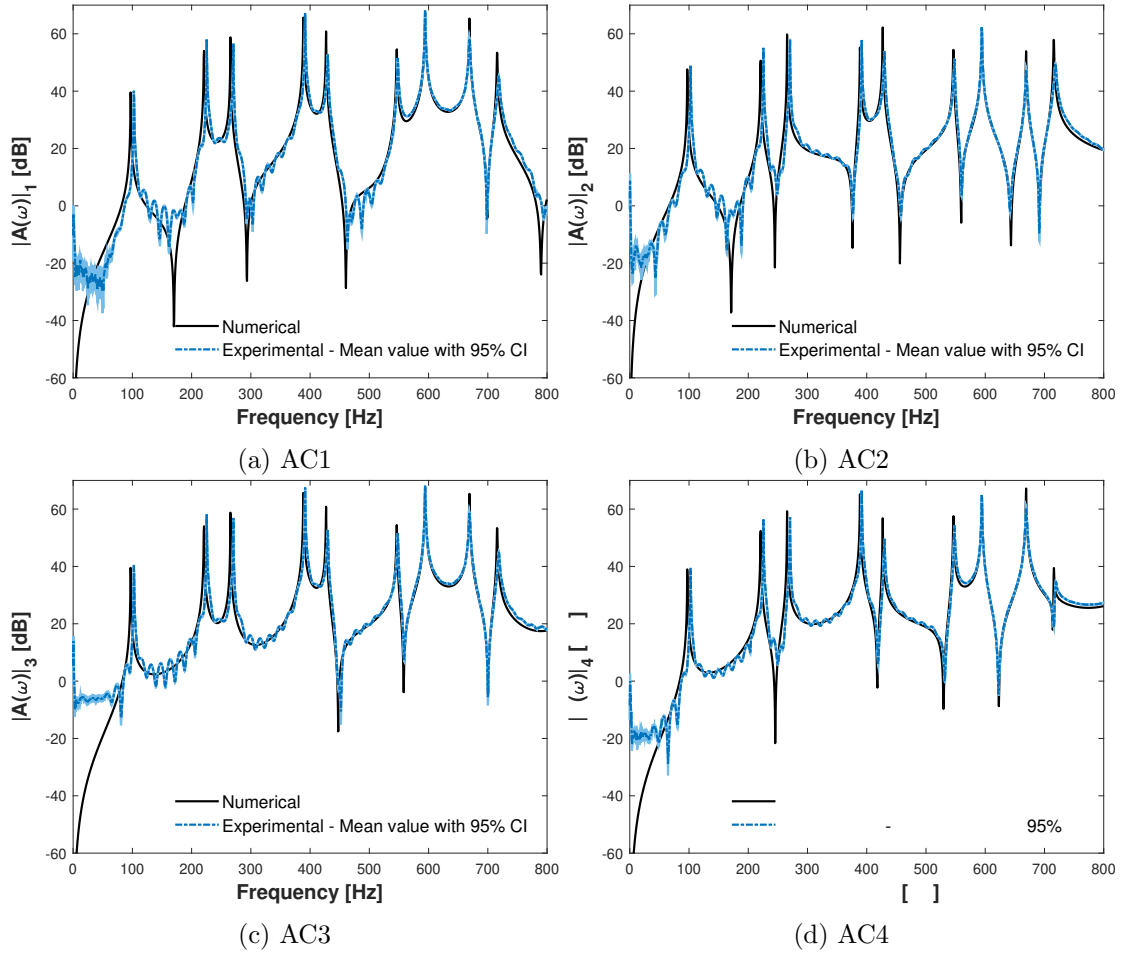


Figure 6.21: Comparisons between the FRFs obtained by experimental measurements and numerical simulations using optimized parameters of configuration 1 used for foam A.

Table 6.12: Comparison between the experimental and numerical resonant frequencies obtained at the location of AC1 of configuration 1 used for foam A.

| | 1 | 2 | 3 | 4 | 5 | 6 | 7 | 8 | 9 |
|------------------------------|-------|-------|-------|-------|-----|-------|-------|-----|-------|
| Experimental [Hz] | 102.5 | 225.5 | 270.5 | 391.5 | 430 | 548 | 594 | 669 | 718.5 |
| Numerical [Hz] | 97 | 221 | 265 | 388.5 | 427 | 546.5 | 594.5 | 669 | 715.5 |
| Discrepancy δf_r [%] | 5.4 | 2.0 | 1.9 | 0.8 | 0.7 | 0.3 | 0.1 | 0 | 0.4 |

It is noteworthy that previous experiments [135] showed that a discrepancy of 5% observed in the first mode of vibration is due to the rigid structure built around the aluminum plate. This is because this frame adds some stiffness to the experimental set-up, but it is not considered in the modeling. For this reason, the model predictions presented here were considered sufficiently accurate.

6.3. STUDY II: SIMPLY SUPPORTED PANELS

The FE model of configuration 2 with foam A was thus implemented. Figure 6.22 compares the measured FRFs with those estimated using the optimized properties shown in Tab. 6.11 of the aluminum plate and the viscoelastic properties shown in Tabs. 6.1 and 6.2 of foam A. It is possible to observe good levels of correlation between the results in terms of resonant frequencies and FRF amplitudes. Similar to configuration 1, the biggest difference between the experimental and numerical resonant frequencies was noticed for the first mode of vibration, but it was less than 5% as presented in Tab. 6.13.

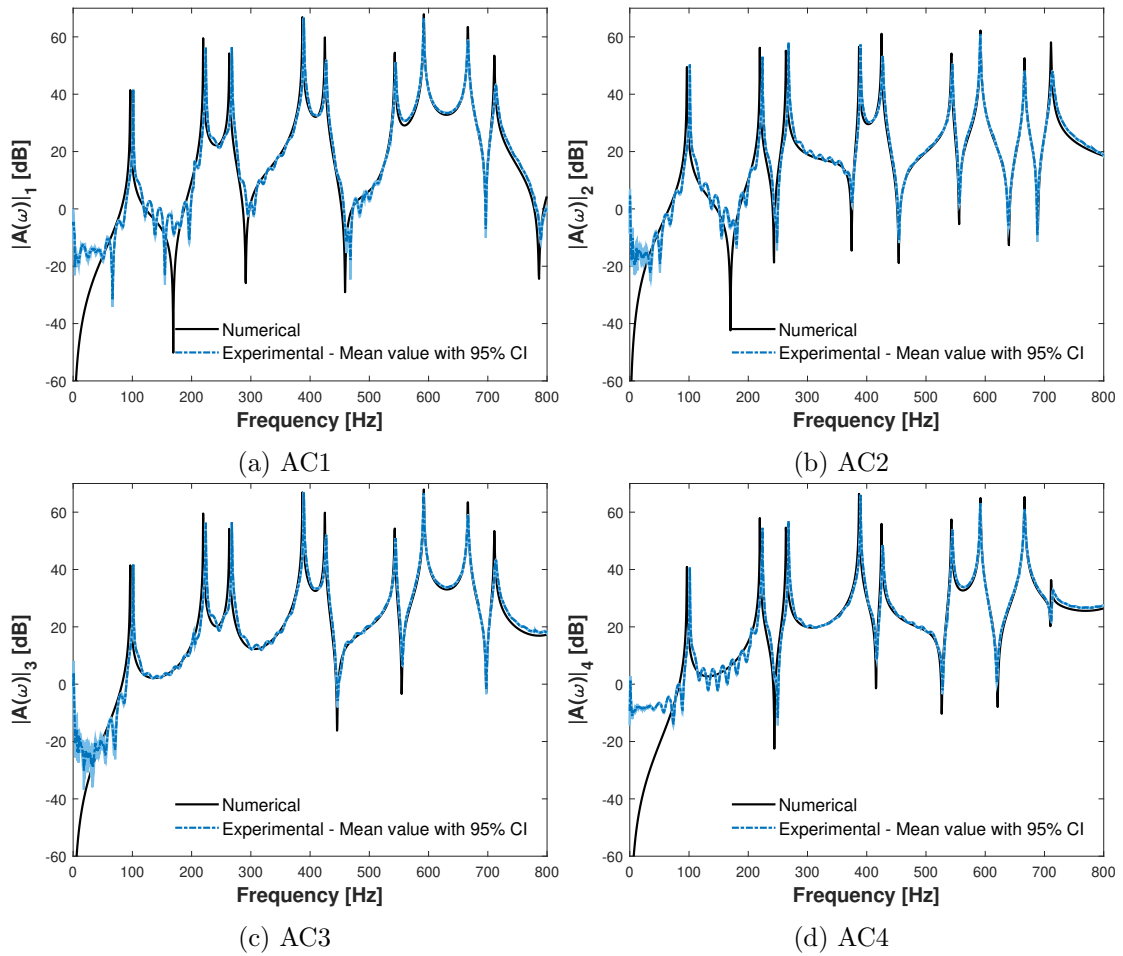


Figure 6.22: Comparisons between the FRFs obtained by experimental measurements and numerical simulations of configuration 2 with foam A.

6.3. STUDY II: SIMPLY SUPPORTED PANELS

Table 6.13: Comparison between the experimental and numerical resonant frequencies obtained at the location of AC1 for configuration 2 with foam A.

| | 1 | 2 | 3 | 4 | 5 | 6 | 7 | 8 | 9 |
|------------------------------|-------|-------|-------|-------|-----|-------|-------|-------|-------|
| Experimental [Hz] | 101.5 | 224 | 268 | 389.5 | 427 | 544.5 | 591.5 | 666.5 | 713.5 |
| Numerical [Hz] | 96.5 | 219.5 | 263.5 | 387 | 425 | 543 | 592 | 666.5 | 711 |
| Discrepancy δf_r [%] | 4.9 | 2.0 | 1.7 | 0.6 | 0.5 | 0.3 | 0.1 | 0 | 0.4 |

It should be pointed out that the system dynamics of configuration 2 with foam A are mainly governed by the aluminum plate as was identified in the comparative analysis of the experimental results in subsection 6.3.1 (see Fig. 6.14).

6.3.4.2 Comparison between experimental data and simulation: foam B

A similar procedure was carried out for the configurations of foam B. The FE model of configuration 1 was first built and then, the properties of the aluminum plate were adjusted by the model updating routine. Table 6.14 compares the initial parameters with the ones estimated in this routine.

Table 6.14: Comparison between the initial and optimized properties for aluminum plate used for foam B.

| | \mathbb{E} [GPa] | ν | ρ [kg/m ³] | η [%] |
|-----------|--------------------|--------|-----------------------------|------------|
| Initial | 69.000 | 0.3500 | 2700.0 | 0.10 |
| Optimized | 70.835 | 0.3581 | 2798.5 | 0.11 |

Figure 6.23 compares the experimental FRFs of configuration 1 used for foam B with the simulated ones computed using the optimal parameters shown in Tab. 6.14. Small differences can be observed as the model underestimated the resonant frequencies, as evidenced in Tab. 6.15. The greatest discrepancy observed in the first mode of vibration stems from the flexibility of the blades linking the plate to the frame built around it, which added some stiffness to the setup. Nevertheless, the curves are superimposed satisfyingly, indicating thus the system dynamics can be described by this FE model.

6.3. STUDY II: SIMPLY SUPPORTED PANELS

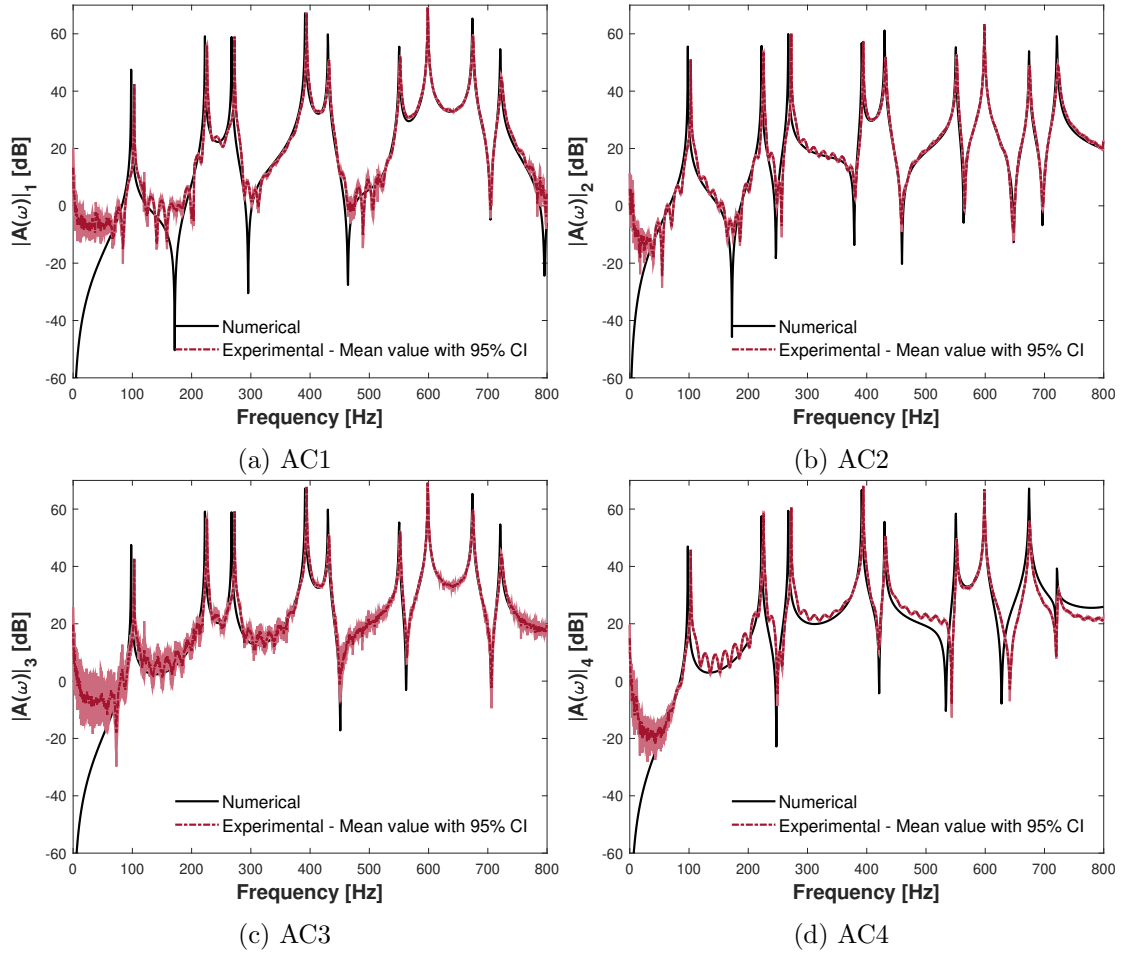


Figure 6.23: Comparisons between the FRFs obtained by experimental measurements and numerical simulations using optimized parameters of configuration 1 used for foam B.

Table 6.15: Comparison between the experimental and numerical resonant frequencies obtained at the location of AC1 of configuration 1 used for foam B.

| | 1 | 2 | 3 | 4 | 5 | 6 | 7 | 8 | 9 |
|------------------------------|-----|-------|-------|-------|-----|-------|-------|-----|-------|
| Experimental [Hz] | 103 | 226 | 272.5 | 394 | 432 | 552 | 598.5 | 675 | 722.2 |
| Numerical [Hz] | 98 | 222.5 | 267.5 | 391.5 | 430 | 550.5 | 599 | 674 | 721 |
| Discrepancy δf_r [%] | 4.9 | 1.6 | 1.8 | 0.6 | 0.5 | 0.3 | 0.1 | 0.2 | 0.2 |

The results of configuration 2 with foam B are compared in Fig. 6.24. On the whole, good levels of agreement were found between the numerical and measured FRFs. There are small discrepancies, especially in the first resonant peak: the model overestimated the damping and underestimated the resonant frequencies. At the location of AC1, for example, the first resonant frequency was identified

6.3. STUDY II: SIMPLY SUPPORTED PANELS

at about 99 Hz with an amplitude of 35.42 dB in the measured data, whereas the model predicted it at a frequency of 93.5 Hz (5.6 % lower) with 41.79 dB amplitude (17.9 % higher). Nevertheless, this was already expected due to the differences observed in configuration 1.

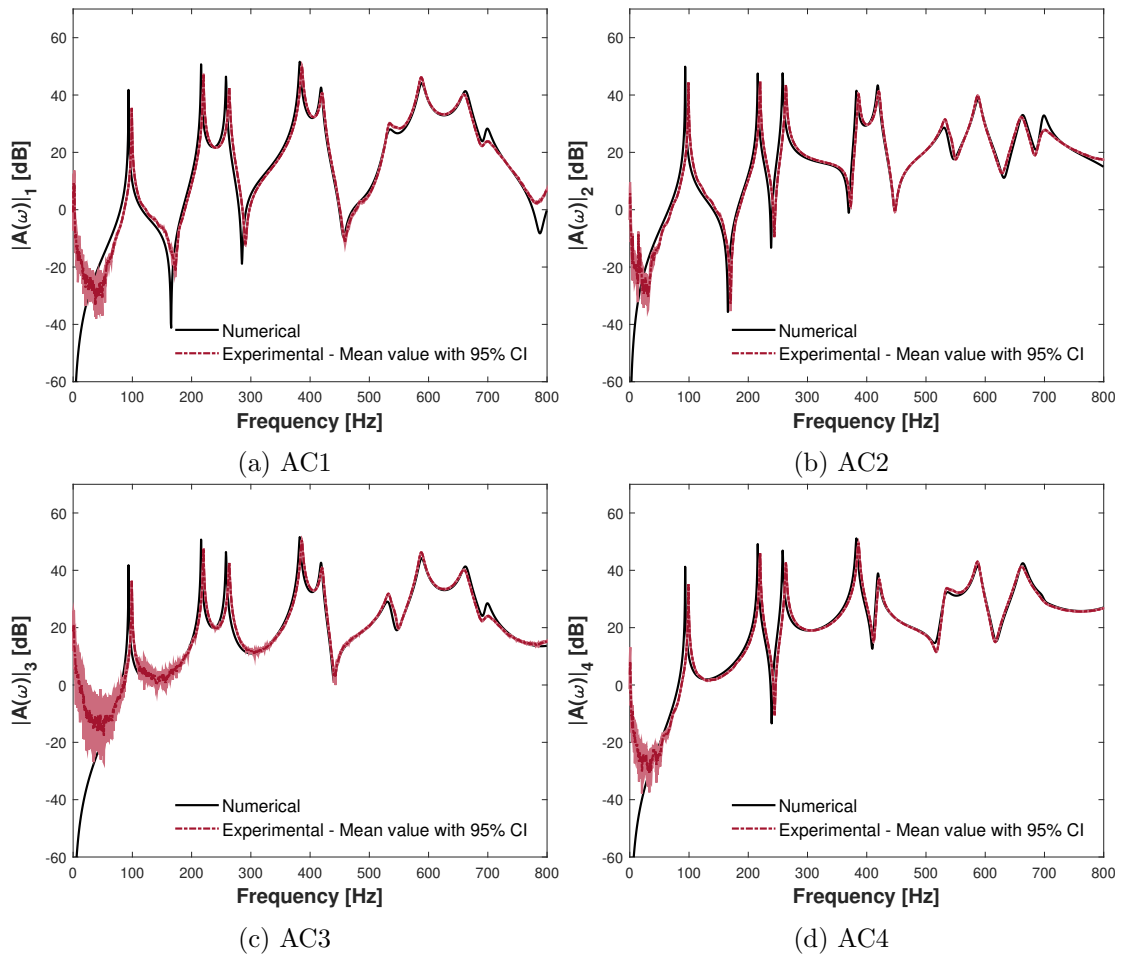


Figure 6.24: Comparisons between the FRFs obtained by experimental measurements and numerical simulations of configuration 2 with foam B.

Finally, Table 6.16 compares the resonant frequencies obtained through experiments and numerical simulations for this case. These results highlight that the model can provide good estimates in the low-frequency range for this type of foam.

6.3. STUDY II: SIMPLY SUPPORTED PANELS

Table 6.16: Comparison between the experimental and numerical resonant frequencies obtained at the location of AC1 of configuration 2 with foam B.

| | 1 | 2 | 3 | 4 | 5 | 6 | 7 | 8 | 9 |
|------------------------------|------|-----|-------|-------|-------|-------|-------|-----|-----|
| Experimental [Hz] | 99 | 220 | 263.5 | 386 | 420 | 534.5 | 587.5 | 660 | 700 |
| Numerical [Hz] | 93.5 | 216 | 258 | 382.5 | 418.5 | 535 | 588.5 | 662 | 699 |
| Discrepancy δf_r [%] | 5.6 | 1.8 | 2.1 | 0.9 | 0.4 | 0.1 | 0.2 | 0.3 | 0.1 |

6.3.4.3 Discussion

To sum up, the performances of two polymeric foams to damp structural vibrations in the low-frequency range were assessed experimentally and numerically. It was shown that one of the foams is capable of introducing significant damping on the system without actually causing major changes in its weight. Moreover, the comparisons between experimental and numerical results indicated the proposed approach was amenable for all configurations. The FE model indeed provided accurate predictions of the system behavior.

Thus, the constitutive models properly calibrated from measured data provided by a torsional rheometer are reliable to be associated with a FE model that considers only the viscoelasticity. This simplified model adopted for the polymeric foams as homogeneous viscoelastic solids proved effective for vibration analyses in low frequencies. It serves for its purposes by reducing the computational time and can be used as an efficient tool to quickly have predictions of such materials.

Another advantage is that the proposed model allows the use of model reduction techniques [139], which provides a further improvement in its computational cost. Figure 6.25, for example, illustrates the case when the multi-modal reduction technique is applied to calculate the response of configuration with foam B, showing a good relationship with the direct method. This makes it even more attractive, mainly, to be used in repeated routines such as optimization and uncertainty propagation.

It is also worth bearing in mind that the measurements were performed under ambient conditions, that is, in the presence of air. External parameters may influence the experimental measurements, and foams are, somehow, sensitive to them [85, 116]. The inherent uncertainties related to the experimental set-up and acquisition of data can also have a certain degree of influence. Small discrepancies were expected, but they were not significant in the present investigation.

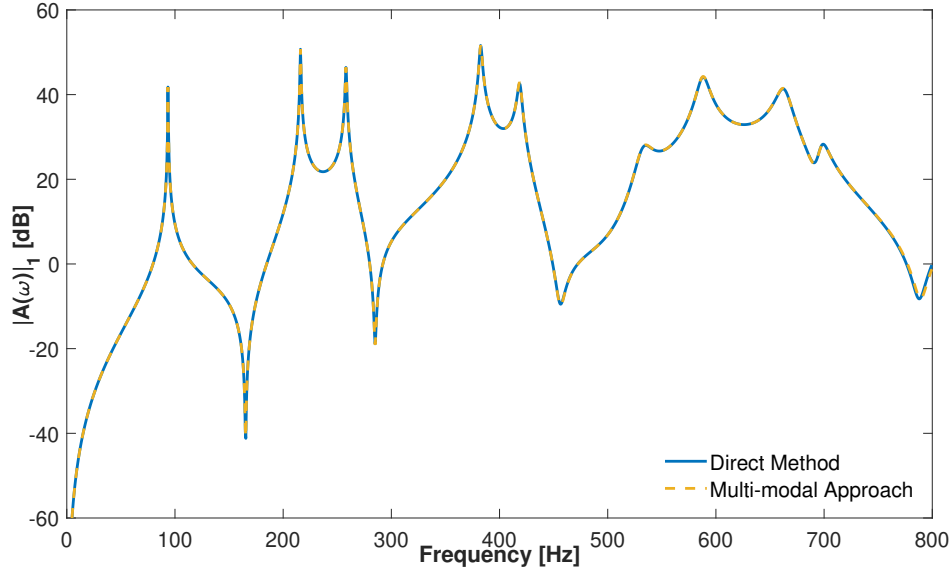


Figure 6.25: Frequency response function of configuration 2 with foam B considering the location of AC1. Performance of multi-modal approach.

6.3.5 Parametric study

As the models provided good agreement with the experimental measurements, an analysis of sensitivity was carried out for each configuration 2 to observe the effects of the geometric and mechanical parameters of the foam layer on the frequency responses. In each case studied, only one parameter was varied, while the others were considered to be constant to observe the individual influence in the damping performance.

Various scenarios in which the free-layer of foam material had different values of model parameters ($G_0, G_\infty, \tau, \alpha$), density, Poisson's ratio, and dimensions of thickness, width, and length (hereinafter referred to as ρ, ν, t, w and L , respectively) were evaluated. The FRFs were computed through the multi-modal approach [139] as it provided a good time-accuracy trade-off to obtain the approximated solutions. Furthermore, they were estimated only for the mesh point located on the position of AC1 (see Tab. 6.5).

Figures 6.26 and 6.27 show the variations of the FRFs by varying $\pm 20\%$ each of the four viscoelastic parameters (G_0, G_∞, τ , and α) for the configurations 2 with, respectively, foams A and B. A related point to consider is that, to better visualize the influence of these model parameters on the structure's

6.3. STUDY II: SIMPLY SUPPORTED PANELS

response with foam A, only the frequency band with the greatest variation is shown.

It can be seen that the variations of model parameters G_0 , G_∞ , and τ resulted in a decrease concerning the reference value of the maximum amplitudes of the FRFs in both structures studied. For the particular case of foam A, the change in its parameters caused a limitation in the model of predicting all resonance peaks. The impacts of α , on the other hand, was noticed only for the structure with foam B, especially when increasing it in 20 %.

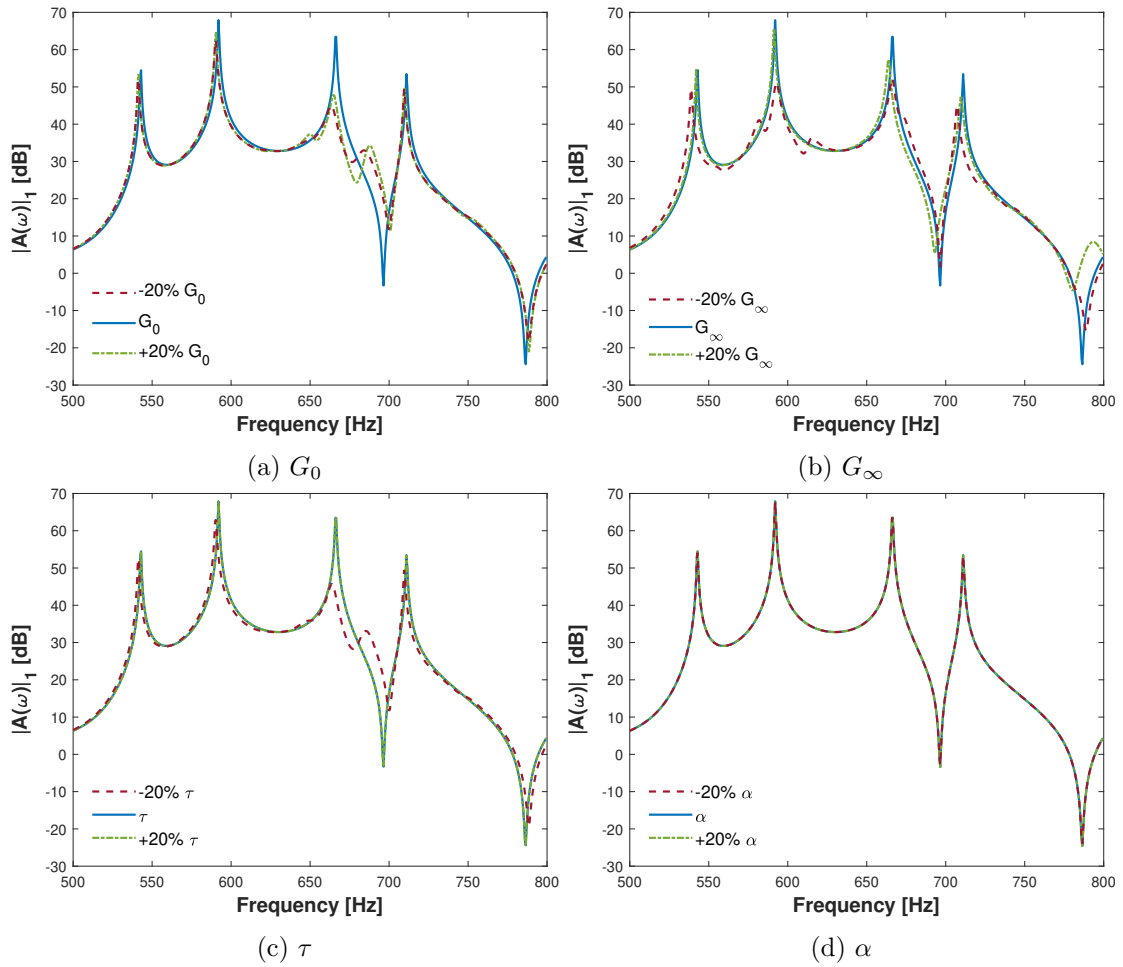


Figure 6.26: Effects of the four model parameters (G_0 , G_∞ , τ and α) on the estimated FRF for configuration 2 with foam A considering the location of AC1.

The influences of the material properties ρ and ν are shown in Figs. 6.28 and 6.29 for configurations 2 with foams A and B, respectively. For the analysis of ρ , a variation of 20 % of its value was used. For the analysis of ν , on the other hand, three values identified in the work of Bonfiglio et al. [98] for these materials were adopted.

6.3. STUDY II: SIMPLY SUPPORTED PANELS

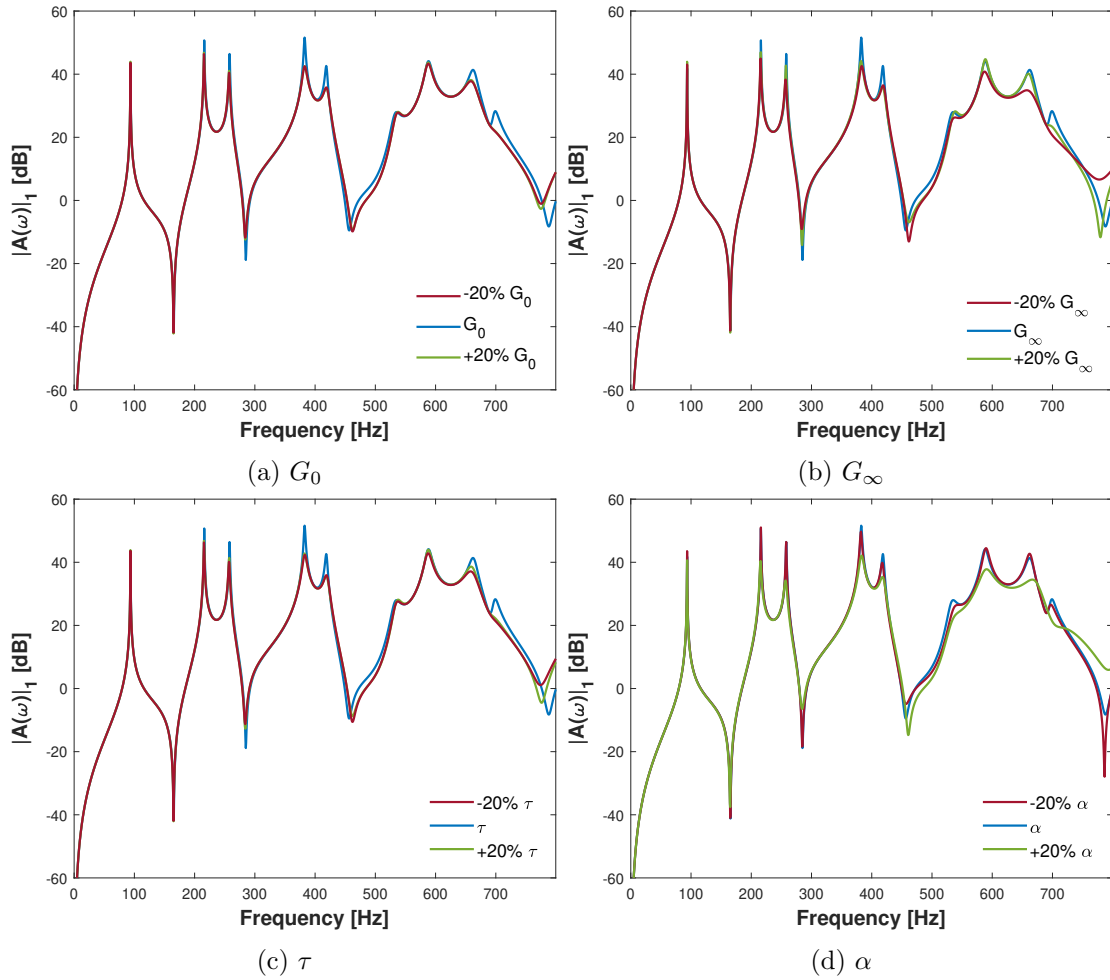


Figure 6.27: Effects of model parameters on the estimated FRF for configuration 2 with foam B considering the location of AC1.

The results obtained for foam A showed that variations in its properties did not result in major changes, even in the highest simulated frequencies. The increase in its ρ slightly decreased the resonance frequencies (up to 1.5 Hz in the last resonant peak), keeping approximately the same amplitudes. The increase in its ν did not lead to remarkable changes.

The results for foam B, on the other hand, showed that the structure is susceptible to changes in both properties. The increase in its ρ caused a decrease in the resonant frequencies and the maximum amplitudes of the FRF. The increase in its ν , in turn, increased both resonance frequencies and maximum amplitudes. For both cases, these variations are more noticeable as the frequency increased; the last resonant frequency, for example, decreased up to 9 Hz for ρ , and increased up to

6.3. STUDY II: SIMPLY SUPPORTED PANELS

5.5 Hz for ν .

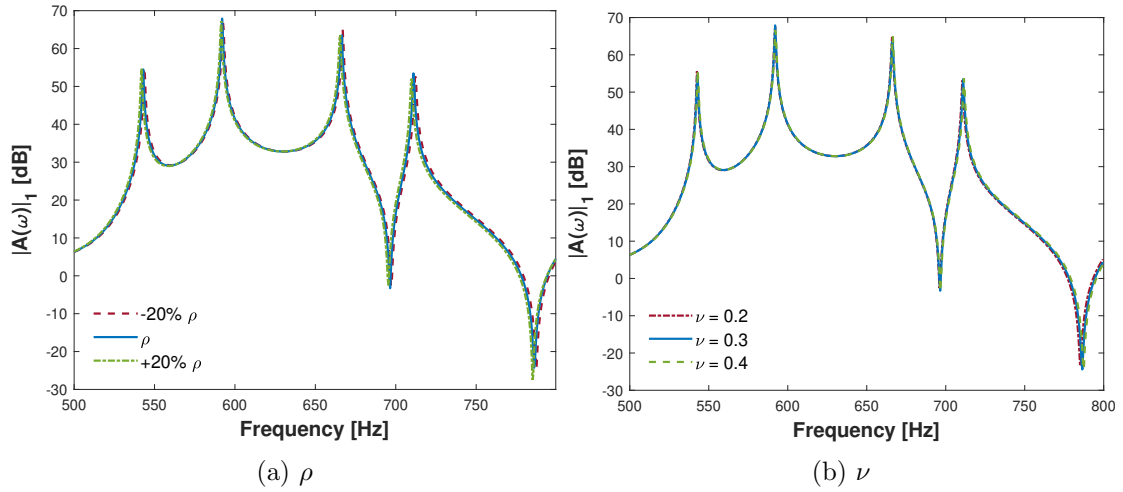


Figure 6.28: Effects of material properties (ρ and ν) on the estimated FRF for configuration 2 with foam A considering the location of AC1.

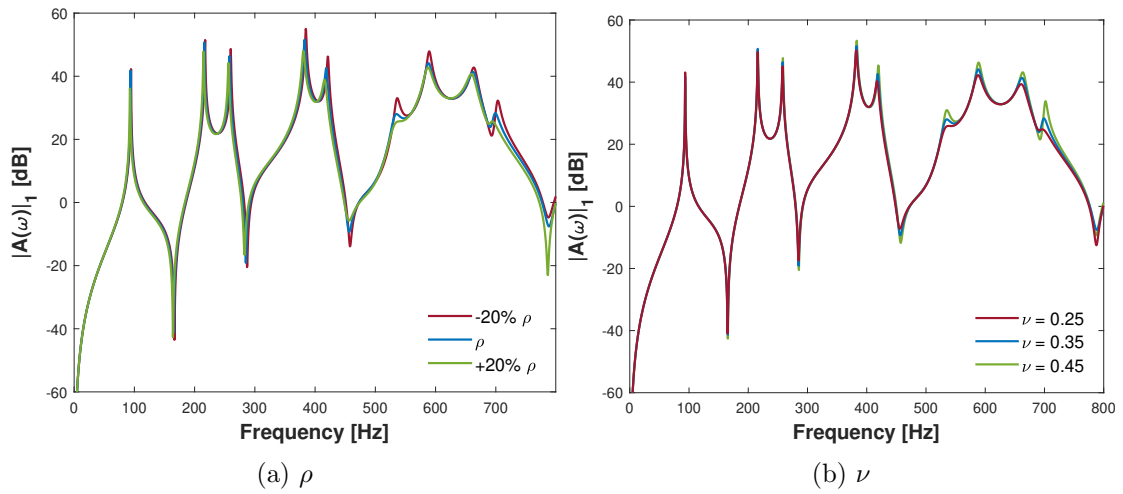


Figure 6.29: Effects of material properties (ρ and ν) on the estimated FRF for configuration 2 with foam B considering the location of AC1.

Finally, Figs. 6.30 and 6.31 show the effects of varying $\pm 20\%$ each geometric parameter L , w and t on the FRFs. For foam A, the effects of geometry are minimal and can be disregarded as with other parameters. For foam B, the effects can be noticed especially around each resonance peak; when the value of the parameter increased or decreased by $\pm 20\%$, both resonant frequency and maximum amplitude of the FRF decreased and increased.

6.3. STUDY II: SIMPLY SUPPORTED PANELS

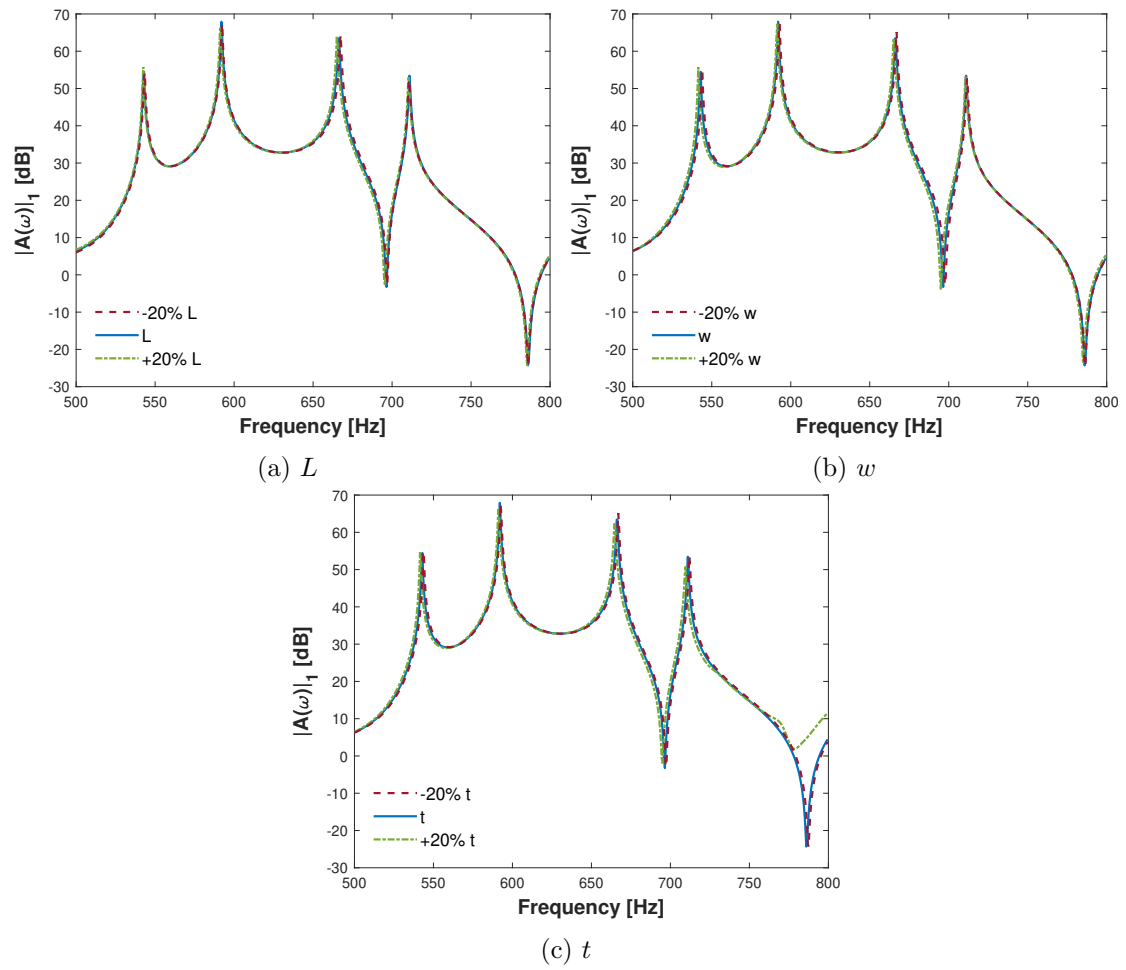


Figure 6.30: Effects of geometry (L , w and t) on the estimated FRF for configuration 2 with foam A considering the location of AC1.

6.3. STUDY II: SIMPLY SUPPORTED PANELS

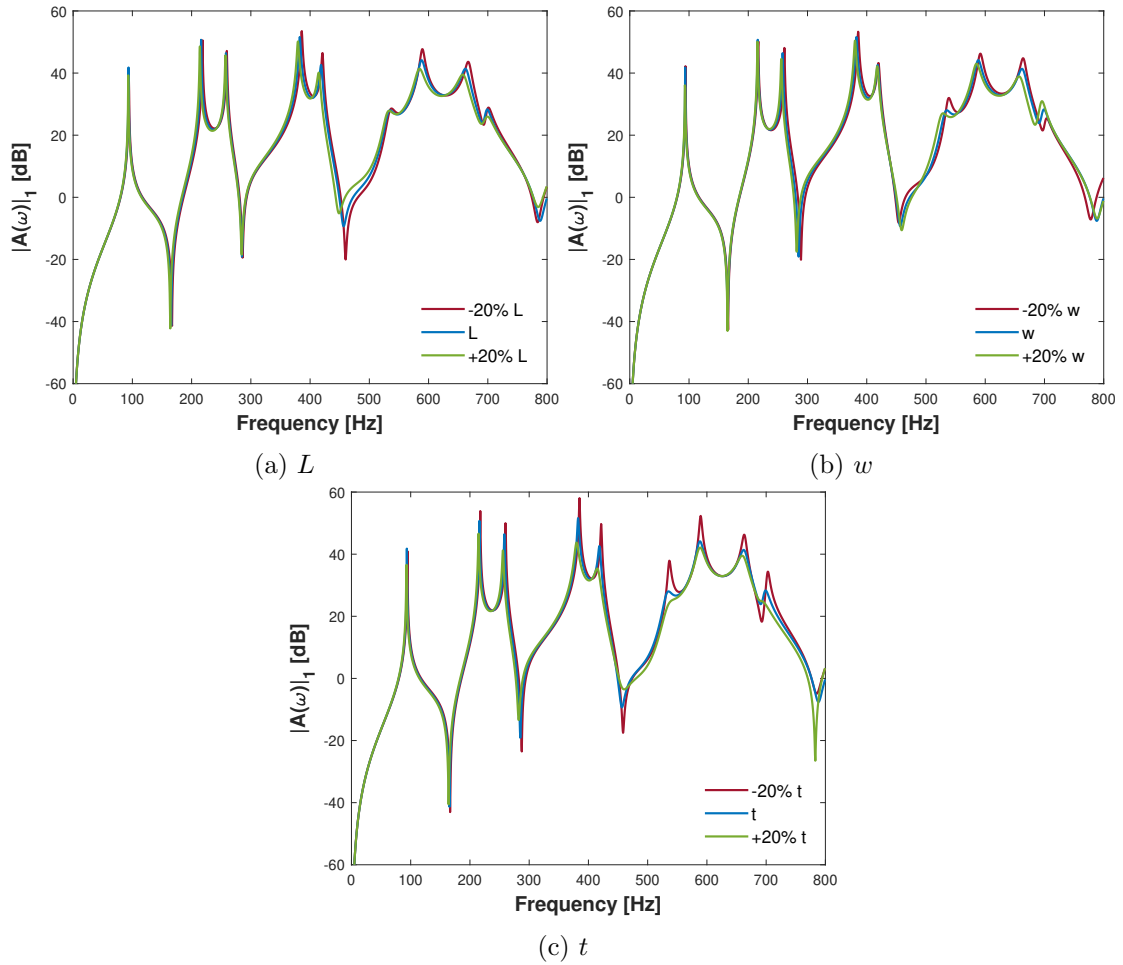


Figure 6.31: Effects of geometry (L , w and t) on the estimated FRF for configuration 2 with foam B considering the location of AC1.

To sum up, the results for foam A showed that the system is not sensitive to its variations even at the highest frequencies of the study, regardless of the parameter analyzed. The results for foam B, in turn, showed that the system response can be even affected since the first resonance peak, suggesting that its parameters could be optimized to improve weight and performance.

6.3.6 Limitations of the model

To illustrate the limitations of the proposed model, experimental tests and numerical simulations were performed again for each configuration 2, increasing the frequency range up to 1600Hz. The procedure adopted was similar to one employed in the previous analyses.

6.3. STUDY II: SIMPLY SUPPORTED PANELS

Figure 6.32 compares the FRFs measured by AC1 for each configuration tested. As observed in the low-frequency range, configuration 2 with foam B has a greater capacity to damp structural vibrations up to 1600 Hz than the one with foam A. Nevertheless, after 1400 Hz, the responses got closer to each other in such a manner as to suggest that the foams decreased their influence and that the response of the structure started to be governed by the aluminum plate and the frame.

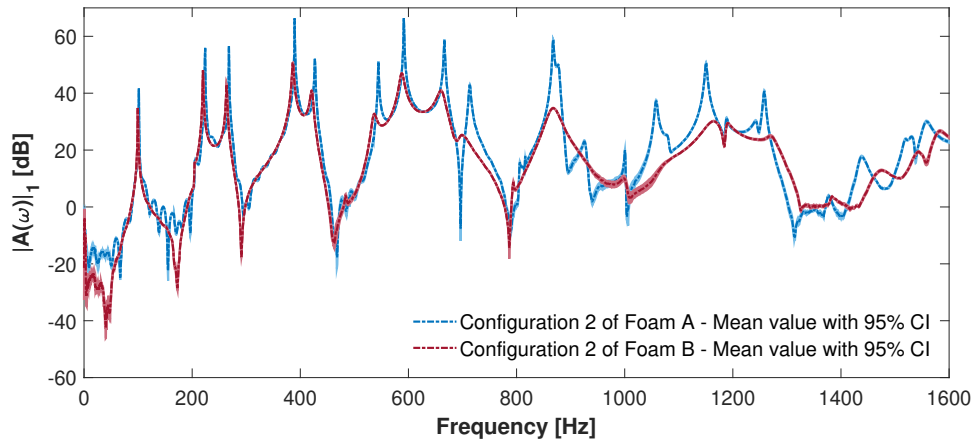


Figure 6.32: Comparison between the experimental FRFs of configurations 2 with foams A and B measured by AC1 considering frequencies up to 1600 Hz.

Figures 6.33 and 6.34 compare the experimental results and models predictions provided by direct method considering the location of AC1. For both foams, it can be observed that the model can predict up to 10th mode of vibration, that is, up to about 900 Hz. After this point, some small observed peaks can be attributed to frame modes; for example, from Fig. 6.33, one can observe small peaks around 1000, 1200, and 1400 Hz. As a consequence, they cannot be predicted by the model developed.

Once again the gaps between the first simulated and measured peaks can be associated with the non-ideal experimental boundary conditions (flexural bending modes of the frame), as previously explained. Accordingly, the finite element model proposed for a structure bonded to a free-layer of foam material is validated for frequencies up to 900 Hz.

6.4. CONCLUSION

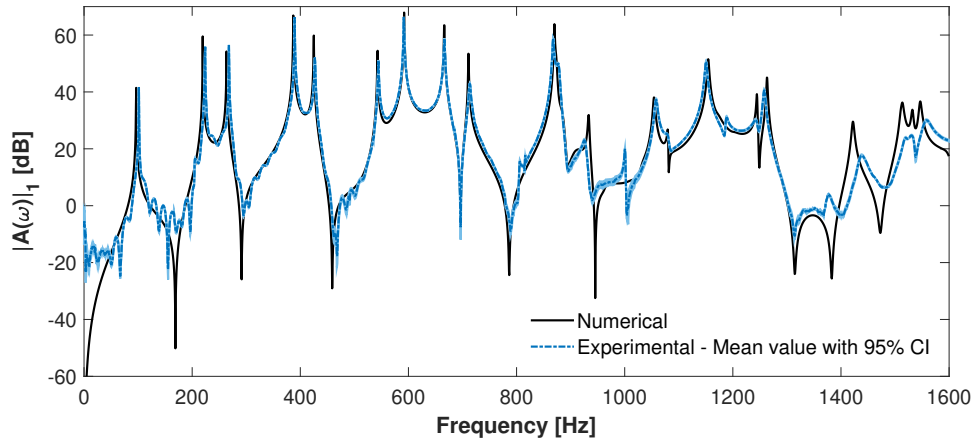


Figure 6.33: Comparison between the FRFs obtained by experimental measurements and numerical simulations of configuration 2 with foam A considering the location of AC1 and frequencies up to 1600 Hz.

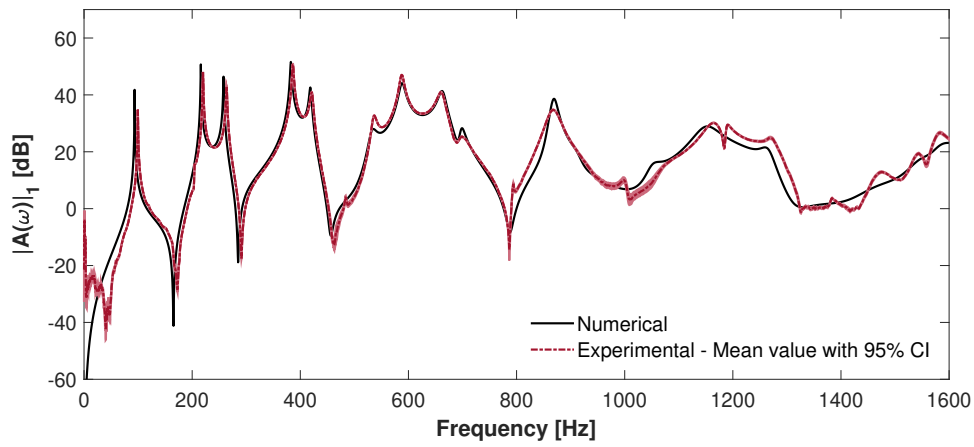


Figure 6.34: Comparison between the FRFs obtained by experimental measurements and numerical simulations of configuration 2 with foam B considering the location of AC1 and frequencies up to 1600 Hz.

6.4 Conclusion

This chapter dealt with the characterization, modeling, and predictions of the mechanical behavior of two different types of polymeric foams. The main objective was to explore the damping performance of these foams in the low-frequency range when considering only the viscoelasticity of their polymer skeletons. In this sense, two case studies were carried out whose main conclusions can be summarized

6.4. CONCLUSION

as follows.

The first study proposed a numerical method to provide predictive scenarios in the time domain of cyclic stress, encompassing different rates and temperatures. It considered the fractional derivative and WLF models both calibrated using measured data from a torsional rheometer. Results evidenced hysteresis in the responses of both foams. They also showed the effects of stress level, stress rate, and temperature on the loops.

The second study performed experimental measurements and numerical simulations on simply supported panels to verify the damping induced by these materials in structural vibrations and the possibility of predicting their mechanical behavior through the use of viscoelastic properties measured by a torsional rheometer. Through the experimental results, it was possible to find a good damping performance with a negligible increase in mass. Through the comparison of numerical and experimental results, it was possible to validate the proposed FE model for all studied configurations.

In conclusion, both studies showed that fractional derivative models calibrated from a torsional rheometer provide predictions about the damping capabilities of polymeric foams. Moreover, they highlighted the potential of one of the foams to be applied as a layer in damping treatments.

Chapter 7

Inverse characterization of viscoelastic properties of porous materials

This chapter presents an experimental-numerical methodology for the inverse characterization of viscoelastic properties of two different porous materials (Henriques et al. [142]). The goal is to calibrate fractional derivative models within the Bayesian framework. In this way, it could be an alternative method to characterize this kind of material.

It should be pointed out that this inverse characterization neglected the air-skeleton interactions since it was performed in the low-frequency range. Accordingly, the porous materials were modeled as monophasic viscoelastic solids with frequency-dependent properties. This assumption proved to be amenable after the studies carried out in Chapter 6.

It is organized as follows. First, Section 7.1 describes the methodology of the present approach. Then, Section 7.2 is dedicated to the experimental set-up. Next, Section 7.3 presents the mathematical formulation for the finite element simulation of the system response. Afterward, Section 7.4 shows and discusses the application of the inversion method used. Finally, Section 7.5 presents the conclusions of this work.

Content

| | | |
|------------|--|------------|
| 7.1 | Methodology | 219 |
| 7.2 | Experiments | 220 |
| 7.2.1 | Description of tested materials | 220 |
| 7.2.2 | Description of testing equipment and test conditions | 221 |
| 7.2.3 | Results | 222 |
| 7.3 | Modeling | 223 |
| 7.3.1 | Finite element formulation | 223 |
| 7.3.2 | Numerical implementation | 224 |
| 7.4 | Results & discussion: identification of viscoelastic parameters | 224 |
| 7.4.1 | Material B | 225 |
| 7.4.2 | Material C | 240 |

| | |
|---------------------------------|------------|
| 7.5 Conclusion | 251 |
|---------------------------------|------------|

7.1 Methodology

This section gives a layout of the methodology applied to assess the viscoelastic properties, more specifically the complex shear modulus $G^*(\omega)$, of two different porous materials from a Bayesian perspective. The latter uses as frequency response function (FRF) the acceleration defined as

$$FRF(\omega) = \frac{\tilde{A}(\omega)}{\tilde{F}(\omega)} \quad (7.1)$$

where $\tilde{A}(\omega)$ and $\tilde{F}(\omega)$ are, respectively, the Fourier transforms of the acceleration in m/s^2 and the force measured in N.

Figure 7.1 shows a schematic diagram of this methodology which was divided into four main stages. The first stage consisted of experimentally measure the FRF of simply supported panels in the low-frequency range at ambient conditions. The second one consisted of numerically estimate the FRFs using the finite element method. The third step, in turn, consisted of quantifying the difference between the experimental and numerical FRFs. Finally, the fourth main stage consisted of the inverse procedure based on the Bayesian approach to assess the viscoelastic properties of the investigated material.

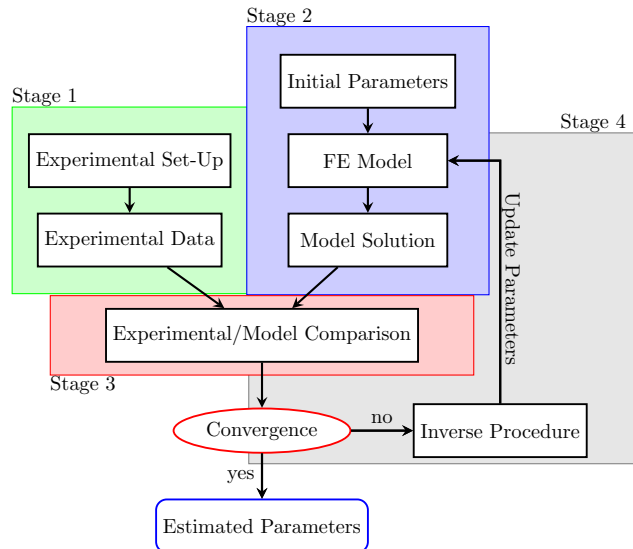


Figure 7.1: Schematic diagram of methodology employed to inverse identify viscoelastic properties of porous materials.

Two different layouts of simply supported panels were used, as shown in Fig. 7.2. The vibratory

response of an aluminum plate was first measured to perform a model updating process to take into account, for example, imperfections in the realization of the boundary conditions. Then, the response of the structure assembled with the free-layer of porous material to be characterized was measured.

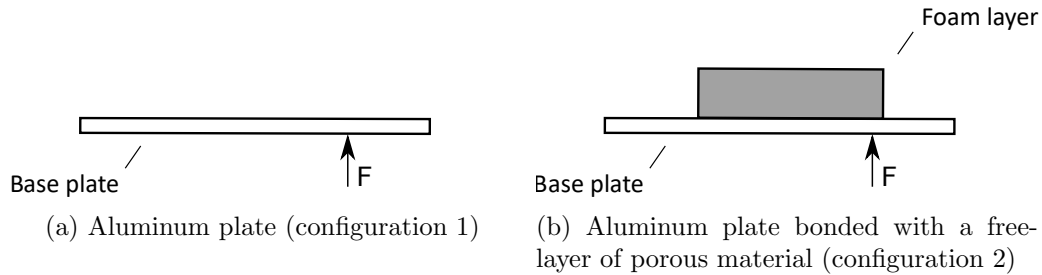


Figure 7.2: Configurations of simply supported panels.

7.2 Experiments

This section outlines the investigated porous materials, the experimental set-up and the corresponding measurement results. All the experiments were performed at Laboratoire de Mécanique des Structures et des Systèmes Couplés (LMSSC) of Cnam.

7.2.1 Description of tested materials

In this chapter, two different porous materials were investigated: one of them was a closed-cell polyurethane foam (hereinafter referred to as material B), and the other was a reconstituted porous rubber (hereinafter referred to as material C). Material B represents the group of closed cell foams and was identical to foam B studied in Chapter 6. Material C, on the other hand, represents the group of consolidated granular materials.

Figure 7.3 shows optical microscope images of the structure of studied materials. It becomes evident the difference between the constituents and the manufacturing process of these materials.

Like material B, material C was also industrially produced and its manufacturing process is not known. Nevertheless, it was also part of the five porous materials characterized in an interlaboratory campaign of Bonfiglio et al. [98] on the dynamic elastic properties of poroelastic media. From the measurement results presented therein, this material can also be modeled as homogeneous and almost isotropic with a constant and real-valued Poisson's ratio.

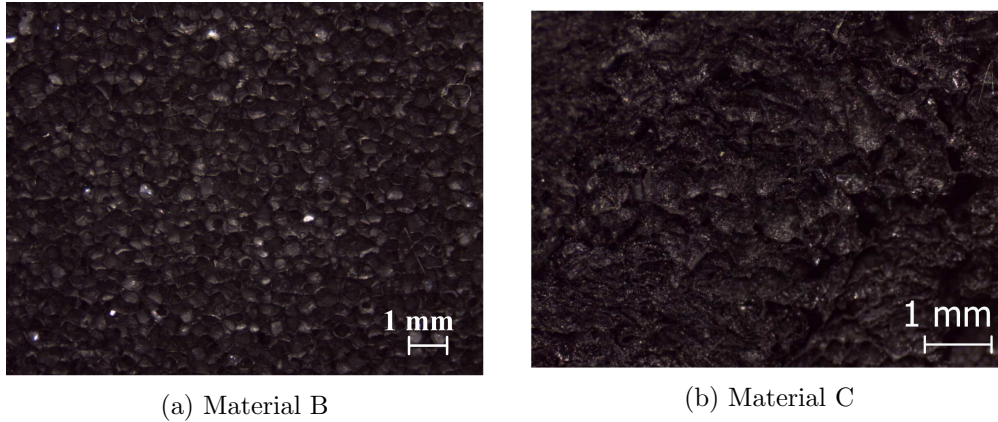


Figure 7.3: Optical microscope images of the structure of the two different porous materials.

Table 7.1 presents the nomenclature adopted as well as selected properties for the development of this work, whereby the materials are sorted by density. Both Poisson's ratio ν and density ρ were extracted from the work of Bonfiglio et al. [98]. It should be highlighted that the value of Poisson's ratio is a representative one chosen from the experimental results presented therein. Moreover, the values for the densities ρ 's were verified (see Appendix C for details).

Table 7.1: Description of tested materials, where ν is the Poisson's ratio and ρ is the nominal density.

| Material | Description | ν | ρ [kg/m ³] |
|----------|-------------------------------|-------|-----------------------------|
| B | closed-cell polyurethane foam | 0.35 | 48 |
| C | reconstituted porous rubber | 0.35 | 240 |

7.2.2 Description of testing equipment and test conditions

The experimental rig and test conditions were the same as the ones used for the second study case of Chapter 6. A detailed description can be found in subsection 6.3.1 of Chapter 6. Aiming at the enhanced readability of this chapter, the main aspects are recalled below.

Frequency response functions (FRFs) of simply supported panels with and without a free-layer of porous material were measured by four accelerometers in a bandwidth of [0-800] Hz with a frequency step of 0.5 Hz at ambient conditions. A total of 10 tests were performed on each structure, allowing statistical analysis.

7.2.3 Results

The experimental results of the structures built for material B are compared in Fig. 6.15 and discussed in subsection 6.3.1 of Chapter 6. Hence, they have not been reported here.

Figure 7.4 compares the experimental FRFs of configurations 1 and 2 of material C. The results illustrate the mean value of the tests together with the confidence interval of 95%. It is possible to observe that the addition of this material greatly affected the response of the structure since the first resonance peak. Indeed, this response became more damped in such a way that only the first five resonance peaks could be distinguished. These results evidenced the strong viscoelastic behavior of this porous material, also pointed out by Bonfiglio et al. [98].

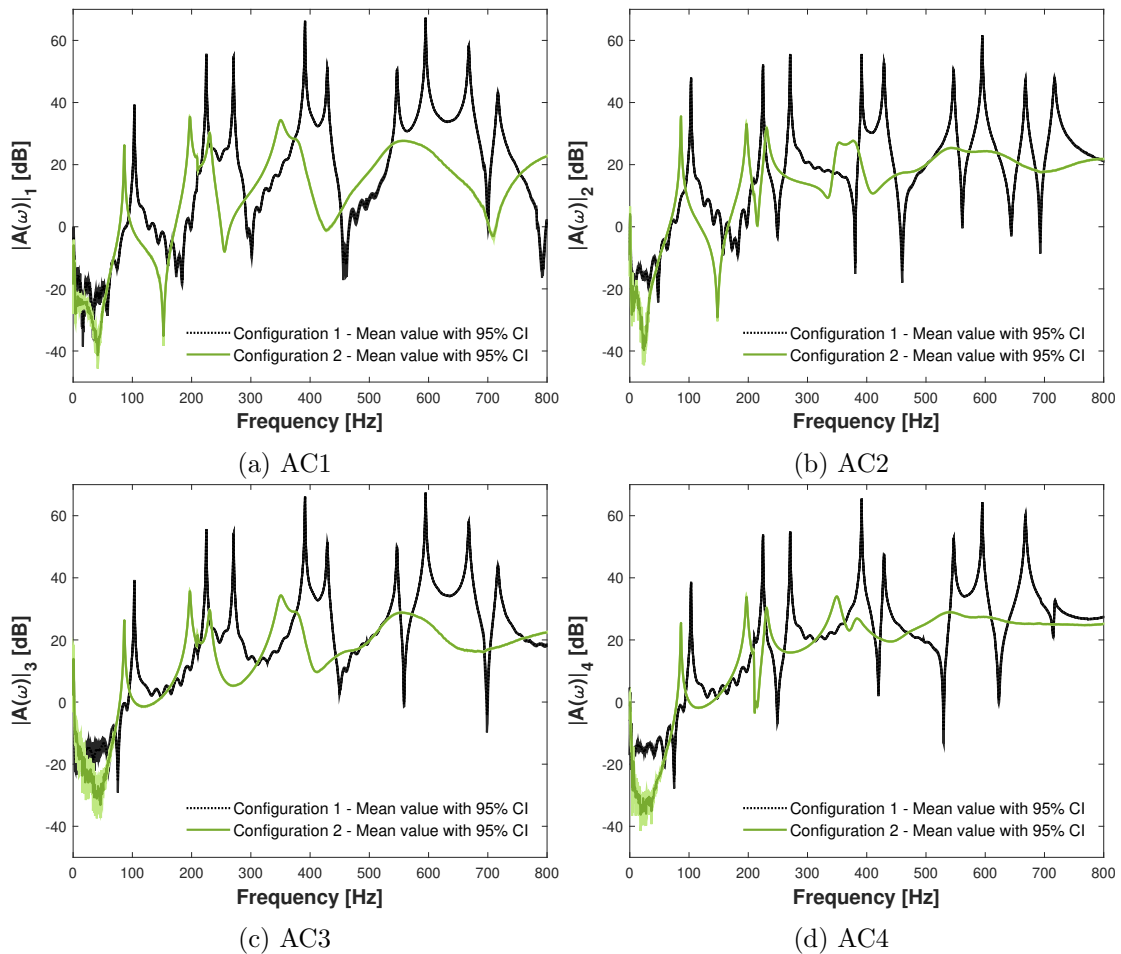


Figure 7.4: Comparisons between the measured FRFs of configurations 1 and 2 of material C.

7.3 Modeling

This section presents the finite element models adopted and the details related to the numerical implementation.

7.3.1 Finite element formulation

The hypotheses adopted were similar to those employed for configurations 1 and 2 studied in Chapter 6. Even though previously developed in subsection 6.3.2 of Chapter 6, the main equations are briefly repeated in the following for the sake of self-contained readability of this chapter.

Thus, for configuration 1, the finite element discretization of the differential equations results in the following equation of motion

$$[(1 + j\eta)\mathbb{K}_E - \omega^2\mathbb{M}_E]\mathbf{U}^S(\omega) = \mathbf{F}^S(\omega), \quad (7.2)$$

where \mathbb{K}_E and \mathbb{M}_E are, respectively, the stiffness and mass matrices related to the elastic component, η is its structural loss factor, and $\mathbf{U}^S(\omega)$ and $\mathbf{F}^S(\omega)$ are, respectively, the displacement and load vectors at angular frequency ω .

For configuration 2, on the other hand, the discretised equation of motion is given by

$$[\mathbb{K}_E + G^*(\omega)\mathbb{K}_V^0 - \omega^2\mathbb{M}]\mathbf{U}^S(\omega) = \mathbf{F}^S(\omega), \quad (7.3)$$

where \mathbb{K}_V^0 is the stiffness matrix related to the viscoelastic component and computed for a unit shear modulus, \mathbb{M} is the global mass matrix, $G^*(\omega)$ is the complex shear modulus of the viscoelastic material modeled herein by the four-parameter fractional derivative model (4PFDM), previously explained in subsection 2.5.1 of Chapter 2, as

$$G^*(\omega) = \frac{G_0 + G_\infty(j\omega\tau)^\alpha}{1 + (j\omega\tau)^\alpha}, \quad (7.4)$$

where G_0 and G_∞ are, respectively, the relaxed and unrelaxed shear moduli, τ is the relaxation time and α is the order of the fractional derivative model. These four parameters $\boldsymbol{\theta} = \{G_0, G_\infty, \tau, \alpha\}$ must obey the thermodynamic constraints shown in Eq. 2.28 and has to be assessed by means of inverse analysis.

7.3.2 Numerical implementation

Similarly to Chapter 6, an in-house program combining GMSH [138] and MATLAB[®] software was used to build the geometries together with the corresponding meshes, and also to compute the FRFs. Here, they were estimated through the model reduction technique known as multi-model approach [139] to reduce the computational time of the problem.

The investigated structures were modeled with the 20-node hexahedral elements since they describe better some physical mechanisms like, for example, the shear behavior of the viscoelastic material. Firstly, the FE model of each configuration 1 tested was implemented to perform a model updating routine to identify the equivalent properties of the aluminum plate together with the frame, similar to what was described in subsection 6.3.3 of Chapter 6. Then, the FE model of each configuration 2 tested was implemented to perform the inverse characterization of the viscoelastic properties of the porous layer. A preliminary study was conducted in an attempt to determine the number of pseudo-normal modes to be included in the projection basis and also to chose the finite element mesh. Figure 7.5 shows the adopted mesh with 14241 degrees of freedom.

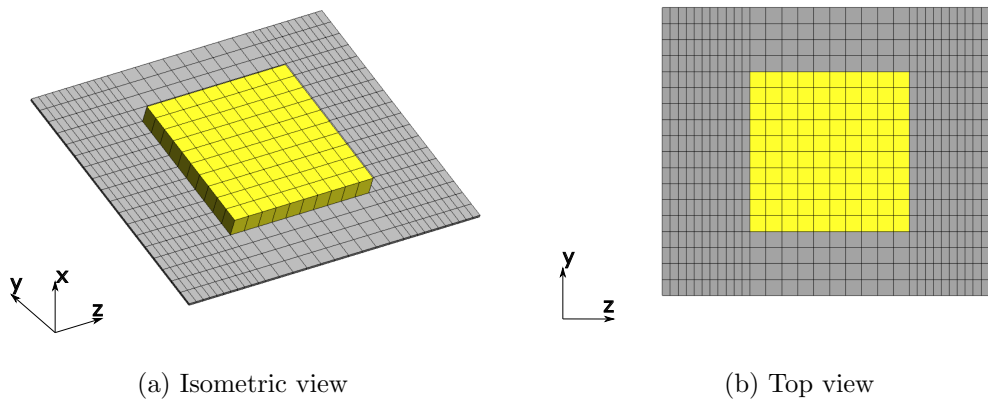


Figure 7.5: Finite element mesh adopted for the inverse method.

7.4 Results & discussion: identification of viscoelastic parameters

This section presents and discusses the results of the calibration of models adopted to describe the viscoelastic behavior of the two porous materials as well as the associated validation. For this, a probabilistic approach based on Bayesian inference, previously explained in Chapter 3, was considered

7.4. RESULTS & DISCUSSION: IDENTIFICATION OF VISCOELASTIC PARAMETERS

to assess information about the posterior probability density function $\pi(\boldsymbol{\theta}|\mathbf{Y})$ of the model parameters $\boldsymbol{\theta} = \{G_0, G_\infty, \tau, \alpha\}$ that characterize the constitutive equation given by Eq. 7.4.

7.4.1 Material B

7.4.1.1 Description of calibration and validation procedures

As previously mentioned, the viscoelastic parameters to be identified in this inverse characterization were defined as $\boldsymbol{\theta} = \{G_0, G_\infty, \tau, \alpha\}^T$. Nevertheless, they vary by some orders of magnitude for the investigated material according to the results presented by Bonfiglio et al. [98] and Henriques et al. [1]. Aiming at enhancing the performance of the identification process [25], they were normalized $\boldsymbol{\theta}_s = \{p_1, p_2, p_3, p_4\}^T$ based on the results presented by Henriques et al. [1] such as

$$p_1 = G_0 \times 10^{-4}[\text{Pa}], \quad (7.5a)$$

$$p_2 = G_\infty \times 10^{-6}[\text{Pa}], \quad (7.5b)$$

$$p_3 = \tau \times 10^8[\text{s}], \quad (7.5c)$$

$$p_4 = \alpha. \quad (7.5d)$$

For both calibration and validation steps, the experimental data \mathbf{Y} comprised the frequency response functions (FRFs) computed from the point excitation force provided by the impact hammer and the response accelerations measured by the four accelerometers $\{AC1, AC2, AC3, AC4\}$, as shown in Fig. 6.13. Some points should be highlighted.

All measured data has been split into two different subsets to quantify the influence of a particular calibration data-set on the model updating process, and because model validation must be independent of model updating, as shown in Tab. 7.2. A measurement subset S_{ijkl} was defined as the set for which calibration was performed using as observed data the FRFs measured by accelerometers $\{ACi, ACj\}$ and for which model validation was quantified using as observed data the FRFs measured by accelerometers $\{ACk, ACl\}$, where $i, j, k, l \in \{1, 2, 3, 4\}$ and $i \neq j \neq k \neq l$.

7.4. RESULTS & DISCUSSION: IDENTIFICATION OF VISCOELASTIC PARAMETERS

Table 7.2: Definition of subsets S_{ijkl} used for model calibration and model validation of material B, where $i, j, k, l \in \{1, 2, 3, 4\}$ and $i \neq j \neq k \neq l$.

| Subset | Model calibration | Model validation |
|------------|--|--|
| S_{1234} | $\mathbf{Y} = \{\mathbf{F}\tilde{\mathbf{R}}\mathbf{F} _{AC1} \mathbf{F}\tilde{\mathbf{R}}\mathbf{F} _{AC2}\}^T$ | $\mathbf{Y} = \{\mathbf{F}\tilde{\mathbf{R}}\mathbf{F} _{AC3} \mathbf{F}\tilde{\mathbf{R}}\mathbf{F} _{AC4}\}^T$ |
| S_{3412} | $\mathbf{Y} = \{\mathbf{F}\tilde{\mathbf{R}}\mathbf{F} _{AC3} \mathbf{F}\tilde{\mathbf{R}}\mathbf{F} _{AC4}\}^T$ | $\mathbf{Y} = \{\mathbf{F}\tilde{\mathbf{R}}\mathbf{F} _{AC1} \mathbf{F}\tilde{\mathbf{R}}\mathbf{F} _{AC2}\}^T$ |

Besides, a specific organization structure of the experimental data was adopted. The complex FRF measured by an accelerometer ACi was organized in a N-dimensional vector $\mathbf{F}\tilde{\mathbf{R}}\mathbf{F}|_{ACi} = \{F\tilde{R}F(\omega_1)|_{ACi}, \dots, F\tilde{R}F(\omega_N)|_{ACi}\}^T$. Accordingly, the measured data \mathbf{Y} for a given subset S_{ijkl} , described in Tab. 7.2, corresponded to a 4N-dimensional vector defined as follows

$$\mathbf{Y} = \{\Re[\mathbf{F}\tilde{\mathbf{R}}\mathbf{F}|_{ACi}]^T \Re[\mathbf{F}\tilde{\mathbf{R}}\mathbf{F}|_{ACj}]^T \Im[\mathbf{F}\tilde{\mathbf{R}}\mathbf{F}|_{ACi}]^T \Im[\mathbf{F}\tilde{\mathbf{R}}\mathbf{F}|_{ACj}]^T\}^T \quad (7.6)$$

where $\Re[\tilde{\mathbf{a}}]$ and $\Im[\tilde{\mathbf{a}}]$ are, respectively, the real and imaginary parts of a complex vector $\tilde{\mathbf{a}}$.

It is important to highlight that the calibration step did not consider all the experimental points obtained in the measurements. Only the experimental points related to the resonance peaks and ten more points linearly-spaced frequency grids ($\Delta f = 1.5$ Hz) located around each resonance peak were selected, as illustrated in Fig. 7.6. This technique improved the computational time since the dimension of the vector \mathbf{Y} reduced drastically; initially, it had 6400 points, but after selection, it reduced to 396 points.

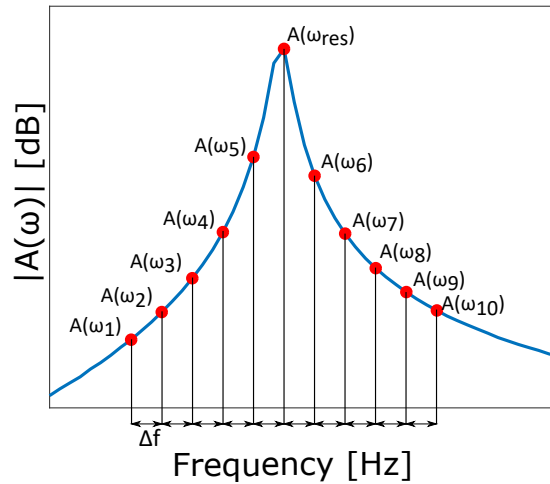


Figure 7.6: Selected points for calibration procedure in which $\Delta f = 1.5$ Hz.

7.4. RESULTS & DISCUSSION: IDENTIFICATION OF VISCOELASTIC PARAMETERS

For the model calibration step using Bayesian inference, it is required one to specify the likelihood $\pi(\mathbf{Y}|\boldsymbol{\theta})$ and the prior $\pi_0(\boldsymbol{\theta})$ as shown in Eq. 3.4. It was assumed herein that the likelihood function $\pi(\mathbf{Y}|\boldsymbol{\theta})$ was defined by the distribution of the additive error, leading to $\mathbf{e} \sim N(\mathbf{0}, \boldsymbol{\Sigma})$. A diagonal covariance matrix $\boldsymbol{\Sigma}$, as shown in Eq. 3.9, was assumed with sample-based error variance. That is, the variance σ_i^2 was treated as an additional random parameter defined by the inverse gamma distribution [25].

Concerning the priors $\pi_0(\boldsymbol{\theta})$, it was assumed herein a uniform prior distribution for the normalized parameters $\boldsymbol{\theta}_s = \{p_1, p_2, p_3, p_4\}^T$. Every random variable was constructed under the hypothesis that they were mutually independent. Moreover, the marginal prior for the variable θ was defined to be within the set D_θ such as

$$D_{p_1} = \{p_1 \in \mathbb{R} | 0 < p_1 < 3\}, \quad (7.7a)$$

$$D_{p_2} = \{p_2 \in \mathbb{R} | 1 < p_2 < 5\}, \quad (7.7b)$$

$$D_{p_3} = \{p_3 \in \mathbb{R} | 3 < p_3 < 6\}, \quad (7.7c)$$

$$D_{p_4} = \{p_4 \in \mathbb{R} | 0 < p_4 < 0.5\}, \quad (7.7d)$$

which the limit values were chosen based on the results presented in the works of Bonfiglio et al. [98] and Henriques et al. [1].

With all parameters defined, the calibration of the model started. Firstly, a deterministic analysis was done to assess the maximum a posteriori (MAP) estimate $\hat{\boldsymbol{\theta}}_{MAP}$ shown in Eq. 3.11. Then, the approximate posterior covariance matrix was determined as $\hat{\boldsymbol{\Sigma}} \approx (\mathbf{J}^T \boldsymbol{\Sigma}_0 \mathbf{J})^{-1}$. The operator \mathbf{J} is related to the model Jacobian evaluated at $\hat{\boldsymbol{\theta}}_{MAP}$ and $\boldsymbol{\Sigma}_0$ corresponds to the initial covariance matrix whose variance was calculated as follows

$$\sigma_0^2 = \frac{\sum_{i=1}^{N_y} [\mathbf{Y} - f(\hat{\boldsymbol{\theta}}_{MAP}, \mathbf{x})]^2}{N_y - N_\theta}, \quad (7.8)$$

where N_y is the number of measured data chosen to be analyzed and N_θ is the number of parameters [25].

Finally, the posterior distribution of the unknown parameters $\pi(\boldsymbol{\theta}|\mathbf{Y})$ was explored with the DRAM algorithm, explained in subsection 3.2.2 of Chapter 3. In the AM method, the adaptation occurred

7.4. RESULTS & DISCUSSION: IDENTIFICATION OF VISCOELASTIC PARAMETERS

at prescribed intervals of length $j_0 = 100$ with a Gaussian candidate distribution. In the DR method, three stages were considered in which $\gamma_s = \{1/5, 1/4, 1/3\}$. A total number of $N_{MC} = 50000$ samples was considered.

7.4.1.2 Model calibration

For all measurement subsets studied, a MAP estimator was first performed to find the best point $\hat{\theta}_{MAP}$ to start MCMC sampling, removing long warm-up steps. As the prior PDFs were described by uniform distributions, this point estimate was reduced to the maximum-likelihood (ML) estimator. Table 7.3 summarizes the results obtained in this step for both measurement subsets S_{1234} and S_{3412} . It can be seen that the estimated parameters varied according to the measurement subset, and the parameters G_∞ and τ were the ones most affected.

Table 7.3: MAP results for the two measurement subsets S_{ijkl} , $i, j, k, l \in \{1, 2, 3, 4\}$ and $i \neq j \neq k \neq l$, of material B.

| Subset | G_0 [Pa] | G_∞ [Pa] | τ [s] | α |
|------------------|--------------------|--------------------|-----------------------|----------|
| Initial | 1.00×10^4 | 2.00×10^6 | 1.00×10^{-8} | 0.5 |
| MAP - S_{1234} | 0.87×10^4 | 2.06×10^6 | 4.25×10^{-8} | 0.39 |
| MAP - S_{3412} | 1.05×10^4 | 2.77×10^6 | 3.07×10^{-8} | 0.42 |

Figure 7.7 compares the measured FRFs with the ones estimated using an initial value θ_0 and using the MAP estimate $\hat{\theta}_{MAP}$. It graphically illustrates the improvement achieved by this point estimator.

After that, the sampling started using DRAM algorithm and the convergence was monitored by computing the cumulative mean in the Markov chain of all the parameters. Figure 7.8 shows the results obtained, evidencing the well-mixing samples and that the stationarity of the posterior distributions has been reached.

7.4. RESULTS & DISCUSSION: IDENTIFICATION OF VISCOELASTIC PARAMETERS

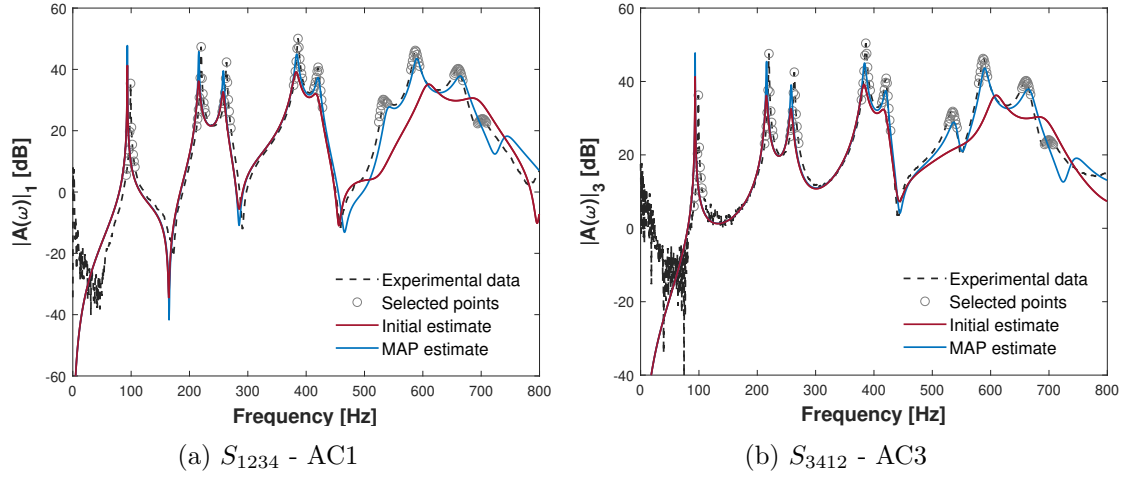


Figure 7.7: Comparison between experimental data and model prediction using MAP estimate $\hat{\theta}_{MAP}$ for both measurement subsets S_{1234} and S_{3412} of material B.

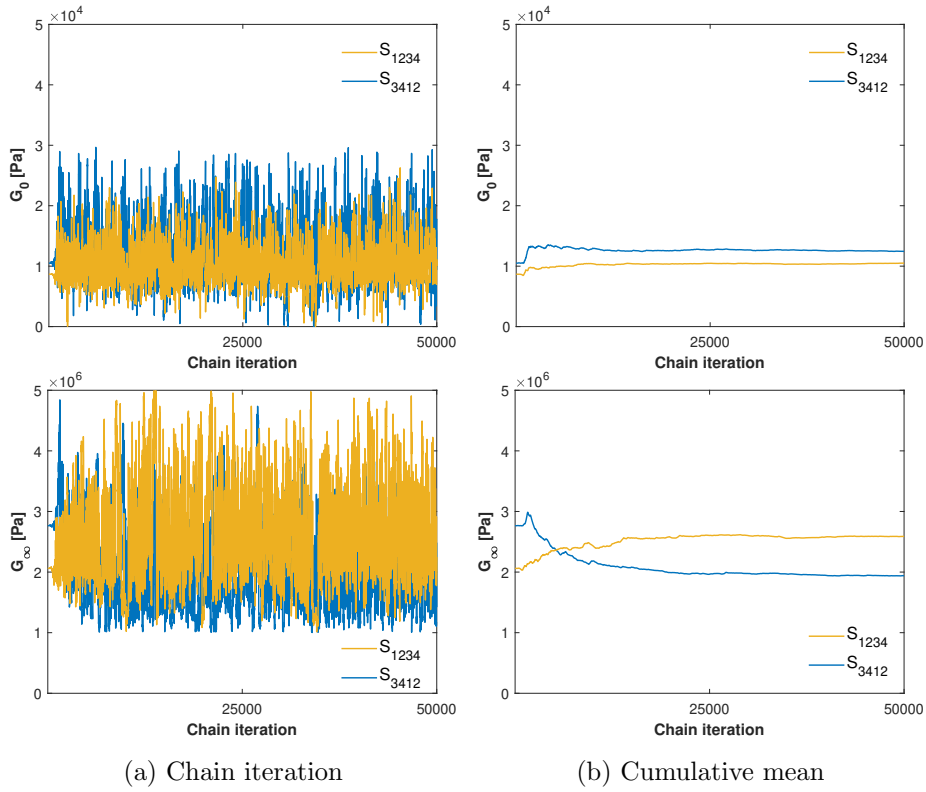


Figure 7.8: Convergence analysis for the 4PFDM using DRAM algorithm of material B.

7.4. RESULTS & DISCUSSION: IDENTIFICATION OF VISCOELASTIC PARAMETERS

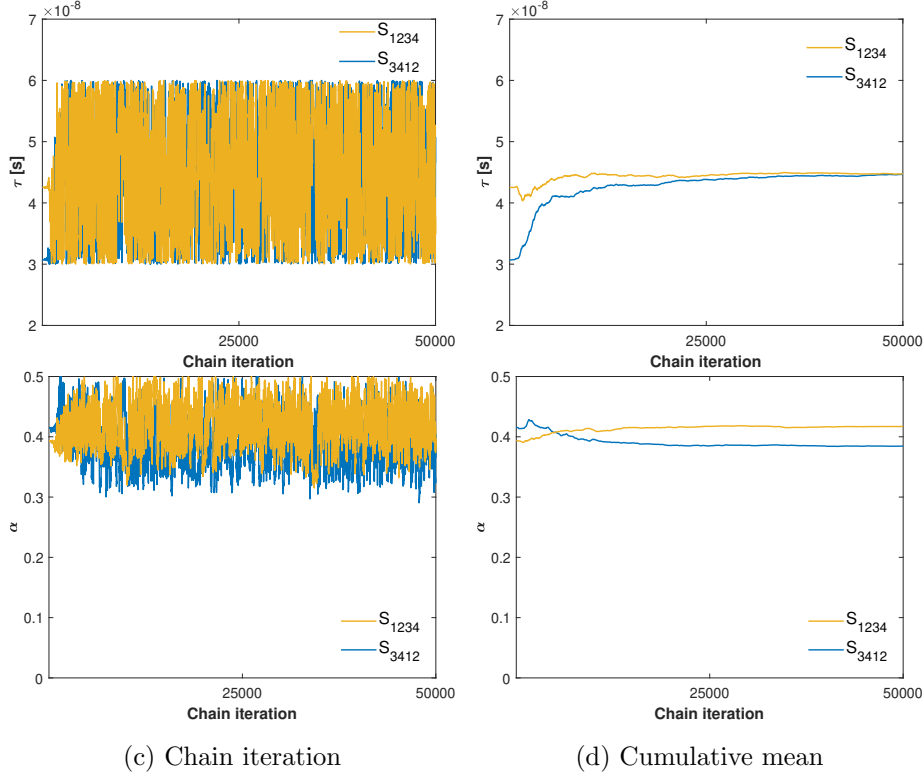


Figure 7.8: Convergence analysis for the 4PFDM using DRAM algorithm of material B.

Table 7.4 summarizes the analyses of the MCMC samples for the two measurement subsets S_{1234} and S_{3412} . For the former, the chain reached the convergence after 35000 samples with an acceptance rate of 36.48%. For the latter, in turn, the convergence was reached after 40000 samples with an acceptance rate of 27.71%. Both analyses showed consistent acceptance rate values.

Table 7.4: MCMC results using DRAM algorithm for the two measurement subsets S_{ijkl} , $i, j, k, l \in \{1, 2, 3, 4\}$ and $i \neq j \neq k \neq l$, of material B.

| Subset | Total samples | Burn-in | Acceptance rate |
|------------|---------------|---------|-----------------|
| S_{1234} | 50000 | 35000 | 36.48 % |
| S_{3412} | 50000 | 40000 | 27.71 % |

After discarding the samples from the burn-in period, Monte Carlo approximations were computed for the posterior mean ($\mathbb{E}[\theta]$) and 95% credibility interval (CI) of each model parameter θ . Table 7.5 shows the results for the two measurement subsets S_{1234} and S_{3412} . It is possible to observe that the mean values of the parameters obtained by the different subsets were very close. The parameter G_∞

7.4. RESULTS & DISCUSSION: IDENTIFICATION OF VISCOELASTIC PARAMETERS

was the one most affected by the measurement subset, while τ was the one less affected.

Table 7.5: Posterior mean value and 95 % credibility interval of the unknown parameters θ for the two measurement subsets S_{ijkl} , $i, j, k, l \in \{1, 2, 3, 4\}$ and $i \neq j \neq k \neq l$, of material B.

| Subset | $\mathbb{E}[G_0]$ 95 % CI | [Pa] | $\mathbb{E}[G_\infty]$ 95 % CI | [Pa] | $\mathbb{E}[\tau]$ 95 % CI | [s] | $\mathbb{E}[\alpha]$ 95 % CI |
|------------|------------------------------|---------------|-----------------------------------|---------------|-------------------------------|------------------|---------------------------------|
| S_{1234} | 1.09 [0.59, 1.89] | $\times 10^4$ | 2.66 [1.45, 4.42] | $\times 10^6$ | 4.42 [3.09, 5.88] | $\times 10^{-8}$ | 0.42 [0.35, 0.49] |
| S_{3412} | 1.21 [0.31, 2.31] | $\times 10^4$ | 1.92 [1.12, 3.37] | $\times 10^6$ | 4.53 [3.08, 5.95] | $\times 10^{-8}$ | 0.38 [0.32, 0.47] |

Even though the independence hypothesis was adopted for all random variables when building the prior PDFs, the samples could still indicate some level of linear correlation once the mapping between the random vector θ and the model prediction was nonlinear. In this regard, scatter plots were studied in an attempt to assess the linear correlation between the parameters as shown in Fig. 7.9. For both S_{1234} and S_{3412} , the model parameters exhibited little or almost no correlation with each other.

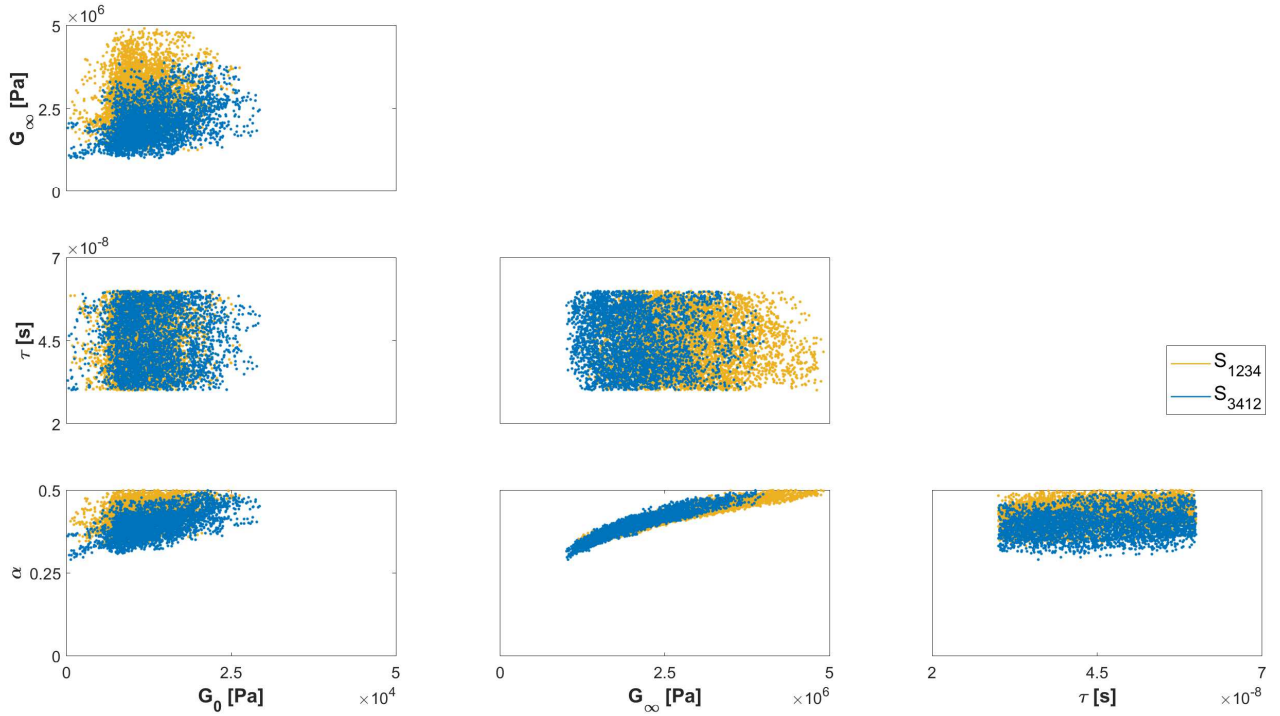


Figure 7.9: Posterior samples generated using DRAM algorithm for the 4PFDM of material B.

7.4. RESULTS & DISCUSSION: IDENTIFICATION OF VISCOELASTIC PARAMETERS

Figure 7.10 shows the marginal posterior PDFs computed for each unknown parameter θ . It can be seen that, in both measurement subsets, the marginal posterior PDF for the relaxation time τ deviated from a Gaussian distribution. However, this parameter was the one less affected by the measurement subset S_{ijkl} : the posterior mean and the 95% credibility interval remained almost unchanged, as shown in Tab. 7.5.

It is worth mentioning that the plate with this porous material is lightly damped from the results presented in the second study case in Chapter 6. Hence, the resonance frequencies (FRF peaks) and the FRF magnitude at these resonance frequencies are much more affected by the stiffness parameters of the aluminum plate, explaining the larger uncertainties to the parameters related to the viscoelastic layer.

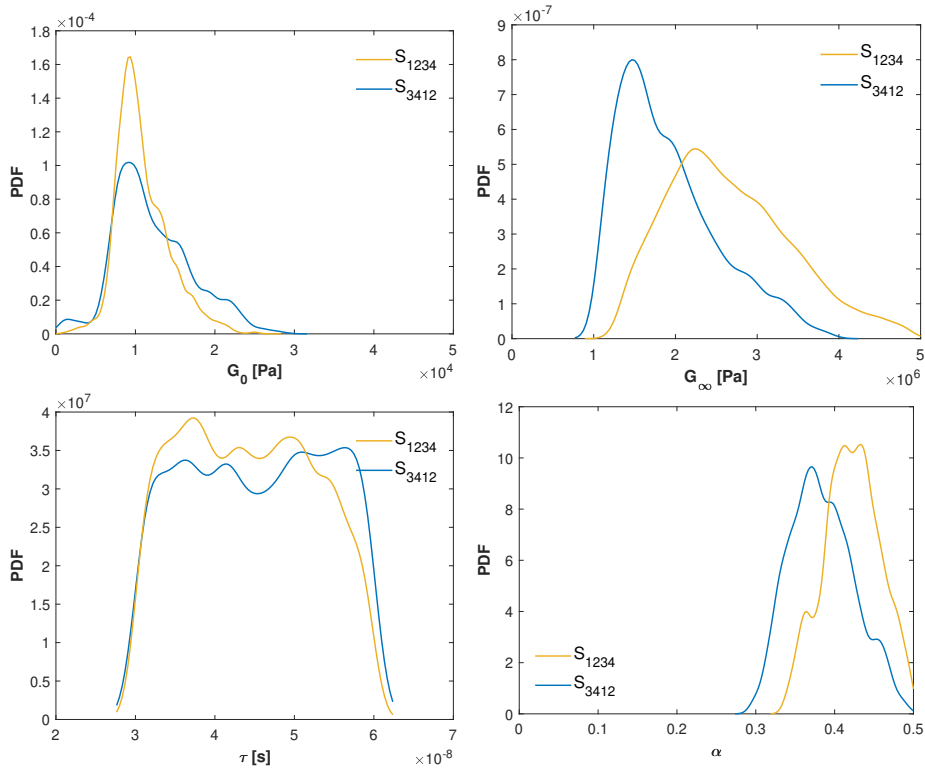


Figure 7.10: PDFs for the parameters of the 4PFDM of material B.

Finally, the uncertainty propagation from the model parameters $\theta \sim \pi(\theta|\mathbf{Y})$ to the structure's frequency response functions $\mathbf{F}\tilde{\mathbf{R}}\mathbf{F}(\omega)$ was done for both measurement subsets S_{1234} and S_{3412} . For this, the FRFs were computed through the multi-model approach considering all frequency range, e.g. from 0 to 800 Hz. All samples $\{\theta^{(1)}, \dots, \theta^{(N_{mc})}\}$ from the posterior distribution $\pi(\theta|\mathbf{Y})$ were

7.4. RESULTS & DISCUSSION: IDENTIFICATION OF VISCOELASTIC PARAMETERS

considered as input to the forward problem in order to guarantee mean square convergence.

Figures 7.11 and 7.12 show the results of this uncertainty propagation. They graphically illustrate the 95 % credibility interval of the calibrated 4PFDM and the FRFs measured by accelerometers ACi and ACj for each measurement subset S_{ijkl} .

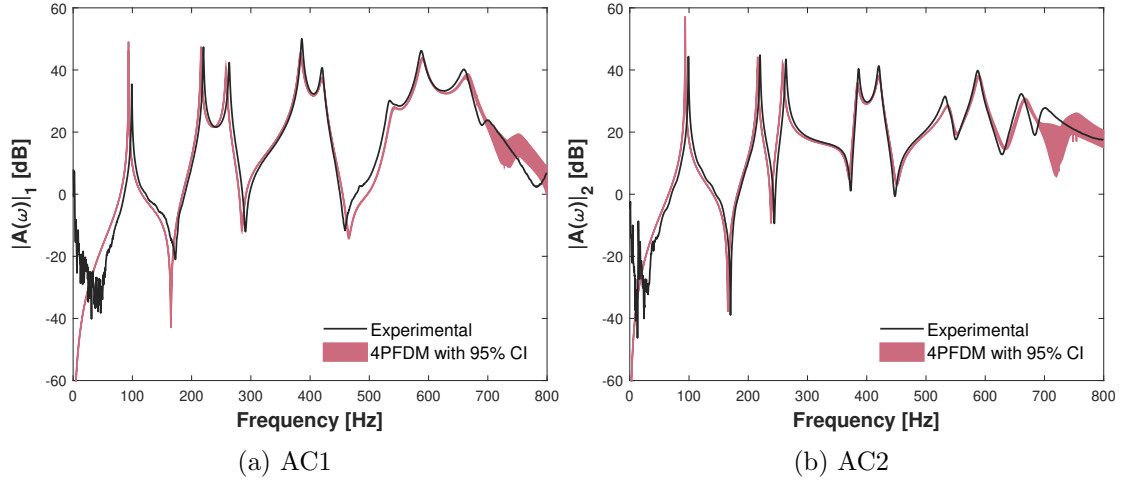


Figure 7.11: Uncertainty propagation when considering $\theta \sim \pi(\theta|Y)$ for measurement subset S_{1234} of material B. Frequency response functions computed for the two accelerometers AC1 and AC2 used in the calibration procedure.

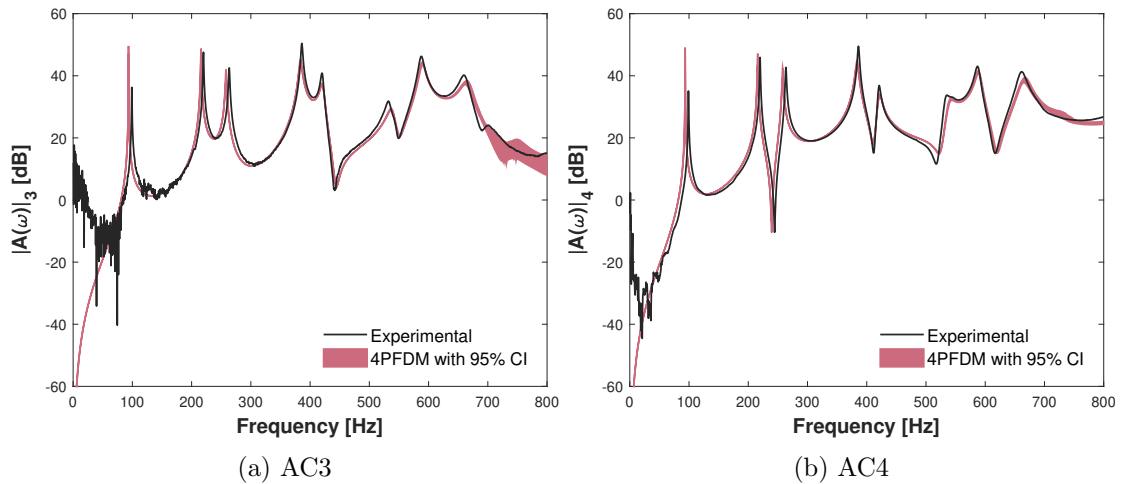


Figure 7.12: Uncertainty propagation when considering $\theta \sim \pi(\theta|Y)$ for measurement subset S_{3412} of material B. Frequency response functions computed for the two accelerometers AC3 and AC4 used in the calibration procedure.

It can be seen that the credibility intervals were quite narrow for most of the frequency range.

7.4. RESULTS & DISCUSSION: IDENTIFICATION OF VISCOELASTIC PARAMETERS

Higher uncertainties appeared after approximately 680 Hz. It can also be noticed that the largest discrepancies between the calibrated model and the corresponding measured data happened in the frequency range [680-800] Hz for both FRFs in the measurement subset S_{1234} and for the FRF obtained by AC3 in the measurement subset S_{3412} . This difficulty may be related to the multi-model approach used to compute the FRFs in the uncertainty propagation. Nevertheless, a good agreement, on the whole, can be observed.

It is worth mentioning that the issue related to high frequencies could be minimized, for example, if the direct method was employed to calculate FRFs. To exemplify this fact, the FRFs were thus computed through the direct method considering only the posterior mean values of the unknown parameters θ due to the computational costs. Figures 7.13 and 7.14 show the results obtained for both data-sets, highlighting the improvements achieved.

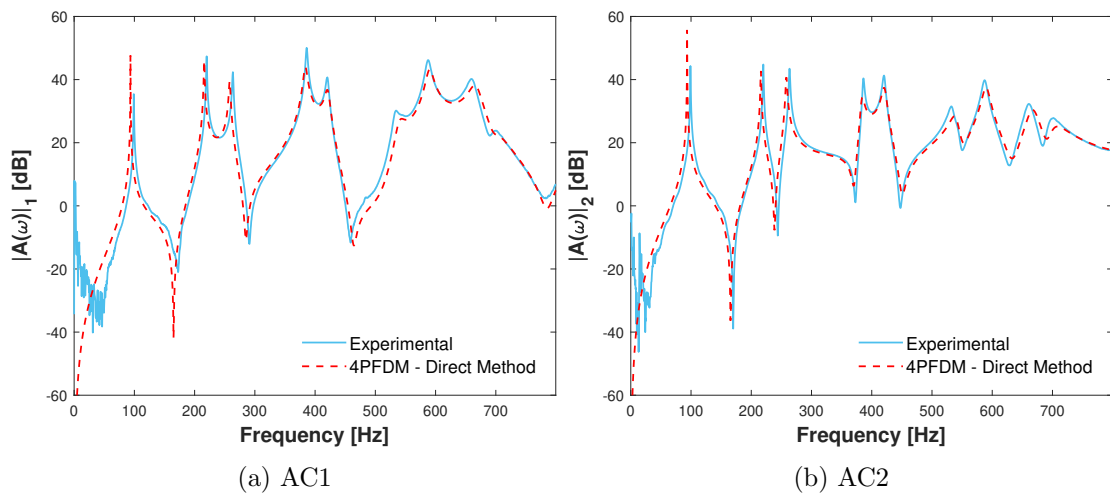


Figure 7.13: Comparison between experimental data and the calibrated model for measurement subset S_{1234} of material B. The frequency response function was computed through the direct method using the posterior mean value of the unknown parameters θ .

7.4. RESULTS & DISCUSSION: IDENTIFICATION OF VISCOELASTIC PARAMETERS

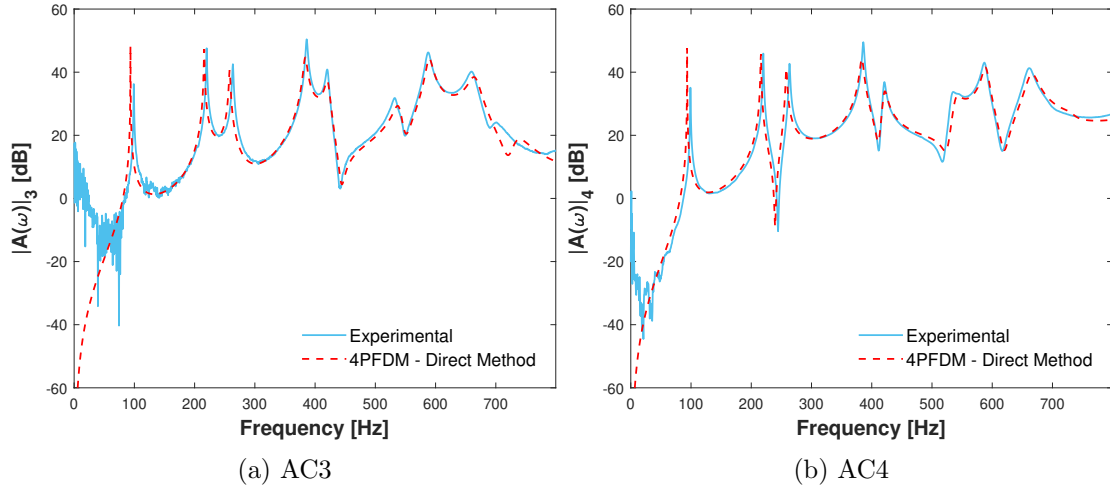


Figure 7.14: Comparison between experimental data and the calibrated model for measurement subset S_{3412} of material B. The frequency response function was computed through the direct method using the posterior mean value of the unknown parameters θ .

7.4.1.3 Model validation

Once a model has been calibrated using a probabilistic approach, the next step is to evaluate the degree to which a given model predicts the response of interest for the studied system. To achieve this goal, the observed data was different from those used in model updating. Two steps, one qualitative and the other quantitative, were carried out.

The first stage of validation consisted of performing the uncertainty propagation for the FRFs of the two accelerometers A_k and A_l in each measurement subset S_{ijkl} . It is worth reminding that the information provided by these two accelerometers was not used to update the model parameters.

The FRFs were thus computed through the multi-model approach from 0 to 800 Hz. All samples $\{\theta^{(1)}, \dots, \theta^{(N_{mc})}\}$ from the posterior distribution $\pi(\theta|\mathbf{Y})$ were considered as input to the forward problem in order to guarantee mean square convergence.

Figures 7.15 and 7.16 show the posterior predictive probabilities for the FRFs of each measurement subset S_{1234} and S_{3412} , respectively. They compare the 95% credibility interval for the 4PFDM, computed after propagating the uncertainty in model parameters, and the FRFs measured by accelerometer AC_k and AC_l for each measurement subset S_{ijkl} .

7.4. RESULTS & DISCUSSION: IDENTIFICATION OF VISCOELASTIC PARAMETERS

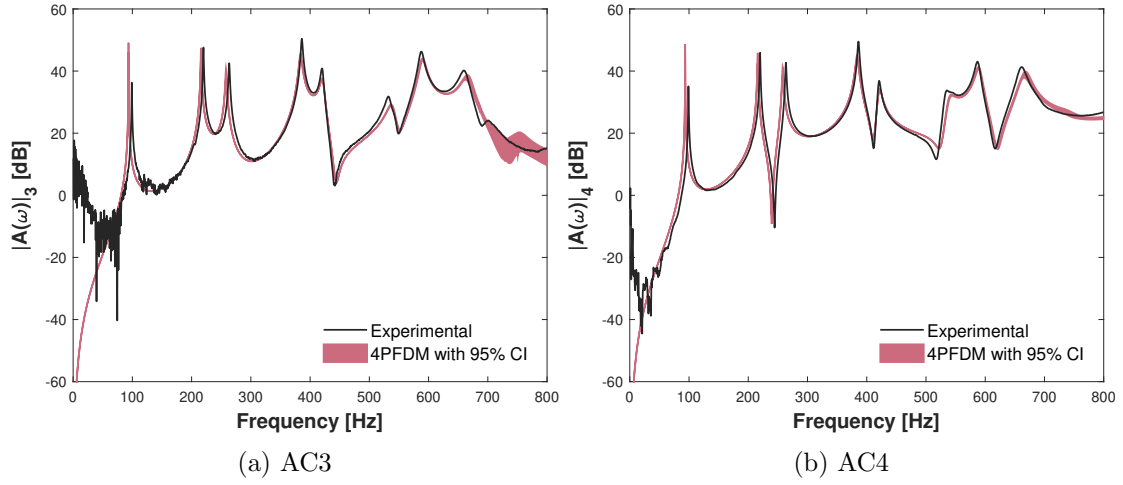


Figure 7.15: Uncertainty propagation when considering $\theta \sim \pi(\theta|Y)$ for measurement subset S_{1234} of material B. Frequency response functions computed for the two accelerometers AC3 and AC4 used in the validation procedure.

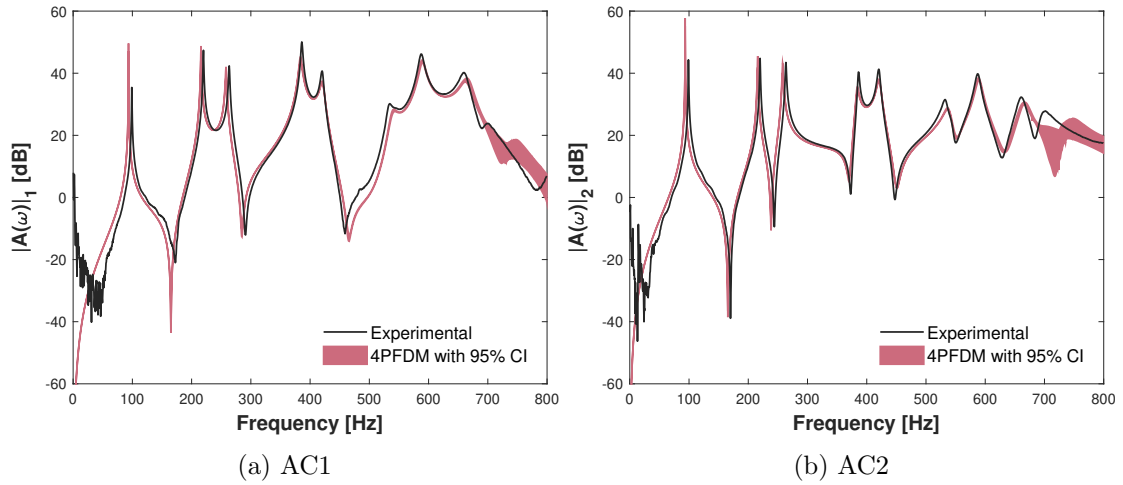


Figure 7.16: Uncertainty propagation when considering $\theta \sim \pi(\theta|Y)$ for measurement subset S_{3412} of material B. Frequency response functions computed for the two accelerometers AC1 and AC2 used in the validation procedure.

For both data-sets, the credibility intervals were quite narrow. After 680 Hz, higher uncertainties appeared, and the largest discrepancies between the model prediction and the corresponding experimental result were observed. As mentioned for the calibration step, this issue at high frequencies may be related to the model reduction technique used and can be minimized if one makes use of the direct method to compute the FRFs.

7.4. RESULTS & DISCUSSION: IDENTIFICATION OF VISCOELASTIC PARAMETERS

Despite this, both model predictions presented good levels of agreement between the experimental measurements and the 95 % credibility intervals. They satisfactorily predicted the resonant frequencies and FRF peaks. These results indicate that the simplified calibrated models have great predictive capabilities of the system's response.

The second stage of validation consisted of measuring the accuracy between experimental data and model predictions. For this, a validation metric was appropriately defined to quantify the discrepancies between the model prediction with measured data.

In this work, a validation metric based on the relative discrepancy for resonant frequencies (hereinafter referred to as δf_r) in [%] was adopted. It was defined as follows

$$\delta f_n^i = \frac{|f_{r-exp}^i - f_{r-sim}^i|}{f_{r-exp}^i} \times 100\%, \quad (7.9)$$

where f_{r-exp}^i and f_{r-sim}^i correspond, respectively, to the i^{th} measured and estimated resonant frequency.

Table 7.6 shows the discrepancies calculated from the resonant frequencies measured by each accelerometer used for the validation step. For both subsets S_{1234} and S_{3412} , it is possible to observe that the highest values estimated were less than 7%. Assuming 20 % as the upper limit on acceptable accuracy for model validation as stated by Schwer [58], one can thus infer that the agreement between the predictions and the experiment is quite high.

Table 7.6: Validation metric δf_r [%] for material B.

| Subset | | δf_n^1 | δf_n^2 | δf_n^3 | δf_n^4 | δf_n^5 | δf_n^6 | δf_n^7 | δf_n^8 | δf_n^9 |
|------------|-----|----------------|----------------|----------------|----------------|----------------|----------------|----------------|----------------|----------------|
| S_{1234} | AC3 | 5.6 | 1.8 | 2.1 | 0.5 | 0 | 0.9 | 0.4 | 0.7 | 6.8 |
| | AC4 | 5.6 | 1.8 | 2.1 | 0.6 | 0.2 | 1.5 | 0.3 | 0.9 | - |
| S_{3412} | AC1 | 5.6 | 1.8 | 2.1 | 0.5 | 0.1 | 1.4 | 0.3 | 0.5 | 5.8 |
| | AC2 | 5.6 | 1.8 | 2.1 | 0.5 | 0 | 1.9 | 0.4 | 0.4 | 5.6 |

The largest discrepancies were estimated for the first and the last mode of vibration and they can be explained as follows. The first is related to the differences between the hypotheses of the numerical model and the experimental apparatus: the blades that connect the aluminum plate to the steel frame built around it were not considered despite adding some stiffness to the system. The last is related to the model reduction technique adopted to compute the system's response.

7.4. RESULTS & DISCUSSION: IDENTIFICATION OF VISCOELASTIC PARAMETERS

Therefore, both measurement subsets led to good levels of fitting for the investigated frequency band. All stochastic models built were in good agreement with the corresponding experimental data. The results of the validation metric reinforced the idea that the model can reproduce the dynamic behavior of the system within the low-frequency range.

7.4.1.4 Comparison with other techniques

As discussed in Chapter 6, the viscoelastic properties of material B were characterized through a torsional rheometer (TR), and from these results, a fractional derivative model was calibrated by the least square method in the work of Henriques et al. [1]. This subsection presents a comparison between the parameters estimated by Henriques et al. [1] and by the proposed inverse method, and their effects on model predictions.

Table 7.7 compares the estimated values of the four parameters $\theta = \{G_0, G_\infty, \tau, \alpha\}$ by the different approaches. It is possible to observe that the average values estimated for the parameters G_∞ and α are more discrepant (in percentage terms) when compared to those estimated by the TR. Nevertheless, if one considers the credibility intervals shown in Tab. 7.5, all estimated parameters had a good agreement with each other, regardless of the calibration procedure.

Table 7.7: Comparison between the four parameters $\theta = \{G_0, G_\infty, \tau, \alpha\}$ estimated by different approaches for material B.

| Method | $\mathbb{E}[G_0]$ [Pa] | $\mathbb{E}[G_\infty]$ [Pa] | $\mathbb{E}[\tau]$ [s] | $\mathbb{E}[\alpha]$ |
|--------------------------|------------------------|-----------------------------|------------------------|----------------------|
| <i>TR</i> | 1.31×10^4 | 2.11×10^6 | 4.70×10^{-8} | 0.30 |
| <i>MCMC</i> – S_{1234} | 1.09×10^4 | 2.66×10^6 | 4.42×10^{-8} | 0.42 |
| <i>MCMC</i> – S_{3412} | 1.21×10^4 | 1.92×10^6 | 4.53×10^{-8} | 0.38 |

As explained in subsection 2.5.1 of Chapter 2, parameters G_0 and G_∞ are related to the modulus value when frequency tends, respectively, to zero and infinity, parameter τ is related to the relaxation time, and α is the order of the fractional model that affects the slope of the curve. Thus, the results obtained suggest that, when evaluating the behavior of the complex shear modulus $G^*(\omega)$ along with the frequency, the greatest impact is related to the slope of the curve as the parameter α varied considerably.

The complex shear modulus was thus calculated using the parameters estimated by each method.

7.4. RESULTS & DISCUSSION: IDENTIFICATION OF VISCOELASTIC PARAMETERS

For the proposed one, all samples from the posterior PDFs were considered for both measurement subsets in order to construct the credibility intervals. Figure 7.18 shows the results obtained for the absolute value, $|G^*(\omega)|$, considering the frequency range from 10^{-4} to 10^{10} Hz. As expected, the main difference among the curves is related to their slope.

Finally, to analyze the impacts of these sets of parameters on the FRFs, model predictions were calculated using the direct method considering the mean values of the parameters for the location of AC1. The results are shown in Fig. 7.18.

It can be seen that all sets of parameters can provide a good correlation with the experimental results. The main difference among them is related to the amplitude of the FRF peaks as the model prediction provided by TR set overestimated them on the whole. The resonance frequencies, on the other hand, were quite similar, as evidenced on Tab. 7.8.

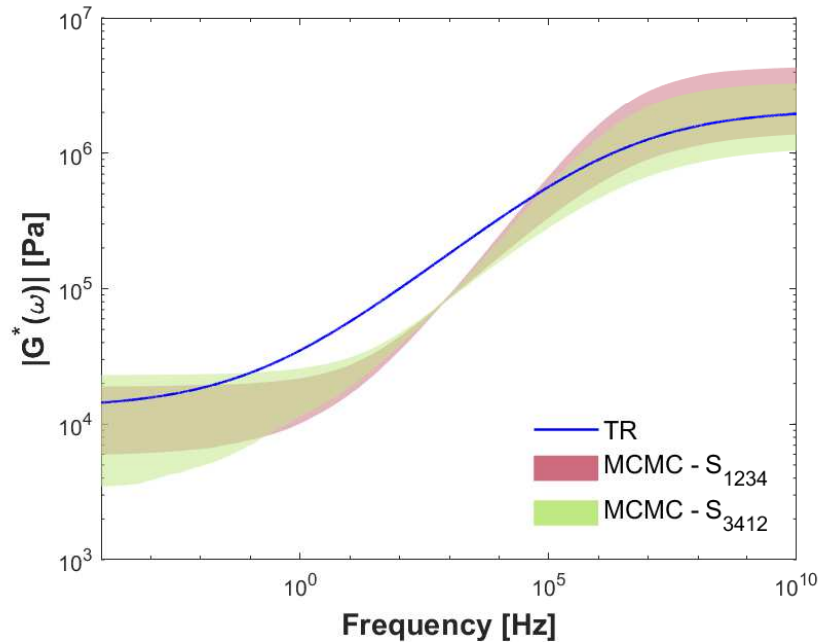


Figure 7.17: Absolute value of complex shear modulus, $|G^*(\omega)|$, of material B. Comparison between the calibrated models from TR measurements [1] and the proposed inverse characterization.

7.4. RESULTS & DISCUSSION: IDENTIFICATION OF VISCOELASTIC PARAMETERS

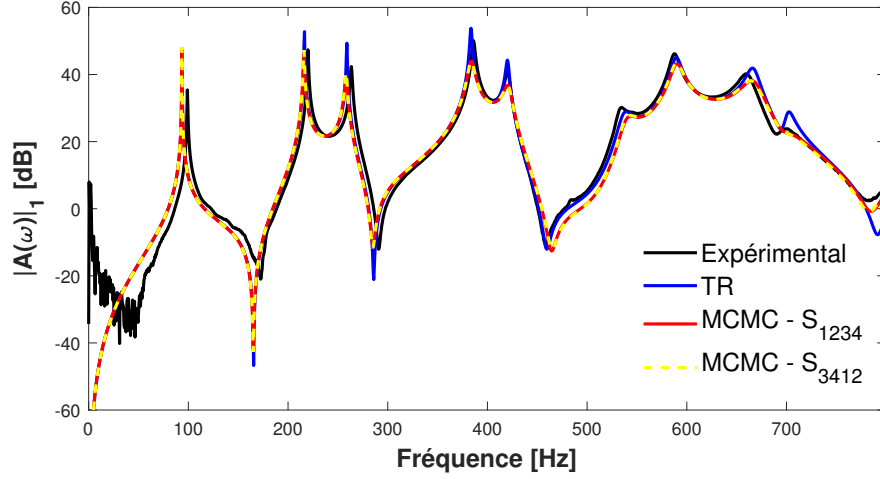


Figure 7.18: FRFs obtained for the location of AC1 for material B. Comparison between experimental data and model predictions using parameters obtained from TR measurements [1] and the ones from the proposed inverse characterization.

Table 7.8: Comparison between the resonance frequencies from measured data and calibrated models by different approaches for material B.

| | 1 | 2 | 3 | 4 | 5 | 6 | 7 | 8 | 9 |
|--------------------------------|------|-------|-------|-------|-------|-------|-------|-------|-------|
| <i>Experimental</i> | 99.0 | 220.0 | 263.5 | 386.0 | 420.0 | 534.5 | 587.5 | 660.0 | 700.0 |
| <i>TR</i> | 93.5 | 216.5 | 259.0 | 383.5 | 420.0 | 539.0 | 589.5 | 666.0 | 702.5 |
| <i>MCMC - S₁₂₃₄</i> | 93.5 | 216.0 | 258.0 | 384.0 | 420.0 | 544.0 | 590.5 | 665.0 | - |
| <i>MCMC - S₃₄₁₂</i> | 93.5 | 216.0 | 258.0 | 383.5 | 420.0 | 543.0 | 590.0 | 664.0 | - |

7.4.2 Material C

7.4.2.1 Description of calibration and validation procedures

The goal of this inverse characterization was again to identify the four viscoelastic parameters $\theta = \{G_0, G_\infty, \tau, \alpha\}$. Nevertheless, these parameters may vary significantly in terms of orders of magnitude, affecting a lot the search for parameters. Since the scale of each parameter was not so well defined for material C, they were rescaled logarithmically to have design parameters with the same order of magnitude to avoid conditioning problems [6, 143] as follows

7.4. RESULTS & DISCUSSION: IDENTIFICATION OF VISCOELASTIC PARAMETERS

$$p_1 = 0.1 \log(G_0), \quad (7.10a)$$

$$p_2 = 0.1 \log(G_\infty), \quad (7.10b)$$

$$p_3 = -0.1 \log(\tau) \quad (7.10c)$$

$$p_4 = \alpha. \quad (7.10d)$$

Similarly to material B, the experimental data \mathbf{Y} for both calibration and validation steps comprised the frequency response functions (FRFs) computed from the point excitation force provided by the impact hammer and the response accelerations measured by the four accelerometers $\{AC1, AC2, AC3, AC4\}$, as shown in Fig. 6.13. Moreover, two different subsets were generated to quantify the influence of a particular calibration data-set on the model updating process, and because model validation must be independent of model updating, as detailed in Tab. 7.9.

Table 7.9: Definition of subsets S_{ijkl} used for model calibration and model validation of material C, where $i, j, k, l \in \{1, 2, 3, 4\}$ and $i \neq j \neq k \neq l$.

| Subset | Model calibration | Model validation |
|------------|--|--|
| S_{1234} | $\mathbf{Y} = \{\mathbf{F}\tilde{\mathbf{R}}\mathbf{F} _{AC1} \mathbf{F}\tilde{\mathbf{R}}\mathbf{F} _{AC2}\}^T$ | $\mathbf{Y} = \{\mathbf{F}\tilde{\mathbf{R}}\mathbf{F} _{AC3} \mathbf{F}\tilde{\mathbf{R}}\mathbf{F} _{AC4}\}^T$ |
| S_{3412} | $\mathbf{Y} = \{\mathbf{F}\tilde{\mathbf{R}}\mathbf{F} _{AC3} \mathbf{F}\tilde{\mathbf{R}}\mathbf{F} _{AC4}\}^T$ | $\mathbf{Y} = \{\mathbf{F}\tilde{\mathbf{R}}\mathbf{F} _{AC1} \mathbf{F}\tilde{\mathbf{R}}\mathbf{F} _{AC2}\}^T$ |

Accordingly, the measured data \mathbf{Y} for a given subset S_{ijkl} , described in Tab. 7.9, was defined as a 4N-dimensional vector such as

$$\mathbf{Y} = \{\Re[\mathbf{F}\tilde{\mathbf{R}}\mathbf{F}|_{ACi}]^T \Re[\mathbf{F}\tilde{\mathbf{R}}\mathbf{F}|_{ACj}]^T \Im[\mathbf{F}\tilde{\mathbf{R}}\mathbf{F}|_{ACi}]^T \Im[\mathbf{F}\tilde{\mathbf{R}}\mathbf{F}|_{ACj}]^T\}^T. \quad (7.11)$$

The calibration step again did not consider all the experimental points obtained in the measurements to improve the computational cost. From the results shown in subsection 7.2.3, however, only the first five resonance peaks were well defined for the structure with material C, resulting in a specific selection. Until 400 Hz, only the experimental points related to the resonance peaks and ten more points linearly-spaced frequency grids ($\Delta f = 1.5$ Hz) located around each resonance peak were selected, similar to that used in the analysis of material B. After 400 Hz, in turn, some experimental

7.4. RESULTS & DISCUSSION: IDENTIFICATION OF VISCOELASTIC PARAMETERS

points linearly-spaced frequency grids were chosen where there was a tendency for resonance peaks. This technique reduced drastically the dimension of the vector \mathbf{Y} : from 6400 to 376 points. Figure 7.19 illustrates the selected points when considering the experimental data provided by AC1.

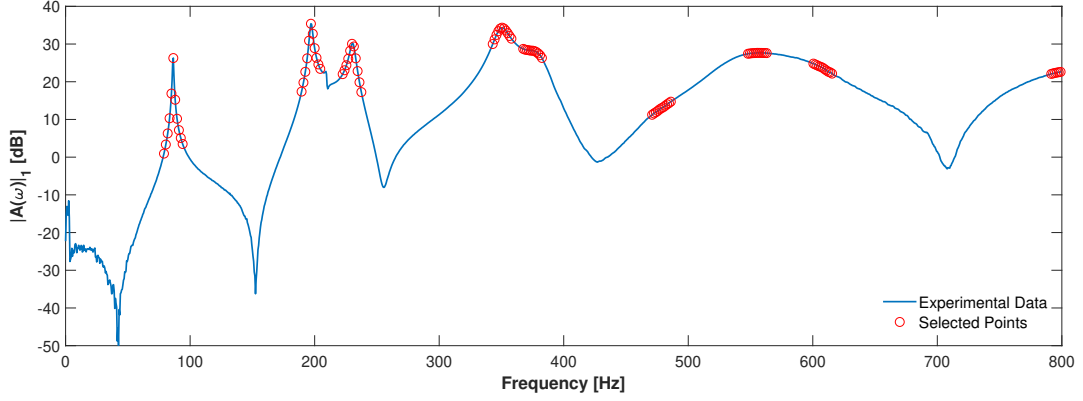


Figure 7.19: Selected points for model calibration procedure for material C.

As for the priors $\pi_0(\boldsymbol{\theta})$ of the design parameters $\{p_1, p_2, p_3, p_4\}^T$, it was assumed uniform distributions whose marginals were defined to be within the set D_θ such as

$$D_{p_1} = \{p_1 \in \mathbb{R} | 0.4 < p_1 < 0.6\}, \quad (7.12a)$$

$$D_{p_2} = \{p_2 \in \mathbb{R} | 0.5 < p_2 < 0.8\}, \quad (7.12b)$$

$$D_{p_3} = \{p_3 \in \mathbb{R} | 0.6 < p_3 < 1\}, \quad (7.12c)$$

$$D_{p_4} = \{p_4 \in \mathbb{R} | 0 < p_4 < 1\}. \quad (7.12d)$$

It is important to underline that every random variable was constructed under the hypothesis that they were mutually independent. Also, the limit values for parameters p_1 and p_2 were chosen based on the results presented in the work of Bonfiglio et al. [98].

The likelihood function $\pi(\mathbf{Y}|\boldsymbol{\theta})$ was once more defined by the distribution of the additive error, leading to $\mathbf{e} \sim N(\mathbf{0}, \boldsymbol{\Sigma})$. A diagonal covariance matrix $\boldsymbol{\Sigma}$, as shown in Eq. 3.9, was considered assuming sample-based error variance. The variance σ_i^2 was considered as an additional random parameter defined by the inverse gamma distribution [25].

Thus, with all parameters defined, the calibration of the model started. Firstly, a deterministic

7.4. RESULTS & DISCUSSION: IDENTIFICATION OF VISCOELASTIC PARAMETERS

analysis was done to assess the maximum a posteriori estimate $\hat{\boldsymbol{\theta}}_{MAP}$ shown in Eq. 3.11. Then, the approximate posterior covariance matrix was determined as $\hat{\Sigma} \approx (\mathbf{J}^T \Sigma_0 \mathbf{J})^{-1}$ whose initial covariance matrix Σ_0 was calculated by Eq. 7.8. Finally, the posterior distribution of the unknown parameters $\pi(\boldsymbol{\theta}|\mathbf{Y})$ was explored with the DRAM algorithm. In the AM method, the adaptation occurred at prescribed intervals of length $j_0 = 100$ with a Gaussian candidate distribution. In the DR method, three stages were considered in which $\gamma_s = \{1/5, 1/4, 1/3\}$. A total number of $N_{MC} = 40000$ samples was considered.

7.4.2.2 Model calibration

The first step of this inverse characterization consisted of performing a MAP estimator to find the best point $\hat{\boldsymbol{\theta}}_{MAP}$ to start MCMC sampling. For this particular case, it was equivalent to performing the ML estimator since uniform prior distributions were adopted for the unknown parameters. Table 7.10 shows the results obtained for the two measurement subsets S_{1234} and S_{3412} . It can be noted that each set of experimental data resulted in a different estimate for the four parameters, among which G_∞ was the one most affected.

Table 7.10: MAP results for the two measurement subsets S_{ijkl} , $i, j, k, l \in \{1, 2, 3, 4\}$ and $i \neq j \neq k \neq l$, of material C.

| Subset | G_0 [Pa] | G_∞ [Pa] | τ [s] | α |
|------------------|--------------------|--------------------|-----------------------|----------|
| Initial | 1.00×10^5 | 1.00×10^7 | 1.00×10^{-8} | 0.20 |
| MAP - S_{1234} | 2.10×10^4 | 7.91×10^7 | 3.31×10^{-8} | 0.62 |
| MAP - S_{3412} | 1.95×10^4 | 4.89×10^7 | 3.48×10^{-8} | 0.57 |

Figure 7.20 compares the measured FRF with the ones estimated using any initial parameters $\boldsymbol{\theta}_0$ and using MAP estimates $\hat{\boldsymbol{\theta}}_{MAP}$. This comparison evidences that $\hat{\boldsymbol{\theta}}_{MAP}$ is more realistic for the measured data than the initial parameters $\boldsymbol{\theta}_0$.

Thereafter, DRAM algorithm explored the posterior PDFs. Figure 7.21 presents the chains together with the corresponding cumulative means. The well-mixing behavior of the chains and the convergence of the method to the stationary posterior PDF can be easily verified in the Markov chain of all the parameters.

7.4. RESULTS & DISCUSSION: IDENTIFICATION OF VISCOELASTIC PARAMETERS

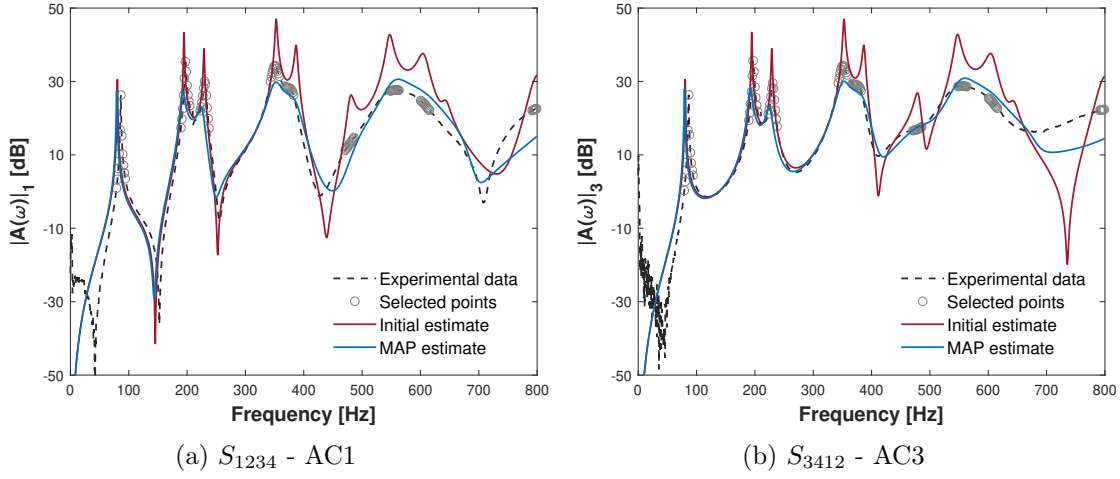


Figure 7.20: Comparison between experimental data and model prediction using MAP estimate $\hat{\theta}_{MAP}$ for both measurement subsets S_{1234} and S_{3412} of material C.

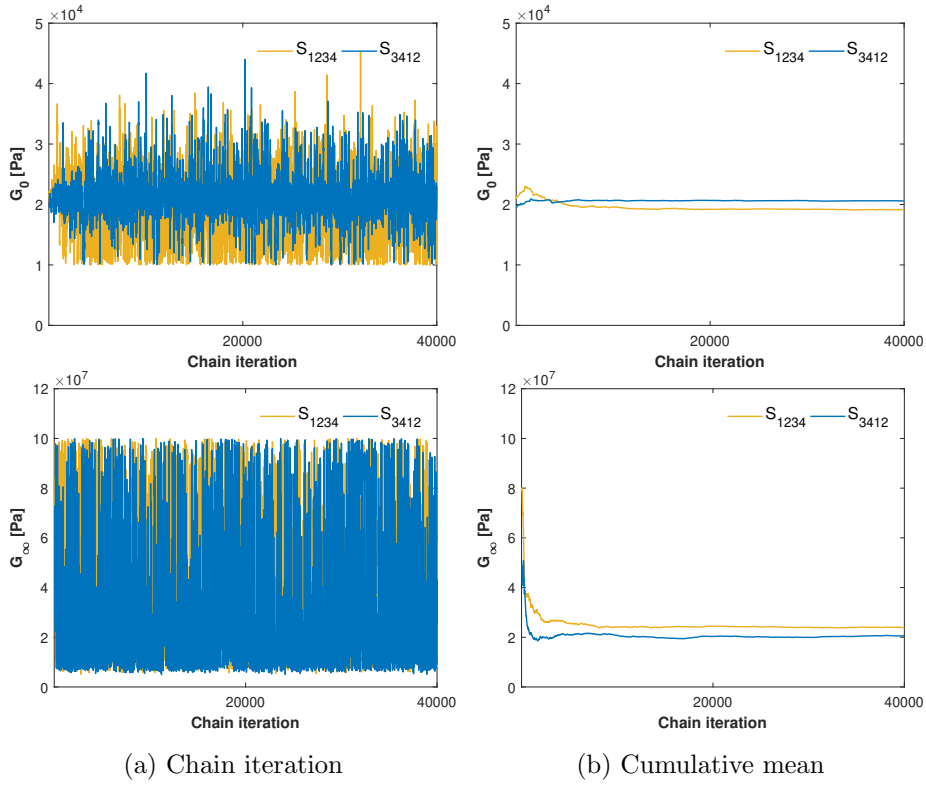


Figure 7.21: Convergence analysis for the 4PFDM using DRAM algorithm of material C.

7.4. RESULTS & DISCUSSION: IDENTIFICATION OF VISCOELASTIC PARAMETERS

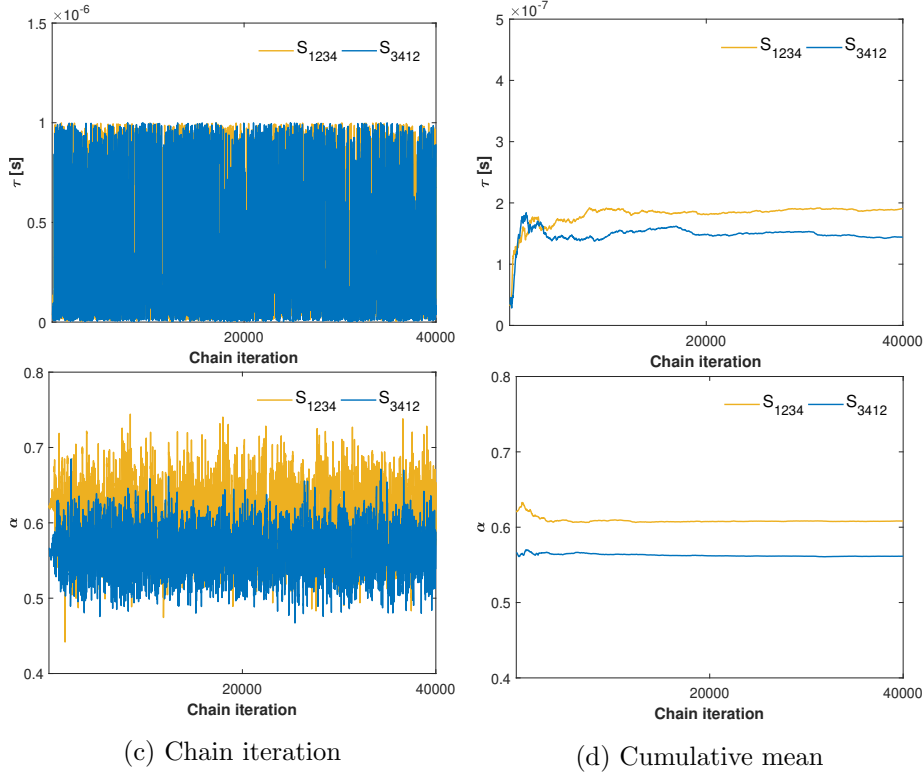


Figure 7.21: Convergence analysis for the 4PFDM using DRAM algorithm of material C.

Table 7.11 summarizes the MCMC sampling for both measurement subsets S_{1234} and S_{3412} . The acceptance rate and the number of samples needed for the convergence varied according to the set of experimental data used during the calibration process. Nevertheless, both sets presented acceptable values.

Table 7.11: MCMC results using DRAM algorithm for the two measurement subsets S_{ijkl} , $i, j, k, l \in \{1, 2, 3, 4\}$ and $i \neq j \neq k \neq l$, of material C.

| Subset | Total samples | Burn-in | Acceptance rate |
|------------|---------------|---------|-----------------|
| S_{1234} | 40000 | 30000 | 54.17 |
| S_{3412} | 40000 | 35000 | 64.92 |

Table 7.12 presents the posterior mean ($\mathbb{E}[\theta]$) together with the 95% credibility interval (CI) of each model parameter θ obtained after discarding the samples from the burn-in period. It can be seen that the results obtained by the different subsets were very close to each other. The parameter α was the one most affected by the measurement subset, while G_∞ was the one less affected.

7.4. RESULTS & DISCUSSION: IDENTIFICATION OF VISCOELASTIC PARAMETERS

Table 7.12: Posterior mean value and 95 % credibility interval of the unknown parameters θ for the two measurement subsets S_{ijkl} , $i, j, k, l \in \{1, 2, 3, 4\}$ and $i \neq j \neq k \neq l$, of material C.

| Subset | $\mathbb{E}[G_0]$ 95 % CI | [Pa] | $\mathbb{E}[G_\infty]$ 95 % CI | [Pa] | $\mathbb{E}[\tau]$ 95 % CI | [s] | $\mathbb{E}[\alpha]$ 95 % CI |
|------------|------------------------------|---------------|-----------------------------------|---------------|-------------------------------|------------------|---------------------------------|
| S_{1234} | 1.90 [1.05, 2.79] | $\times 10^4$ | 2.36 [0.80, 9.10] | $\times 10^7$ | 1.93 [0.14, 9.56] | $\times 10^{-7}$ | 0.61 [0.53, 0.68] |
| S_{3412} | 2.03 [1.26, 2.94] | $\times 10^4$ | 2.22 [0.71, 9.04] | $\times 10^7$ | 1.24 [0.08, 9.33] | $\times 10^{-7}$ | 0.56 [0.51, 0.62] |

Scatter plots were thus constructed to assess whether the independence hypothesis adopted for all random variables was coherent. Figure 7.22 shows the results obtained for both calibrations performed, evidencing little or no correlation between the parameters.

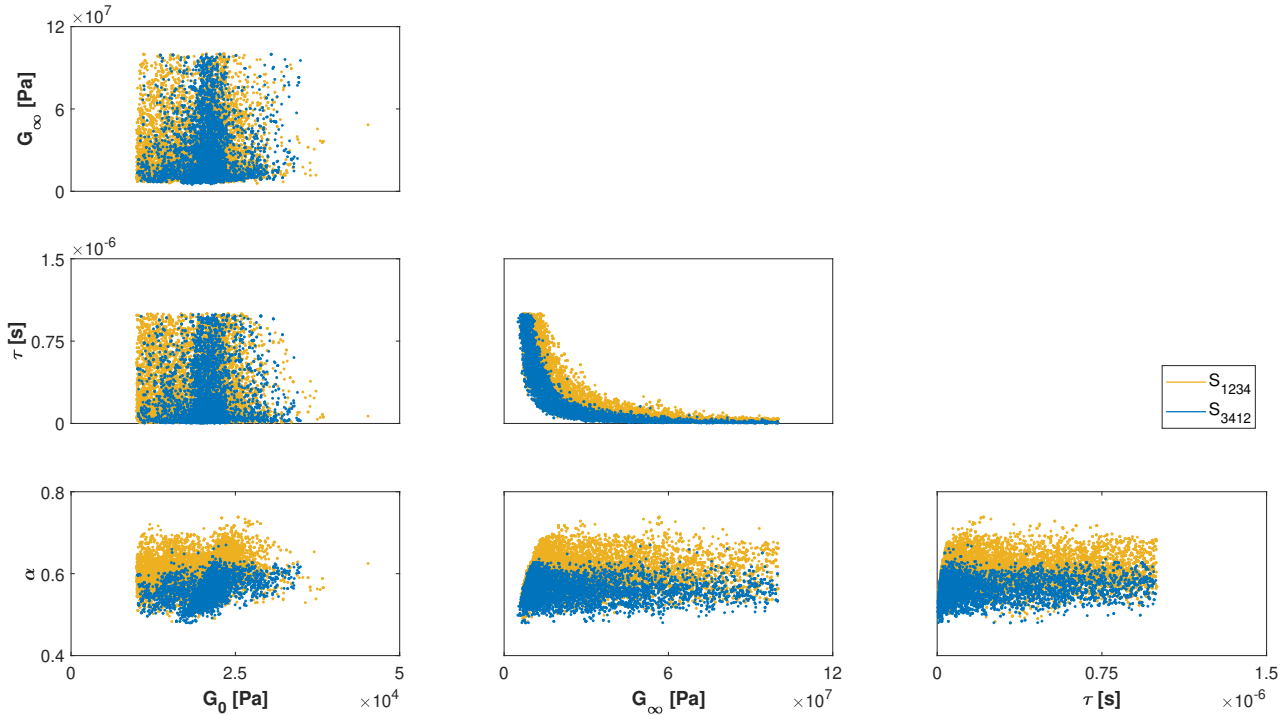


Figure 7.22: Posterior samples generated using DRAM algorithm for the 4PFDM of material C.

Figure 7.23 shows the marginal posterior PDFs computed for each unknown parameter. In both measurement subsets, the PDFs for parameters G_∞ and τ deviated from Gaussian distribution. Nevertheless, they almost did not differ with the data-set used in the calibration step.

7.4. RESULTS & DISCUSSION: IDENTIFICATION OF VISCOELASTIC PARAMETERS

Finally, the uncertainties related to the estimated parameters $\boldsymbol{\theta} \sim \pi(\boldsymbol{\theta}|\mathbf{Y})$ were propagated for both sets to observe the behavior of the calibrated models. In this regard, the FRFs were computed through the multi-model approach considering all frequency range. All samples from the posterior PDF $\pi(\boldsymbol{\theta}|\mathbf{Y})$ were used as input to the forward problem, ensuring the mean square convergence.

Figures 7.24 and 7.25 graphically compare the 95% credibility interval of the calibrated 4PFDM with the corresponding experimental result for both subsets S_{1234} and S_{3412} , respectively. It can be seen that the credibility intervals were quite narrow, increasing with frequency. The largest differences observed in the highest frequencies can be associated with the model reduction technique used to calculate the FRFs and also with the model assumptions.

Besides that, it can also be noted that the models underestimated the resonant peaks in terms of amplitude and frequency. Despite this, these simplified calibrated models are capable of describing the dynamic behavior of the system.

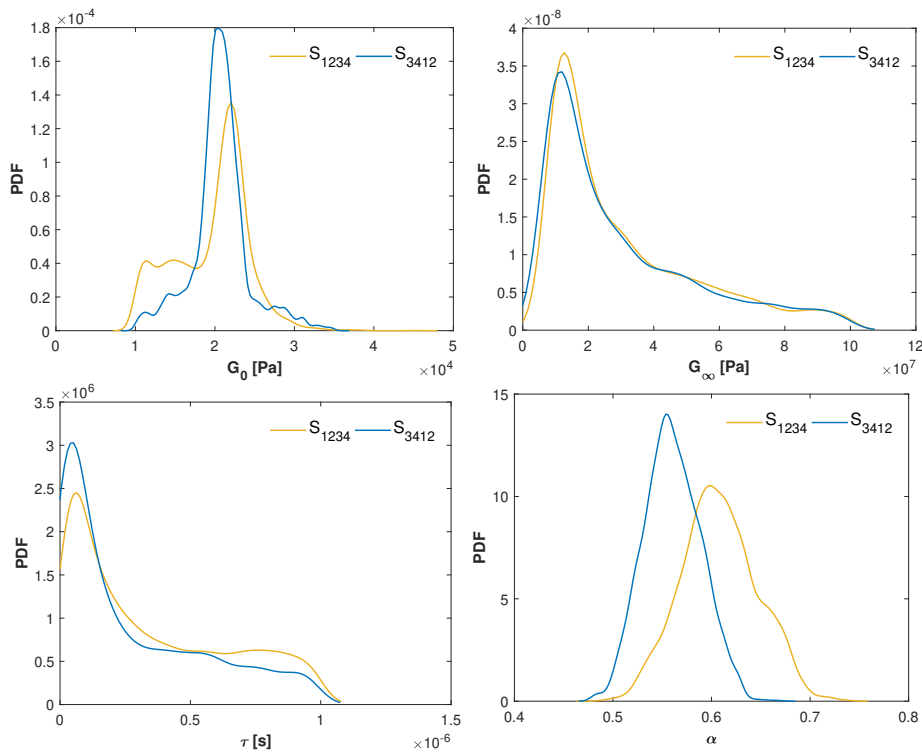


Figure 7.23: PDFs for the parameters of the 4PFDM of material C.

7.4. RESULTS & DISCUSSION: IDENTIFICATION OF VISCOELASTIC PARAMETERS

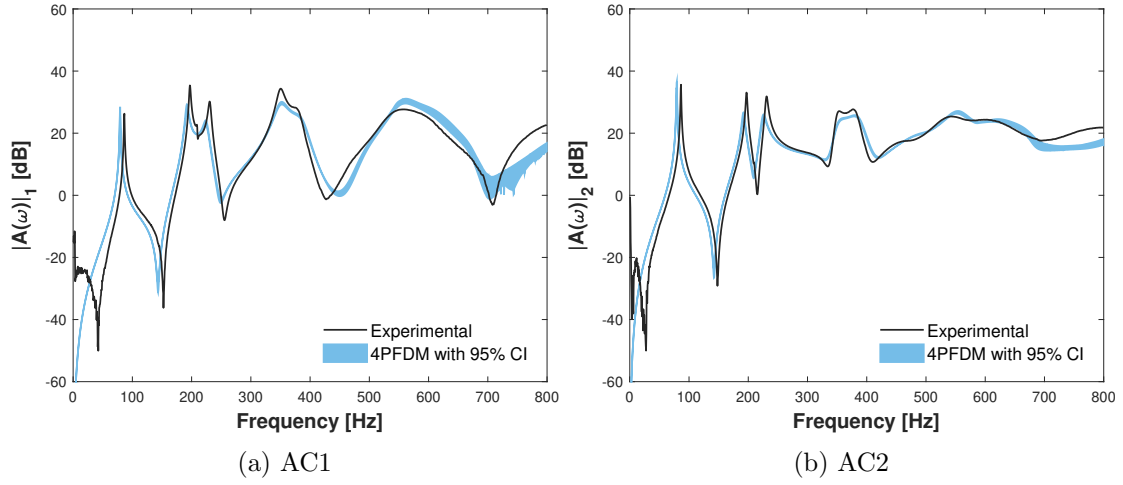


Figure 7.24: Uncertainty propagation when considering $\theta \sim \pi(\theta|\mathbf{Y})$ for measurement subset S_{1234} of material C. Frequency response functions computed for the two accelerometers AC1 and AC2 used in the calibration procedure.

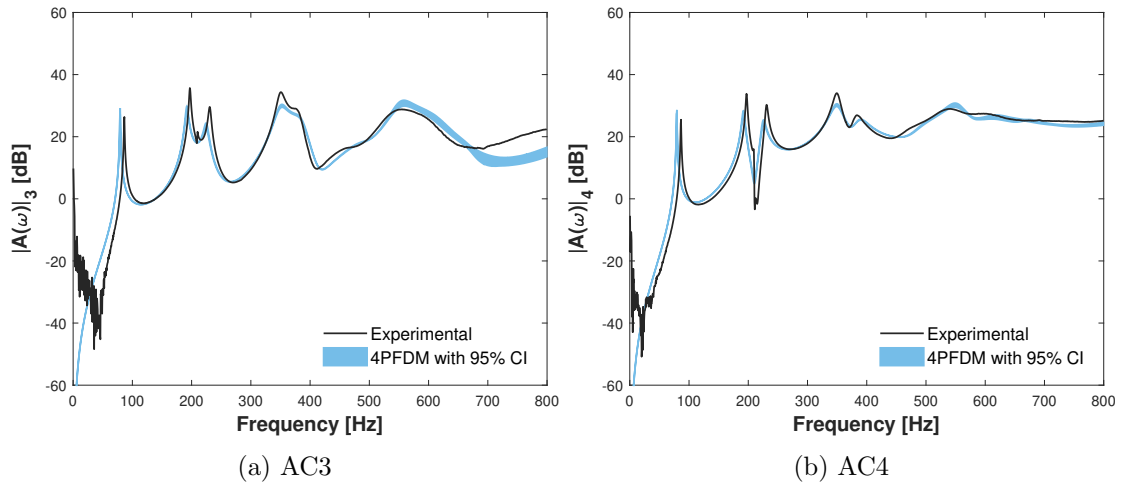


Figure 7.25: Uncertainty propagation when considering $\theta \sim \pi(\theta|\mathbf{Y})$ for measurement subset S_{3412} of material C. Frequency response functions computed for the two accelerometers AC3 and AC4 used in the calibration procedure.

7.4.2.3 Model validation

This section aims to assess the credibility of the calibrated models through the basic principles of a validation process. The observed data analyzed was thus different from the one used for the calibration step. Validation was performed by graphically comparing estimated and measured quantities, and by computing the validation metrics similarly to what was done to material B.

7.4. RESULTS & DISCUSSION: IDENTIFICATION OF VISCOELASTIC PARAMETERS

To start the validation procedure, the uncertainties inherent of the estimated parameters $\boldsymbol{\theta} \sim \pi(\boldsymbol{\theta}|\mathbf{Y})$ were propagated to the structure's frequency response functions $\mathbf{FRF}(\omega)$ of the two accelerometers A_k and A_l in each measurement subset S_{ijkl} . The FRFs were calculated using all samples $\{\boldsymbol{\theta}^{(1)}, \dots, \boldsymbol{\theta}^{(N_{mc})}\}$ from the posterior PDF $\pi(\boldsymbol{\theta}|\mathbf{Y})$ through the multi-model approach for the investigated frequency band.

The results of this forward uncertainty propagation for the subsets S_{1234} and S_{3412} are, respectively, represented in Figs. 7.26 and 7.27. In both cases, the 95 % credibility intervals of the 4PFDM are compared to the related experimental measurements, showing good accordance. The intervals were, on the whole, quite narrow. Also, higher discrepancies mainly related to the approximate method of calculating the FRFs can be observed after 500 Hz, as previously discussed in the calibration step.

To continue the process, the validation metric based on the relative discrepancy for resonant frequencies expressed in Eq. 7.9 was computed to quantify the degree of accuracy of the model predictions. Table 7.13 shows the computed values for the first five resonant peaks for both data-sets S_{1234} and S_{3412} .

It can be noted that the largest discrepancy of approximately 9 % was estimated for the first resonant peak. This value can be explained by the experimental assembly of the aluminum plate to the steel frame: the blades used to fix the aluminum plate added some stiffness to the system, which, in turn, was not taken into account in the modeling. Nevertheless, the upper limit of 20 % recommended by Schwer [58] for model validation was respected.

Therefore, both qualitative and quantitative results presented herein give a position in favor of the calibrated models. One may conclude that they reproduced quite well the dynamic behavior of the system.

7.4. RESULTS & DISCUSSION: IDENTIFICATION OF VISCOELASTIC PARAMETERS

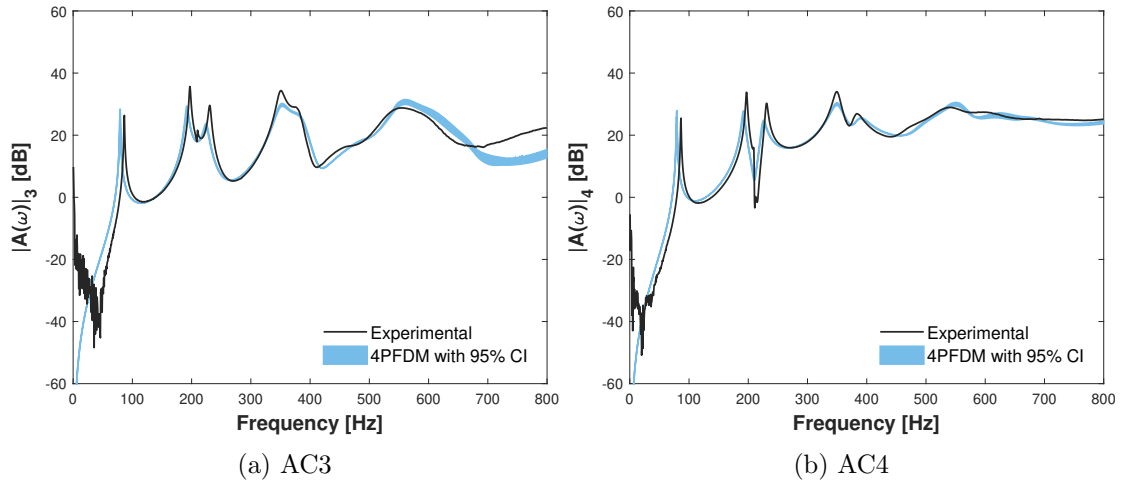


Figure 7.26: Uncertainty propagation when considering $\theta \sim \pi(\theta|Y)$ for measurement subset S_{1234} of material C. Frequency response functions computed for the two accelerometers AC3 and AC4 used in the validation procedure.

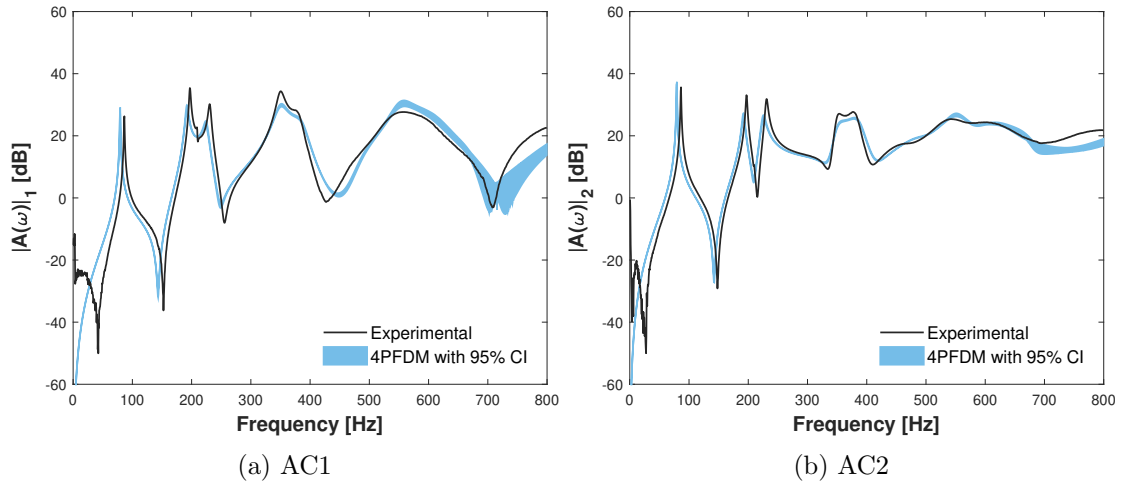


Figure 7.27: Uncertainty propagation when considering $\theta \sim \pi(\theta|Y)$ for measurement subset S_{3412} of material C. Frequency response functions computed for the two accelerometers AC1 and AC2 used in the validation procedure.

Table 7.13: Validation metric δf_r [%] for material C.

| Subset | | δf_n^1 | δf_n^2 | δf_n^3 | δf_n^4 | δf_n^5 |
|------------|-----|----------------|----------------|----------------|----------------|----------------|
| S_{1234} | AC3 | 8.7 | 2.5 | 2.6 | 0.7 | 0 |
| | AC4 | 8.7 | 2.5 | 1.9 | 0 | 1.8 |
| S_{3412} | AC1 | 8.1 | 2.5 | 3.0 | 0.4 | 0 |
| | AC2 | 8.1 | 2.5 | 2.2 | 0 | 0.5 |

7.5 Conclusion

This chapter offered a promising approach for the inverse identification of the viscoelastic properties of porous materials based on a Bayesian framework. The adopted strategy enabled the calibration and validation of fractional derivative models for two different materials, taking into account the inherent uncertainties from modeling and measurements. The main findings may be summed up as follows.

The method based on Bayes' rule was robust since it added a priori information about the parameters to build the cost function. It employed the DRAM algorithm to explore the sample space, generating posterior PDFs for the parameters rather than only point estimates. This allowed the computation of some statistics, such as the mean and credibility intervals, which enabled a richer analysis of the results. The joint PDFs were also obtained during this process, allowing the assessment of a possible dependency between the parameters.

Furthermore, stochastic models were computed, showing a reasonable level of correlation with measured data. Small differences were observed, however, some guide lines were given during results analysis to help the user to assess their reliability and, if necessary, to improve their quality.

7.5. CONCLUSION

Conclusions and Perspectives

Chapter 8

Conclusions and perspectives

In this thesis, two main problems related to viscoelastic and poro-viscoelastic materials were investigated. In the first problem, the characterization technique known as DMA, which is commonly used to determine the complex modulus of these materials, was analyzed in detail. In the second problem, the dissipation of mechanical energy caused by some porous materials due to their intrinsic viscoelasticity was explored.

This chapter gathers the most important contributions of each problem, also giving prospects for future works.

Content

| | | |
|------------|--|------------|
| 8.1 | Dynamic mechanical analysis (DMA) | 256 |
| 8.1.1 | Achievements and outlook | 256 |
| 8.1.2 | Perspectives for future works | 257 |
| 8.2 | Poro-viscoelastic materials | 258 |
| 8.2.1 | Achievements and outlook | 258 |
| 8.2.2 | Perspectives for future works | 260 |

8.1 Dynamic mechanical analysis (DMA)

8.1.1 Achievements and outlook

Dynamic mechanical analysis is a versatile technique commonly used to characterize the thermo-mechanical behavior of viscoelastic materials. One of its advantages is to perform different tests under distinct conditions, which provides a significant amount of information and enables a better understanding of the material's response. However, DMA results indeed depend on various factors. It is problematic as applications require a consistent measurement of properties, as uncertainties and wrong estimates can affect the development of a project critically.

On the first evaluation of this work, the complex modulus was measured as a function of temperature by three different DMA machines in a single cantilever, dual cantilever, and three-point bending modes. All experimental results evidenced the three main regions of the viscoelastic behavior and, consequently, allowed the identification of the glass transition temperature of the material. However, these results were not consistent between operational modes and even equipment.

It was noticed some differences in the values measured for the modulus, especially in the glassy state, and also for the glass transition temperature. Concerning the operational modes, three-point bending estimated the highest values. Regarding the equipment, these divergences were more prominent on single and dual cantilever modes, where clamp effects and sample size had the biggest influences. As a result, a parametric study was carried out to verify the effects of each parameter from the mathematical models adopted by each DMA machine. This analysis showed that different approaches were used for the same type of test and the hypothesis of a constant Poisson's ratio seems reasonable, for example.

On the second evaluation, the complex modulus was measured as a function of temperature and frequency by two different DMA machines again in the flexural modes. All measurement results indicated the thermo-rheological simple behavior, which made it possible to apply the time-temperature superposition principle for the generation of master curves. The optimized shift factors estimated in this procedure were very consistent, being even fitted by the WLF equation. Moreover, the long-term behavior identified by the different tests was quite similar.

Nevertheless, such as observed in the first study, the results showed differences in the values of the modulus. The three-point bending mode once again identified the highest estimates. This variation,

8.1. DYNAMIC MECHANICAL ANALYSIS (DMA)

however, varied according to the investigated frequency. It drew attention since these experimental master curves are often used for the calibration of mechanical models to be applied in numerical predictions of the material's behavior.

Finally, on the third evaluation, a five-parameter fractional derivative model was calibrated within the Bayesian framework for each data-set aiming at analyzing the impacts on model predictions. From the results, it was possible to observe a relatively good agreement between the model parameters when considering the estimated credibility intervals. That is, when taking into account the uncertainties of measurements and model assumptions, it was possible to obtain very similar predictions, especially at lower frequencies.

A key aspect here is that the modulus estimate provided by DMA equipment is a physical property and although some variations may naturally stem from data uncertainties, its variations as a function of equipment or operational modes are meaningless from the physical point of view. It means that, when analyzing the results, it has to be kept in mind the entire experimental description, that is, from the test conditions to the same model of equipment.

8.1.2 Perspectives for future works

The use of viscoelastic materials has been intensified on many applications due to their attractive mechanical properties. However, there is still a need for better standard tests and methods to measure these materials' mechanical properties as the applications require more reliable results and better predictions of the material's behavior.

The results presented suggest that further investigations are necessary to understand more deeply the discrepancies between each DMA machine and to create a precise and reliable way to measure the viscoelastic properties of a material using these machines. These include the study of:

- the clamp effects, especially for the single cantilever mode as it was the most unreliable between the flexural modes analyzed when the sample dimensions were modified;
- the sample's size as it may cause the appearance of other effects on the material, for example, the shear stress;
- the mathematical formulation as it may be necessary to compensate the equipment stiffness;

- the correlation between these DMA operational modes and mechanical tests (tension and three-point bending) on universal machines as Instron;

Furthermore, it becomes interesting to carry out the same studies for other types of viscoelastic materials to see how far these differences can go.

8.2 Poro-viscoelastic materials

8.2.1 Achievements and outlook

Porous materials have been applied to different areas of engineering and applied sciences. The dissipative properties due to viscoelasticity have been proved to be beneficial for some applications. Recently, there is a great interest in studying the responses of these materials to low-frequency vibrations as they have the potential to be used for passive damping of structures as constrained or extensional layers.

With this in mind, this work dealt with the characterization, modeling, and predictions of the dissipation of mechanical energy by three different porous materials in the low-frequency range. A total of three investigations were carried out focusing on the damping performance of these materials when considering only the viscoelasticity of their porous skeletons, neglecting thus the fluid phase and the air-structure interactions.

In the first study, a numerical approach was proposed to provide predictive scenarios in the time domain of cyclic stress through the use of calibrated viscoelastic models. This technique allowed the evaluation of stress levels, stress rates, and temperatures. Two polymeric foams were examined.

The numerical results evidenced hysteresis loops commonly associated with viscoelastic materials in the responses of the two investigated foams. It was shown that the dissipation of mechanical energy increased with the increase in stress level and temperature. Additionally, it was suggested that one of these foams exhibited good damping ability.

The second study, in turn, assessed the damping introduced by a polymeric foam on simply supported panels through vibrational tests in the low-frequency range. Then, a finite element model combined with a fractional derivative model calibrated using measured data from a torsional rheometer was proposed and validated. An important point to be detached is that the porous materials were

modeled as homogeneous isotropic linear viscoelastic solid materials.

The experimental results showed that the introduction of one of the foams on the system could indeed damp structural vibrations. One of the advantages was that this particular foam did not affect the system's mass significantly. In this way, it was demonstrated that it is possible to benefit from a good trade-off between damping and weight.

The comparison between the experimental and numerical results showed that the proposed model was amenable for all configurations tested. The model predictions regarding the damping effects showed relevant accuracy in the low-frequency range. Therefore, the viscoelastic properties measured by a torsional rheometer are reliable to be used in FE models that consider the viscoelastic foams as homogeneous monophasic solid.

As a result, a parametric study was carried out to verify the effects of geometric and mechanical parameters of foams. This analysis evidenced that these parameters could be optimized for weight and performance, depending on the material. Furthermore, an additional investigation was done to assess the predictive capacity of the proposed model, which demonstrated its limitation to low frequencies.

It is worth noting that this model reduces computational time considerably. It can be even optimized through the use of model reduction techniques. Therefore, this method becomes attractive to be used in the pre-design of structures integrating foams as passive damping treatments.

Finally, in the third study, an inverse characterization procedure was proposed to calibrate viscoelastic models for two porous materials within the Bayesian framework. The uncertainties from model assumptions and experimental measurements could be quantified. The influence of the experimental data-sets employed for the calibration step could also be analyzed.

The results showed that the data-set could indeed influence the estimates generated by the method and that some parameters were still more sensitive to these variations than others. However, it was possible to have a good agreement between them when taking into account the credibility intervals generated by their uncertainties. It is worth recalling that this method does not aim to determine the parameters with the highest reliability, but rather to determine the best set of parameters, estimating confidence intervals for them.

Furthermore, the estimates obtained for one of the investigated materials were even compared with the results obtained by other characterization techniques. This correlation showed good agreement

and, consequently, reliability in this approach.

8.2.2 Perspectives for future works

The results presented in this thesis highlighted the great potential of some porous materials with viscoelastic features to be used as damping treatment. It thus became evident that this field deserves more attention to better understand and benefit from these materials.

Concerning the first case study of Chapter 6, the following perspective can be pointed out:

- the accomplishment of experimental cyclic loading tests as it could validate the numerical method presented and also could shed light on possible limitations;

As regards the second case study of Chapter 6, the following steps can be highlighted:

- the modeling of the two phases of porous materials and their coupling effects using Biot's theory to include other dissipation mechanisms such as thermal and viscous ones aiming to better describe their behavior at higher frequencies;

To do that, there is a need for

- Bayesian inverse identification of all material parameters needed to model the solid and fluid phases of the material from experimental measurements on an impedance tube;
- the analysis of improvements in model predictions due to the use of Biot's theory;
- the construction of a new model by the introduction of viscoelastic properties on Biot's theory to properly describe both phases of the porous material, taking into account the viscoelasticity of the solid phase;
- the analysis of the newly developed method to evaluate its performance;
- the investigation of the possibility to perform inverse characterization of foams at higher frequencies.

Bibliography

- [1] I. R. Henriques, L. Rouleau, D. A. Castello, L. A. Borges, and J. F. Deü. Viscoelastic behavior of polymeric foams: Experiments and modeling. *Mechanics of Materials*, 148:103506, 2020.
- [2] L. Rouleau, J.-F. Deü, A. Legay, and F. Le Lay. Application of Kramers–Kronig relations to time–temperature superposition for viscoelastic materials. *Mechanics of Materials*, 65:66–75, 2013.
- [3] D. A. Castello, F. A. Rochinha, N. Roitman, and C. Magluta. Constitutive parameter estimation of a viscoelastic model with internal variables. *Mechanical Systems and Signal Processing*, 22(8):1840–1857, 2008.
- [4] Pravin P. Hujare and Anil D. Sahasrabudhe. Experimental Investigation of Damping Performance of Viscoelastic Material Using Constrained Layer Damping Treatment. *Procedia Materials Science*, 5:726–733, 2014.
- [5] Lucie Rouleau, Rogério Pirk, Bert Pluymers, and Wim Desmet. Characterization and Modeling of the Viscoelastic Behavior of a Self -Adhesive Rubber Using Dynamic Mechanical Analysis Tests. *Journal of Aerospace Technology and Management*, 7(2):200–208, 2015.
- [6] L. Rouleau, B. Pluymers, and W. Desmet. Characterisation of Viscoelastic Layers in Sandwich Lightweight Panels. In *Proceedings of NOVEM 2015*, page 48983, Dubrovnik, 2015.
- [7] D A Rade, J.-F. Deü, D A Castello, A M G de Lima, and L Rouleau. *Passive Vibration Control Using Viscoelastic Materials*, chapter 5. Springer, Cham, 2019.
- [8] John D Ferry. *Viscoelastic properties of polymers*. Wiley, New York, 3 edition, 1980.
- [9] R M Christensen. *Theory of Viscoelasticity - An Introduction*. Academic Press, New York, 2 edition, 1982.

BIBLIOGRAPHY

- [10] Alan S. Wineman and K.R. Rajagopal. *Mechanical Response of Polymers*. Cambridge University Press, New York, 1 edition, 2000.
- [11] Roderic Lakes. *Viscoelastic materials*. Cambridge University Press, 1 edition, 2009.
- [12] D.A. Castello, L.A. Borges, V.O.B. Santos, B.G. Soares, S.A. Martins, and A.A. Silva. A general approach for viscoelastic model validation applied on the analyses of epoxy resin modified by end-functionalized liquid polybutadiene. *Journal of the Brazilian Society of Mechanical Sciences and Engineering*, 39(3):993–1007, 2016.
- [13] N W Tschoegl. Time Dependence in Material Properties: An Overview. *Mechanics of Time-Dependent Materials*, 1(1):3–31, 1997.
- [14] W P Hernández, D A Castello, N Roitman, and C Magluta. Thermorheologically simple materials: A bayesian framework for model calibration and validation. *Journal of Sound and Vibration*, 402:14–30, 2017.
- [15] R. S. Lakes. Viscoelastic measurement techniques. *Review of Scientific Instruments*, 75(4):797–810, 2004.
- [16] Kevin P. Menard. *Dynamic mechanical analysis : a practical introduction*. CRC Press, Boca Raton, 1 edition, 1999.
- [17] I.R. Henriques, L.A. Borges, M.F. Costa, B.G. Soares, and D.A. Castello. Comparisons of complex modulus provided by different DMA. *Polymer Testing*, 72:394–406, 2018.
- [18] Isadora R. Henriques, Lavinia A. Borges, and Daniel A. Castello. The Mechanical Behavior of Viscoelastic Materials in the Frequency Domain. In Agenor de T Fleury, Domingos A Rade, and Paulo R G Kurka, editors, *Proceedings of DINAME 2017*, pages 65–81. Springer, Cham, 2019.
- [19] Bernard D Coleman and Morton E Gurtin. Thermodynamics with Internal State Variables. *The Journal of Chemical Physics*, 47(2):597–613, 1967.
- [20] F.C.L. Borges, D.A. Castello, C. Magluta, F.A. Rochinha, and N. Roitman. An experimental assessment of internal variables constitutive models for viscoelastic materials. *Mechanical Systems and Signal Processing*, 50-51:27–40, 2015.

BIBLIOGRAPHY

- [21] R L Bagley and P J Torvik. A Theoretical Basis for the Application of Fractional Calculus to Viscoelasticity. *Journal of Rheology*, 27(3):201–210, 1983.
- [22] R L Bagley and P J Torvik. On the Fractional Calculus Model of Viscoelastic Behavior. *Journal of Rheology*, 30(1):133–155, 1986.
- [23] Alexander Lion. On the thermodynamics of fractional damping elements. *Continuum Mechanics and Thermodynamics*, 9(2):83–96, 1997.
- [24] Francesco Mainardi. *Fractional calculus and waves in linear viscoelasticity*. Imperial College Press, London, 1 edition, 2010.
- [25] Ralph C. Smith. *Uncertainty quantification: theory, implementation, and applications*. Society for Industrial and Applied Mathematics, Philadelphia, 2013.
- [26] Jari P. Kaipio and Erkki Somersalo. *Statistical and computational inverse problems*, volume 160. Springer, New York, 2005.
- [27] Richard Aster, Brian Borchers, and Clifford Thurber. *Parameter estimation and inverse problems*. Academic Press, 1 edition, 2005.
- [28] Jean-Daniel Chazot, Erliang Zhang, and Jérôme Antoni. Acoustical and mechanical characterization of poroelastic materials using a Bayesian approach. *The Journal of the Acoustical Society of America*, 131(6):4584–4595, 2012.
- [29] W. P. Hernández, D. A. Castello, and C. F.T. Matt. On the model building for transmission line cables: a Bayesian approach. *Inverse Problems in Science and Engineering*, 26(12):1784–1812, 2018.
- [30] Nicholas W. Tschoegl. *The Phenomenological Theory of Linear Viscoelastic Behavior*. Springer-Verlag Berlin Heidelberg, 1 edition, 1989.
- [31] E Wiechert. *Ueber elastische Nachwirkung*. Hartungsche buchdr., 1889.
- [32] G. A. Lesieutre and E. Bianchini. Time domain modeling of linear viscoelasticity using anelastic displacement fields. *Journal of Vibration and Acoustics, Transactions of the ASME*, 117(4):424–430, 1995.

BIBLIOGRAPHY

- [33] K. Dovstam. Augmented Hooke's law based on alternative stress relaxation models. *Computational Mechanics*, 26(1):90–103, 2000.
- [34] Mikael Enelung and Peter Olsson. Damping described by fading memory - analysis and application to fractional derivative models. *International Journal of Solids and Structures*, 36:939–970, 1999.
- [35] T. Pritz. Analysis of four-parameter fractional derivative model of real solid materials. *Journal of Sound and Vibration*, 195(1):103–115, 1996.
- [36] T. Pritz. Five-parameter fractional derivative model for polymeric damping materials. *Journal of Sound and Vibration*, 265(5):935–952, 2003.
- [37] F. Schwarzl and A. J. Staverman. Time-Temperature Dependence of Linear Viscoelastic Behavior. *Journal of Applied Physics*, 23(8):838–843, 1952.
- [38] Chang Dae Han and Jin Kon Kim. On the use of time-temperature superposition in multicomponent / multiphase polymer systems. *Polymer*, 34(12):2533–2539, 1993.
- [39] Marniz Van Gorp and Jo Palmen. Time-Temperature Superposition for Polymeric Blends. *Rheology Bulletin*, 67(1):5–8, 1998.
- [40] Kwang Soo Cho. *Viscoelasticity of Polymers : Theory and Numerical Algorithms*. Springer Netherlands, 1 edition, 2016. doi:10.1007/978-94-017-7564-9.
- [41] J Dealy and D Plazek. Time-Temperature Superposition - A Users Guide. *Rheology Bulletin*, 78(2):16–31, 2009.
- [42] Igor Emri and Marina Gergesova. *Time-Dependent Behavior of Solid Polymers*, volume 1. 2010.
- [43] Malcolm L. Williams, Robert F. Landel, and John D. Ferry. The Temperature Dependence of Relaxation Mechanisms in Amorphous Polymers and Other Glass-forming Liquids. *Journal of the American Chemical Society*, 77(14):3701–3707, 1955.
- [44] F Bueche. The Viscoelastic Properties of Plastics. *The Journal of Chemical Physics*, 22(4):603–609, 1954.

BIBLIOGRAPHY

- [45] M. J. Colaço, H. R. B. Orlande, and G. S. Dulikravich. Inverse and optimization problems in heat transfer. *Journal of the Brazilian Society of Mechanical Sciences and Engineering*, XXVIII (1):1–24, 2006.
- [46] Jacques Hadamard. *Lectures on Cauchy's Problem in Linear Partial Differential Equations*. Dover, New York, 1 edition, 1952.
- [47] Hoon Kim, Christian P. Robert, and George Casella. *Monte Carlo Statistical Methods*. Springer, New York, 2 edition, 2004.
- [48] Nicholas Metropolis, Arianna W. Rosenbluth, and Marshall N. Rosenbluth. Equation of state calculations by fast computing machines. *Journal of Chemical Physics*, 21(6):1087–1092, 1953.
- [49] W. K. Hastings. Monte Carlo sampling methods using Markov chains and their applications. *Biometrika*, 57(1):97–109, 1970.
- [50] Heikki Haario, Marko Laine, Antonietta Mira, and Eero Saksman. DRAM: Efficient adaptive MCMC. *Statistics and Computing*, 16(4):339–354, 2006.
- [51] Heikki Haario, Eero Saksman, and Johanna Tamminen. An adaptive Metropolis algorithm. *Bernoulli*, 7(2):223–242, 2001.
- [52] Antonietta Mira. On Metropolis-Hastings algorithms with delayed rejection. *Metron - International Journal of Statistics*, 59(3-4):231–241, 2001.
- [53] Andrew Gelman, Gareth O Roberts, and Walter R Gilks. Efficient Metropolis jumping rules. *Bayesian Statistics*, 5:559–607, 1995.
- [54] AIAA. Guide for the Verification and Validation of Computational Fluid Dynamics Simulations. Technical report, Reston, 1998.
- [55] ASME. Guide for the verification and validation in computational solid dynamics. Technical report, American Society of Mechanical Engineers, 2006.
- [56] W Oberkampf and Christopher Roy. *Verification and Validation in Scientific Computing*. Cambridge University Press, 1 edition, 2010.

BIBLIOGRAPHY

- [57] William Oberkampf and Matthew Barone. Measures of Agreement Between Computation and Experiment: Validation Metrics. *Journal of Computational Physics*, 217(1):5–36, 2006.
- [58] Leonard E. Schwer. Validation metrics for response histories: perspectives and case studies. *Engineering with Computers*, 23(4):295–309, 2007.
- [59] Christopher J. Roy and William L. Oberkampf. A comprehensive framework for verification, validation, and uncertainty quantification in scientific computing. *Computer Methods in Applied Mechanics and Engineering*, 200(25-28):2131–2144, 2011.
- [60] Yu Liu, Wei Chen, Paul Arendt, and Hong-Zhong Huang. Toward a Better Understanding of Model Validation Metrics. *Journal of Mechanical Design*, 133(7):071005, 2011.
- [61] Daniel Alves Castello, Carlos Frederico, and Trotta Matt. A Validation Metrics Based Model Calibration Applied on Stranded Cables. *Journal of the Brazilian Society of Mechanical Sciences and Engineering*, 33(4):417–427, 2011.
- [62] Pejman Honarmandi and Raymundo Arróyave. Uncertainty Quantification and Propagation in Computational Materials Science and Simulation-Assisted Materials Design. *Integrating Materials and Manufacturing Innovation*, 9(1):103–143, 2020.
- [63] David D. Shepard and Benjamin Twombly. Simultaneous dynamic mechanical analysis and dielectric analysis of polymers. *Thermochimica Acta*, 272(1-2):125–129, 1996.
- [64] O. Martin and L. Averous. Plasticization and properties of biodegradable multiphase systems polymer. *Polymer*, 42:6209–6219, 2001.
- [65] A. Haque, M. Shamsuzzoha, F. Hussain, and D. Dean. S2-glass/epoxy polymer nanocomposites: Manufacturing, structures, thermal and mechanical properties. *Journal of Composite Materials*, 37(20):1821–1838, 2003.
- [66] Wenbo Luo, Xiaoling Hu, Chuhong Wang, and Qifu Li. Frequency- and strain-amplitude-dependent dynamical mechanical properties and hysteresis loss of CB-filled vulcanized natural rubber. *International Journal of Mechanical Sciences*, 52(2):168–174, 2010.

BIBLIOGRAPHY

- [67] A J W McClung, Gyaneshwar Tandon, Dean Foster, and J Baur. Influence of post-cure and repeated cycling on thermomechanical characterization of shape memory polymers and composites. In *Proceedings of the International SAMPE Symposium and Exhibition 2010*, Seattle, 2010.
- [68] S Raa Khimi and K L Pickering. A new method to predict optimum cure time of rubber compound using dynamic mechanical analysis. *Journal of Applied Polymer Science*, 131(6):1–6, 2014.
- [69] Manex Martinez-Agirre, Silvia Illescas, and María Jesús Elejabarrieta. Characterisation and modelling of prestrained viscoelastic films. *International Journal of Adhesion and Adhesives*, 50: 183–190, 2014.
- [70] Luís Carlos Oliveira da Silva and Bluma Guenther Soares. Effects of graphene functionalization on the long-term behavior of epoxy/graphene composites evaluated by dynamic mechanical analysis. *Journal of Applied Polymer Science*, 134(20):1–10, 2017.
- [71] Steven Eric Zeltmann, Keerthana A Prakash, Mrityunjay Doddamani, and Nikhil Gupta. Prediction of modulus at various strain rates from dynamic mechanical analysis data for polymer matrix composites. *Composites Part B: Engineering*, 120:27–34, 2017.
- [72] Arnaldo G. Leal, Carlos Marques, Anselmo Frizera, and Maria Jose Pontes. Dynamic Mechanical Analysis on a PolyMethyl Methacrylate (PMMA) Polymer Optical Fiber. *IEEE Sensors Journal*, 18(6):2353 – 2361, 2018.
- [73] Tom Ehrig, Niels Modler, and Pawel Kostka. Compression and frequency dependence of the viscoelastic shear properties of flexible open-cell foams. *Polymer Testing*, 70:151–161, 2018.
- [74] L. R. Orlandini, I. R. Henriques, D. A. Castello, L. A. Borges, and B. G. Soares. Dynamic mechanical characterization of epoxy-based thermosetting materials loaded with lignin. *Journal of the Brazilian Society of Mechanical Sciences and Engineering*, 42(8):394, 2020.
- [75] A. Opreni, S. Mariani, M. Dossi, and M. Brennan. Combined effects of temperature and humidity on the mechanical properties of polyurethane foams. *Journal of Rheology*, 64(161):161–176, 2020.

- [76] Christian Nielsen and Sia Nemat-nasser. Crack healing in cross-ply composites observed by dynamic mechanical analysis. *Journal of the Mechanics and Physics of Solids*, 76:193–207, 2015.
- [77] P Kostka, K Holeczek, A Filippatos, and N Modler. Extension and application of dynamic mechanical analysis for the estimation of spatial distribution of material properties. *Polymer Testing*, 52:184–191, 2016.
- [78] Zhanzhan Jia, Alireza V Amirkhizi, Wiroj Nantasetphong, and Sia Nemat-nasser. Experimentally-based relaxation modulus of polyurea and its composites. *Mechanics of Time-Dependent Materials*, 20:155–174, 2016.
- [79] Steffen Ropers, Marton Kardos, and Tim A Osswald. A thermo-viscoelastic approach for the characterization and modeling of the bending behavior of thermoplastic composites. *Composites Part A: Applied Science and Manufacturing*, 90:22–32, 2016.
- [80] T Leonard and G Goberman. An investigation into DMTA clamping. *Measurement Science and Technology*, 3(3):275–282, 1992.
- [81] Pearl Lee-Sullivan and Donna Dykeman. Guidelines for performing storage modulus measurements using the TA Instruments DMA 2980 three-point bend mode. II. Contact stresses and machine compliance. *Polymer Testing*, 19(2):239–250, 2000.
- [82] Pearl Lee-Sullivan and Donna Dykeman. Guidelines for performing storage modulus measurements using the TA Instruments DMA 2980 three-point bend mode. I. Amplitude effects. *Polymer Testing*, 19(2):155–164, 2000.
- [83] Igor Lacík, Igor Krupa, Marek Stach, Anton Kučma, Janka Jurčiová, and Ivan Chodák. Thermal lag and its practical consequence in the dynamic mechanical analysis of polymers. *Polymer Testing*, 19(7):755–771, 2000.
- [84] N. M. Alves and J. F. Mano. Temperature correction of dynamic mechanical and thermomechanical analysers during heating , cooling and isothermal experiments. *Thermochimica Acta*, 346:133–145, 2000.
- [85] M. A. Rodríguez-Pérez, O. Almanza, J. L. Del Valle, A. González, and J. A. De Saja. Improve-

BIBLIOGRAPHY

- ment of the measurement process used for the dynamic mechanical characterization of polyolefin foams in compression. *Polymer Testing*, 20(3):253–267, 2001.
- [86] J. F. Mano and J. P. Cahon. A simple method for calibrating the temperature in dynamic mechanical analysers and thermal mechanical analysers. *Polymer Testing*, 23(4):423–430, 2004.
- [87] Shiqiang Deng, Meng Hou, and Lin Ye. Temperature-dependent elastic moduli of epoxies measured by DMA and their correlations to mechanical testing data. *Polymer Testing*, 26(6):803–813, 2007.
- [88] G Swaminathan and K Shivakumar. A re-examination of DMA testing of polymer matrix composites. *Journal of Reinforced Plastics and Composites*, 28(8):979–994, 2008.
- [89] Rasa Kazakeviciute-Makovska, Safa Mogharebi, Holger Steeb, Gunther Eggeler, and Klaus Neuking. A Critical Assessment of Experimental Methods for Determining the Dynamic Mechanical Characteristics of Shape Memory Polymers. *Advanced Engineering Materials*, 15(8):732–739, 2013.
- [90] Wei Sun, Anastasios P Vassilopoulos, and Thomas Keller. Effect of thermal lag on glass transition temperature of polymers measured by DMA. *International Journal of Adhesion and Adhesives*, 52:31–39, 2014.
- [91] Ian M. McAninch, Giuseppe R. Palmese, Joseph L. Lenhart, and John J. La Salsa. DMA Testing of Epoxy resins: the importance of dimensions. *Polymer Engineering And Science*, 55:2761–2774, 2015.
- [92] Daniela Ionita, Mariana Cristea, and Dorel Banabic. Viscoelastic behavior of PMMA in relation to deformation mode. *Journal of Thermal Analysis and Calorimetry*, 120(3):1775–1783, 2015.
- [93] Jiemin Feng and Zhansheng Guo. Temperature-frequency-dependent mechanical properties model of epoxy resin and its composites. *Composites Part B: Engineering*, 85:161–169, 2016.
- [94] J F Gerard, S J Andrews, and C W Macosko. Dynamic mechanical measurements: Comparison between bending and torsion methods on a graphite reinforced and a rubber modified epoxy. *Polymer Composites*, 11(2):90–97, 1990.

BIBLIOGRAPHY

- [95] K Pournoor and J C Seferis. Instrument-independent dynamic mechanical analysis of polymeric systems. *Polymer*, 32(3):445–453, 1991.
- [96] R Hagen, L Salmen, H Lavebratt, and B Stenberg. Comparison of Dynamic-Mechanical Measurements and Tg Determinations with 2 Different Instruments. *Polymer Testing*, 13(2):113–128, 1994.
- [97] J. Wolfrum, G. W. Ehrehstein, and M. A. Avondet. Dynamical mechanical thermo analysis of high performance composites - influences and problems. *Journal of Composite Materials*, 34(21): 1788–1807, 2000.
- [98] Paolo Bonfiglio, Francesco Pompoli, Kirill V. Horoshenkov, Mahmud Iskandar B.Seth A. Rahim, Luc Jaouen, Julia Rodenas, François Xavier Bécot, Emmanuel Gourdon, Dirk Jaeger, Volker Kursch, Maurizio Tarello, Nicolaas Bernardus Roozen, Christ Glorieux, Fabrizio Ferrian, Pierre Leroy, Francesco Briatico Vangosa, Nicolas Dauchez, Félix Foucart, Lei Lei, Kevin Carillo, Olivier Doutres, Franck Sgard, Raymond Panneton, Kévin Verdiere, Claudio Bertolini, Rolf Bär, Jean Philippe Groby, Alan Geslain, Nicolas Poulain, Lucie Rouleau, Alain Guinault, Hamid Ahmadi, and Charlie Forge. How reproducible are methods to measure the dynamic viscoelastic properties of poroelastic media? *Journal of Sound and Vibration*, 428:26–43, 2018.
- [99] I.R. Henriques, L.A. Borges, M.F. Costa, B.G. Soares, and D.A. Castello. Differences between DMA modes and testing equipments. In *Proceedings of the 4th Brazilian Conference on Composite Materials*, Rio de Janeiro, 2018.
- [100] S Timoshenko and J. N. Goodier. *Theory of Elasticity*. McGraw-Hil, New York, 1 edition, 1969.
- [101] Montgomery T. Shaw and William J. MacKnight. *Introduction to Polymer Viscoelasticity*. Wiley, 4 edition, 2018.
- [102] Gottfried W. Ehrenstein, Gabriela Riedel, and Pia Trawiel. Dynamic Mechanical Analysis. In *Thermal Analysis of Plastics: Theory and Practice*, chapter 6, pages 236–299. 2004.
- [103] A. D. Drodzdov. *Mechanics of Viscoelastic Solids*. Wiley, 1 edition, 1998.
- [104] R. S. Lakes and A Wineman. On Poisson’s Ratio in Linearly Viscoelastic Solids. *Journal of Elasticity*, 85(1):45–63, 2006.

BIBLIOGRAPHY

- [105] Harry H. Hilton. Elastic and Viscoelastic Poisson's Ratios: The Theoretical Mechanics Perspective. *Materials Sciences and Applications*, 8:291–332, 2017.
- [106] G N Greaves, A L Greer, R S Lakes, and T Rouxel. Poisson's ratio and modern materials. *Nature Materials*, 10(11):823–837, 2011.
- [107] S. Pandini and A. Pegoretti. Time and temperature effects on Poisson's ratio of poly(butylene terephthalate). *Express Polymer Letters*, 5(8):685–697, 2011.
- [108] V. Placet and E. Foltête. Is Dynamic Mechanical Analysis (DMA) a non-resonance technique? *EPJ Web of Conferences*, 6:41004, 2010.
- [109] G. A. Arzoumanidis and K. M. Liechti. Linear viscoelastic property measurement and its significance for some nonlinear viscoelasticity models. *Mechanics Time-Dependent Materials*, 7(3-4): 209–250, 2003.
- [110] Olivier Coussy. *Poromechanics*. John Wiley & Sons Ltd, 1 edition, 2004.
- [111] Olivier Coussy. *Mechanics and Physics of Porous Solids*. John Wiley & Sons Ltd, 1 edition, 2010.
- [112] A. Sfaoui. On the viscoelasticity of the polyurethane foam. *The Journal of the Acoustical Society of America*, 97(2):1046–1052, 1995.
- [113] M. A. Rodríguez-Pérez, S. Rodríguez-Llorente, and J. A. De Saja. Dynamic mechanical properties of polyolefin foams studied by DMA techniques. *Polymer Engineering and Science*, 37(6): 959–965, 1997.
- [114] S. Sahraoui, E. Mariez, and M. Etchessahar. Mechanical testing of polymeric foams at low frequency. *Polymer Testing*, 20(1):93–96, 2000.
- [115] O. Danilov, F. Sgard, and X. Olny. On the limits of an "in vacuum" model to determine the mechanical parameters of isotropic poroelastic materials. *Journal of Sound and Vibration*, 276 (3-5):729–754, 2004.
- [116] M Etchessahar, S Sahraoui, L Benyahia, and J F Tassin. Frequency dependence of elastic properties of acoustic foams. *The Journal of the Acoustical Society of America*, 117(3):1114–1121, 2005.

BIBLIOGRAPHY

- [117] Jacques Cuenca, Christophe Van Der Kelen, and Peter Göransson. A general methodology for inverse estimation of the elastic and anelastic properties of anisotropic open-cell porous materials - With application to a melamine foam. *Journal of Applied Physics*, 115(8), 2014.
- [118] M. A. Biot. Theory of deformation of a porous viscoelastic anisotropic solid. *Journal of Applied Physics*, 27(5):459–467, 1956.
- [119] M. A. Biot. Theory of Propagation of Elastic Waves in a Fluid-Saturated Porous Solid I. Low-Frequency Range. *Journal of the Acoustical Society of America*, 28(2):168–178, 1956.
- [120] M. A. Biot. Mechanics of Deformation and Acoustic Propagation in Porus Media. *Journal of Applied Physics*, 33(4):1482–1498, 1962.
- [121] K. V. Horoshenkov and K. Sakagami. A method to calculate the acoustic response of a thin, baffled, simply supported poroelastic plate. *The Journal of the Acoustical Society of America*, 110(2):904–917, 2001.
- [122] N. Dauchez, S. Sahraoui, and N. Atalla. Investigation and modelling of damping in a plate with a bonded porous layer. *Journal of Sound and Vibration*, 265(2):437–449, 2003.
- [123] Elke Deckers, Stijn Jonckheere, Dirk Vandepitte, and Wim Desmet. Modelling Techniques for Vibro-Acoustic Dynamics of Poroelastic Materials. *Archives of Computational Methods in Engineering*, 22(2):183–236, 2015.
- [124] Luc Jaouen, Amélie Renault, and Mickael Deverge. Elastic and damping characterizations of acoustical porous materials: Available experimental methods and applications to a melamine foam. *Applied Acoustics*, 69(12):1129–1140, 2008.
- [125] E. Gourdon, C. Sauzéat, H. Di Benedetto, and K. Bilodeau. Seven-Parameter Linear Viscoelastic Model Applied to Acoustical Damping Materials. *Journal of Vibration and Acoustics, Transactions of the ASME*, 137(6):1–9, 2015.
- [126] Xinxin Guo, Guqi Yan, Lazhar Benyahia, and Sohbi Sahraoui. Fitting stress relaxation experiments with fractional Zener model to predict high frequency moduli of polymeric acoustic foams. *Mechanics of Time-Dependent Materials*, 20(4):523–533, 2016.

BIBLIOGRAPHY

- [127] Sohbi Sahraoui and Nouredine Zekri. On fractional modeling of viscoelastic foams. *Mechanics Research Communications*, 96:62–66, 2019.
- [128] I. Henriques, L. Rouleau, D. Castello, L. Borges, and J. F. Deü. Damping performance of porous materials through dynamic analysis. In *Proceedings of the 48th International Congress and Exhibition on Noise Control Engineering*, Madrid, 2019.
- [129] Laith Egab, Xu Wang, and Mohammad Fard. Acoustical characterisation of porous sound absorbing materials: a review. *International Journal of Vehicle Noise and Vibration*, 10(1-2): 129, 2014.
- [130] A. Renault, L. Jaouen, and F. Sgard. Characterization of elastic parameters of acoustical porous materials from beam bending vibrations. *Journal of Sound and Vibration*, 330(9):1950–1963, 2011.
- [131] Paolo Bonfiglio and Francesco Pompili. Inversion problems for determining physical parameters of porous materials: Overview and comparison between different methods. *Acta Acustica united with Acustica*, 99(3):341–351, 2013.
- [132] E. Mariez, S. Sahraoui, and J. F. Allard. Elastic Constants of Polyurethane Foam’s Skeleton for Biot Model. In *Proceedings of the 25th International Congress and Exhibition on Noise Control Engineering*, pages 951–954, Liverpool, 1996.
- [133] Igor Podlubny. Matrix approach to discrete fractional calculus. *Fractional Calculus and Applied Analysis*, 3(4):359–386, 2000.
- [134] I Podlubny, T Skovranek, and B M Vinagre Jara. Matrix approach to discretization of fractional derivatives and to solution of fractional differential equations and their systems. In *Proceedings of 12th IEEE International Conference on Emerging Technologies and Factory Automation*, pages 1–6, Palma de Mallorca, 2009.
- [135] Olivier Robin, Jean-Daniel Chazot, Romain Boulandet, Marc Michau, Alain Berry, and Nouredine Atalla. A Plane and Thin Panel with Representative Simply Supported Boundary Conditions for Laboratory Vibroacoustic Tests. *Acta Acustica united with Acustica*, 102(1):170–182, 2016.

BIBLIOGRAPHY

- [136] D. J. Ewins. *Modal Testing: Theory, Practice and Application*. Wiley, 2 edition, 2009.
- [137] Anders Brandt. *Noise and Vibration Analysis*. Wiley, 1 edition, 2011.
- [138] Christophe Geuzaine and Jean-François Remacle. Gmsh: A 3-D finite element mesh generator with built-in pre- and post-processing facilities. *International Journal for Numerical Methods in Engineering*, 79(11):1309–1331, 2009.
- [139] Lucie Rouleau, J.-F. Deü, and Antoine Legay. A comparison of model reduction techniques based on modal projection for structures with frequency-dependent damping. *Mechanical Systems and Signal Processing*, 90:110–125, 2017.
- [140] Lucie Rouleau. *Vibro-acoustic modelling of sandwich structures with viscoelastic materials*. Ph.d. dissertation, Conservatoire national des arts et métiers, 2013.
- [141] O Robin, A Berry, N Atalla, M Aucejo, B Lossouarn, L Rouleau, and J.-F. Deü. Setting Up Plane And Thin Panels With Representative Simply Supported Boundary Conditions : Comparative Results And Applications In Three Laboratories. In *Proceedings of the 47th International Congress and Exhibition on Noise Control Engineering*, Chicago, 2018.
- [142] I.R. Henriques, L. Rouleau, D.A. Castello, L.A. Borges, and J.-F. Deü. Inverse characterization of the damping performance of porous materials. In *Proceedings of the e-Forum Acusticum 2020*, Lyon, 2020.
- [143] L. Lei, J. D. Chazot, and N. Dauchez. Inverse method for elastic properties estimation of a poroelastic material within a multilayered structure. *Applied Acoustics*, 148:133–140, 2019.
- [144] K S Miller and B Ross. *An Introduction to the Fractional Calculus and Fractional Differential Equations*. John Wiley & Sons Ltd, New York, 1 edition, 1993.
- [145] Igor Podlubny. *Fractional differential equations*. Mathematics in Science and Engineering. Academic Press, London, 1 edition, 1998.
- [146] J. M. M. Silva and N. M. M. Maia. *Modal Analysis and Testing*, volume 363. Springer Netherlands, 1 edition, 1999.

- [147] R Allemang and D Brown. A Complete Review of the Complex Mode Indicator Function (CMIF) with Applications. In *Proceedings of ISMA2006: International Conference on Noise and Vibration Engineering*, volume 6, Leuven, 2006.
- [148] Patrick Guillaume, Peter Verboven, Steve Vanlanduit, Herman Van der Auweraer, and Bart Peeters. A poly-reference implementation of the least-squares complex frequency-domain estimator. In *Proceedings of the International Modal Analysis Conference - IMAC 2003*, volume 21, Orlando, 2003.
- [149] P Verboven, B Cauberghe, E Parloo, S Vanlanduit, and P Guillaume. User-assisting tools for a fast frequency-domain modal parameter estimation method. *Mechanical Systems and Signal Processing*, 18:759–780, 2004.
- [150] Jer-Nan Juang and Richard S Pappa. An Eigensystem Realization Algorithm for Modal Parameter Identification and Model Reduction. *Journal of guidance Control and Dynamics*, 8(5), 1985.
- [151] W Heylen, S Lammens, and P Sas. *Modal Analysis Theory and Testing*. Katholieke Universiteit Leuven, Faculty of Engineering, Department of Mechanical Engineering, Division of Production Engineering, Machine Design and Automation, 1998.
- [152] Randall J Allemang. The Modal Assurance Criterion - Twenty Years of Use and Abuse. *Journal of Sound and Vibration*, 1:14–21, 2003.

BIBLIOGRAPHY

Appendix A

Fractional Calculus

A.1 Fractional derivative

Fractional calculus is a topic as old as classical calculus [144]. However, it was only in the last few decades that it has gained prominence in the most diverse areas of engineering and applied science. For instance, one may cite the use of fractional derivatives in linear viscoelasticity [21, 22, 24] and signal processing.

Several definitions of fractional derivatives can be found in the literature [144, 145]. Each one possesses its features. In the following, we introduce two definitions commonly employed in viscoelastic problems given by Riemann-Liouville and by Caputo.

Definition 1 (Riemann-Liouville) Let ${}_0D_t^\alpha$ be the Riemann-Liouville fractional derivative operator defined for any $t > 0$ with order $\alpha > 0$. Let m be a positive integer ($m \in \mathbb{N}$) such that $m - 1 < \alpha \leq m$. The Riemann-Liouville fractional derivative of order α of a function $f(t)$ is given by

$${}_0D_t^\alpha [f(t)] := \begin{cases} \frac{1}{\Gamma(m - \alpha)} \frac{d^m}{dt^m} \int_0^t \frac{f(\tau)}{(t - \tau)^{\alpha+1-m}} d\tau, & \text{if } m - 1 < \alpha < m, \\ \frac{d^m}{dt^m} f(t), & \text{if } \alpha = m, \end{cases} \quad (\text{A.1})$$

where Γ is the well-known Euler Gamma function.

Definition 2 (Caputo) Let ${}^*D_t^\alpha$ be the Caputo fractional derivative operator defined for any $t > 0$ with order $\alpha > 0$. Let m be a positive integer ($m \in \mathbb{N}$) such that $m - 1 < \alpha \leq m$. The Caputo fractional derivative of order α of a function $f(t)$ is expressed as follows

$${}_0D_t^\alpha[f(t)] := \begin{cases} \frac{1}{\Gamma(m-\alpha)} \int_0^t \frac{f^m(\tau)}{(t-\tau)^{\alpha+1-m}} d\tau, & \text{if } m-1 < \alpha < m, \\ \frac{d^m}{dt^m} f(t), & \text{if } \alpha = m. \end{cases} \quad (\text{A.2})$$

A.2 Integration method for fractional differential equations

One of the main issues when dealing with fractional derivative equations is the fact that few problems offer an analytical and closed solution. For this reason, the use of special functions is often required, such as the so-called Mittag-Leffler function [24]. Different methods can be found in the literature to solve this kind of equation, the matrix approach proposed by Podlubny [133] was adopted in this thesis and implemented in MATLAB[®] software, making use of some functions provided by Podlubny et al. [134].

In general terms, this particular approach consists in solving a linear ordinary fractional differential equation by formulating a system of algebraic equations, rather than using recurrence relations. It makes use of triangular strip matrices to combine numerical differentiation of integer order and m -fold integration, resulting in the simplification of the numerical solution [133, 134]. In the following, the mathematical strategy is briefly described.

Let a causal function $f(t)$ be defined in a support $[a, b]$ such that $f(t) \equiv 0$ if $t < a$. The Riemann-Liouville fractional derivative of order $\alpha \in [m-1, m[$ is thus given by

$$D_t^\alpha f(t) = \frac{1}{\Gamma(m-\alpha)} \frac{d^m}{dt^m} \int_a^t \frac{f(\tau)}{(t-\tau)^{\alpha-m-1}} d\tau. \quad (\text{A.3})$$

Let the time support $t \in [a, b]$ be discretized in $N+1$ equidistant points with step h as $t_k = hk$ ($k = 0, 1, 2, \dots, N$), where $t_0 = a$ and $t_N = b$. Applying the backward fractional difference approximation for the α^{th} derivative at points t_k , one obtain

$$D_t^\alpha f(t) \approx \frac{\nabla^\alpha f(t_k)}{h^\alpha} = h^{-\alpha} \sum_{j=a}^k (-1)^j \binom{\alpha}{j} f_{k-j}. \quad (\text{A.4})$$

Considering all $N+1$ points, Eq. A.4 can be written in the matrix form as follows

A.2. INTEGRATION METHOD FOR FRACTIONAL DIFFERENTIAL EQUATIONS

$$\begin{bmatrix} h^{-\alpha} \nabla^\alpha f(t_0) \\ h^{-\alpha} \nabla^\alpha f(t_1) \\ \vdots \\ h^{-\alpha} \nabla^\alpha f(t_N) \end{bmatrix} = \mathbb{B}_N^\alpha \begin{bmatrix} f_0 \\ f_1 \\ \vdots \\ f_N \end{bmatrix}, \quad (\text{A.5})$$

where the matrix \mathbb{B}_N^α is defined as the discrete analog of left-sided fractional differentiation of order α expressed by

$$\mathbb{B}_N^\alpha = \frac{a}{h^\alpha} \begin{bmatrix} \omega_0^\alpha & 0 & 0 & 0 & \dots & 0 \\ \omega_1^\alpha & \omega_0^\alpha & 0 & 0 & \dots & 0 \\ \omega_2^\alpha & \omega_1^\alpha & \omega_0^\alpha & 0 & \dots & 0 \\ \ddots & \ddots & \ddots & \ddots & \dots & \dots \\ \omega_{N-1}^\alpha & \ddots & \omega_2^\alpha & \omega_1^\alpha & \omega_0^\alpha & 0 \\ \omega_N^\alpha & \omega_{N-1}^\alpha & \ddots & \omega_2^\alpha & \omega_1^\alpha & \omega_0^\alpha \end{bmatrix}, \quad (\text{A.6})$$

with

$$\omega_j^\alpha = (-1)^j \binom{\alpha}{j}, \quad j = 0, 1, 2, \dots, N. \quad (\text{A.7})$$

A similar procedure can be done for non-equidistant points. In this situation, let consider the causal function $f(t)$ and the Riemann-Liouville fractional integral of order $\alpha \in \mathfrak{R}^+$ such as

$$D_t^{-\alpha} f(t) = \frac{1}{\Gamma(\alpha)} \int_a^t (t - \tau)^{\alpha-1} f(\tau) d\tau. \quad (\text{A.8})$$

Let the time support $t \in [a, b]$ be discretized in non-equidistant points as follows

$$D_t^{-\alpha} f(t) = \frac{1}{\Gamma(\alpha)} \int_0^{t_k} (t_k - \xi)^{\alpha-1} f(\xi) d\xi \quad (\text{A.9a})$$

$$= \sum_{j=1}^k f(\xi_j) \frac{(t_k - t_{j-1})^\alpha - (t_k - t_j)^\alpha}{\Gamma(\alpha + 1)}, \quad (\text{A.9b})$$

where $t_0 = 0$, $t_k = t$ and $t_{j-1} \leq \xi_j \leq t_j$. Considering $\xi_j = t_j$, for instance, Eq. A.9b reduces to

$${}_0 D_{t_k}^{-\alpha} f(t) = \sum_{j=1}^k \left[\frac{(t_k - t_{j-1})^\alpha - (t_k - t_j)^\alpha}{\Gamma(\alpha - 1)} \right] f(t_j), \quad (\text{A.10})$$

which can be written for all $N + 1$ points in a matrix equation as

$$\begin{bmatrix} g_{t_0} \\ g_{t_1} \\ \vdots \\ g_{t_{N-1}} \\ g_{t_N} \end{bmatrix} = \mathbb{I}_{\mathbb{N}}^\alpha \begin{bmatrix} f_0 \\ f_1 \\ \vdots \\ f_{N-1} \\ f_N \end{bmatrix} \quad (\text{A.11})$$

The term $\mathbb{I}_{\mathbb{N}}^\alpha$ is defined as the discrete analog of fractional integration on non-equidistant points. Therefore, in a natural way, the fractional differentiation for non-equidistant points can be obtained by simply inverting matrix $\mathbb{I}_{\mathbb{N}}^\alpha$.

Appendix B

Complex modulus measured by PE machine

This annex presents the results obtained for the temperature and frequency-dependent complex modulus measured by the PE machine discussed in Chapters 4 and 5.

B.1 Experimental results

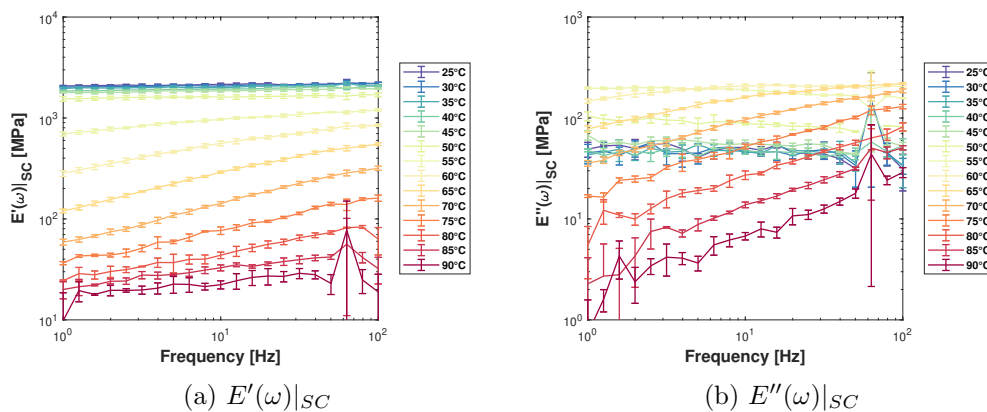


Figure B.1: Complex modulus measured in SC mode by PE machine.

B.1. EXPERIMENTAL RESULTS

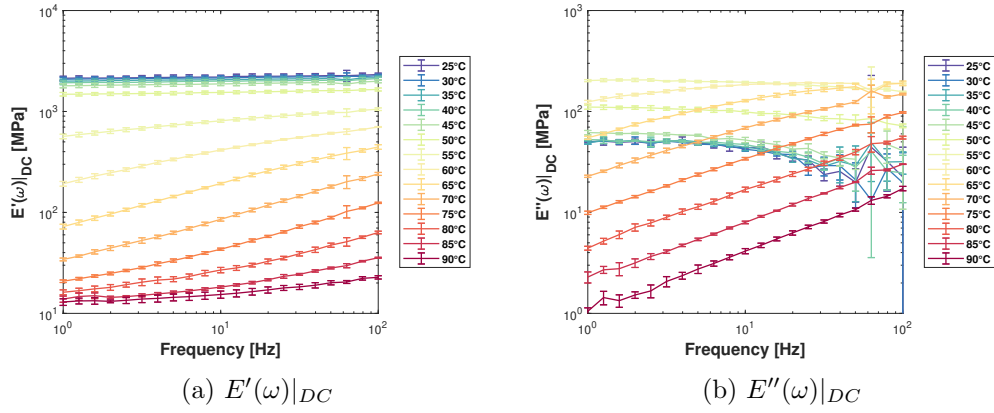


Figure B.2: Complex modulus measured in DC mode by PE machine.

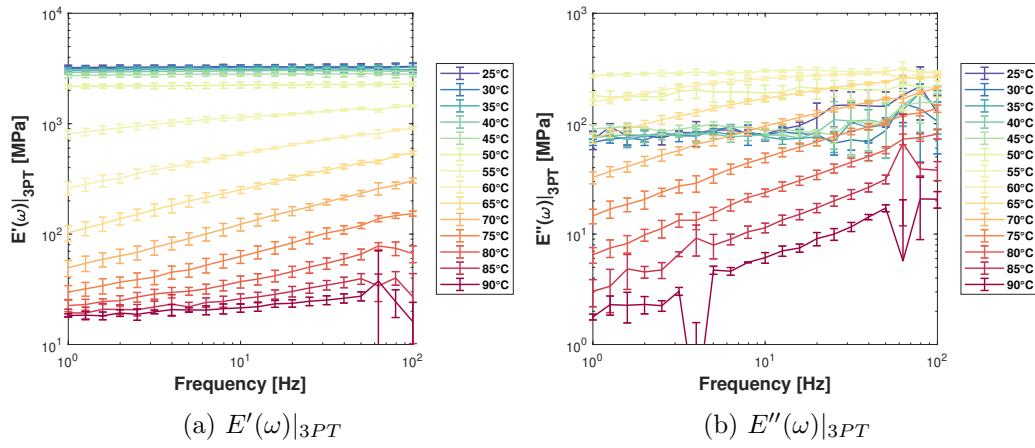


Figure B.3: Complex modulus measured in 3PT mode by PE machine.

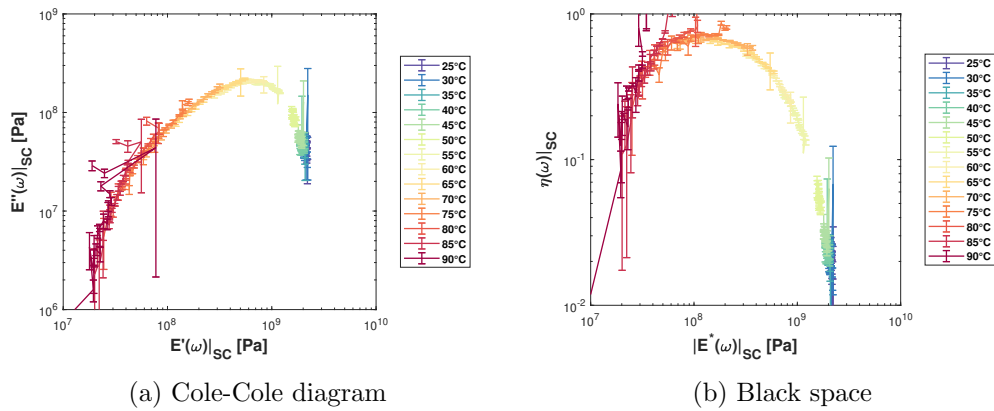


Figure B.4: Validation of thermo-rheological simple behavior considering measurements in SC mode by PE machine.

B.1. EXPERIMENTAL RESULTS

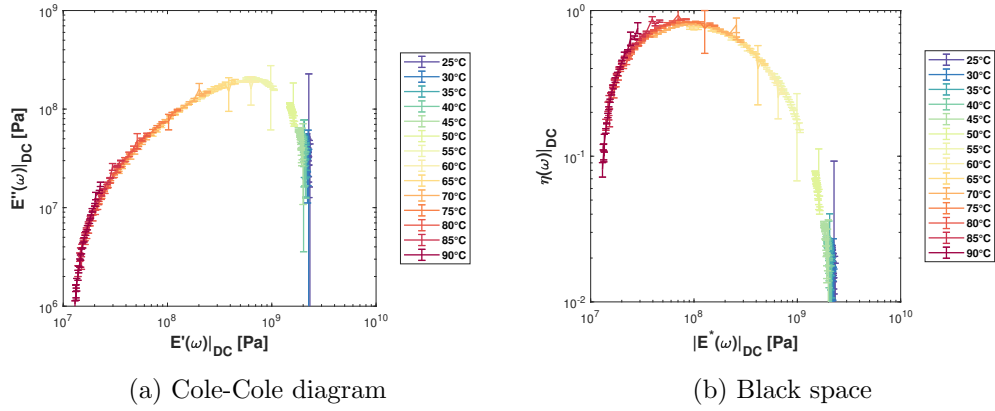


Figure B.5: Validation of thermo-rheological simple behavior considering measurements in DC mode by PE machine.

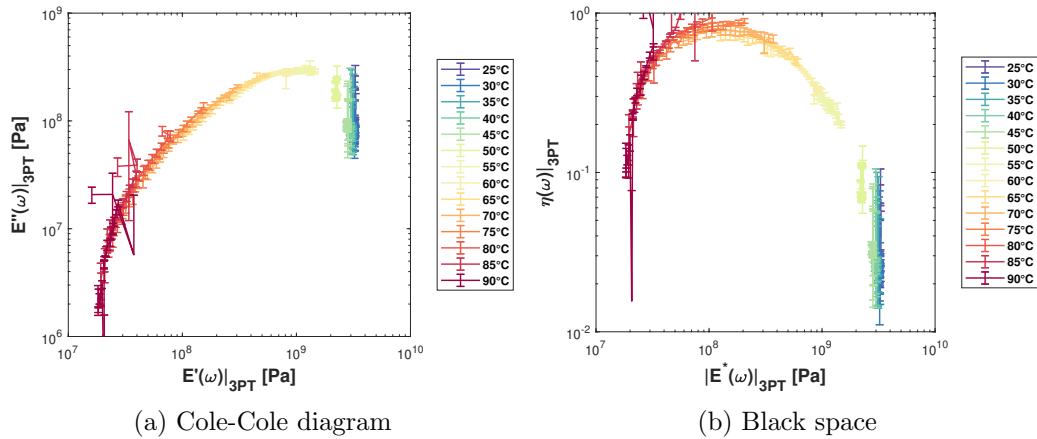


Figure B.6: Validation of thermo-rheological simple behavior considering measurements in 3PT mode by PE machine.

Table B.1: Empirical constants of WLF equation calibrated using measurements obtained by PE machine.

| Constants | SC mode | DC mode | 3PT mode |
|-----------|---------|------------------|------------------|
| C_1 | 8.52 | 9.31 ± 0.47 | 7.65 ± 0.58 |
| C_2 [K] | 57.6 | 63.36 ± 4.14 | 54.15 ± 0.47 |

B.1. EXPERIMENTAL RESULTS

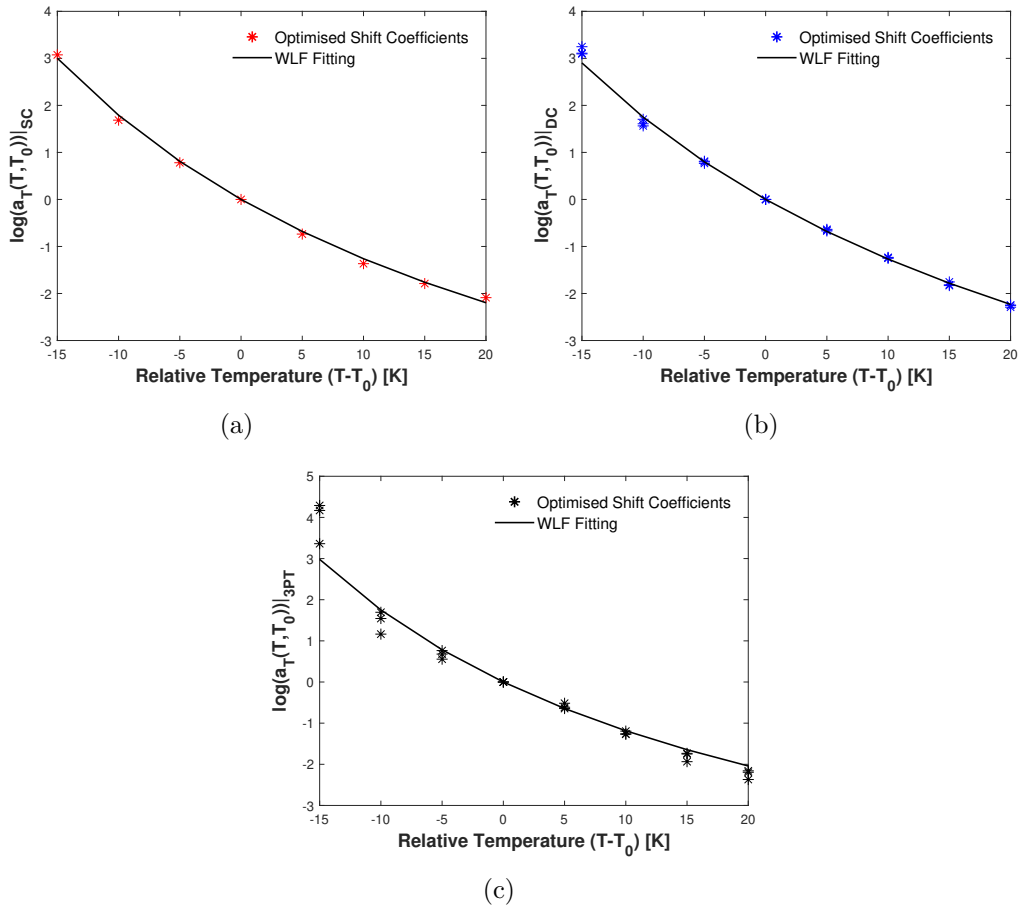


Figure B.7: Horizontal shift coefficients $a_T(T, T_0)$ applied to the isotherms from measurements obtained by PE machine, shown in Figs. B.1-B.3. The optimised coefficients are fitted by WLF equation.

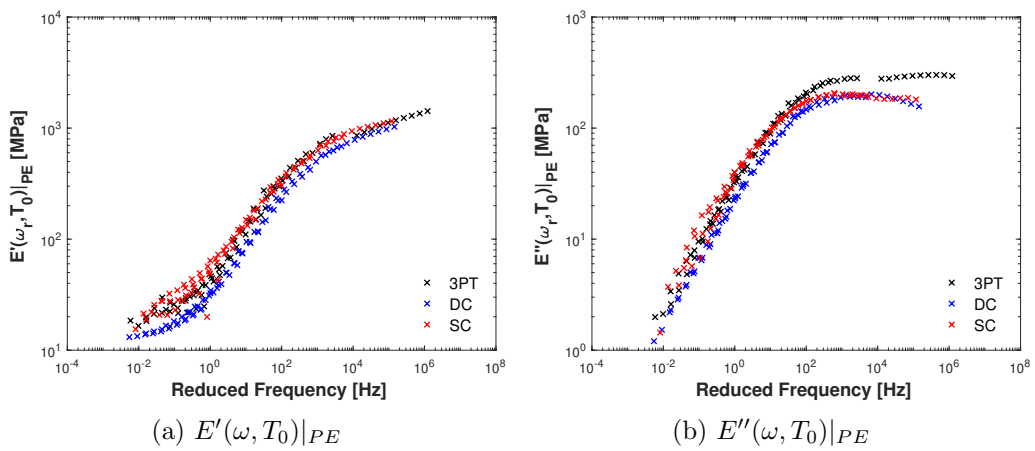


Figure B.8: Comparison between experimental master curves built at $T_0 = 70^\circ\text{C}$ considering measurements of complex modulus by PE machine.

B.2 Modelling temperature and frequency effects

Table B.2: MAP results for the measurements subsets SC, DC and 3PT from PE machine.

| Subset | E_0 [Pa] | E_∞ [Pa] | τ [s] | α | β |
|-----------|--------------------|--------------------|-----------------------|----------|---------|
| Initial | 1.00×10^7 | 1.00×10^9 | 0.50×10^{-3} | 0.5 | 0.5 |
| MAP - SC | 1.55×10^7 | 0.78×10^9 | 1.12×10^{-3} | 0.52 | 0.45 |
| MAP - DC | 1.09×10^7 | 0.64×10^9 | 0.84×10^{-3} | 0.56 | 0.48 |
| MAP - 3PT | 2.50×10^7 | 0.54×10^9 | 3.16×10^{-3} | 0.70 | 0.59 |

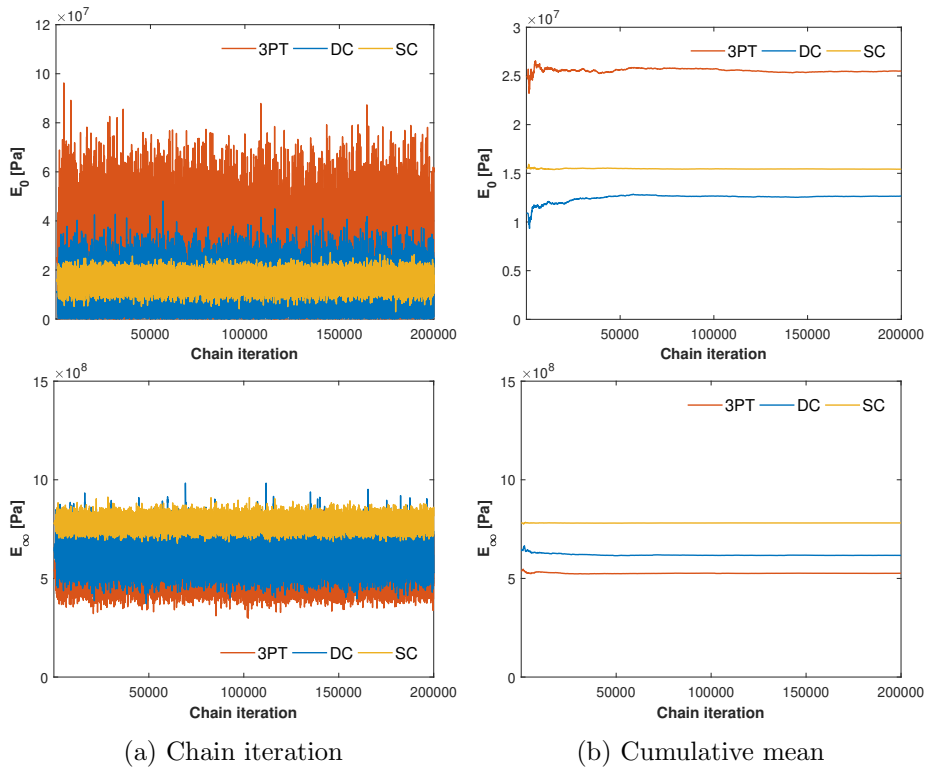


Figure B.9: Convergence analysis for the 5PFDM using DRAM algorithm with each data set from PE machine.

B.2. MODELLING TEMPERATURE AND FREQUENCY EFFECTS

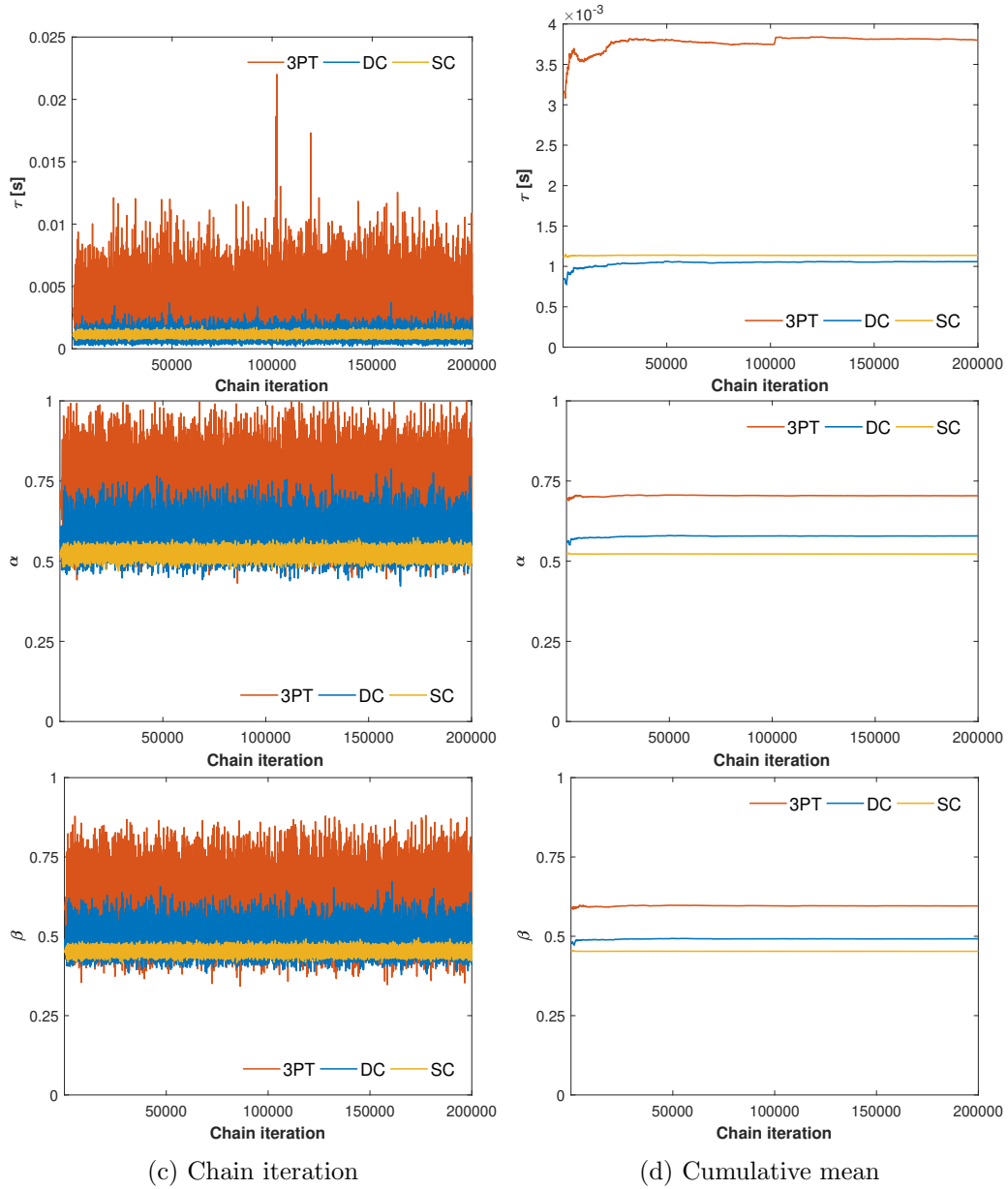


Figure B.9: Convergence analysis for the 5PFDM using DRAM algorithm with each data set from PE machine.

Table B.3: MCMC results using DRAM algorithm for each data set from PE machine.

| Mode | Total samples | Burn-in | Acceptance rate |
|------|---------------|---------|-----------------|
| SC | 200000 | 150000 | 78.20 |
| DC | 200000 | 150000 | 64.40 |
| 3PT | 200000 | 150000 | 72.73 |

Table B.4: Posterior mean value and 95 % credibility interval (CI) of the unknown parameters θ for each data set from PE machine.

| Mode | $\mathbb{E}[E_0] [\times 10^7 \text{ Pa}]$ | $\mathbb{E}[E_\infty] [\times 10^9 \text{ Pa}]$ | $\mathbb{E}[\tau] [\times 10^{-3} \text{ s}]$ | $\mathbb{E}[\alpha]$ | $\mathbb{E}[\beta]$ |
|------|--|---|---|----------------------|----------------------|
| | 95 % CI | 95 % CI | 95 % CI | 95 % CI | 95 % CI |
| SC | 1.53 [1.01, 2.08] | 0.78 [0.73, 0.84] | 1.13 [0.86, 1.45] | 0.52 [0.50, 0.55] | 0.45 [0.44, 0.47] |
| DC | 1.30 [0.11, 2.77] | 0.61 [0.47, 0.81] | 1.08 [0.36, 2.24] | 0.58 [0.49, 0.69] | 0.49 [0.43, 0.58] |
| 3PT | 2.59 [0.21, 5.75] | 0.53 [0.41, 0.67] | 3.78 [1.58, 7.67] | 0.71 [0.55, 0.87] | 0.60 [0.46, 0.75] |

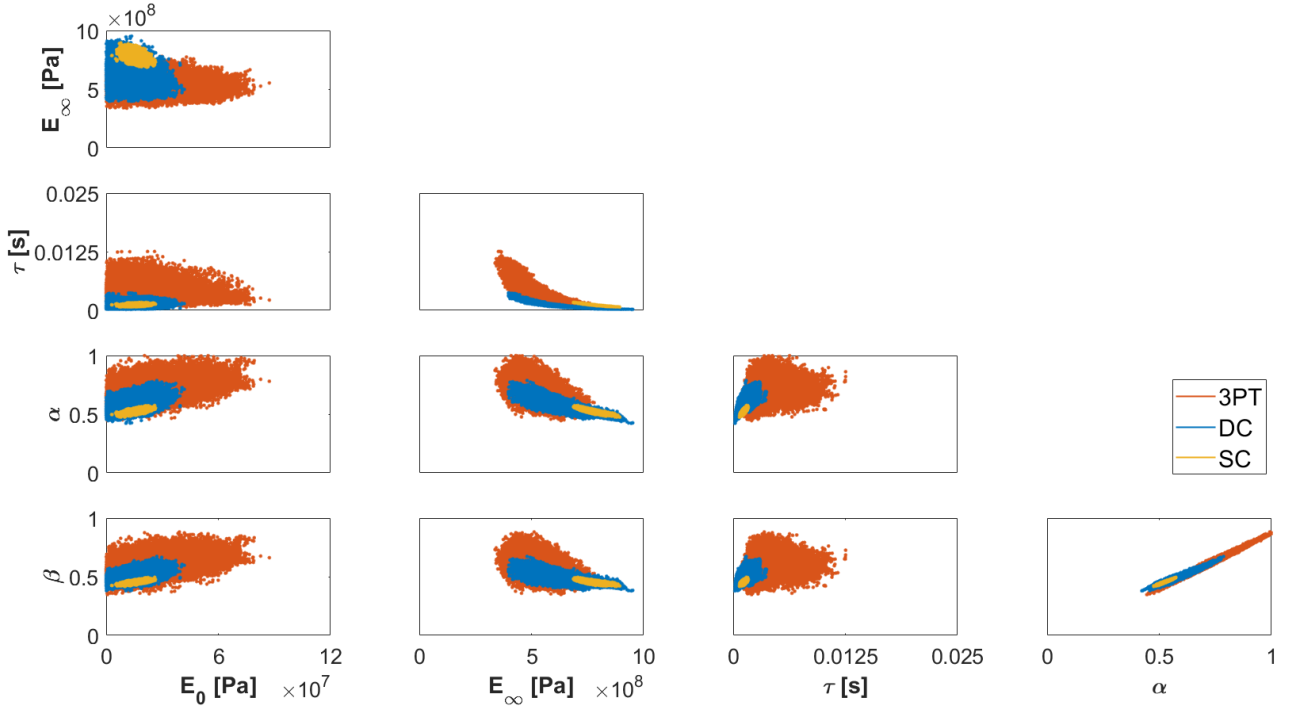


Figure B.10: Posterior samples generated using DRAM algorithm with each data set from PE machine.

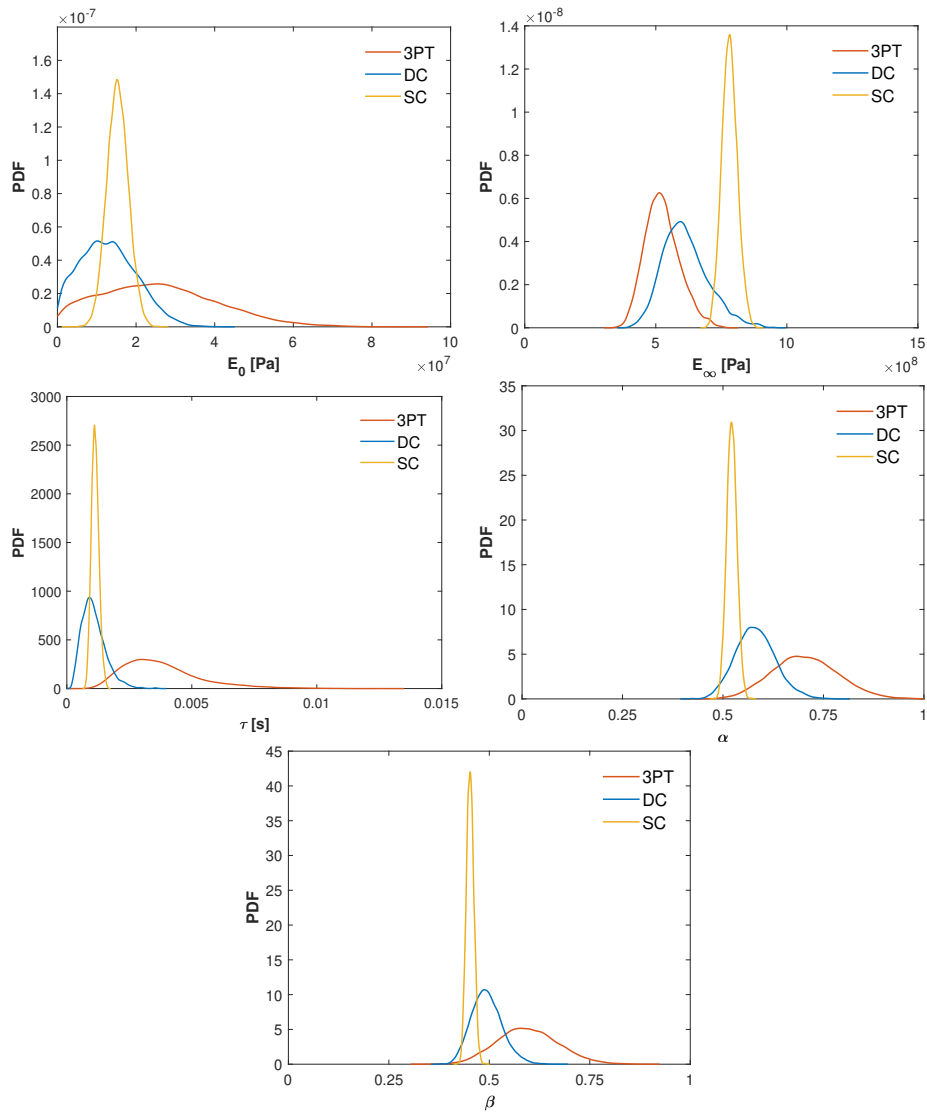


Figure B.11: PDFs for the parameters generated using DRAM algorithm with each data set from PE machine.

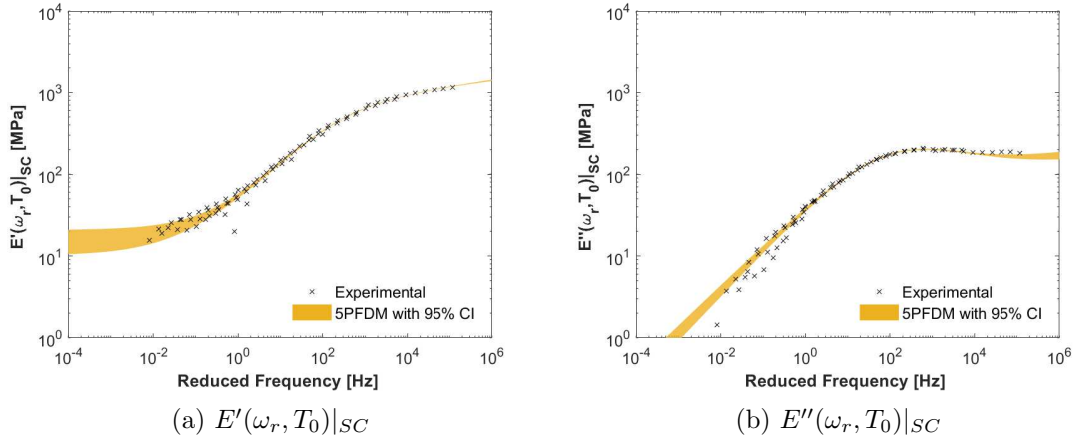


Figure B.12: Uncertainty propagation when considering $\theta \sim \pi(\theta|\mathbf{Y})$ for the data-set of SC mode from PE machine.

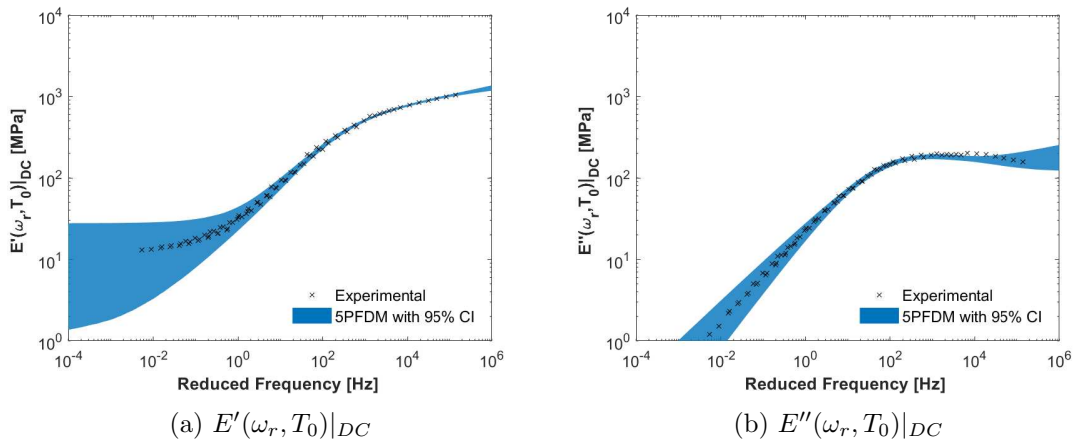


Figure B.13: Uncertainty propagation when considering $\theta \sim \pi(\theta|\mathbf{Y})$ for the data-set of DC mode from PE machine.

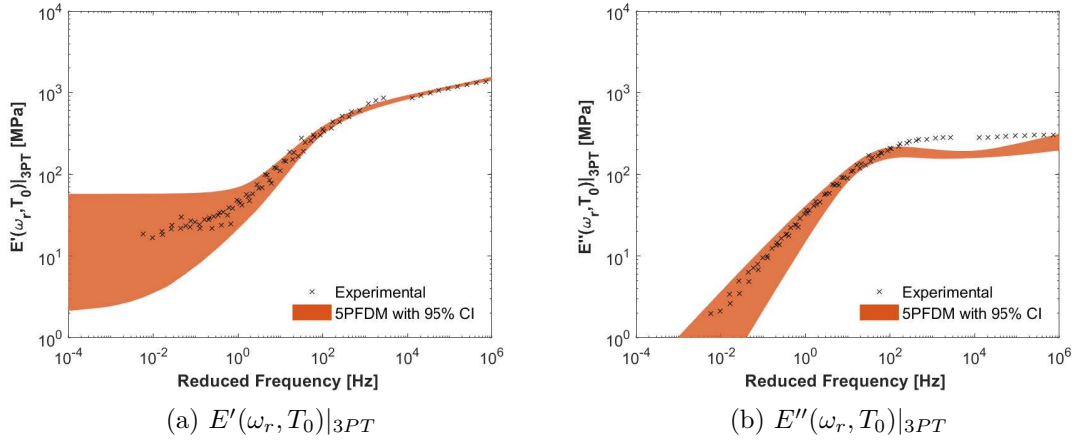


Figure B.14: Uncertainty propagation when considering $\theta \sim \pi(\theta|Y)$ for the data-set of 3PT mode from PE machine.

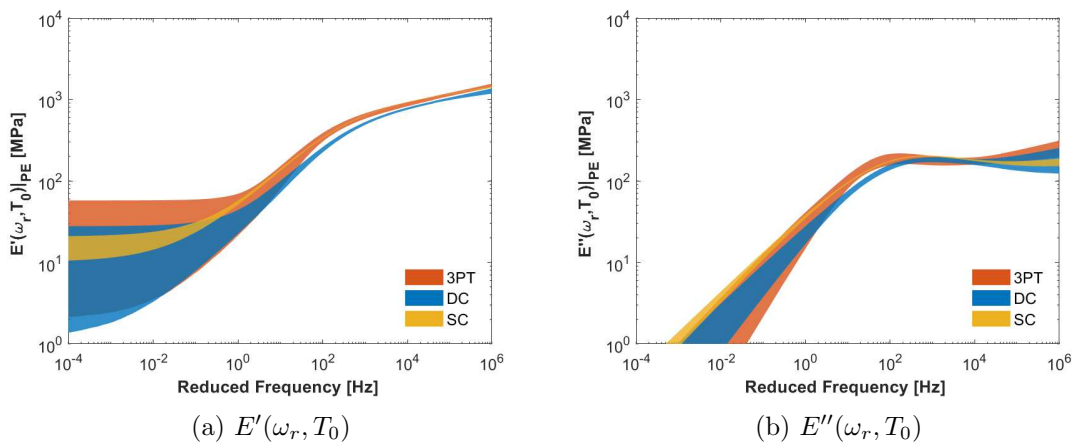


Figure B.15: Comparison between the calibrated models from SC, DC, and 3PT modes of PE machine.

Appendix C

Identification of density ρ

This annex presents the experimental procedure as well as the results of the density ρ of the porous materials described in Section 6.1 of Chapter 6, and subsection 7.2.1 of Chapter 7. All experiments were performed at Centro de Mecânica Não-Linear (MECANON) of COPPE/UFRJ.

C.1 Description of experimental procedure

Cubic samples, having dimensions of approximately $0.025\text{ m} \times 0.015\text{ m} \times 0.015\text{ m}$, were first cut by hand using a box cutter from the same block of material used in the work of Henriques et al. [1], as shown in Fig. C.1. Afterward, they were weighted on a microgram scale (model ATX224 from SHIMADZU), as shown in Fig. C.2.

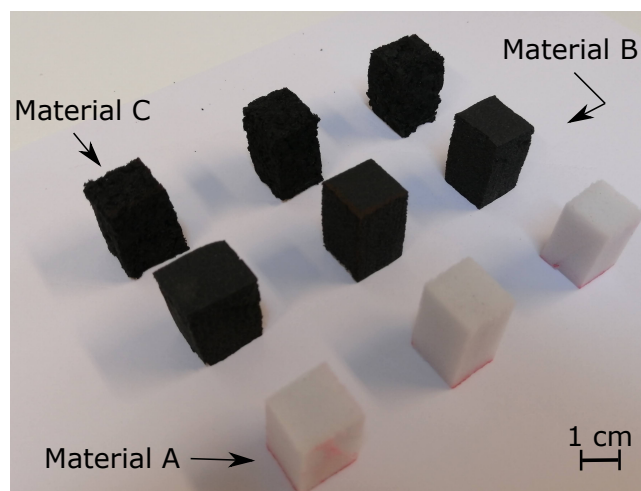


Figure C.1: Photograph showing the samples of materials A, B and C. They were cut by hand using a box cutter.



Figure C.2: Photograph of the microgram scale (model ATX224 from SHIMADZU).

A total of 3 samples of each material were weighted to reduce the risks of abnormalities due to the manufacturing process, and also to verify the repeatability of the measurements. Besides, the normal statistics of sampling and data analysis were performed.

C.2 Results

Table C.1 shows the results obtained of each sample weighted as well as the empirical mean and standard deviation.

Table C.1: Estimated densities ρ [kg/m³] for materials A, B and C, where $\mathbb{E}\{\rho\}$ is the mean value and σ_ρ is the corresponding standard deviation.

| Foam | Sample 1 | Sample 2 | Sample 3 | $\mathbb{E}\{\rho\}$ | σ_ρ |
|------------------------|-----------------|-----------------|-----------------|--|---------------------------------|
| A [kg/m ³] | 9.96 | 9.70 | 10.21 | 9.96 | 0.25 |
| B [kg/m ³] | 47.72 | 50.29 | 49.65 | 49.22 | 1.34 |
| C [kg/m ³] | 236.79 | 248.54 | 243.35 | 242.89 | 5.88 |

Appendix D

Identification of T_g of polymeric foams through DSC technique

This annex presents the experimental procedure as well as the results of the glass transition temperature T_g of the polymeric foams described in Section 6.1 of Chapter 6. All experiments were performed at Centro de Mecânica Não-Linear (MECANON) of COPPE/UFRJ.

D.1 Description of testing equipment and test conditions

Differential scanning calorimetry (DSC) was performed with a DSC 200 F3 from Netzsch, shown in Fig. D.1, to identify the glass transition temperature T_g of the foams studied in this thesis. The experimental procedure followed the recommendations provided by DIN EN ISO 11357-2:2014-07.



Figure D.1: Photograph of DSC 200 F3 from Netzsch.

D.1. DESCRIPTION OF TESTING EQUIPMENT AND TEST CONDITIONS

Initially, the samples were cut by hand using a box cutter, weighted on a microgram scale (model ATX224 from SHIMADZU), and individually sealed in a hermetic aluminum pan using a sealing press (model 6.240.10-80 from Netzsch). Afterward, the sample was put on a chamber with a constant known flux of pure nitrogen. Figure D.2 shows photographs of these experimental apparatus. Finally, two heating/cooling cycles were performed on the machine while measuring the heat flux on the chamber. An empty hermetic aluminum pan was used as a reference. The post-processing was performed by the analysis software provided by the equipment manufacturer.



(a) Microgram scale (model ATX224 from SHIMADZU)



(b) Sealing press (model 6.240.10-80 from Netzsch)



(c) DSC chamber

Figure D.2: Photographs of the experimental set-up.

It is worth mentioning that the first cycle evaluated the material's properties in the as-molded condition. Therefore, it was applied only to erase the material's thermal history and set a known thermal profile upon the sample. The second one, in turn, assessed the inherent properties of the material. As a consequence, it could be used to determine the glass transition temperature T_g .

The description of test conditions for the characterization of each foam is given next.

D.1.1 Foam A

Foam A samples weights of approximately 5 mg were used. Afterward, they are manipulated with pincers and sealed on the aluminum pans individually, as can be seen in Fig. D.3. The experiments were performed on two samples as follows.

Initially, the temperature was set at room temperature about 20 °C. Afterward, constant heating

D.2. RESULTS

was applied to the sample up to 400 °C followed by a constant cooling down to -50 °C (first heating/cooling cycle). Finally, the second heating ramp was applied from 50 to 450 °C followed by the second cooling ramp down to -50 °C. All thermal loads were carried out at a controlled temperature rate of 20 K/min and flow of pure nitrogen of 50 ml/min. The isothermal hold at the beginning of each ramp was 5 min.

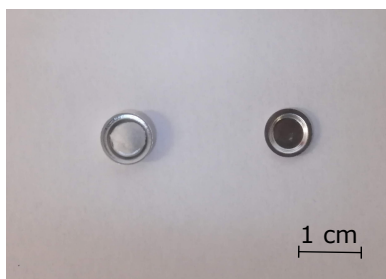


Figure D.3: Photograph showing one of the samples of foam A inside the aluminum pan before it was closed. The sample was cut by hand using a box cutter.

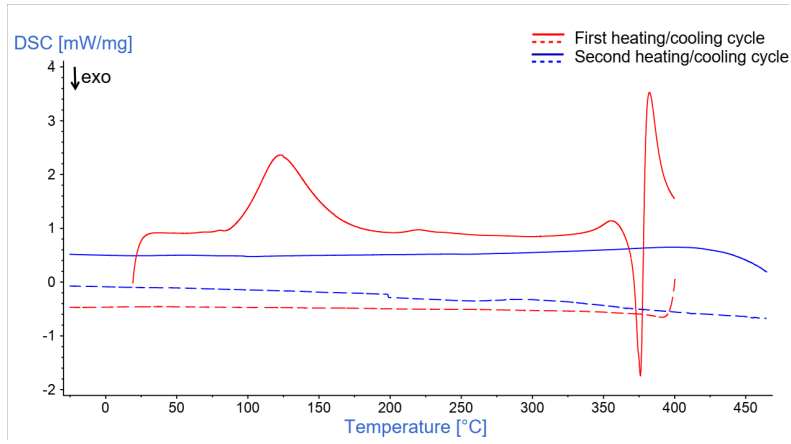
D.1.2 Foam B

As for foam B, sample preparation followed the same procedures described for foam A, with sample weights of approximately 7 g. The experiments were performed on two samples individually with the same temperature rates, nitrogen flow conditions, and isothermal holds used for foam A. Nevertheless, the temperature ranges were different.

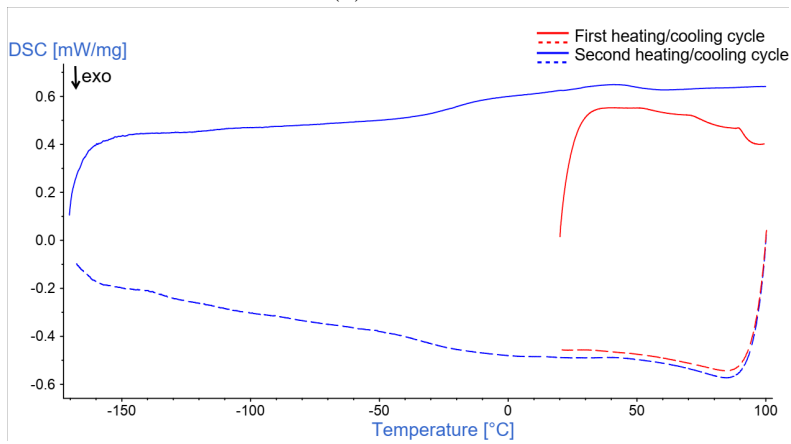
Initially, the temperature was set at room temperature about 20 °C. Afterward, the first heating ramp was applied to the sample up to 100 °C, followed by the first cooling ramp down to -170 °C. In sequence, the second heating ramp was applied from -170 to 100 °C, followed by the second cooling ramp down to -170 °C.

D.2 Results

Figure D.4 illustrates the temperature scans performed for one of the samples of each material studied.



(a) Foam A



(b) Foam B

Figure D.4: DSC scans.

Table D.1 summarizes the results obtained for each foam material tested. It is important to mention that these values were estimated using the onset point.

Table D.1: Estimated glass transition temperature T_g [°C] for foams A and B, where $\mathbb{E}\{T_g\}$ is the mean value and σ_{T_g} is the corresponding standard deviation.

| Foam | $\mathbb{E}\{T_g\}$ | σ_{T_g} |
|--------|---------------------|----------------|
| A [°C] | - | - |
| B [°C] | -35.5 | 0.02 |

Appendix E

MIMO tests and experimental modal analysis

This annex presents the experimental procedure as well as the results of the MIMO (Multiple-Input, Multiple-Output) tests performed for each configuration 2 tested in the second case study (Section 6.3) of Chapter 6. All the experiments were performed at Laboratoire de Mécanique des Structures et des Systèmes Couplés (LMSSC) of Cnam.

E.1 Methodology

Experimental modal analysis was divided into two main parts. The first one is concerned with the experimental measurements of the frequency response functions (FRFs) and the coherence of structure. The second one is related to the modal parameter estimation (natural frequencies, damping coefficients, and mode shapes).

In this work, the roving hammer test was first conducted. Four accelerometers were thus fixed at four different locations, and the structure was impacted at several points to obtain a fair representation of the mode shapes. Figure E.1 illustrates all impact points equally distributed on the panel and the locations of the four accelerometers.

The measurements were recorded up to 800 Hz, with a frequency resolution of 0.5 Hz at ambient conditions (room temperature and in the presence of air). Each FRF was determined from the measured input and output based on averaging three measurements in the complex domain at each frequency.

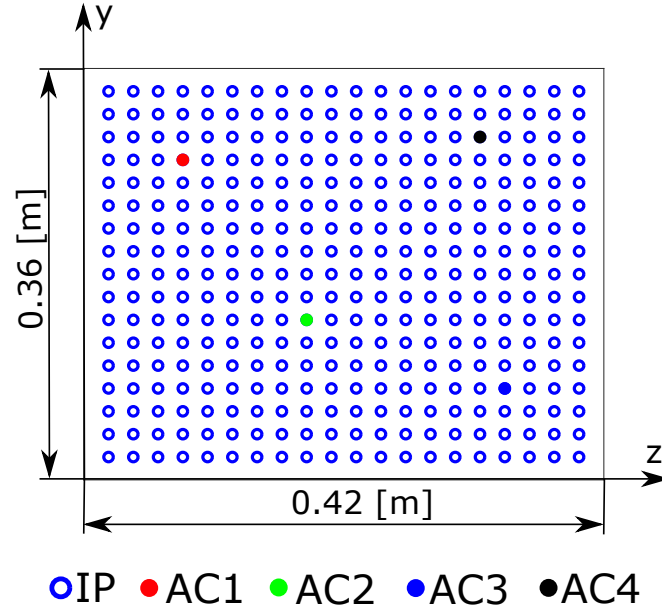


Figure E.1: Experimental mesh.

Then, the post-treatment was performed on an in-house toolbox developed on MATLAB[®] software. The list below summarizes the procedure adopted, evidencing the methods implemented for each step when necessary.

1. Evaluation of the measured FRFs and the principle of reciprocity [136, 146]
2. Evaluation of the measured coherence functions
3. Estimation of the modes of vibration
 - Complex Mode Indicator Function (hereinafter referred to as CMIF) [147]
4. Estimation of the poles
 - Least-Squares Complex Frequency (hereinafter referred to as LSCF) [148]
5. Estimation of the residues
 - Least-Squares Frequency-Domain (hereinafter referred to as LSFD) [148, 149]
6. Estimation of the mode shapes and modal participation

E.2. RESULTS

- Singular Value Decomposition (hereinafter referred to as SVD) [148, 149]

7. Modal validation

- Mean-Phase-Correlation (hereinafter referred to as MPC) [148, 150, 151]
- Mean-Phase-Deviation (hereinafter referred to as MPD) [151]
- Modal Assurance Criterion (MAC) [152]

E.2 Results

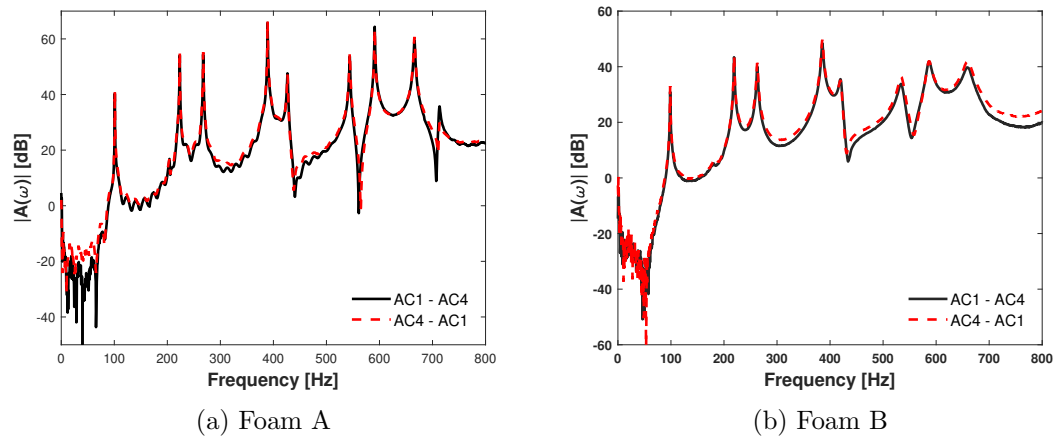


Figure E.2: Averaged coherence function showing the quality of the FRF measurements performed in each configuration 2 tested.

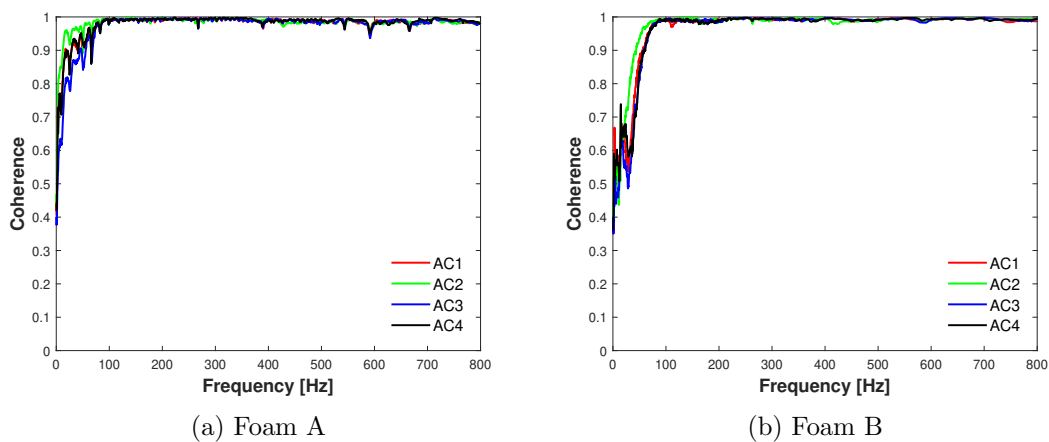


Figure E.3: Averaged coherence function showing the quality of the FRF measurements performed in each configuration 2 tested.

APPENDIX E

Table E.1: Estimated natural frequencies (f_n) and damping coefficients (ζ) for each configuration 2 tested.

| Material | Modal Parameter | 1 | 2 | 3 | 4 | 5 | 6 | 7 | 8 | 9 |
|----------|-----------------|-------|-------|-------|-------|-------|-------|-------|-------|-------|
| A | f_n [Hz] | 101.0 | 223.3 | 267.7 | 389.0 | 426.6 | 544.1 | 590.9 | 665.9 | 712.3 |
| | ζ [%] | 0.10 | 0.06 | 0.06 | 0.05 | 0.16 | 0.14 | 0.07 | 0.14 | 0.25 |
| B | f_n [Hz] | 98.6 | 219.1 | 262.8 | 385.4 | 420.1 | 538.4 | 586.8 | 659.8 | 692.1 |
| | ζ [%] | 0.30 | 0.24 | 0.38 | 0.36 | 0.60 | 0.64 | 0.71 | 1.18 | 1.58 |

Table E.2: Validation of the estimated modes for each configuration 2 tested.

| Method | | 1 | 2 | 3 | 4 | 5 | 6 | 7 | 8 | 9 |
|--------|---------|------|------|------|------|------|------|------|------|------|
| A | MPC [%] | 87.4 | 95.9 | 96.6 | 96.5 | 99.6 | 99.7 | 98.5 | 99.5 | 99.6 |
| | MPD [°] | 6.4 | 6.4 | 5.7 | 5.3 | 2.5 | 2.4 | 3.7 | 4.0 | 3.0 |
| B | MPC [%] | 99.4 | 99.9 | 99.9 | 99.8 | 99.6 | 99.7 | 99.9 | 97.2 | 94.6 |
| | MPD [°] | 1.6 | 1.3 | 1.6 | 1.3 | 2.9 | 2.0 | 2.0 | 7.5 | 11.0 |

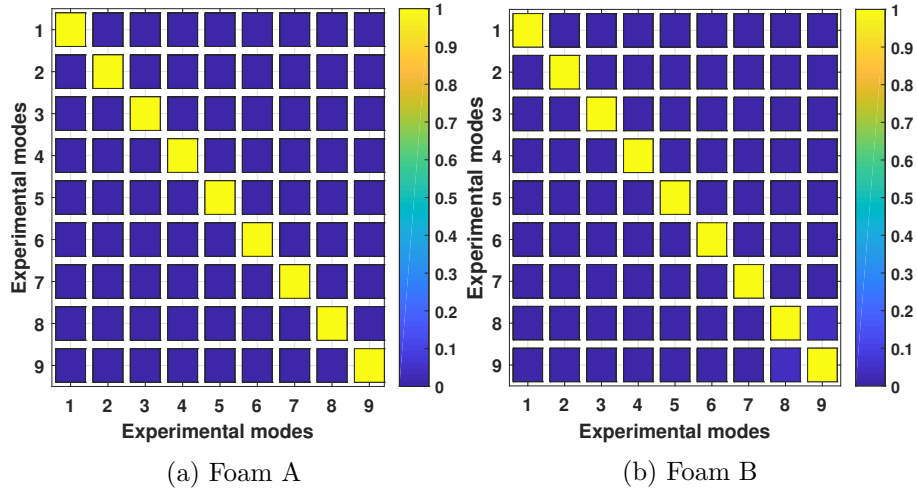


Figure E.4: Auto-MAC with experimental modes for each configuration 2 tested.

Résumé : Cette thèse porte sur la modélisation et la caractérisation du comportement thermomécanique des matériaux viscoélastiques et poro-viscoélastiques. Le travail est divisé en deux parties principales : une concerne la technique expérimentale d'analyse mécanique dynamique (Dynamic Mechanical Analysis DMA) et l'autre s'intéresse aux performances d'amortissement des matériaux poro-viscoélastiques. Dans la première partie, les propriétés viscoélastiques décrites à partir du module complexe et mesurées par DMA en flexion, sont analysées en profondeur à la fois d'un point de vue théorique et expérimental. Une attention particulière est accordée aux effets des modes opératoires et des machines d'essais utilisées sur les propriétés mesurées. Afin d'obtenir une meilleure analyse de l'influence des écarts constatés, des modèles à dérivées fractionnaires (FDM) sont calibrés dans le cadre bayésien. Les résultats montrent qu'il existe une grande variabilité en fonction des modes de fonctionnement ou des fabricants de machines et que les modèles statistiques peuvent expliquer ces différences. Dans la deuxième partie, la dissipation de l'énergie mécanique due à la viscoélasticité de trois matériaux poreux différents est explorée dans la gamme des basses fréquences. Dans un premier temps, une approche numérique est proposée pour générer des prédictions dans le domaine temporel du comportement hystérique des matériaux sous différentes conditions de chargement. Ensuite, un modèle éléments finis utilisant un FDM est proposé pour décrire le comportement de panneaux simplement appuyés et recouverts d'une couche libre de matériau poreux. Des expériences sont réalisées pour valider le modèle proposé. Enfin, une méthode inverse basée sur l'inférence bayésienne est présentée pour identifier les propriétés viscoélastiques de ces matériaux à partir d'essais de vibration. Les résultats de ces analyses montrent le grand potentiel des matériaux poro-viscoélastiques pour l'amortissement des vibrations mécaniques.

Mots clés : Matériaux viscoélastiques, Matériaux poreux, DMA, Essais mécaniques, Modélisation thermomécanique, Inférence bayésienne.

Abstract : This thesis deals with the modeling and characterization of the thermomechanical behavior of viscoelastic and poro-viscoelastic materials. The work is divided into two main parts: one concerning the experimental technique Dynamic Mechanical Analysis (DMA) and the other related to the damping performance of poro-viscoelastic materials. In the first part, the viscoelastic property known as complex modulus measured by the flexural modes of DMA is deeply examined theoretically and experimentally. Special attention is paid to the effects of operational modes and machines on various properties. Aiming to obtain a better analysis of the impacts of the discrepancies found, fractional derivative models (FDM) are calibrated within the Bayesian framework. Results show that DMAs have a great variability between modes or manufacturers and statistical models may mitigate these issues. In the second part, the dissipation of mechanical energy inherent to the viscoelasticity of three different porous materials is explored in the low-frequency range. Initially, a numerical approach is proposed to generate predictions in the time domain of the hysteretic behavior of the analyzed materials under different loading conditions. Then, a finite element model that considers a FDM is proposed to describe the behavior of simply supported panels covered with a free-layer of porous material. Experiments are carried out to validate the proposed model. Finally, an inverse method based on Bayesian inference was presented to identify the viscoelastic properties of these materials from vibration tests. The results of these analyses showed the great potential of poro-viscoelastic materials to be applied to damp mechanical vibrations.

Keywords : Viscoelastic materials, Porous materials, DMA, Mechanical testing, Thermomechanical modeling, Bayesian inference.